Volume 16

THE NUCLEAR SOCIETIES OF ISRAEL

The Israel Nuclear Society
The Israel Health Physics Society
The Israel Society of Nuclear Medicine
Radiation Research Society of Israel
The Israel Society of Medical Physics

TRANSACTIONS

JOINT MEETING 1990

HERZLIYA

December 17-18, 1990

Volume 16

THE NUCLEAR SOCIETIES OF ISRAEL

The Israel Nuclear Society
The Israel Health Physics Society
The Israel Society of Nuclear Medicine
Radiation Research Society of Israel
The Israel Society of Medical Physics

TRANSACTIONS

JOINT MEETING 1990

HERZLIYA

December 17-18, 1990

ORGANIZING COMMITTEE

A. Ketter (Chairman), Israel Atomic Energy Commission

J. Szabo (Editor), Israel Atomic Energy Commission

Z. Alfassi, Ben-Gurion University, Negev

T. Biran, Nuclear Research Center, Yavnne

E. Elias, Technion

D. Litai, Israel Atomic Energy Commission

E. Riklis, Nuclear Research Center, Negev

L. Tepper, Israel Electric Corporation

T. Tzwas, Tel-Hashomer Hospital

E. Wacholder, Technion

THIS MEETING WAS MADE POSSIBLE BY THE
ASSISTANCE AND GENEROSITY OF:

The Israel Electric Corporation Ltd.

Israel Atomic Energy Commission

The Israel Academy of Science and Humanities

Ministry of Science and Technology

Ministry of Energy and Infrastructure

Table of Contents

MESSAGE TO THE 16TH MEETING OF THE NUCLEAR SOCIETIES IN ISRAEL

OIL, CLEAN AIR AND NUCLEAR ENERGY

Louis Tepper
President, The Israel Nuclear Society

This message is being written six weeks before our Meeting, due to the printers' deadline. The Gulf crisis being what it is, no one knows how things will look like when the Convention opens. What is the bearing of this crisis on our Meeting?

The meeting is all about peaceful applications of nuclear energy, whether electric power, nuclear medicine, radiation protection, research, industrial uses. The Gulf crisis on the other hand, is basically about oil, even if it manifests itself by aggression and a corresponding worldwide response. I shall try to show here that a crisis was bound to explode and that other crises are still waiting in the wings, unless a fresh look is taken to tackle the ever present energy problem.

Oil is an energy life-line for modern civilization. Cutting that life-line, or even threatening to cut it, is like withholding food from starving people. At the time of the Yom-Kippur war, when Israel's very existence was at stake, the industrial world got very anxious, not about Israel but about the spectrum of oil scarcity. Most nervous of all got Japan, and for good reasons: An industrial super-power on the one hand, totally dependent on foreign energy supplies on the other. Japan's whole economy is based on a continuous and uninterrupted flow of goods and raw materials into and out of the country, as well as within it. A constant supply of fuel for industry and transport is vital and any interruption may spell total crumbling of that colossal and intricately balanced industrial structure.

Japan seems to have learned the lesson and is today in the forefront of the process of conversion from fossil to nuclear energy, gradually reducing its day-to-day dependence on foreign oil. Though still far behind France in the fraction of nuclear electric power in its grid, Japan is building and putting into operation modern nuclear plants at a pace unequaled elsewhere. France of course pioneered oil-independent electricity and today produces about 80% nuclear.

It may be argued that even if all electricity were generated from nuclear energy, this would still not solve the problem of oil dependency, since electricity counts for only a fractional use of total primary energy. It is also true that nuclear is not the only alternative: there is coal, there are the renewables such as hydro, *geothermal, solar or wind power.*

Let us examine the above points one by one. First the use of electricity, then coal as fuel, lastly the renewables.

Electricity accounts today for 34% of the industrial countries' primary energy consumption, whereas in the developing countries it is only 15%. Clearly industrialization goes together with electrification. Japan is on top with 41%, the USSR only 28%. Countries with the highest proportion of electricity in primary energy consumption are also those with the highest energy efficiency, when measured as the ratio of energy consumption over gross national product: In first place are Japan (again) and France, with an efficiency nearly 4 times higher than that of the Soviet Union (0.2 toe/1000 $ GNP [tons of oil equivalent per Gross National Product] as against 0.7 in the USSR).

On top of the advantages of higher energy efficiency, more electrification means that a larger amount of energy can be made oil-independent. For example, if all the industrial countries would have an electricity percentage like that of Japan today (41%), and if it were all nuclear or renewable, then the fossil part of primary energy consumption would come down from the present 87% to just 59%, and that means a lot. It means a reduction of one third of total fossil consumption. It means, in terms of today's energy consumption, burning 1,500 million tons of oil equivalent less a year. 11 billion barrels!

As a matter of fact, OECD estimates for the year 2000 point to 42% of primary energy for electricity in Europe and North America, and 45% in the Pacific Basin. There is no reason why these figures cannot be achieved and surpassed. And there is no reason why this electricity should not be nuclear, instead of the meager 7% today. Or nuclear and renewable (13% today).

There is a huge area of energy consumption which seems to be "reserved" for oil: transport. In the industrial countries transport uses about a quarter of total primary energy, much of it taken up by road transport. On this subject one thinks of oil almost as an axiom. However I can see no fundamental reason why all or much of road transport should not be electrified, just as most of West European rail is all-electric today. And I am not thinking of some fantastic web of overhead trolley-type electric feeders. I am thinking of batteries, powerful and light enough to run electric vehicles for reasonable distances before recharge or exchange.

Much research is being done on this subject, but in my mind not nearly enough, if one thinks of the extraordinary advantages worldwide in respect of oil-dependency, air pollution and the greenhouse effect. In a sense it seems odd that a century after the motor-car's invention it still carries basically the same internal-combustion engine it had at the beginning of the motor-age. This in a century of unequaled technological revolutions: the nuclear age, the computer age, the jet age, radar, interplanetary navigation, to mention only a few. Why then the curious spectacle of half a billion power stations on wheels rumbling on this planet's roads! And a car's engine is a miniature power plant. It works in a way not much different, basically, from a station generating 10,000 times more power.

If a major part of road transport were electrified, then at least two thirds of primary energy could be electric in the industrial countries. In other words, nuclear fuel and renewables could make up for most energy needs, dramatically reducing oil-dependency and air pollution.

The second point to be examined is coal as alternative to oil. As a matter of fact, since the first oil crisis in 1973, most industrial countries have indeed used both coal and nuclear in new power stations, and coal in many applications where oil was used before. Israel is an excellent example. Oil dependency has been reduced. Modern techniques of exhaust purification are capable of keeping the air fairly free of pollution. However, all fossil fuels, including of course coal, release CO_2, which is largely responsible for the greenhouse effect, the global warming which could have disastrous consequences for the planet as a whole, even if there are no direct local effects.

The last point are the renewables. Hydroelectric and geothermal plants account for some 6% of primary energy in the industrial countries. There doesn't seem to be very much room for increase in this area, either because of lack of available locations or because of the great ecological damage inflicted. Then there is solar power which is now on the increase, but which for large central power stations where vast areas of sunshine collection are necessary, will hardly become economically competitive and practical in the foreseeable future.

Solar will definitely have a place in special applications, in certain locations and for time-peaking purposes. Wind power is attracting much interest, but probably will also be practical for special locations only. These and other renewable sources of energy should and will be exploited, and their efficiency improved. But they cannot be considered seriously as major primary energy providers, of the class of coal, oil or nuclear.

All the facts described so far are well known. Why then is nuclear electricity not being massively increased in order to reduce oil dependency, air pollution and global warming? It seems that decision makers in the West prefer in general to go along lines of least resistance and not always take the long look, at least not when in their minds the problem is not of an urgent nature. So, since an anti-nuclear cult swept large parts of Europe and North-America, the easiest thing was either not to decide, or even decide to phase out nuclear altogether, as in Sweden; until, that is, they realized power is running out and decided to <u>increase</u> the nominal power of certain nuclear plants in order to close down two other plants according to schedule. Now the whole issue of phasing-out nuclear is being reconsidered in Sweden.

It is interesting to read learned articles in reputable journals, analyzing the dual problems of oil scarcity and global warming, in which every imaginable source of energy is scrutinized except nuclear; it is either ignored completely, or dismissed as impractical because of public suspicion.

One of the fallacies of the anti-nuclear movement is that the problem can be solved by saving energy. Of course energy should not be wasted, and certainly there is plenty of waste to be trimmed off in the industrial countries. However, it is wishful thinking to believe that energy supply can be cut beyond a certain level. Economic needs do not allow for such pious remedies. Economy is stronger than any ideology, even if that ideology were good for humanity, and it is not: Thanks to plentiful supply of energy and accompanying revolutionary advances in science and technology, man lives better and at least 20 years longer than a century ago, in the industrial countries. In developing countries the quest for a better life is closely linked to the abundant supply of inexpensive energy.

It is one thing to preach energy-saving from the comfort of a well heated home and all the modern amenities. Another view altogether exists in that major part of the world called the developing countries. Four billion people in the developing countries consume today two thirds of the amount of energy which one million in the industrial countries consume.

In other words, the per capita consumption of energy is six times larger in the industrial countries. Do the anti-nuclear energy-savers in the West want all of us to descend to the level of developing countries? I hardly think so. Do they believe that the developing countries will stay content with the present division of energy between rich and poor countries?

Civilization goes hand in hand with energy supply. The natural instinct of man - and nations - is to live better. Sometimes he will fight to achieve just that. I shall take the liberty of quoting myself from my message to the 15th Meeting, March 1989 in Beer-Sheba: "This trend (the unpopularity of nuclear power) will probably change only when the next unavoidable energy crisis occurs, hopefully without war".

We are now in the middle of just such a crisis and, whatever the outcome, a new outlook on the whole energy landscape is unavoidable. Things cannot just go back where they were, "business as usual". After this crisis, others are in the offing sooner or later. Let us not forget that two thirds of the world oil reserves are in this area.

If decision makers will draw the necessary conclusions for long-term solutions, increased electrification, nuclear power and renewable sources of energy will be high in the agenda of energy planners. It should not be that much of an Utopia to think of a world in which most of the energy is delivered electrically and oil is not being burnt anymore but used mainly for structural materials. This will largely eliminate oil-dependency and contribute a great deal to solving the global warming problem.

INVITED PAPERS

Risk and Risk Aversion in Our Society

Bernard L. Cohen
University of Pittsburgh
Pittsburgh, PA 15260

Abstract

A large variety of risks are quantified in terms of the loss of life expectancy they cause in the U.S. Risks considered include diseases, accidents of various types at home, at work, in public, and in motor vehicles, unemployment, being unmarried, using small cars, smoking, air pollution, other environmental pollutants leading to cancer and non-cancer effects, purposely ingested substances, sports participation, geography, medical care, epidemics, natural hazards, socioeconomic factors, radon and other radiation, and energy conservation.

Can Nuclear Power Improve Israel's Economic Security?

Bernard J. Snyder
President
Energy and Management Consultants Corp.
Potomac, Maryland, USA

Introduction

The question of Israel's economic security, which is one essential element of national security, is tied to the issue of adequate, safe, reliable, and cost effective sources of electric energy. Although there are many well-known political impediments to initiation of a nuclear power design and construction program, there are also many considerations that argue in support of such a program. This paper will examine the following three aspects of this vital question: (1) Possible strategies for Israel to follow, (2) Current status of advanced nuclear power plant design in the U.S. and potential opportunities for Israel, and (3) Lessons to be learned from other developing country's indigenous nuclear power programs.

Objective for an Expanded Electric Energy Supply for Israel

The primary objective of any future electric energy program should be ensuring a safe, secure and highly reliable supply of electric power to expand the Israeli economy with reasonably priced electricity. This objective should be met without outside reliance on fuel supplies which are vulnerable to interruption by Israel's adversaries. Current dependence on fossil fuels, without sufficient domestic supplies, appears to place Israel in a highly undesirable position.

(1) Possible Strategies

Nuclear power could satisfy this objective. Use of a proven, standardized nuclear plant, sized to not reduce the reliability of the Israeli power grid would be a requirement. Assurance of fuel supply could be provided by use of the same proven design of fuel assemblies in all nuclear plants, and acquisition or fabrication of a number of cores which would be safely stored within the country. Fuel supplies could be assured for decades, providing Israel with energy independence for production of electricity.

Israel's options for acquiring one or more nuclear power plants from foreign suppliers has been constrained, in the past, by the political decision not to sign the (Nuclear) Non-Proliferation Treaty, or NPT. However some recent events

indicate that there may be more flexibility by suppliers than previously has been the case.

Earlier this year, it was announced that France had agreed to supply a 900MWe-class PWR to Pakistan, following President Mitterrand's visit to Pakistan. In April, French officials met in Pakistan, and Frametome negotiators were to follow. Pakistan is not an NPT signatory, but apparently has agreed to permit international inspection of any nuclear power facility that the French would supply. This approach is analogous to that which occurred in 1988 when the Soviet Union sold two reactors to India, without full-scope safeguards applied to all Indian nuclear facilities. China has also announced that they would supply a reactor to Pakistan, although the status of this project is uncertain.

Following this precedent for these two protagonists who are non-signatories of the NPT, Israel may be able to acquire one, or more nuclear power plants by agreeing to international inspection for those plants.

Based upon public reports, Israel apparently has taken some initiative along these lines with the Canadians for possible acquisition of a CANDU system. It was reported that the Israeli and Canadian Energy Ministers met in Ottowa in the fall of 1989, and discussed a CANDU reactor facility with a commitment by Israel to international inspection. Such a reactor design would be highly desirable for Israel if no enrichment of uranium were required and domestic supplies could be utilized. In fact, the natural uranium, heavy water design may be the best option for Israel, even if the design and construction were to be undertaken as an indigenous project, with little, or no outside assistance.

The possible strategies for Israel to follow appear to be: (a) Continuing to pursue purchase of a CANDU system, or a light water reactor (LWR) with a commitment to international safeguards inspections, (b) Developing an indigenous nuclear program, preferably based on a natural uranium, heavy water system, or (c) Combination of both (a) and (b). In any case, Israel should ensure that any nuclear program include training and technology transfer to the maximum feasible extent. Israel should also maximize the domestic supply of components, including fuel.

(2) U.S. Advanced Plant Designs and Opportunities for Israel

Before discussing the U.S. advanced reactors, it is useful to consider some basic statistics on the U.S. and world-wide usage of nuclear energy in order to properly context the future nuclear plans. At the end of 1989, nuclear was 17% of the world-wide total of electricity generation, or about 1.85 trillion KwH. This nuclear energy generation is equivalent to all sources of electric energy production in 1958. About 3.35 billion barrels of oil would have been required to replace this nuclear generation. To date, more than 5200 reactor years of operating experience has been achieved world-wide. By the end of 1990, it is anticipated that 449 reactors will be operating world-wide, with 112 operating in the U.S. These reactors represent an operating capacity of about 350,000 MWe and 100,000 MWe, respectively.

For the U.S., nuclear represents almost 20% of installed electric generation capacity, second only to coal. Recent legislation to provide cleaner air, along with generally greater concerns about environmental effects and global warming, coupled with reduced generating capacity margins in the northeastern and southeastern areas will improve nuclear's chances of a major revival in the U.S. in the next five years.

Major efforts are underway in the U.S. to design and license improved nuclear power plants. These efforts involve the major nuclear plant designers: Westinghouse, General Electric, ABB Combustion Engineering, and General Atomic, along with the U.S. Department of Energy (DOE) and the Electric Power Research Institute (EPRI). In addition, the U.S. Nuclear Regulatory Commission (NRC) is reviewing designs for certification under their new licensing reform regulations.

Table I. provides a summary of all future reactor designs that are currently being considered by the NRC. As may be seen, three categories of reactors are being considered: Evolutionary LWRs of 1300MWe derived directly from current LWRs, Advanced Passive LWRs, and Advanced Non-LWR Designs.

Advanced reactor designs that are the most viable options for the near future are those based on the more than 30 years experience with Light Water Reactors (LWR). Gas cooled and liquid metal cooled reactors will not, in my opinion, be near-term options. The future Advanced Reactor designs will be developed with the following characteristics:

- Simplified Design - Plant designs will be simplified and modularized to permit prefabrication of major sections at an offsite manufacturing facility. Increased complexity

in current U.S. plants is adversely affecting initial capital cost, operating costs, availability, operability, and maintainability. The mistakes of the past designs must not be repeated.

- Design Margins - Substantially increased design margins will be provided to accommodate adverse situations during normal operations, transients and accidents. One of the lessons learned from the TMI-2 accident is that plant designs must be "more forgiving", easier to control and less dependent upon operator actions.

- Proven Technology - Plants designs must be based upon successfully proven technology, preferably through operational experience, but allowances must be made for prototype testing where advances in designs are dictated by safety or economic considerations.

- Safety - Safety must continue to be the dominant consideration in plant designs. Nuclear safety requires a management approach that encourages teamwork, discipline and the attitude that safety practices and design principles are inviolate. Chernobyl demonstrated that a serious nuclear accident anywhere is an accident everywhere, not only because radioactive fission products do not respect national borders, but also because the political fallout rains on every nation. Safety considerations will include:

  o Simplification - Simplified designs have enhanced reliability and will be more likely to perform their intended functions. With greater design margins, simplified systems will reduce demands on the operator during both normal and emergency situations.

  o Passive Safety Systems - Inherently safe, passive safety systems will be incorporated in the advanced designs. For example, natural circulation to the ultimate heat sink and stored energy devices will be included.

  o Severe Accident Considerations - Both prevention and mitigation of severe accidents will be provided, with high confidence, by the design.

Some of the design characteristics of the Westinghouse/Burns and Roe Advanced Design are given in Table II., as an example of the current approaches being developed. This 600MWe PWR, designated AP-600, is one of the two LWR designs partially supported by the U.S. DOE and EPRI. Figure I. provides a schematic view of key features of the AP-600 nuclear island.

The other 600MWe design selected for DOE and EPRI support is the Simplified BWR of GE.

It is conceivable that Israel might be able to participate in the revitalization of the nuclear power industry by evaluating the applicability of the Advanced Design efforts and considering requesting proposals for supply of one of the plants. Obviously the political climate will need to change before this strategy can be considered feasible. This change is not impossible, given the desire for the sale of a U.S. supplied reactor, coupled with increased U.S. support for the viability of the Israeli economy that could be one outcome of the current Persian Gulf crisis.

(3) Indigenous Nuclear Power Programs

Lessons may learned by reviewing the experience of indigenous nuclear power programs of other developing countries. The largest of these programs has been underway in India for many years. Although only moderately successful, there is much to be learned from the Indian experience. The Indian civilian nuclear power program started with the two TAPS BWRs supplied by GE in the 1960's and the two RAPS CANDUs supplied by Canada in the 1970's, With the cutoff of nuclear supplies, India embarked on their indigenous program which produced the two MAPS and two NAPS PHWRs reactors, each rated at 235 MWe. Many problems have plagued this program over the past twenty years, resulting in the capacity factors given in Table III.

The total capacity of plants in operation and under construction is approximately 3100MWe, with additional planned capacity of approximately 9000MWe. Using domestic uranium supplies, producing their own heavy water, and providing over 90% of all equipment and components for their first indigenous units (MAPS-1&2) is an impressive accomplishment by India. However the plants have not been extremely reliable power producers and have been controversial. A comprehensive review of the Indian experience would appear to be a logical early step by Israel to help evaluate the feasibility of pursuing an indigenous program of their own.

Conclusion

My response to the question posed in the title of this paper is: Yes, but many questions will have to be addressed and political, as well as technical obstacles overcome. If Israel were to embark on a nuclear power program, the best chance for success is if the IEC is an astute and demanding customer. Furthermore, a concerted effort must be made to maximize the technology transfer from any supplier and to build the industrial infrastructure necessary to support and expand the program.

Israel has an advantage over others considering such a program because many knowledgeable individuals in the U.S. nuclear industry would have the desire and ability to provide invaluable assistance.

Table I - Future Reactor Designs

Reactor	Lead Industry Developer	Power Level, Mwe	Schedule, Remarks
Evolutionary Light Water Reactors (LWRs)			
Advanced LWR Requirements Document	Electric Power Research Institute	-	SER - 3/91
Advanced Boiling Water Reactor (ABWR)	General Electric	1300	FDA - 12/90 Certification - 3/92
Standard Plant for the '90s (SP/90)	Westinghouse	1300	PDA - 6/90 FDA - *
System 80 Plus	Combustion Engineering	1300	FDA - 12/91 Certification - 3/93
Advanced Passive LWRs			
Passive LWR Requirements Document	Electric Power Research Institute	-	SER - 2/92**
Advanced Passive (AP600)	Westinghouse	600	Preapplication review request under consideration**
Process Inherent Ultimate Safety (PIUS)	ASEA Brown Boveri	600	Preapplication review request under consideration**
Simplified Boiling Water Reactor (SBWR)	General Electric	600	No review request
Safe Integral Reactor (SIR)	Combustion Engineering	300	No review request

* - No application intended at this time by Westinghouse for Certification.
** - The Commission has directed that the review of the Passive LWR Requirements Document be completed prior to review of any passive LWR design for Certification
PDA - Preliminary Design Approval
FDA - Final Design Approval
SER - Safety Evaluation Report

Advanced Non-LWR Designs	Lead Industry Developer	Power Level, Mwe	Schedule, Remarks
Modular High Temperature Gas-Cooled Reactor (MHTGR)	General Atomics	540 (4 units)	Preapplication SER - 11/90
Power Reactor Inherently Safe Module (PRISM)	General Electric	1245 (9 units)	Preapplication SER - 11/90
LMR Sodium Advanced Fast Reactor (SAFR)	Rockwell International	1400 (4 units)	Preapplication SER - 6/90*
CANDU-3 Pressurized Heavy Water Reactor	Atomic Energy of Canada Limited	450	No application for Certification received

* - DOE has eliminated funding. NRC to complete draft SER at DOE's request.

Table II. - Westinghouse Advanced Passive Reactor
Some Design Characteristics of the AP-6000

Power level - 600MWe

Safety Aspects -

- Passive and simplified natural circulation cooling systems for residual heat removal and containment
- Core melt frequency < $1x10^{-5}$/year
- Low power density core
- Pump seal Loss of Coolant Accident eliminated
- Leak before break Reactor Coolant System (RCS) Design
- Segregation of safety grade systems
- All safety systems within containment

Design Simplification -

- Major plant modules prefabricated offsite in manufacturing facility
- Canned motor RCS pumps mounted integral with steam generators
- Reduced components compared to reference Westinghouse two loop PWR, including:
    - o 58% less NSSS valves,
    - o 75% less NSSS piping,
    - o Elimination of both safety grade diesel generators,
    - o Simplified RCS pipe supports and elimination of pipe whip restraints,
    - o Elimination of auxiliary feedwater, essential service water, and boron recycle systems
- Cooling water, HVAC and AC power systems non-safety grade and simplified
- Proven equipment utilized throughout
- Design essentially complete before starting major construction
- Load following design using control rods

Table III.

Indian Nuclear Power Plants

Unit	MWe	Startup	Capacity Factor,%
TAPS-1 (BWR)	210*	1969	52
TAPS-2 (BWR)	210*	1969	53
RAPS-1	220	1973	23**
RAPS-2	220	1981***	58
MAPS-1	235	1984	50
MAPS-2	235	1986	40
KAPS-1	235	1990	--
KAPS-2	235	1991	--
Kaiga-1&2	2x235	construction	--
RAPS-3&4	2x235	construction	--
TAPS-3&4	2x500	licensed	--
Kaiga-3-6	4x235	planned	--
RAPP-5-8	4x500	planned	--
PHWR-6 units	6x500	planned	--
VVER-1000 (PWR)	2x1000	planned	--

*Downrated to 160MWe
**Large number of scrams due electrical net instabilities
***Delayed due to cutoff of supplies from Canada

Note: All units are PHWRs, except where noted.

Figure I. Westinghouse Advanced

Reactor Design AP-600

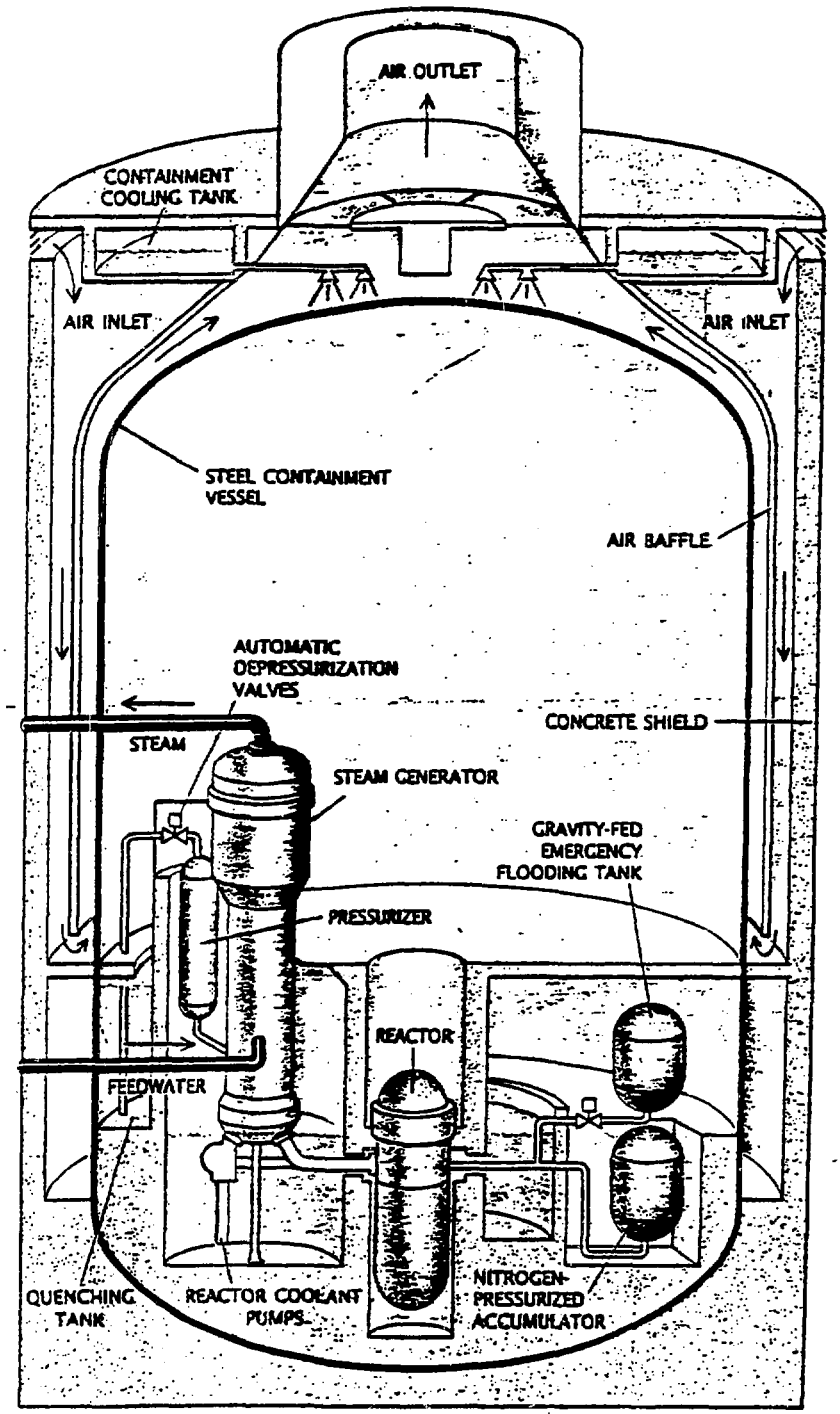

Up-To-Date Isotope Diagnostic Methods for the Cardiological Practice

L. Csernay

Department of Nuclear Medicine
Albert Szent-Gyorgyi Medical University Szeged, Hungary

Abstract

During the past fifteen-twenty years a large number of sophisticated nuclear cardiological methods were developed. A lot of them were quickly introduced into the clinical practice based on world-wide accepted routine technologies.
At our department, nuclear cardiological studies are performed in a close co-operation with the cardiologists from the medicine clinic, from the department of cardiac surgery of our university hospital and from a large cardiac rehabilitation center, therefore special attention will be paid in the presentation to the changes of the spectrum of the clinical indications and of the acceptance of the results by the cardiologists during the past years.

The following methods will be discussed extensively from a practical point of view:

1. ECG-gated radionuclide ventriculography at rest.

2. Plenar and SPECT myocardial perfusion scintigraphy with 201-Tl, with 99mTc-MIBI at rest, after bicycle ergometric stress and after dipyridamole loading.

The conclusions regarding results, applicability and optimal use are based on our own experience with the above methods in several thousand patients.

Nuclear Based Techniques for Detection of Explosives

Tsahi Gozani
Corporate Vice President/Chief Scientist
Science Applications International Corporation
Santa Clara, California, U.S.A.

Since 1985, great strides were made in the research, development and demonstration of nuclear based techniques for the detection of bulk explosives. These techniques are shown to provide the only feasible approach for meeting the operational criteria of high detection, low rate of false positives and acceptable high throughput of screened luggage and cargo against concealed explosives in air transportation. These explosive detection techniques are a powerful tool for combating terrorism in air transportation and in other similar applications.

The nuclear based techniques are characterized by probing the screened object (e.g., luggage) with highly penetrating radiation, i.e., neutrons or energetic gamma rays. Attenuation of the probing radiations and the high energy gamma rays produced by them are, in general, characteristic to the elemental composition of the objects. The transmitted and generated radiations are detected by arrays of appropriate detectors placed near or around the object. The intensity, energy and spatial distribution of the detected radiations and their relationship to the primary radiation allow a computer to determine the presence or absence of explosives.

Feasible techniques for explosive detection will be reviewed and current status of the most promising ones will be reported.

ELECTROCHEMICAL GENERATION AND UTLIZATION OF HYDROGEN FOR LOAD LEVELING AND MOBILE APPLICATIONS

E. Gileadi
School of Chemistry
Raymond and Beverly Sackler
Faculty of Exact Sciences
Tel-Aviv University

The fundamental principles of electrode kinetics, related to water electrolysis and the H_2/O_2 fuel cell, will be discussed. The importance of current efficiency and ETE (electric to electric) efficiency will be explained.

Different methods of hydrogen storage, including cryogenic, high pressure, metal hydride and chemical, will be compared. The use of hydrogen for transporting energy over very long distances will be compared to other modes of energy transmission.

The long term ecological advantages of using hydrogen as a fuel, either in a fuel cell or in an internal combustion engine (as H_2 or after conversion to another fuel, such as methanol) will be emphasized.

Inherent limitations of the H_2/O_2 fuel cell in terms of its power density (or its space-time yield), initial investment and maintenance costs will be discussed.

THE RADIOLOGICAL ACCIDENT AT SOR-VAN

Dan Litai - Israel Atomic Energy commission

On June 21,1990 around 17:45 a radiation accident occurred at the SOR-VAN Company's irradiation facility, which is a commercial enterprise that sterilizes medical products and spices for the food industry by exposing them to high gamma doses. The facility is located within the premises of the Soreq Nuclear Research Center.

A company employee entered the irradiation room while the 340,000 Ci Co-60 source was partly stuck above the cell floor. He stayed there for about 1-2 minutes receiving a gamma dose of the order of 10 Gy. First signs of radiation sickness apeared a few minutes later and the 32 years old worker was then promptly removed to a hospital where a preliminary evaluation of his symptoms and blood tests confirmed the estimate of the magnitude of his dose. The operator died on July 27, the 36th day after his tragic exposure.

The accident was initiated by a transport jam in the facility caused by some twisted cartons that had been present on the conveyors - a not infrequent situation. Normally, the control system would respond by stopping the transport system and by lowering the source into the storage pool. On this occasion, however, a twisted carton hindered the source's descent and it remaind stuck above the floor. A falsely activated limit switch erroneously indicated on the control panel that the source was down.

As a result both the transport jam alert and the gamma alarm were activated. An operator was called from home, and on noticing the confilicting signals (source down - gamma alarm) decided that the gamma alarm was false. He then overcame the irradiation-cell door's interlocks and entered.

Since the source was completely veiled by the carton stacks he did not notice his error, but when strange sensations beset him, he became frightened and left the room. Shortly afterwards he became sick and started to retch.

A detailed description of the accident and its causes as revealed by the investigation which followed is given in the paper.

Test of the Linear-no Threshold Theory For Radiation Carcinogenesis

Bernard L. Cohen
University of Pittsburgh
Pittsburgh, PA 15260

Abstract

It was previously shown that a correlation between lung cancer rate and radon exposure in a large number of U.S. counties is as valid as case-control studies for testing a linear-no threshold relationship between them, provided there is extensive effort to reduce effects of confounders by stratification and multiple regression analysis. In such a procedure, the usual objections to ecological studies do not apply. This work involves such analyses for 965 U.S. counties, with multiple regression on 17 potential confounding factors and stratification in turn on each of these 17 plus geography. Lung cancer rates tend strongly to decrease with increasing radon exposure, contrary to the strong increase predicted by the theory. Stratification on geography by national region eliminates the decrease, but finer stratification and multiple stratification fail to give an increase, leaving a very strong discrepancy with theory.

Using Optimization Techniques for Finding Potential Superior Reload Configurations for the TMI-1 Cycle-9

by

S.H. Levine, D. Bai

The Pennsylvania State University
University Park, PA 16802

and

J.D. Luoma, M. Mahgerefteh

GPU Nuclear Corporation
Parsippany, NJ 07054

Optimization techniques have been developed for reloading nuclear power plants for more than a decade.[1-4] In the most recent paper by Suh and Levine,[4] a method was proposed for optimizing a PWR using simple direct optimization techniques. These techniques have now been further improved to determine superior reload configurations for the TMI-1 Cycle-9, expeditiously.

The TMI-1 cycle lengths have been increased to where the TMI-1 Cycle-9 produces energy for approximately 600 effective full power days (EFPD). This automatically establishes the need for 76 or 80 fresh fuel assemblies in the reload core. Since almost all of these fuel assemblies will incorporate burnable poisons, they cannot be placed in control rod positions. There are several other crucial specifications that establish strict guidelines for placing fresh fuel and used fuel into the core, which limit the flexibility in designing the reload core.

With these guidelines the OPHAL computer code[4] is used to establish a priority scheme for loading the fuel in the core. Basically, two priority schemes are developed,

one for fresh fuel and one for used fuel. Using these priority schemes results in fuel arranged as shown in Table 1. It has been found that the OPHAL code results are dependent on the initial loading pattern. However, this characteristic is overcome by using past priority results of Ahn and Levine[1] to develop the input to OPHAL. OPHAL then produces optimization patterns which have a global optimum characteristic. It is found that changing input based on the various priority schemes reported in Ref. 1, makes very little difference in the final results of OPHAL. However, a problem does arise when one places into the core the actual fuel assemblies based on the OPHAL priority schemes. This is because the k_∞ values developed by OPHAL for BOC loading is much different than that from the available fuel assemblies as shown in Table 1. The difference between used fuel and fresh fuel k_∞'s over the majority of the core fuel assembly positions induce a major change between the ideal core and the practical core. As a consequence, a new approach must be taken at the next step.

First, the core is adjusted to establish cross sections and correct lifetime using the Penn State Fuel Management Codes.[4] Then a Haling power distribution is calculated for the practical core which allows determining the hot spots in the core, because the Haling power distribution has the lowest possible power peak for this core design. If hot spots occur, the fuel enrichments must be divided. Thus, this calculation identifies where peak power occurs and if such powers exceed the allowed constraints. Since a maximum of 1.37 has been set by fuel management guidelines to prevent pin power peaks from being exceeded, the Haling power distribution must be below this to allow for incorporating practical burnable poison (BP) designs. This is because when actual

burnable poisons are introduced they do not follow close to a Haling power distribution, but allow the power peaks to exceed the Haling power peak up to approximately 5%.

Thus, at this stage, the results of the Haling power distribution are used to determine that the TMI-1 core the fresh fuel enrichment must be split and in addition, identifies which fuel assemblies must carry the lower enrichment. Fuel assemblies which have NP's $\geq$ 1.32 must be assigned the lower enrichment. The high speed codes are then used to quickly determine the required split enrichment conserving the ^{235}U content in the core needed to obtain a desired power distribution.

The next step, is to place the BP's in the fresh fuel. This is done very fast, manually using a logical procedure for minimizing the power peaks at the middle of the cycle when power peaks are at a maximum.

The 2 year (600 EFPD) Cycle-9 for the TMI-1 core and the specifications for minimizing the fast neutron flux at the pressure vessel greatly restrict the flexibility in shuffling the fuel in the core. These constraints, applied in conjunction with the optimization techniques presented in this paper allow fast determination of the optimum core reloads for this reactor. The results of these analysis and methods used to obtain these results will be reported in detail at the meeting.

References

1. D. AHN and S. LEVINE, *Nucl. Technol.*, 71, p. 535 (1985).

2. T. MORITA, Y.A. CHAO, A.J. FEDEROWICZ, and P.J. DUFFEY, *Trans. Am. Nucl. Soc.*, 52 p. 41 (1986).

3. Y. KIM, T. DOWNAR, and A. SESONSKE, *Nucl. Sci. Eng.*, 96, p. 85 (1987).

4. J.S. Suh and S.H. Levine, *Nucl. Sci. Eng.*, 105, p. 371 (1990).

Table 1
Priority Scheme

Priority	Core Position	OPHAL k_∞	Actual k_∞
1	6	1.378	1.398
2	19	1.374	1.398
3	23	1.374	1.398
4	13	1.359	1.172
5	12	1.355	1.398
6	5	1.343	1.158
7	22	1.342	1.158
8	4	1.342	1.398
9	18	1.341	1.149
10	26	1.331	1.125
11	11	1.329	1.127
12	2	1.328	1.398
13	3	1.328	1.125
14	24	1.327	1.124
15	17	1.321	1.398
16	9	1.317	1.125
17	10	1.316	1.398
18	16	1.312	1.123
19	7	1.299	1.123
20	1	1.275	1.098
21	27	1.256	1.398
22	25	1.256	1.398
23	20	1.256	1.123
24	14	1.256	1.100
25	29	1.242	1.107
26	28	1.003	1.398
27	21	1.003	1.058
28	15	1.003	1.038
29	8	1.003	1.013

REACTOR PHYSICS

A "Non-Proliferating" Nuclear Fuel for LWR

Y. Ronen and Y. Kimhy
Department of Nuclear Engineering Ben-Gurion University
Beer-Sheva, Israel

The spread of nuclear-power reactors and nuclear technology to developing countries once again focuses attention on the problem of nuclear weapons proliferation. There are two main senarios, both highly unlikely that might connect nuclear -power reactors to nuclear weapons.

The first is related to the divergence of plutonium from the spent fuel of power reactors. The "advantage" of this approach is that there is no interference in the operation of the reactor. On the other hand , the plutonium in the spent fuel of a power reactor is not military grade plutonium.

The second senario related to the proliferation problem is - obtaining the plutonium only after short irradiation in the reactor. In this way, military grade plutonium can be obtained, however, it creates serious interference in the reactor's operation.

It should be mentioned that there are safeguards which are implemented by the IAEA to prevent these and other senarios. In general, these measures are considered adequate. However, tney are not completely fool-proof. Furthermore, any country who signed the NPT can withdraw its signature from the treaty after obtaining the reactor and the fuel. So, although both these senarios are very unlikely and are also unsuitable ways for obtaining nuclear weapons, there is still concern about them.

We suggest addressing this problem by using a nuclear fuel with a better proliferation resistance. A "non proliferation" nuclear fuel can be obtained by increasing the relative amount of ^{238}Pu in the plutonium. Some of the characteristic properties of ^{238}Pu compared to ^{240}Pu are given in Table 1. We can see from this table that the amount of heat and alpha radiation damage caused by ^{238}Pu compared to ^{240}Pu is greater by a factor of 74.5, as obtained from the half-lives. Also, the neutron production by spontaneous fission (S.F.) as determined by the S.F half-life is greater in ^{238}Pu compared to ^{240}Pu.

There are two aspects to power reactors spent fuel with high content of ^{238}Pu. Firstly, plutonium with a high content of ^{238}Pu is a nonmilitary grade plutonium, and secondly, a high content of ^{238}Pu makes it practically impossible to reprocess the spent nuclear fuel. Today,the practical limit for reprocessing nuclear fuel is for a fuel with less than 2% of ^{238}Pu, namely $^{238}Pu/Pu \leq 0.02$. With the current reprocessing techniques, the upper limit ratio of ^{238}Pu to the total Pu discharge is 5% [1]. It is considered prudent that this ratio not be exceeded. The main reason for this limit is that ^{238}Pu heats up the fuel, affecting fabrication and reprocessing. Furthermore, the relatively high percentage of neutrons from S.F adds to the difficulties of reprocessing and handling.

Increasing the ^{238}Pu ratio in the total plutonium is possible by adding ^{237}Np to the fuel at the beginning of life BOL. The ^{238}Pu is obtained from ^{237}Np by neutron capture:

$$^{237}Np + n \longrightarrow {}^{238}Np \xrightarrow[50.8\ h]{\beta^-} {}^{238}Pu$$

The thermal cross section for this reaction is relatively high and has a value of 169 barns.

In our analysis we set the limiting ratio of ^{238}Pu to the total discharged plutonium at 5%. Namely, if the discharged plutonium has a content of ^{238}Pu equal to or more than 5%, the spent fuel, for all practical reasons, can be considered a "non proliferating" fuel.

For the analysis, we have chosen unit 1 of the Zion station[2]. This station is a PWR of 3250 MWth.

To simplify the calculations of the reactor we have assumed a one enrichment core. The enrichment chosen for our analysis was 2.92% (At.) A linear reactivity model was assumed.

The validity of the linear reactivity model for teh reactor calculation (No Np core) can be justified from Fig. 1. We can see that the change in k_{eff} during burnup is quite linear, which makes the linear reactrivity model quite good as a first approximation.

The analysis was performed with the cluster option of the WIMS-D code[3], using the 1986-WIMS cross section library[4]. This library is characterized by inclusion of the ^{237}Np-^{238}Pu chain. The analysis was performed in four energy groups.

The fuel radius considered is 0.4743 cm with 0.0617 Zr cladding. The Dancoff factor used in our analysis was 0.725. The reactor dimensions for the geometrical buckling calculations were the core diameter 337 cm and the active height of 366 cm.

The power density for the depletion calculation was 37.6 kW/kg U. The results are given in Fig. 1 for the no Np case. We introduced 98 kg of ^{237}Np into the fuel. The effects of the introduction of ^{237}Np on k_{eff} as well as on the $^{238}Pu/Pu$ ratio are given in Fig. 1 and 2. Three important facts can be obtained from these results:

1. The $^{238}Pu/Pu$ ratio is alway equal or greater than 5%.
2. In particular, at BOL up to 1000 MWD / tonne the $^{238}Pu/Pu$ ratio is the highest.
3. The penality for the introduction of ^{237} Np on the effective multiplication factor-k_{eff} is 1.68 % at BOL, 1% at k_{eff} = 1.0 and 0.59% at EOL with 33132 MWD/tonne.

The main conclusion of these results is that with a penalty in k_{eff} of less than 1% it is possible to have a $^{238}Pu/Pu$ ratio of more than 5% during the entire fuel cycle.

Table 1
Comparison between ^{238}Pu an ^{0}Pu

Isotope	Spontaneous Fission Half-life (year)	α – Decay Half life (years)
^{238}Pu	$4.75 \pm 0.09 \times 10^{10}$	87.75
^{240}Pu	$1.16 \pm 0.02 \times 10^{11}$	6537

References

1. S. Pilate, R. de Wouters, G. Evard, H.W. Wiese and U. Wehmann, "Mixed Oxide Fuels with Minor Actinides for the Fast Reactor", PHYSOR-90, International Conference on the Physics of Reactors, Vol 1, I - 73, April 23-27, 1990 Marseille, France.
2. Zion Station Units 1 and 2, Directory of Nuclear Reactors, Vol X, International Atomic Energy Agency, Vienna 1976.
3. R. Askew, F.J. Fayers, and P.B. Kemshell, J.Br. Nucl. Energy Soc. **5**, 564, 1966.
4. M.J. Halsall and C.J. Taubman, "The '1986' WIMS Nuclear Data Library", Reactor Physics Division AEE Winfrith Report AEEW-R-2133 (1986).

List of Figures: 1. The Effective Multiplication Factors with and without Np During Burnup
2. The $^{238}Pu/Pu$ ratio During Burnup.

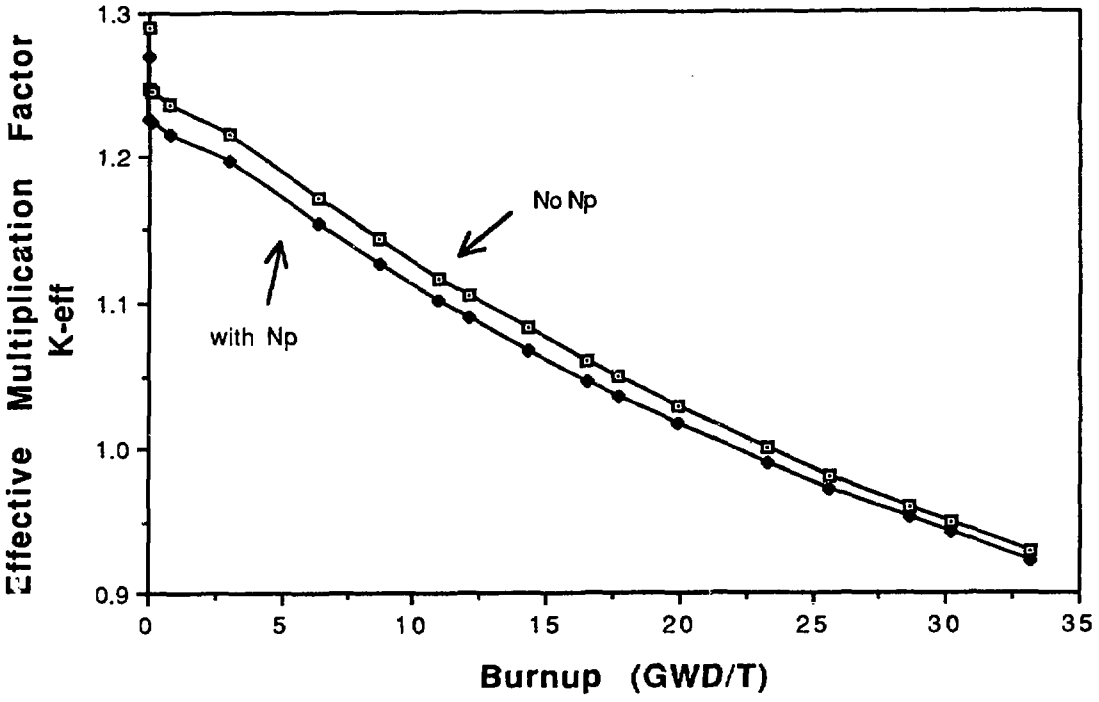
Effective Multiplication Factor
K-eff
1.3
1.2
1.1
1.0
0.9
0
5
10
15
20
25
30
35
Burnup (GWD/T)
No Np
with Np

FIG. 1

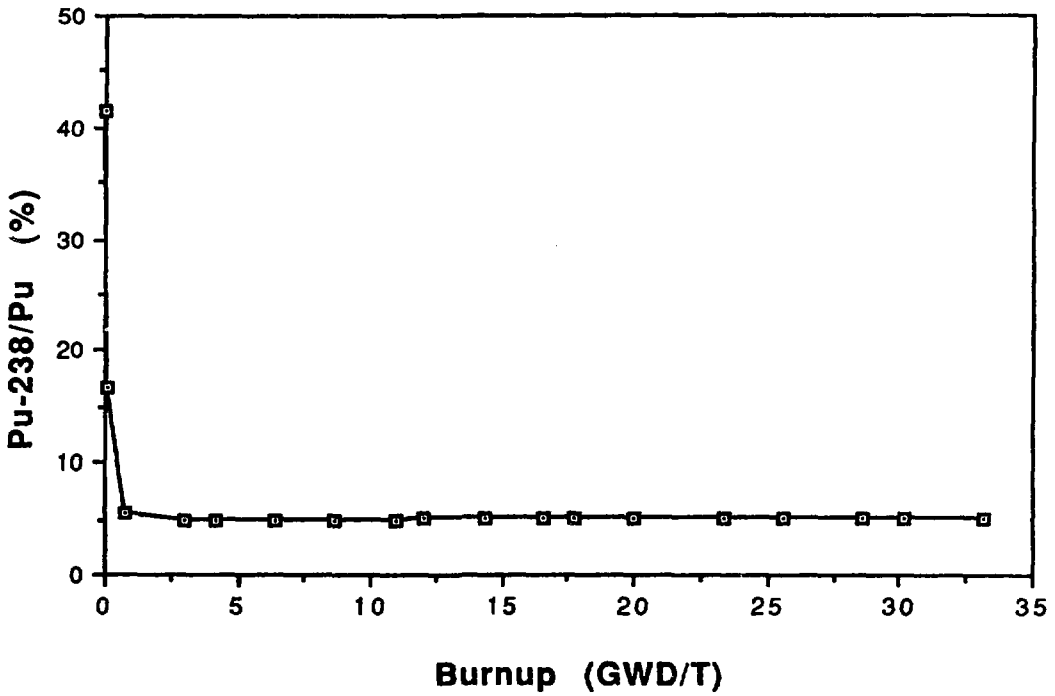

FIG. 2

One Dimensional Transport in Random Media

Jacob Hecht, Dov Shvarts
Physics Department, Nuclear Research Center Negev,
P.O.B. 9001, Beer-Sheva

Several physical problems involve the description of particle or radiation transport in inhomogeneous media. Examples of such problems include porous radiation shielding in nuclear reactors[1] and radiation transport in turbulent fluids. Some inhomogeneous media with a complex structure may be described statistically by giving the probabilities of finding their various configurations. We will deal with problems in which the medium is a mixture of two materials who's properties (e.g. cross-sections) are known. This medium is described by giving the probability of finding each material in every point in space, the correlation functions of the two materials and higher moments of the random field.

We shall consider the transport equation for particles moving with velocity v, which takes the generic form for the angular flux $\psi(t,x,\Omega)$:

$$\frac{1}{v}\frac{\partial\psi}{\partial t}+\Omega\cdot\nabla\psi+\Sigma_t(x)\psi=\int\Sigma_s(x,\Omega'\to\Omega)\psi(\Omega')d\Omega'+S(x)$$

where $\Sigma_t(x),\Sigma_s(x)$ are the total and scattering cross-sections, and $S(x)$ is an external source. In our particular problem Σ_t,Σ_s,S depend on position through the material being in position x, which is a space dependent random process. Solving the problem means finding the mean flux $<\psi(x)>$, correlations of the flux $<\psi(x)\psi(y)>$ and possibly higher moments of the random field ψ. It would be preferable to find a closed equation for the mean flux ,hopefully of a form similar to the original equation, but possibly with effective coefficients. We should also understand in what ways the possible statistics of the medium influence the solution.

The simplest problem is this context is that of a purely absorbing medium. In this case the transport equation reduces to :

$$\frac{d\psi}{dx}+\Sigma(x)\psi=0$$

This equation was solved[2] for the mean flux for a large class of statistics: those in which we draw segments of alternating materials from two given distributions which characterize the chord length distributions (CLD) of the two materials. This general solution is achieved by writing renewal equations for the mean flux, which after Fourier transform take a form similar, but not identical, to that of one-dimentional transport problems with scattering[3]. Another approach which only sometimes can be taken is first to solve the equation generally, in our case $\psi(x)=\psi(0)\exp\left(-\int_0^x\Sigma(x')dx'\right)$, and then average over this solution.

Figure 1 shows the importance of knowing the chord length distribution by comparing solutions for different CLDs which have the same averages. In particular note the deviation of the solutions from that of a homogeneous mixture of the two materials. Further restricting the chord length distributions to have the same variance significantly narrows down the variability in the solutions. Another meaningful outcome of the equation is the variance of the flux which is shown in Fig. 2 for the same CLDs as in Fig. 1. The variance gives the possible deviations from the mean solution, and may be important in many practical physical applications such as radiation shielding.

The next step is to solve the transport equation with scattering along a line (narrow rod geometry). In the case of pure isotropic scattering the equation takes the form:

$$\frac{d\psi_+}{dx}=-\frac{1}{2}\Sigma(x)\psi_+(x)+\frac{1}{2}\Sigma(x)\psi_-(x)$$

$$\frac{d\psi_-}{dx}=-\frac{1}{2}\Sigma(x)\psi_+(x)+\frac{1}{2}\Sigma(x)\psi_-(x)$$

where ψ_+, ψ_- are the forward and backward fluxes respectively. The solution of this equation is more complicated because it is a boundary value problem, that is ψ_+ is known at the left end of the rod but ψ_- is a random variable there (it is known exactly only at the right end of the rod). Indeed, it has been solved analytically only in the case where the CLDs are exponentially distributed[4]. It is possible, though, to solve the equation numerically. Examples are shown in Fig. 3. It can be seen that the variability of the solution is reduced in comparison with the purely absorbing case, though the atomic mix solution deviates from the other three. This is because the sure boundary conditions are given ,and because the back and forth scattering enhances the randomization of the medium. Fig.4 shows that the variance of the different solutions is very similar.

We may extend the above to the case of absorbing and scattering materials. We have also used the solution of the above equation to find how to average over diffusion coefficients in one dimensional problems. We will discuss some difficulties in solving the problem in two dimensions.

References:

1. "Engineering Compendium on Radiation Shielding", ed. Jaeger R. G., Springer-Verlag, 1986.
2. Levermore C. D. et. al., J. Math Phys. 29,995 (1988).
3. Pomraning G. C., J. Quant. Spectrosc. Radiant. Transfer 42,279 (1989).
4. Vanderhaegen D., Deutch C., J. Stat. Phys. 54,331 (1989).

Figure 1

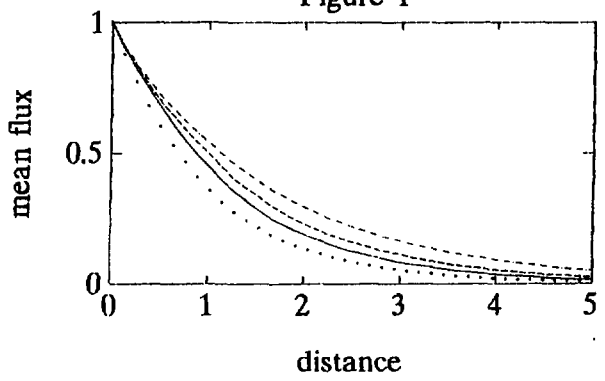

Figure 2

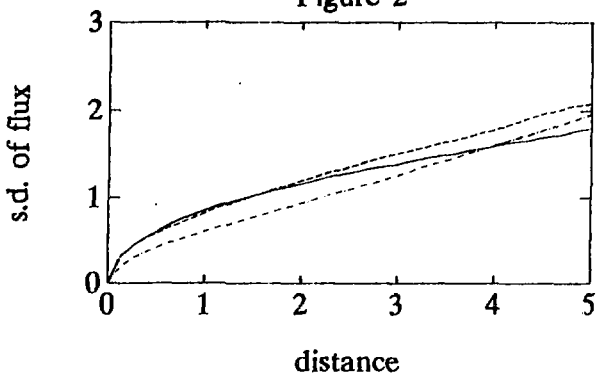

Figure 3

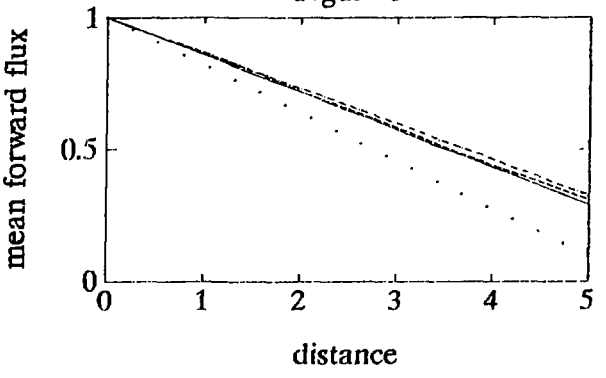

Figure 4

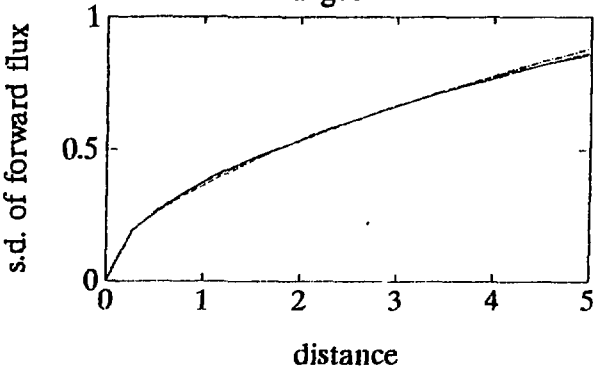

Figure Captions:

In all figures the following key applies to the CLDs used:

full line - Gamma distribution with m=4
dashed line - Gamma distribution with m=2
dash dotted - Exponential distribution (Gamma with m=1)
dotted - Atomic mix

Length units are chosen such that $\bar{\Sigma} = 1$ ($\bar{\Sigma}$ is a simple -'atomic mix'- average of the cross-sections).

The statistics of the materials along the line is:
Material no.1 occupies 90% of the line, its cross-section is .1, and its mean chord length is .99 .
Material no.2 occupies 10% of the line, its cross-section is 9.09, and its mean chord length is .11 .
We used thew same statistics for both absorbing and scattering problems.

Fig. 1 - The mean flux for a purely absorbing case.
Fig. 2 - The relative standard deviation (=s.d./mean) of the flux for a purely absorbing case.
Fig. 3 - The mean forward flux for the purely scattering case.
Fig. 4 - The relative standard deviation of the forward flux for the purely scattering case.

Reconstruction of LWR Pin Powers from Nodal Calculations [1]

M.Segev, A.Gaiperin, M.Aboudi
Ben Gurion University
Dep. of Nuclear Engineering

Nodal calculations serve primarily the purpose of efficient fuel cycle scoping, generating at each time–point the criticality and the global, assembly–by–assembly, power distribution. The detailed distribution inside the assemblies is not directly available, but recent publications [1, 2, 3] indicate that, with specially devised interpolation methods, the inner distribution can be reestablished with good accuracy. The reconstructed pin power distribution is the product of a global shape and a local form. The first is an intranodal distribution based on the nodal input and output, namely on the nodal two group cross sections and the nodal flux and face currents. The second is the power distribution from the single–assembly calculations (carried out with reflective boundary conditions) which initially generate the collapsed–homogenized nodal cross sections. It is the first factor that requires a special mathematical development and a measure of experimentation. The importance of pin power reconstruction must not be underestimated. Fig. 1 shows hot pin powers in a corner of a PWR core, for a typical MOX fuel loading. The values in the figure represent the intranodal power shape, but normalized to an average of 1.00 in each assembly. It can be appreciated that without reconstruction the estimation of the hot power remains extremely poor. Our method for etablishing the intranodal power shape derives from the combined findings of Koebke [1] and Smith [2], with features deriving from our experience. The intranodal flux, both for the fast (1st) and the thermal (2nd) groups, is represented as a 21 term polynom in x(cm) and y(cm), the horizontal coordinates for the node, (0,0) designating the node center.

$$f(x,y) = a_{00} \cdot F_{00}\,(x,y) + \sum_{l=0}^{4}\sum_{m=0}^{4} a_{l,m} F_l\,(x) \cdot F_m\,(y) \qquad l,m \neq \begin{vmatrix} 0,0 \\ 3,3 \\ 3,4 \\ 4,3 \\ 4,4 \end{vmatrix} \qquad (1)$$

[1]This study was performed under the STARS project and supported by the Schweiz. Bundesamt für Energiewirtschaft

where,

	group 1	group 2
F_{00} (x,y)	1	f_1 (x,y)
F_0 (u)	1	1
F_1 (u)	u	sinh (k/2*u)
F_2 (u)	u**2	cosh (k/2*u)
F_3 (u)	u**3	sinh (k*u)
F_4 (u)	u**4	cosh (k*u)

where,

$$k = \sqrt{\sum_2 / D_2} \tag{2}$$

The choice of base functions for the thermal flux derives from the observation that, in a node nested heterogenously with others, the 2nd (negative) material buckling of the 2G eigenvalue problem for the node starts to manifest itself, giving rise to deviations from the fundamental (1st buckling) mode,these deviations occuring in the vicinity of the node interfaces with its neighbours. In a 1D problem k would be identically the square root of the absolute value of the second mode buckling; for the 2D problem our choice of k, however related to the 2nd mode buckling, has to be approximate the material buckling k**2 cannot be accurately divided into x and y geometrical bucklings. Since the chice of k is anyway approximate, the second mode buckling can also be approximated. In particular one may ignore the dependence of the buckling on the criticality of the core by assuming the value of eq. (2). The table below, prepared for the ZION reactor at BOL, shows that the formula of eq. (2) indeed generates values quite close to the 2nd mode bucklings.

2nd mode buckling vs. k**2 of eq. (2) for ZION BOC1 assemblies

assembly type	-(2nd mode buckling)	k**2
1	0.130	0.110
2	0.161	0.148
3	0.158	0.143
4	0.155	0.139
5	0.142	0.122
6	0.174	0.161
7	0.165	0.150
8	0.165	0.147
9	0.165	0.148
10	0.156	0.136

21 coefficients are needed for representing the intranodal flux as in eq.(1) above. They have to be determined such that nodal quantities are preserved. There are only 9 direct nodal output quantities, namely one nodal flux, four face fluxes, and four face currents. The remaining twelve quantities are not directly nodal output: they are the flux, the x–wise current, and the y–wise current, at each of the node corner points. These quntities are derived from the direct nodal output by a specific interpolation approximation. At a corner point the derived quantity is assumed to be an average of four interpolated values. Each of these interpolated values is obtained by interpolating within one of the four nodes defining the corner. The within–node interpolation is based on the assumption of x,y flux separabilty. We have experimented also with other within–node interpolation methods (i.e. Koebke's 32 term expansions about the corner) but found them to be inferior. Stating the requirment that the 21 (per group) quantities be preserved leads to an algeraic system of 21 equations. Cast in the matrix form of

$$\underline{\underline{A}}\,\underline{a} = \underline{s}$$

where $\underline{\underline{A}}$ is a 21*21 matrix and $\underline{a}$ and $\underline{s}$ are 21*1 column vectors, an inversion routine is then utilized to yield the vector of coefficients a. All the developmental pieces ,as briefly described above, are integrated in a routine which operates on an output file of a nodal calculation of a core and generates the pin power distribution of any desired assembly in the core [4]. The quality of the distribution thus generated was tested by setting up typical PWR and BWR core layouts,then calculating these cores accurately, utilizing the code DOT4.2 with a small mesh size. These latter calculational values are designated 'REFERENCE' in Fig.1 below. It can be appreciated that the reconsruction routine offers a means by which pinpower distributions may be reestablished from pure nodal calculational data.

Fig. 1: Hot Pin Powers at the North–East Corner of a PWR Core

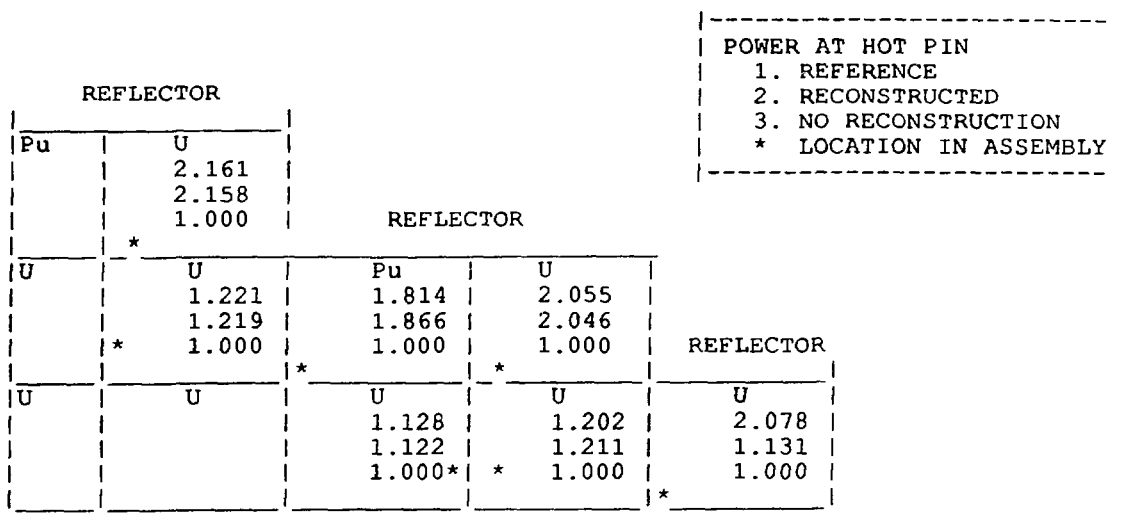

References

[1] K. Koebke, L.Hetzelt ,"On the Reconstruction of Local Homogenous Neutron Flux and Current Distributions of LWR's from Nodal Schemes", NSE 91 1985.

[2] K.R. Kempe, K. Smith, A.F. Henry, "SIMULATE-3 Pin Power Reconstruction", NSE 103 1989.

[3] K. Smith, K.R. Kempe, "Mixed-Oxide and BWR Pin Power Reconstruction in SIMULATE–3" PHYSOR-90, Marseille, April 1990.

[4] A. Galperin, M. Segev, "Pinwise LWR Power Distribution Derived from Nodal Diffusion Calculations", PSI Reports N76 and N77, August 1990.

DETERMINATION OF THE H-CONCENTRATION IN A CONCRETE WALL USING A NEUTRON ATTENUATION TECHNIQUE.

A. Kinrot, M. Blau
Physics Department
Nuclear Research Centre-Negev
P.O.Box 9001, Beer-Sheva, Israel

ABSTRACT

The H concentration of concrete can be determined by measuring the reflected thermal neutrons from a concrete wall, of a known thickness. The source of radiation used are Am-Be neutrons. The reflected thermal neutrons are captured by a He^3 detector.

INTRODUCTION

The H content of building materials can be determined by pulsed neutron methods and by stationary methods[1]. Here we investigate the feasibility of using a stationary neutron source, for determining the H concentration of a concrete wall. Thermal neutrons resulting from the moderation of Am-Be neutrons by collisions with H atoms in concrete, are detected by a He^3 counter. This method is based on the much greater slowing-down "power" of H compared with the other elements in concrete. Thus, the flux of the reflected thermal neutrons depends predominantly on the H concentration and the concrete thickness. In this paper, calculations are performed to asses the feasibility of determining the H concentration in a concrete wall of a given thickness.

DETERMINATION OF H-CONCENTRATION.

First, calculations have been made to asses the impact of different H concentrations, on the reflected thermal neutrons absorption rate in a He^3 counter. Six different H concentrations for 15 and 35 cm. thick concrete walls have been considered. All calculations have been performed with DOT-3.5[2], a two-dimensional discrete ordinates code. for the Portland Ordinary Concrete [3] with different H concentrations. The obtained results are shown in Table 1.

Table 1. The reflected thermal neutron absorption rate (per source neutron) as a function of the H concentration in the concrete wall.

Concrete Thickness (cm.)	H Concentration (gram/cc) 0.455-2 (HMMM)	0.955-2 (HMM)	1.455-2 (HM)	1.955-2 (HO)*	2.455-2 (HP)	2.955-2 (HPP)
15.0	2.65-5	1.07-4	2.66-4	-	7.60-4	1.06-3
35.0	1.42-4	3.72-4	6.28-4	-	1.17-3	1.45-3

* - Portland Ordinary Concrete

From Table 1 it can be seen that the thermal neutrons absorption rate in He^3, increases strongly with the H concentration in the concrete wall. Higher H concentration leads to a more effective neutron thermalization for the same concrete thickness and finally, to a higher neutron absorption rate at the detector. The neutron absorption rate depends also upon the concrete wall thickness; in thicker walls, more neutrons are attenuated and the neutron absorption rate is higher. Therefore, for the determination of the H concentration in concrete walls, detailed information of the thermal neutron absorption rate as a function of the H concentration and the concrete wall thickness is needed. A large number of calculations has been performed for the six different H concentrations and different concrete wall thicknesses (from 5 to 45 cm., in steps of 5 cm.). The obtained results are illustrated in Fig. 1. These results have been processed by smoothing the data for each H concentration, by using least square polynomials.

The H concentration of a concrete wall having a thickness of d cm. and a measured neutron absorption rate T_x, is determined as following:
Let T_u and T_l be the upper and lower calculated bounds of the measured absorption rate T_x ($T_u > T_x > T_l$), corresponding to wall thickness d. Let H_u and H_l be the H concentrations corresponding to T_u and T_l respectively. Then, H_x, the H concentration to be determined. is given by:

$$H_x = H_l + (H_u - H_l) * [(T_x - T_l) / (T_u - T_l)]$$

Preliminary measurements have been made for several thicknesses of a concrete wall, having the same composition (including H concentration). The obtained H concentrations, using the proposed methodology, are within 10% of each other.

Fig. 1 Thermal neutron absorption rate as a function of H-concentration and wall thickness.

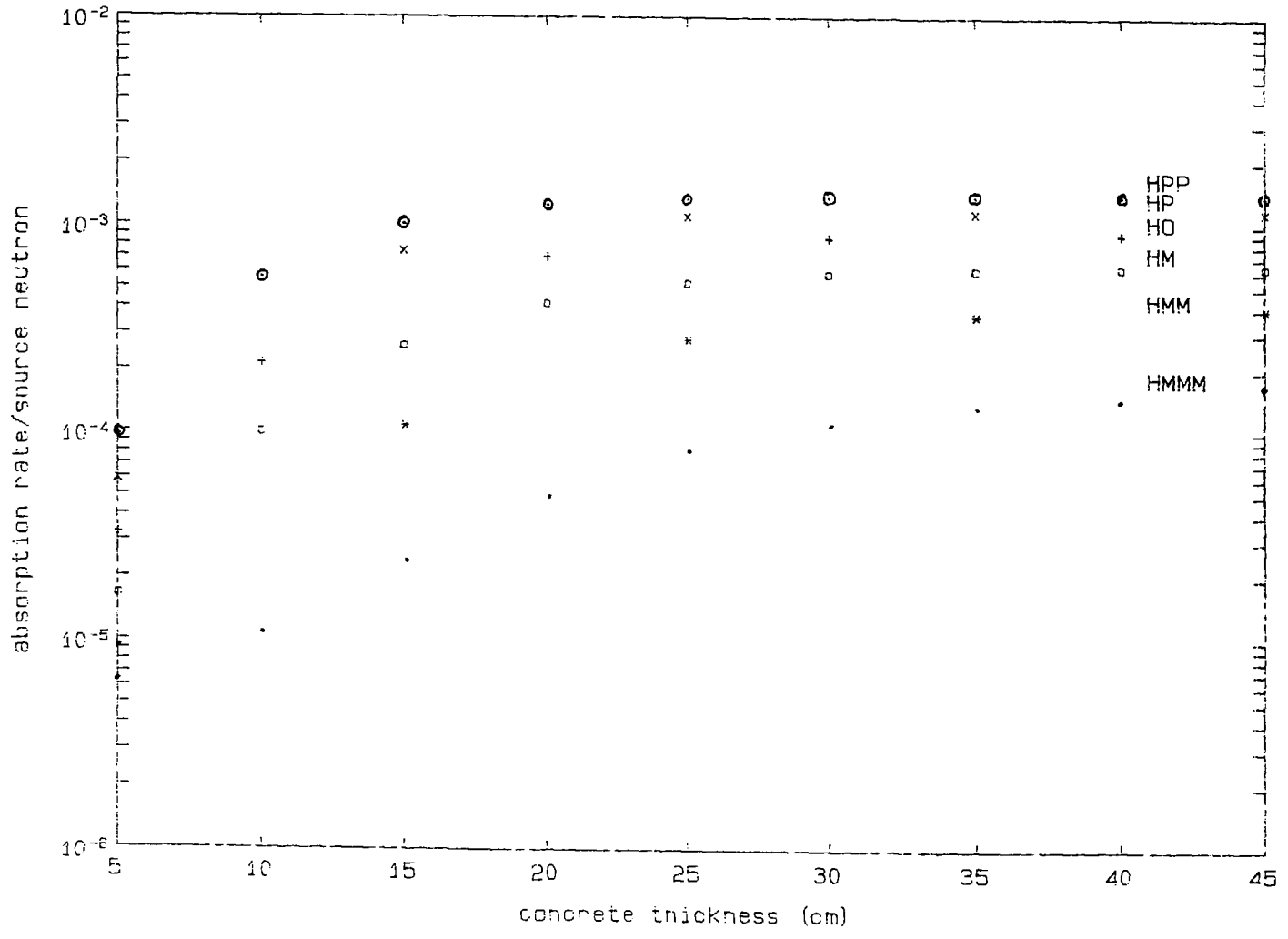

REFERENCES

(1) J. Csikai, CRC Handbook of Fast Neutron Generators, CRC Press, 1987.

(2) Mynatt,F.R. et al., The DOT-3.5 A Two Dimensional Discrete Ordinates Transport Code, Oak Ridge National Laboratry, Oak Ridge, TN., ORNL/TM-4280 (1973).

(3) P.E.Blizard, editor, Reactor Handbook, pp 92-93, Interscience (1962).

The Radioactivity Source in the Core of the Swimming-Pool-Type Reactor at Nahal Soreq

Z. Shayer
Israel Atomic Energy Commission, Licensing Division
P.O.Box 7061, Tel-Aviv, 61070

The radioactivity source strengh in a swimming-pool-type reactor was calculated using the EPRI-CINDER[1] code for two distinct modes of reactor operation at a certain power level: continuous operation and intermittent operation. An example of the fission products inventory for one fuel rod containing, at T=0.280g U^{235}, is depicted in Figure 1. The top line in the figure indicates the maximum radioactivity inventory for long continuous operation. After 2 weeks of continuous operation the fuel rod contains more than 70% of the total maximum inventory; this indicates that most of the radioactivity source is contained in the short half-life isotopes (few hours and days), most of which reach their saturation levels. It is also seen that the radioactive inventory is reduced threefold from continuous to intermittent operation. These results have a significant effect on the consequence of risk analysis and the potential for melting the reactor core.

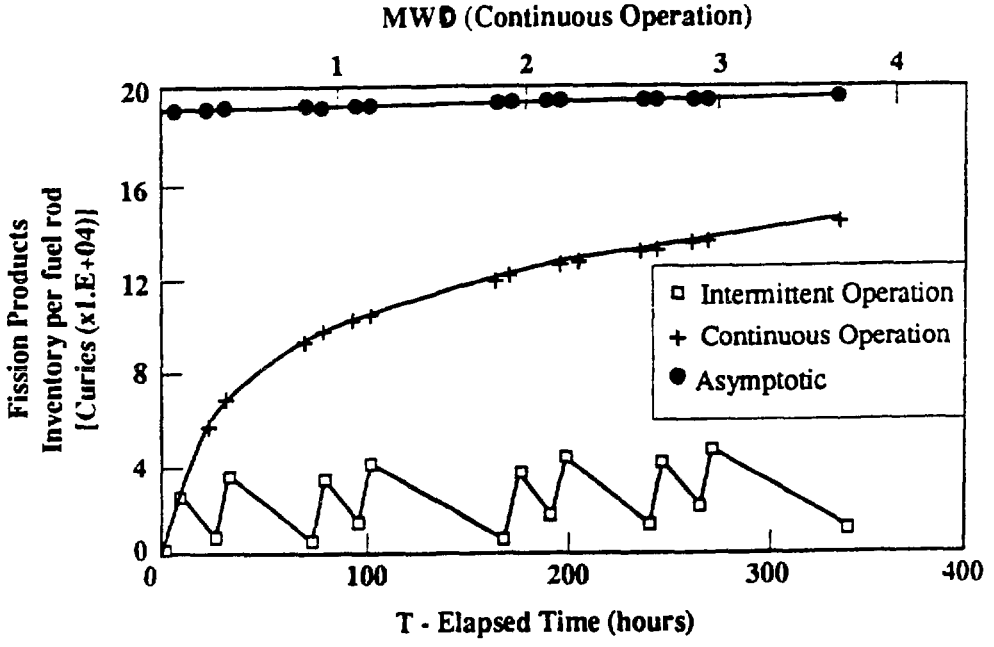

Fig. 1: The radioactivity source per fuel rod for continuous and intermittent operation.

The radioactivity inventory source term in the whole core was calculated by dividing the fuel rods into five representative groups, based on the average burnup and resident time in the core.

The average activity of isotop k in the whole core was calculated as follow:

$$A_k = 2.7 \times 10^{-11} \quad V_{core} \sum_{i=1}^{5} W_i \lambda_k N_k$$

where:

$\lambda_k N_k$ - Number of distegrations per sec/cm^3
V_{core} - The core volume
W_i - The normalized fraction of the representative group i.

We think that this approach will give us a reasonable estimate of the source term inventory for safety analysis.

Reference:

(1) EPRI-CINDER, General Point-Depletion and Fission Produce Code and Four-Group Fission Product Neutron Absorption Chain Data Library Generated From ENDF/B-IV for Thermal Reactors. EPRI NP-356(1976).

Advanced Computer Architectures in Nuclear Engineering Applications

Z. Shayer
Israel Atomic Energy Commission, Licensing Division
P.O.Box 7061, Tel-Aviv, 61070

The scientists and engineers who tackle relatively large problems, desire always to solve them with high accurcey and minimal computing time. The complexity of phisical phenomena that occur in nuclear power plants, leads to high levels of computing power. High-performance in computing can be achieved via parallelism. This, due to the fact that we approach the computational limits of a single processor. The idea of parallelism has been around as long as the history of the computers, but in the early days this idea was rejected by engineers due to the cost and unreliability of the components. Although an improvement of both of these was to occur by 1970. There was some delay in the entering of the parallel architecture computers into the market, mainly due to the leak of reliable software for these machines.

Today a number of commercial parallel computers are available in the price range from few hundred thusand dollars up to few millions. The former are usually classified as mini-supercomputers and the later as supercomputers. We would like to note that due to the diversify of advanced computer architectures, it is a very different task to classify computers based on the architecture structure alone. One of the old and common used toxonomies was suggested by Flynn[1]. He classified the computer into four categories:

1) SISD — Simple Instruction Stream, Single Data Stream.
2) SIMD - Single Instruction Stream, Multiple Data Stream.
3) MISD - Multiple instruction Stream, Single Data Stream.
4) MIMD - Multiple instruction stream, Multiple Data Stream.

Although these categories give a helpful coarse division, many of today's computers are really of hybrid design. For example the CRAY X-MP supercomputer series have up to four processors (MIMD), but each processor uses piplining (SIMD) for vectorization computing. Moreover, where three are multiple processors, the memory can be local, global, or a combination of these. There may or may not be caches and virtual memory systems, and the interconnections can be by crossbar switches, multiple bus-connected system, time-shared bus system, etc.

It is very difficult to predict what will be the dominant computer architecture in the future. Whether missively parallel, local-memory system, which consist of several bundreds of CPUs, or a few powerful vectorized CPUs global of memory system. Moreover, many massive parallel systems will also contain the

capability of vector arithmetic. In order to take advantage of parallel-vector computing, we would like to develop an efficient mathematical algorithm, ideally, suited to each processor; we would like to assign. Relatively large tasks which require little communication and synchronization and which can be carried out with a high degree of vectorization. In terms of gramulerity, our goal for parallel-vector computers is to develop parallel algorithims with large-scale gramularity for tasks, each of which has small-scale vectorizable gramulerity.

One of the main goals in nuclear engineering is to follow up the power distribution in the reactor core under different conditions (normal and abnormal, fuel management etc.). The common way to do this is by solving the multigroup diffusion equation in finite difference approximation.

For example we examine, among others[2-6], the implementation of one of the well known techniques of spatial domain decomposition, which is often called red-black ordering of grid points (or checkerboard), to the solution of the diffusion equation by LSOR interative method. Tables 1 and 2 present some basic characteristics of these computers, on which these algorithm were implemented (range from supercomputer up to mini-supercomputer), along with computing performance. We would like to point-out that up to a decade ago, such type calculation was about two orders of magnitude more time consuming on a very large computers such as CDC-7600.

Beside the algorithm mentioned above there are a lot of mathematical models in the nuclear engineering fieled that lend themselves to parallel processing algorithms, such as batching of particle histories and importance sampling for variance reduction methods in Monte-Carlo techniques, and some additional methods for splitting spaitial operators, along with interation processes.

Finally it is obvious that the more cost-effective computing capacities, can be achieved only via parallel-vector computers with improved sturdiness of numerical analysis and by the better understanding of physical phenomena that occur in nuclear power plants. These will be reflected in the improvement of design, better definition of safety margins, optimized operating points, upgrading the automatic control devices. It will also help us develop rules and procedures for more cost-effective safety operating systems. In addition the high level of computing performance can open up new areas of research in nuclear science and engineering.

References:

1. M.J. Flynn, "Very High-Speed Computing Systems", Proc. IEEE, Vol. 54, pp. 1901-1909 (1966).

2. I.K. Abu-Shumays, "Vectorization of Transport and Diffusion Computation on the CDC Cyber 205", Nucl. Sci. and Engr., 92, 4 (1986).

3. W.A. Rhoades and R.E. Flanery, "3-D Discrete Ordinates Calculation with Parallel Vector Processors". Topical Meeting on Advances in Nucl. Engr. Comp. and Radiation Shielding, Santa-Fe, N.M. April 9-13, 1989, p. 69.

4. I.K. Abu-Shumays, "Vectorization of Diffusion Computation in the Presence of Periodic Boundary Condition", Top. Meet. on Adv. in Nucl. Engr. Comp. and Rad. Shiel. Santa-Fe, N.M. April 9-13, 1989, p.22.

5. W.A. Thomas and E.E. Lewis "Two Vectorized Algorithms for the solution of Three-Dimensional Neutron Diffusion Equation", Nucl. Sci. and Engr. 84, 67 (1983).

6. S.K. Zee, P.J. Turinsky and Z. Shayer, "Vectorized and Multi-Tasked Solution of the Few-Group Neutron Diffusion Equation" Nucl. Sci. and Engr. 101, 3, p. 205 (1989).

Table 1: Some of the basic characteristic performance of various parallel-vector computers

FEATURE	ALLIANT	CONVEX	CRAY	IBM
Model	FX/8	C220	X/MP-48	3090-600E
Peak Performance (MFLOPS)	11.8	50	210	80
Elock Cycle	85 nsec	40 nsec	8.5 nsec	17.2 nsec
Range of Available Memory	8-64 MB	128 MB	8 MB	64-256 MB
Operating System	UNIX 4.2	UNIX 4.2	UNIX-based OS	VMS/CMS
Cost range	250,000-500,000	1.0 M	5M - 15M	5M-15M

Table 2: Computing Performance (on one CPU) of DIFPA3D[6] Code on various parallel-vector computers (total number of unknowns: 17x17x19x2)

TYPE OF OPERATION	ALLIANT	CONVEX	CRAY	IBM
CPU (Sec)				
Inner Iter.	21.99	2.51	0.52	2.27
Outer Iter.	14.93	1.48	0.19	1.13
Total	42.60	4.62	0.90	3.98
MFLOPS	0.85	8.25	40.45	9.15
Vector Speedup	2.50	-	9.40	2.07

Finite Element Neutron Transport Calculations in Lattice Physics: Convergence Characteristics

W. Rothenstein

Nuclear Engineering, Technion, Haifa

Introduction

Finite Element neutron transport calculations for benchmark problems in lattice physics have now advanced to the stage, where their convergence characteristics can be understood much more clearly than was possible after earlier investigations[1].

The present paper will describe the nature of the calculations without mathematical detail in order to emphasize its special features. A full description of the studies made recently has been submitted for publication in the *Annals of Nuclear Energy*. Results obtained by means of an appropriate code for resonance absorption calculations in a two-dimensional lattice unit cell will be presented in order to show their convergence trends, when the order of the expansions used to describe the space and direction dependence of the flux is increased. The trends are compared and contrasted with the results of similar calculations for the thermal disadvantage factor in a one-dimensional slab lattice for a single broad energy group. The difference of the behavior of the finite element calculations for the two types of problems is discussed. It is suggested that application of the finite element method to the calculation of space-dependent neutron spectra at thermal energies might throw further light on the convergence trends of complementary variational solutions of two alternative forms of the neutron transport equation. These characteristics will determine the potential of finite element techniques as a tool for the accurate calculation of reaction rates in two-dimensional fuel unit cells at epithermal energies on the one hand, and for the determination of thermal neutron spectra in heterogeneous assemblies on the other.

The Finite Element Method as Applied to the Fuel Unit Cell

A representative portion of the unit cell with reflecting boundaries is used as the assembly in which the neutron flux is to be determined as a function of the energy, space and direction coordinates. For infinite square arrays of similar fuel rods, an octant of the unit cell is analyzed for this purpose; one twelfth of the unit cell is adequate for hexagonal arrays of fuel rods. The two-dimensional assembly is subdivided into a set of triangles which are the finite elements. Consequently, outer surfaces of the fuel rods and their cladding are replaced by many-sided polygons. The flux is calculated at a set of nodes in each finite element. Interpolation polynomials are used to evaluate the flux throughout the triangles. The number of nodes depends on the order of the interpolation polynomials; there are 3, 6 and 10 nodes per triangle for linear, quadratic and cubic interpolation respectively. The direction dependence of the flux is described by truncated spherical harmonics expansions, their coefficients being the flux moments. Consequently, flux moments at the nodes are the quantities which are determined by the finite element calculations. They are interpolated as discussed above, and the orders of the spherical harmonics in angle are determined by two integers n and m. When both n and m are even (or odd), the spherical harmonic is even (or odd) with respect to reversal of the neutron direction of motion. Reflecting boundary conditions at the outer boundaries of the assembly described above are expressible as simple constraints imposed on the flux moments at nodes which are located on the boundaries, and which depend, for a particular order of spherical harmonic (n, m), on the sine or cosine of m times the azimuth angle.

Variational techniques[2] can be applied to solve the second order forms of the neutron transport equation, which can be derived from the usual Boltzmann equation by separating it into individual equations of even and odd parities with respect to reversing the direction variable. These separate equations relate to the (unknown) true flux distributions. The lowest moment of the even parity

flux is the scalar flux; the lowest order moments of the odd parity flux are the components of the neutron current. In addition to the two second order transport equations, there are auxiliary equations for calculating the odd parity flux, when the even parity transport equation is solved, and vice versa. The complementary variational methods, which are used to solve the two equations, are based on the definition of a suitable bilinear functional of two trial functions which are to be approximations to the true flux distributions with even or odd parities. When the two trial functions are both chosen to be the difference between a single trial function and the true flux of a given parity, the functional can be maximized, subject to the boundary constraints; it leads effectively to a least square fit of the chosen trial function to the true flux of this parity. As stated previously, the trial function is a truncated spherical harmonics expansion in the direction coordinates and a (low order) polynomial in the space coordinates in each finite element in the assembly. The flux moments at the nodes are determined by solving a set of linear equations by the inversion of a matrix which becomes large, if high order expansions are used both for the space and the direction variables. Although different variational procedures are available, the K^+ method is usually chosen when the optimal trial function is sought for the even parity flux, while the complementary K^- method gives the best fit to the odd parity flux.

The energy variable may refer to a single broad energy group, a number of groups which may be fine, or a set of discrete energies. The appropriate reaction cross sections must be available, including the Legendre moments of the scattering cross section. The source for the solution of the transport equation at each energy or in each group, must also be expressed as a spherical harmonics expansion. Unlike the expansion of the direction-dependent flux, the slowing down source for resonance absorption calculations is usually taken to be isotropic (the moment of order zero), but linearly anisotropic terms can be included, if sufficient computer resources are available. The isotropic source contains a contribution due to in-group scattering which, when subtracted from the total collision rate, gives the absorption rate in problems involving a single broad energy group at thermal energies. For multigroup treatments, the in-group scattering cross sections are quite small, if the groups are fine. Even in the case of a discrete energy, there is an in-group scattering term which diminishes the collision rate. It is due to the fact that the source is given by a scattering integral for the transfer of neutrons to the energy E under consideration from other energies. When the integral is evaluated numerically, the contribution at the energy E itself is effectively due to "in-group" or "self" scattering. The reduction of the collision rate is quite small if a fine energy mesh is used.

The natural choice of variational principle for problems with isotropic sources is the K^+ procedure, since it leads to estimates of the distribution of the even parity flux. Its lowest moment, the scalar flux, is needed to calculate the isotropic source contributions needed to solve the transport equation at other energies. It is continuous at the interface between neighbouring finite elements. On the other hand, one can start with the odd parity flux estimate, obtained by applying the K^- principle to the second order transport equation of odd parity. The auxiliary equation, which expresses the even parity flux in terms of the isotropic source and the flux of odd parity, is then applied to the truncated odd parity flux expansion to estimate the scalar flux as the moment of order zero of the even parity flux. It is, in general, discontinuous at the interfaces between neighbouring finite elements. For the calculation of the scalar flux in a finite element, the auxiliary equation merely equates the collision rate, corrected for in group scattering, to the difference between the isotropic source in the element and the outward leakage derived from the normal components of the currents at its outer surfaces.

The average scalar flux in a finite element, derived in the K^- procedure from the division of source minus leakage by the total cross section (diminished by the zeroth moment of the "in-group" scattering cross section), is affected by the total cross section discontinuity in triangles close to the fuel/clad interface, in a resonance absorption treatment which uses hyperfine energy groups, or closely-spaced discrete energies. This should be contrasted with what happens in a single broad energy group at thermal energies. Here the difference of the total and in-group scattering cross sections is the absorption cross section; the average scalar flux in a finite element in the fuel close to the clad is defined in such a way that its contribution to the overall "source/absorption rate"

neutron balance is satisfied. Any errors in the K^- flux estimates, caused by balancing the (source minus leakage), and the collision rates in the resonance absorption problem, are propagated to lower energies where the source depends on the scalar flux calculated at previous energies.

Results and Conclusion

In the light of the above discussion regarding scalar flux estimates obtained by the K^- variational method for problems involving a single broad group in the thermal energy region, and multi-energy resonance absorption problems at epithermal energies, the convergence characteristics of the calculation of the thermal disadvantage factor in a Uranium/Graphite slab lattice are contrasted with those of effective ^{238}U resonance integrals over a limited energy range in a 2-D mixed oxide PWR unit cell. The former were quoted in a previous paper[1], and are more fully available in the literature[3].

The two-dimensional effective resonance integral calculations have now been examined more fully by studying their convergence for interpolation polynomials of different orders in the finite elements, and for different P_L approximations of the angular flux. It was suggested by Altiparmakov[4] that the orders of both types of expansions should be increased in a reasonably correlated manner in convergence studies. Results for three P_L approximations with equal increments of L can be extrapolated to high order if one assumes that they converge exponentially. Similarly for a particular L, the results for linear, quadratic, and cubic interpolation in the finite elements can be extrapolated to high order interpolation polynomials. This is done in Tables 1 and 2 for the K^+ and K^- procedures. Along the rows, the extrapolation to high order refers to the space variables, along the columns to the direction variables. Further extrapolation in the fourth column and fourth row leads to the final extrapolated results for both types of expansion.

In summary, Table 3 lists the final extrapolated results of Tables 1 and 2. They are compared with similar results when more finite elements, or higher order P_L approximations, are used. Table 3 also shows extrapolated results for the Uranium/Graphite lattice thermal disadvantage factor.

The convergence characteristics of the two types of problems are in line with the observations, made in the last paragraph of the previous section, regarding the use of the K^- variational principle in multi-energy problems. The gaps between the final extrapolated K^- values of effective resonance integrals, and the corresponding K^+ results, suggest that one should rely on the latter since they are based on calculated fluxes, which are continuous at all nodes. It will be of great interest to see if the gap disappears when the two finite element variational procedures are applied to multigroup space-dependent spectrum calculations in a 2-D unit cell at thermal energies. In such problems, source iteration is needed in the different energy groups until overall source/absorption neutron balance is satisfied for both the K^+ and K^- variational procedures in the unit cell. This will place both procedures on the same footing, which is not the case in an epithermal slowing down problem.

References

[1] Rothenstein, W., *Transactions of the Nuclear Societies of Israel*, 15, 40, 1989.

[2] Ackroyd, R.T., *Ann. Nucl. Energy*, 5, 75, 1978.

[3] Ackroyd, R.T. and Nanneh, M.M., *Ann. Nucl. Energy*, 15, 241, 1988.

[4] Altiparmakov, D., Boris Kidric Institute, Yugoslavia, Private Communication, 1990.

Acknowledgement

The partial support received from the Israel Electric Corporation for this research is gratefully acknowledged.

Table 1

Convergence of K^+ Values of I_{eff} for U-238 (22.60–17.60 eV.)
(NB3 Lattice – 16 Finite Elements)

	Linear	Quadratic	Cubic	High Order Space Polyn.
P_1	2.85530	2.76894	2.74242	2.73067
P_3	2.63347	2.53468	2.50529	2.49284
P_5	2.56496	2.45724	2.42725	2.41568
High Order P_N	2.53435	2.41900	2.38897	2.37840 2.37862

Table 2

Convergence of K^- Values of I_{eff} for U-238 (22.60–17.60 eV.)
(NB3 Lattice – 16 Finite Elements)

	Linear	Quadratic	Cubic	High Order Space Polyn.
P_2	1.68386	1.82432	1.83726	1.83857
P_4	1.82734	2.10132	2.11924	2.12049
P_6	1.86467	2.18586	2.21374	2.21639
High Order P_N	1.87780	2.22300	2.26137	2.26618 2.26583

Table 3

Extrapolated Values of I_{eff} for U-238 (22.60–17.60 eV.) for 2-D Square Unit Cell (NB3 Lattice)
Linear, Quadratic and Cubic Interpolation Polynomials Extrapolated to High Order

L Values*	Number of F.E.'s**	I_{eff} (K^+) barns	I_{eff} (K^-) barns
1,3,5	16	2.379	2.266
1,3,5	48	2.375	2.268
3,5,7	16	2.362	2.283

* L Values used to extrapolate the results of P_L approximation (for K^+), and P_{L+1} approximation (for K^-), to high L

**16 F.E.'s : 4 in fuel rod interior, 4 near fuel rod surface, 4 in clad, 4 in moderator
48 F.E.'s : 15 in fuel rod interior, 6 near fuel rod surface, 6 in clad, 21 in moderator

Extrapolated Values of Thermal Disadvantage Factor (d) for 1-D Uranium/Graphite Slab Lattice
(20 Finite Elements, Quadratic Interpolation)

Number of Moments*	$d(K^+)$	$d(K^-)$
1,3,5	1.7126	1.7240
5.10, 15	1.7164	1.7176

* Number of Moments used to extrapolate the results to high order spherical harmonics.

Sensitivity of Multiplication Calculations to the Representation of the Fission Spectrum

R. L. Perel, J. J. Wagschal
Racah Institute of Physics
The Hebrew University of Jerusalem
91904 Jerusalem, ISRAEL

SUMMARY

The treatment of the fission spectrum has undergone many refinements over the last two decades. In early times[1] it was generally accepted to use for all materials in a single calculation the same, incident neutron independent, fission spectrum. Later[2] it became evident that the fission spectrum is material dependent and depends on the incident neutron energy. Since the results of calculations (criticality or shielding) are sensitive to this effect, an increasing number of calculations are done with the full fission matrix. An other refinement of the description of the fission process, that is well known, is the description of the fission process as the sum of direct fission, first chance fission (E > ~ 6 MeV), second chance fission (E > ~ 12 MeV) and so on; in ENDF/B[3] terminology the fission process is differentiated as (partial) reactions MT=19, MT=20, MT=21 and MT=38 respectively, in addition to their sum, the total fission MT=18.

We were interested to see the sensitivity of simple reactor calculations to the representation of the fission process. Moreover, while the evaluators of ENDF/B formatted libraries generally made sure that the partial cross sections (MF=3) of these reactions sum up to the total fission cross section, the fission spectrum (MF=5) of the total fission given in libraries is generally not equivalent to the fission spectrum obtained from all partial spectra. Usually (in ENDF/B-IV or in the data for U^{235} in ENDF/B-V) the total fission spectrum is given as either a Maxwellian or as a Watt spectrum, while the partial spectra are given as mixture of a fission spectrum (Maxwellian or Watt) for the fission part of the reaction and as an evaporation spectrum for the inelastic part of the reaction. The data of the relevant materials in ENDF/B-VI are not yet available at the time of writing. Since the data are inconsistent, there is also the need to know how results of calculations are effected.

In order not to obstruct the calculation with irrelevant data, we propose to demonstrate in the summary results for a bare spherical system composed of one isotope only. On one hand we checked the change in the k_{eff} of a Jezebel-like assembly (radius = 6.385 cm, density = 15.44 g/cm^3) of pure Pu^{239}, and on the other hand we computed the leakage out of a somewhat smaller sphere (radius of 5.8 cm, same density) when a pulse of 14 MeV neutrons is applied at its center. These transport computations were done according to the CSEWG[4] recommendations:

- 34 energy groups (26 energy groups of half lethargy width from 10 MeV and lower, augmented and refined by groups of 1 MeV width between 6 Mev and 15 MeV in order to be able to detect the sought effects)
- S_n order of 16
- 40 radial intervals in the sphere
- multipolarity L of 3.

The group cross sections were generated using the NJOY.87[5] code with data from ENDF/B-IV.* This code can either use the sum of the partial fission spectra in its computations or compute the fission matrix with the total fission cross section and with the total fission spectrum (MT=18 only).

It was found that the k_{eff} eigenvalue computed with the total fission spectrum is higher than k_{eff} computed with the partial spectra by about 0.4 mk: k_{eff} is 1.00589 vs. 1.00545. In the inhomogenous case, the total leakage computed with a single total fission spectrum is higher than the leakage computed utilizing the sum of the partial spectra by 1% (28.28 vs. 27.97). The leakage is higher in all energy groups.

Although these differences are relatively small, they can be calculated accurately, and relative to an experimental uncertainty of 1.7 mk they are not neglible.

---

* This library was chosen, since it is the only data file universally available that includes data on higher chance fission. Anyway the effects demonstrated here are qualitatively independent of the specific representation of the individual spectra.

Discussion

In ENDF/B-IV the fission part of all reactions (MT=18-21) is defined as Maxwellian, the temparature of it being the same for all reactions. The inelastic part of MT=20 and MT=21 is described as evaporation spectrum, which is softer than the Maxwellian. Therefore the spectrum of total fission is harder than the spectrum of the sum of all partial reactions. Since in the fast energy range $\nu\sigma_{fis}$ increases with energy, it is clear that k_{eff} and the multiplication in the inhomogenous problem, are higher for the single total fission representation.

Conclusion

While evaluating and editing cross section files, care should be taken to define the spectra of the total and of partial fission process representations consistently. While handling cross section data one should know whether the datafile contains inconsistent information. Once again the rule which each researcher should know is confirmed: Do not rely blindly on your cross section processing code, be sure to use the better data as appropriate in each case.

References

1. W. W. Engle, Jr. "ANISN, A One-Dimensional Discrete Ordinates Transport Code with Anisotropic Scattering", K-1693, Oak Ridge Gaseous Diffusion Plant (1967).
2. J. J. Wagschal and A. Yaari, "A Systematic Test of the ENDF/B-III Evaluated Cross-Section Library on 'Clean' Critical Assemblies", in "Nuclear Data in Science and Technology II", IAEA-SM-170/19, International Atomic Energy Agency (1973).
3. ENDF-102, "Data Formats and Procedures for the Evaluated Nuclear Data File", ENDF, Revised by R. Kinsey, National Nuclear Data Center, Brookhaven National Laboratory (1979).
4. ENDF-202, "Cross Section Evaluation Working Group Benchmarks Specifications", National Neutron Cross Section Center, Brookhaven National Laboratory, (1974 with later revisions and additions).
5. R. E. MacFarlane, D. W. Muir, and R. M. Boicourt, "The NJOY Nuclear Data Processing System", Vols 1 to 4, LA-9303-M, (ENDF-324), Los Alamos National Laboratory, (May 1982 to December 1985).

CRISY: a CRItical Assemblies Documentation SYstem

U. Salmi, R. L. Perel, J. J. Wagschal
Racah Institute of Physics
The Hebrew University of Jerusalem
91904 Jerusalem, ISRAEL

SUMMARY

The exact specification of the dimensions and material composition of any benchmark system are a necessary condition for any validation calculation or cross section adjustment attempt. Experience has shown that currently available compilations of critical assemblies specifications[1] sometimes have a few major shortcomings. These include:

a. Lack of some information on the dimensions or material composition of an assembly;

b. Seemingly redundant data that indicate inconsistencies in the description;

c. Incomplete description of "corrections" applied to experimental data in order to compensate for experimental difficulties.

CRISY, a CRItical assemblies documentation SYstem, reflects the experience of generating input data for reactivity calculations of critical assemblies. CRISY consists of two parts:

a. An electronic spreadsheet that has entries for the data given in the literature, entries for the the necessary input for transport codes and the linking formulae used.

b. Documentation of the data available for each critical assembly.

The documentation includes:

1. A replica of the data used, a discussion of lacking or redundant data and a detailed explanation of the considerations that led to the final input data for the transport calculations.

2. A "completeness index" indicating the level of completeness, consistency and additional information needed for each assembly.

3. A discussion of quoted experimental uncertainties and the resulting uncertainties in calculated reactivities.

As an example we bring the elucidation of the description of the critical system consisting of 7.601 kg of ^{233}U reflected by natural Uranium. The measurements and the data for this system were first reported in reference 2. The diameter, weight and density of the core are given but are inconsistent: e.g. the weight calculated from diameter and density differs slightly from the given weight. Reference 3 describes the evaluated data of a different critical system also with a core of 7.601 kg of ^{233}U reflected by enriched Uranium. The reported core mass is equal to that in ref. 2, but the density is different. Ref. 3 does not give the diameter of this system, but when this diameter is calculated it is found to be equal to the diameter given in ref. 2. Since the experiments in ref. 2 consisted of measuring criticality of the same cores with different reflector materials, we conclude that the two descriptions describe the same core. Therefore in CRISY the diameter, weight and density of the natural Uranium reflected system are based on reference 3. Similarly the isotopic content of the core is given in greater detail in reference 3 and therefore it is adopted in CRISY also for the natural Uranium reflected core. On the other hand reference 3 lacks data on the natural Uranium reflector itself; therefore the data of ref. 2 were used in CRISY since no inconsistency in the reflector data was found.

CRISY will be used for consistency tests of the new ENDF/B-VI data and for cross section adjustments that can substantially reduce the uncertainty in calculated reactor performance and safety data[4].

References

1. See e.g. H. C. Paxton and N. L. Pruvost, "Critical Dimensions of Systems Containing ^{235}U, ^{239}Pu, and ^{233}U", 1986 Revision, LA-10860-MS.
2. E. A. Plassmann and D. P. Wood, Nucl. Sci. Eng., **8**, 615-620 (1960).
3. G. E. Hansen and H. C. Paxton, "Reevaluated Critical Specifications of Some Los Alamos Fast-Neutron Systems", LA-4208, (1969).
4. See e.g. J. R. White and T. F. DeLorey, "Data Uncertainty Reduction in High Converter Reactor Designs using PROTEUS Phase II Integral Experiments", PHYSOR90 International Conference on the Physics of Reactors: Operation, Design and Computation. Vol 3, p. III-107 (1990).

OPTIMIZATION OF GEMSTONE IRRADIATION IN THE IRR-1

R. Dagan, H. Hirshfeld and A. Nagler
Soreq Nuclear Research Center, Yavne 70600, Israel

and

M. Segev
Nuclear Engineering Department, Ben Gurion University of the Negev, Be'er Sheva , Israel

The IRR-1 was one of the first reactors in the world in which gemstones (topaz and diamonds) were colored successfully. Some of the ways by which one can alter the appearance of gemstones are thermal treatment and gamma or beta irradiation. Another method, which is used in the IRR-1, is to bombard the gemstone crystal with neutrons.

In the case of topaz crystals ($Al_2SiO_4(F,OH)_2$) the neutron irradiation technique is based on a high energy neutron which collides with an oxygen atom, and knocks it out of its ordered position in the crystal. Some of the electron density involved in the silicon-oxygen bond that was broken by the neutron remains in the voided oxygen location. This site is now referred to as a "void". The void behaves quite differently from the oxygen atom with respect to visible light. It absorbs the red wavelengths from the spectrum giving the transmitted light - and hence the topaz crystal - a blue color.

Due to impurities within the topaz there is always undesirable activation. The thermal neutrons which activate most of the impurities are cut off by a cadmium cover that surrounds the irradiation positions. Other impurities (mainly tantalum) within the topaz are activated in the 1 to 100 ev region, where they have high absorption resonances. The goal of this work was therefore to find an optimized core structure that would increase the high energy flux, absorb the thermal neutrons and reduce the epithermal neutron flux in the resonance region.

For accurate evaluation of the neutron flux, the heterogeneous structure of the fuel elements and the irradiation positions require a transport solution. The DOT code, used mainly in power plant core calculation, solves the transport equations. In order to adapt the code to the IRR-1 core configuration, some modifications were necessary. Once the code conformed with the referenced measurements in the core, the optimization calculation was executed.

The code was run with different reflectors (beryllium , aluminum and water as a test case) which were compared with the graphite reflector in the core. The results show that five beryllium rods (locations 23,33,43,53,63 in fig. 1) increase the core reactivity by 0.9% (abs.). In the irradiation position the 1 to 10 Mev neutrons are reduced by 10%, and integrating all the neutrons above the cadmium cutoff (0.5 ev) shows an average growth of approximately 15% in the neutron flux. The reason for these results is the 2 Mev threshold energy in the (n,2n) reaction, while the emitted neutrons are in the Kev region.

Five aluminum rods located at the same site mentioned above, reduce the core reactivity by 2% with respect to the graphite reflector. In the irradiation positions there is a 10% growth of the 1 to 10 Mev neutrons, while the integral fast neutron flux shows a decrease of approximately 5%. The phenomena concerning the aluminum reflector are due to the fact that the aluminum atom density is less than the graphite one although its nucleus is heavier.

Concerning the core irradiation location, three positions (32,42,52 in Fig. 1) are better than position 76 (Fig. 1), since the three decrease the core reactivity only by 0.5% (position 76 1.1%), and enhance the amount of gemstones irradiated within the same time interval.

Based on the calculations in this work, and other measurements, it was possible to produce blue topaz commercially. This commercial processing has been in practice with the IRR-1 for the past several months. Additional experiments to enhance optimization are currently being done.

	10	9	8	7	6	5	4	3	2	1
10										
20	C	C	C					C	C	
30	C	C	F	F		F	F	C	C	C
40	C	C	F	FC	F	FC	F	C	T	C
50	C	C	F	F	F	F	F	C	T	C
60	C	C	F	FC	F	FC	F	C	T	C
70	C	C	F	F	F	F	F	C	C	C
80	C	C	TD	F	T	F23				
90										
100										
110										

Fig. 1: Present core configuration

C - Graphite rod.
F - Fuel rod.
FC - Special fuel rod (control).
T - Irradiated topaz rod.
TD - Irradiated diamonds rod.
A - Aluminum rod.
Empty square - Water.

RADIO CHEMISTRY

DETERMINATION OF THE ANGLE OF MINIMUM ENERGY WIDTH FOR 14 MEV NEUTRON EMISSION FROM A NEUTRON GENERATOR

A. TSECHANSKI and R. OFEK

Department of Nuclear Engineering, Ben Gurion University of the Negev, P.O.Box 653, Beer Sheva 84120, Israel

The D-T (deuterium-tritium) neutron generator is extensively used as a fast neutron source in integral experiments for fusion reactor blanket studies. Neutron energy spectra are obtained in such experiments by either the TOF (time of flight) method, or by measuring proton recoil spectra in liquid scintillators which are consequently unfolded into neutron energy spectra. In both methods, the measurement of a spectrum of uncollided neutron beam serves as an effective tool for energy calibration of the neutron spectrometer and testing its validity.

The theoretical dependence of the energy of a neutron outgoing a D-T reaction on the angle of emission and the energy of the deuteron impinging the tritium nucleus is well known, and it is implied from the kinematics of the reaction[1-2]. But neutrons of ~14 MeV, commonly produced from the D-T reaction, are generated using a beam of deuterons of several hundred keV incident upon a "thick" (relative to the range of the bombarding deuterons) solid Ti - T target. Therefore, there is a somewhat spread in the energies of the produced neutrons, due to slowing down and scattering of the deuterons in the target. Hence, the mean neutron energy cannot be calculated, but must be measured, since the exact tritium disposition in the target, and the slowing down and scattering events which the deuterons are undergoing, are unknown. Furthermore, even if the mean energy of the neutron beam is determined accurately, the energy spread of the neutrons in the beam disturbs the monoenergeticity required for integral experiments with a "clean" neutron field.

This difficulty may be overcome by carrying out the experiments with neutrons emitted in an angle of a minimum dependence of the neutron energy on the energy of the incident deuteron.

Hence, the question that immediately arises now is : what is the angle of emission (relative to the direction of the deuteron beam) at which the neutron beam is most monoenergetic ?

From a pure kinematical point of view, the direction of emitted neutrons, where the neutron energy E_n is almost independent of the incident deuteron E_d, is roughly perpendicular to the direction of the deuteron beam[3]. However, many values for the angle of minimum energy width in actual D-T neutron generators are given in the literature, spreading from 90° (for incident deuteron energies between 100 to 500 keV) up to 108° (with a deuteron energy of 700 keV)[4-10].

Such a variety in substantially different recommended values to the angle of minimum neutron energy width, for a ~14 MeV neutron beam, deserves an investigation devoted to this problem.

Returning to the kinematics, the angle of minimum dependence of the neutron energy E_n on the deuteron energy E_d, where $0 < E_d < 500$ keV, ranges between 90° to 100°. However, *there is no single value of this angle,* and it is a smoothly increasing function of E_d.

The problem may be treated analytically with the classical approach (the relativistic contribution is relatively small, and may be discarded herein). The classical conservation laws, assuming a net energy change (the Q-value of the reaction, which is 17.58 MeV) between the initial and the final states of the reaction result in the following relation between E_n, E_d, and the direction of the outgoing neutron (in the laboratory coordinates system)[2]:

$$E_n = m_d m_n E_d \left[\frac{(\eta + \cos^2\theta)^{\frac{1}{2}} + \cos\theta}{m_n + m_\alpha} \right]^2 , \qquad (1)$$

with

$$\eta = \frac{(m_n + m_\alpha)[(m_\alpha - m_d)E_d + m_\alpha Q]}{m_d m_n E_d} , \qquad (2)$$

and where m_d, m_n, and m_α are the rest masses of deuteron, neutron, and alpha particle respectively ; θ is the neutron emission angle in the laboratory system ; and Q is the Q value of the reaction.

The problem of determination of the angle of minimum source linewidth can be solved relatively easily from Eqs. (1), (2) under some limitations imposed on the energy distribution function of the deuterons entering the D - T reaction in the solid Ti -T target under consideration. If it is assumed that all the deuteron energies between E_d^{min} and E_d^{max} are equiprobable (where E_d^{min} is the minimum energy into which the deuteron is slowed down before undergoing the fusion reaction with the tritium nucleus, and E_d^{max} is the energy of the deuteron when it reaches the target), then :

$$\cos\theta = -1 + \sqrt{1 - 2\frac{(E_d^{max}\eta_{max})^{\frac{1}{2}} - (E_d^{min}\eta_{min})^{\frac{1}{2}}}{(E_d^{max})^{\frac{1}{2}} - (E_d^{min})^{\frac{1}{2}}}} , \qquad (3)$$

where η_{min} and η_{max} are given by Eq. (2) by substituting either E_d^{min} or E_d^{max} for E_d respectively.

Values of θ^{min}, the angle of minimum dependence of the neutron energy on the deuteron energy, at some values of E_d^{min}, and at E_d^{max} = 150 keV, are given in Table 1.

E_d^{min} (keV)	θ^{min}(deg.)
10^{-3}	94°18'
10	95°26'
30	96°20'

Table 1.

However, the assumption of an equal probability of deuteron energies between E_d^{min} and E_d^{max} is only a crude approximation to the real situation, since the cross section of the D-T reaction changes with the energy of the incident deuteron. It is increased from zero at $E_d = 0$ to the value of 5b at E_d = 107 keV, then it decreases so that it equals 3.8b at E_d = 150 keV [11].

As noted above, the angle of emission of neutrons of minimum energy width in actual D-T neutron generators have to be determined experimentally. The energy linewidth is expressed in term of the parameter FWHM, the full width at half maximum of the ~14 MeV peak in the energy spectrum of an uncollided neutron beam. The procedure for measuring the FWHM is described elsewhere[3]. Measured values of FWHM at some angles of neutron emission relative to the axis of the neutron generator (the direction of the incident deuteron beam) are given in Table 2.

θ	FWHM (keV)
0	1010.5 ± 17.7
85	937.3 ± 37.3
90	805.9 ± 21.6
95	754.8 ± 15.9

Table 2.

Hence, it may be seen that the parameter FWHM decreases considerably at $\theta \sim 96^{o}$.

Measurements of FWHM at the whole range of $90^{o} < \theta \leq 100^{o}$ are carried out within the present study.

Meanwhile, it may be summarized that for a thick solid Ti - T target, the optimum angle of emission of neutrons with minimum energy width, at a 150 kV nominal accelerating voltage, is between 95^{o} to 96^{o}.

REFERENCES

1. H. Liskien and A. Paulsen, Nucl. Data Tables, **11**, 569 (1973).
2. J. Monahan, "*Kinematics of Neutron- Producing Reactions*," in *Fast Neutron Physics*, Part I, edited by J.B. Marion and J.L. Fowler, Interscience Publishers Inc., New York (1960).
3. A. Tsechanski and G. Shani, Fusion Technol., **7**, 125 (1979).
4. E. Amaldi, "*The Production and Slowing down of Neutrons*," in *Handbuch der Physik* , Bd. xxxviii / 2, Springer (1959).
5. S.S. Nargolwalla and E.P. Przybylowicz, "*Activation Analysis with Neutron Generators*," John Willey & Sons (1973).
6. D.W. Mingay, J.P.F. Sellschop, and P.M. Johnson, Nucl. Instr. Meth., **94**, 497 (1971).
7. J.L. Kammerdiener, "*Neutron Spectra Emitted by ^{239}Pu, ^{235}U, Pb, Nb, Ni, Al, and C Irradiated by 14 MeV Neutrons*," Report UCRL-51232 (1972).
8. T.B. Ryves and K.J. Zieba, Nucl. Instr. Meth., **167**, 449 (1979).
9. V.E.Lewis and E.J. Axton, Nucl. Instr. Meth., **159**, 401 (1979).
10. H. Sekimoto, K. Hojo, and T. Hojo, J. Nucl. Sci. Technol., 22, 174 (1985).
11. N. Jarmie, R.E. Brown, and R.A. Hardekopf, "*Fusion-Energy Reaction D(t, α)n from E_t=12.5 to 117 keV* ," Report LA-UR 84-835, Los Alamos National Laboratory (1984).

PRODUCTION OF ^{73}Se VIA THE $^{70}Ge(\alpha,n)^{73}Se$ REACTION AT A COMPACT CYCLOTRON USING Cu_3Ge ALLOY AS A HIGH CURRENT TARGET MATERIAL

N. Lavi*, G. Blessing, S.M. Qaim and G. Stöcklin
Institut für Chemie 1 (Nuklearchemie), Kernforschungsanlage Jülich GmbH
D-5170 Jülich, Federal Republic of Germany

Summary

Cu_3Ge alloy electrodeposited on Cu-backing was developed as a high current target material for the production of ^{73}Se (7.1 h) via the $^{70}Ge(\alpha,n)^{73}Se$ reaction. It was found to withstand power densities of 1 KW cm^{-2}. A thermochromatographic technique was developed to separate radioselenium in a no-carrier-added form from the irradiated target. The distillation yield of radioselenium at 900 °C (at a constant He flow rate of 4.1 l/h) is > 90%. Radioselenium was found to be of high radionuclidic purity, the impurity levels being: ^{75}Se (0.44-0.55%), ^{66}Ga (0.42-0.44%), ^{65}Zn (0.7-0.9%) and ^{72}Se (0.65-0.68%). The radioselenium is released from the distillation apparatus (quartz tube) by H_2O_2. It exists probably as selenite (SeO_3^{2-}).

The experimental thick target yield of ^{73}Se is 80 μCi/μAh, corresponding to about 41% of the theoretical value, taking into account that the Ge concentration in the Cu_3Ge alloy is 28%. Using a thick target (20 mg Cu_3Ge/cm^2, E_α = 28 → 10 MeV), and an irradiation time of 2 h at an α-particle beam of 60 μA, about 10 mCi of ^{73}Se (at EOB) is produced. Using 97% enriched ^{70}Ge, under the same experimental conditions about 50 mCi of ^{73}Se (at EOB) would be formed. The feasibility of using an intermetallic compound of the copper-germanium system, as an external target material was investigated experimentally. Intermetallic compounds with Ge content ranging between 28 and 40% can also withstand power densities of up to 1 KW cm^{-2}.

---

* Guest scientist from Soreq Nuclear Research Center, Yavne, Israel

ELECTRON TRANSFER BETWEEN TYROSINE AND TRYPTOPHAN IN PROTEINS, A PULSE RADIOLYSIS STUDY. HEN EGG-WHITE LYSOZYME*.

Marcelo Weinstein+, Zeev B. Alfassi+, Michael R. DeFelippis#, Michael H. Klapper# and Moshe Faraggi#+,

(+) Department of Nuclear Engineering, Ben-Gurion University of the Negev, Beer-Sheva (#) Department of Chemistry, Ohio State University, Columbus, Ohio 43210, U.S.A. (±) Department of Chemistry, Nuclear Research Centre-Negev, Beer-Sheva.

Hen egg-white lysozyme is perhaps the most extensively studied protein. It is a small protein (13.7 kDalton), roughly ellipsoidal (4.5x3x3 nm) of known crystal structure.

Egg-white lysozyme contains six tryptophyl (trpH) and three tyrosyl (tyrOH) residues at various locations which determine its exposure to the solvent and distances separating them. According to x-ray crystallography trpH 62, 63 and 108 are part of the active site of lysozyme, however the first two trpH (62 and 63) and trpH 123 are exposed to the solvent.

According to recent theoretical calculations the best exposed active site tryptophyl residue is trpH 62. On the other hand it was shown that the protein can be inactivate upon iodine oxidation of trpH 108 . Therefore this residue was assigned as the residue responsible for the radiation inactivation of lysozyme.

Experimental evidence for intramolecular long range electron transfer (LRET) in proteins and polypeptides has been verified by observations of LRET between donor/acceptor redox centers with known (crystallographic) separation distances . As part of a program to unravel the mechanistic basis of LRET in proteins, we have begun a systematic investigation of electron transfer between tyrosine and tryptophan in proteins. As reported in the literature, one can observe 1-electron transfer between tyrosine and the neutral indolyl radical of tryptophan (trp$^{\bullet}$) as part of the following reaction series:

$$e^{-\bullet}_{aq} + N_2O \xrightarrow{H_2O} OH^{\bullet} + N_2 \qquad [1]$$

$$OH^{\bullet} + N_3^- \longrightarrow OH^- + N_3^{\bullet}$$

$$N_3^{\bullet} + trpH{=}X{=}tyrOH \longrightarrow trp^{\bullet}{=}X{=}tyrOH + N_3^- + H^+ \qquad [2]$$

$$N_3^{\bullet} + trpH{=}X{=}tyrOH \longrightarrow trp{=}X{=}tyrO^{\bullet} + N_3^- + H^+ \qquad [2']$$

$$trp^{\bullet}{=}X{=}tyrOH \rightleftharpoons trpH{=}X{=}tyrO^{\bullet} \qquad [3]$$

$$trpH{=}X{=}tyrO^{\bullet} \text{ (or } trp^{\bullet}{=}X{=}tyrOH) \longrightarrow \text{Products} \qquad [4]$$

Where the pulse radiolytically generated primary radicals, the hydrated electron ($e_{aq}^{-\cdot}$) and hydroxyl radical ($OH^{\cdot}$),are converted by the two reactions of into the azide radical ($N_3^{\cdot}$) within the *first μsec after the pulse.* Similar reactions convert the primary radicals to $Br_2^{-\cdot}$ (solutions containing 50mM Br^- at pH < 5) or to $Cl_2^{-\cdot}$ (solutions containing 100 mM Cl^- at pH ≤ 2.5). The indolyl side chain of tryptophan (trpH) is oxidized to the neutral tryptophan radical approximately 30x more rapidly by the azide radical (or $Br_2^{-\cdot}$ or $Cl_2^{-\cdot}$)than is the side chain of tyrosine (tyrOH) and this preferential oxidation in reaction (2) sets up the 1-electron transfer reaction of (3) . Finally, the radicals (primarily the $tyrO^{\cdot}$ but it could be also the $trp^{\cdot}$) decay via reaction (4). This reaction determines therefore the stability of the phenoxy radicals ad may be that of the indolylradicals, the first two amino acid radicals recently found in natural biological oxidation reactions .Since both amino-acid radicals absorb in the visible region ($trp^{\cdot}$ at 510 nm, $tyrO^{\cdot}$ at 405 nm), this one electron transfer can be monitored as an absorbance change (decay at 510 nm, formation at 405 nm). Kinetic results obtained for hen egg-white lysozyme are reported. This includethe 2nd order rate constants for the formation of the indolyl radical by the azide radical (or the bromide radical anion and the chloride radical anion in acid solutions), the first order intramolecular electron transfer from the phenoxy side chain to the indolyl radical (≥30 s^{-1} at pH 7), and the stability of the phenoxy radical in this protein ($t_{½}$ ≳ 1 s).

Moreover, we found that the pH profile of the intramolecular electron transfer rate constant resembles the pH-rate profile of the enzyme-catalysed reaction. Based on this finding and the structure of the protein, we suggest that the active site of the enzyme is associated with the long range intramolecular process. We also suggest that the correlation between these results and the radiation inactivation of egg-white lysozyme is due to the slow equilibrium decay of of the phenoxy radicals.

(\$) This work was supported by NIH grant GM-35718 and by Grant from the United States-Israel Binational Science Foundation (BSF 8600206) Jerusalem, Israel.

A Two-Steps Coprecipitation Method for Differentiating Chromium Species in Natural Waters, followed by Neutron Activation Analysis

Z.B. Alfassi , C.R. Lan and M.H. Yang

Department of Nuclear Engineering , Ben Gurion University , Beer Sheva and

Institute of Nuclear Science, National Tsing Hua University , Hsinchu, Taiwan

Chromium can be present in natural waters in two different valence states, Cr (III) and Cr(VI). Trivalent chromium is an essential element whereas Cr(VI) is a toxic material. The determination of chromium in natural waters requires a preconcentration prior to determination, due to its low concentration and the high concentration of the interferences. This preconcentration step is specially essential for Neutron Activation Analysis, due to the limitaiton of the size of the irradiated sample, and due to the limitation of time of irradiation for wet samples.

We were looking for a preconcentration method, that will simultaneously differentiate the two species of Cr. The method is based on the different patterns of coprecipitation yields with $Pb(PDC)_2$ as a function of pH as can be seen in table 1. Using two different pH's both species can be determined separately. First Cr(VI) is coprecipitated at pH = 4.0 and then the pH is changed and Cr(III) is coprecipitated at pH = 9.0.

If only total chromium is required, it is determined by reduction of Cr(VI), followed by coprecipitation at pH = 9.0.

Table 2 give the results for Cr(III) and Cr(VI) in several natural waters.

Table 1. Yield of recovery of Cr(III) and Cr(VI) by coprecipitation with $Pb(PDC)_2$ as a function of the pH.(in percents)

	Distilled water		Tap water		Sea water	
pH	Cr(III)	Cr(VI)	Cr(III)	Cr(VI)	Cr(III)	Cr(VI)
3	0.8	92	0.8	92	0.5	95
4	1.8	98	1.8	95	0.5	95
5	3.6	95	3.6	95	0.5	95
6	13.2	95	13	95	4	34
7	88	58	66	58	67	14
8	93	52	93	52	96	14
9	97	44	97	44	95	16

Condition: 250 ml of water, 100μg Cr(III) or Cr(VI), 100 mg of APDC and 2 mg $Pb(NO_3)_2$

Table 2. Analytical results of Cr(III) /Cr(VI) in natural water(ng/mL)

Sample	Cr(VI)	Cr(III)	Total Cr
Sea Water	0.10 ± 0.01	0.49 ± 0.04	0.54 ± 0.03
Well Water	0.13 ± 0.05	0.11 ± 0.02	0.25 ± 0.02
Tap Water	0.14 ± 0.04	0.20 ± 0.05	0.33 ± 0.05

Oxidation Reactions of Perfluorobutylperoxyl radical - A model radical, for radical induced by radiolysis of polytetrafluoroethylene (PTFE)

Zeev B. Alfassi and G. Nahor
Department of Nuclear Engineering, Ben Gurion University, Beer Sheva
and Chemical Kinetics Division, National Institute of Standar

Radiolysis of PTFE leads mainly to C-C bond ruptures but also to C-F bond ruptures. Both reactions leads to perfluoroalkyl radicals. The reactivity of these radicals were not studied until now and the only available data is the yield of final products upon radiolysis. We decided to study the rate constants of reactions of perfluorobutyl radical (PFB) as a model system for the reactivity of perfluoroalkyl radicals.

The n-C_4F_9 radicals (PFB) were produced by pulse radiolysis of solutions of n-C_4F_9(PFBI) in various solvents. The solubility of PFBI in water is too low to produce sufficient amounts of radicals and consequently we used alcohols, acetone or their mixture with water (1 : 1) . PFB is formed by the reactions

$$e^- + PFBI \longrightarrow PFB\cdot + I^-$$

$$R + PFBI \longrightarrow PFB\cdot + RI$$

were R is a radical produced from the solvent.

It was found that while in deaerated solution , PFB did not react with any of several reducing compounds studied, in aerated solution they were oxidized, as proven by the appearance of the spectra of the oxidized form of the substrates - chloropromazine, trolox and hydroquinone. The requirement of the presence of oxygen , indicates that the reaction is due to the peroxyl radical ($PFBO_2$) rather than to PFB radical

$$(1)\ PFB + O_2 \longrightarrow PFBO_2$$

$$(2)\ PFBO_2 + A \longrightarrow PFBO_2^- + A^+$$

Another evidence for the involvement of oxygen is found in the dependence of the rate constant for formation of A^+(k) on the concentration of A(c). For low concentration of A, k is a linear function of C, however for high concentration of A, k is reaching a saturation value, which is due to reaction 2 becoming faster than reaction 1. The reaction of reaction 1 is limited by the solubility of oxygen.

The observation that $PFBO_2$ is a considerable more potent oxidant than PFB, is similar to what is known concerning CH_3, CCl_3 and CF_3. Table 1 gives the rate constant for the reactions of $PFBO_2$ with three substrates in various solvents.

The results in this table, show that $PFBO_2$ is a very strong oxidant compared to other peroxyl radicals. The main difference is seen for trolox and hydroquinone , since chloropromazine is very reactive and the difference between the various radicals is very small.

The results for chloropromazine shows a slight dependence on the polarity of the solvent, much smaller than was found for CCl_3O_2 and CF_3O_2.[1,2].

References

1. Z.B. Alfassi, S. Mosseri and P. Neta, J. Phys. Chem. 91, 3383 (1987).
2. P. Neta, R.E. Huie, P. Maruthamuthu and S. Steenken, J. Phys. Chem. 93, 7654 (1989).

Table 1. Rate constant for the reactions of peroxyl radicals ($x10^7$ $M^{-1}s^{-1}$)

Substrate	Solvent	$PFBO_2$	CF_3O_2	CCl_3O_2	CBr_3O_2
Chloropromazine	2-propanol	28		29	
	Acetone	57			
	Methanol	59			
	Methanol : H_2O(1:1)	190			
Trolox	2-propanol	60		2.1	3.7
	Acetone	77			
	Methanol	64	15	3.1	
	Methanol : H_2O(1:1)	79	74	3.6	46
Hydroquinone	2-propanol	12			
	Acetone	11			
	Methanol : H_2O (1:1)	10	7.9	1.0	1.8

NUCLEAR INSTRUMENTATION AND DOSIMETRY

TWO METHODS OF REASSESSMENT OF HIGH DOSES WITH LiF:Ti,Mg

B. Ben-Shachar, Y. Rachmian, U. German , E. Naim .
Department of Radiation Protection and Safety
NRC-Negev, P.O.B. 9001, Beer-Sheva, 84190, Israel.

1. Introduction.

The thermoluminescent dosimeter is becoming increasingly important in all aspects of personnel and environmental monitoring. The main limiting factor that has prevented even wider usage is the inability of dose reassessment after the initial readout.

LiF has been extensively used in dosimetry and is even today the most widely used material (1). The LiF:Ti,Mg, proposed by Cameron (2), is a good compromise between the various desired characteristics. It is not as sensitive as certain other materials, but allows doses of 0.1 mGy to be measured with high performance equipment. The absence of thermal and optical fading (when different annealings are used) and almost tissue equivalence makes it the most useful TL material in radioprotection. There are two ways of reassessing high doses: by measuring the residual dose (the second reading of the TL chips) and by photo-transferred thermoluminescence (PTTL).

PTTL is thermoluminescence due to the u.v. light exposure in a phosphor (3) which had been earlier exposed to ionizing radiation and then annealed and readout, leaving some TL as a residual (RTL). The LiF:Ti,Mg has deep traps that can be significantly populated by high doses of ionizing radiation. Because normal readout procedures (heating to about 300°C) usually do not depopulate these traps, a second uv irradiation followed by the conventional readout can produce a response which is proportional to the original high dose. These "memory effects" in TL materials can be employed for the re-estimation of doses and have been reported in several previous papers (4,5).

The aim of the present work was to measure the residual dose and the PTTL for high doses (to 7.5 Gy), and to determine the accuracy of the methods.

2. Materials and methods.

The measurements of the residual doses and the PTTL were performed with the standard Harshaw manufactured TLD-100 chips (3mm x 3mm x 0.9mm) and G-1 or G-7 cards. The TLD chips were annealed in air for 400°C/1h, followed by a fast cool (10 minutes) to room temperature before irradiation and readout. No annealing was performed for the TLD cards. The chips were irradiated by a 1.11xE11 Bq Co-60 gamma ray source and evaluated by a manual Harshaw 2000C reader. The TLD cards were read in an automatic Harshaw 2271 reader after being irradiated by a Sr-90/Y-90 source built in the reader. The uv irradiation was performed by a 15 mW uv lamp (254nm) at a distance of 11cm.

3. Experimental results.

Four TLD-100 chips or two TLD cards were irradiated to different doses between 0.15 and 7.5 Gy. The phosphors were evaluated immediately after the irradiation and a second reading was performed, to measure the residual dose. After the second reading, the chips or cards were irradiated by the uv lamp for 15 minutes and then read again (to measure the PTTL). The average results of the residual dose and PTTL are presented in table 1.

Table 1: The average results of the residual doses and PTTL for exposures of 0.15 - 7.5 Gy.

Exposure (Gy)	Residual dose (mGy)	% of exposure	PTTL (mGy)	% of exposure	PTTL/res. dose
0.15	0.20 ± 0.10	0.13	4.8 ± 0.5	3.20	24.5
0.30	0.35 ± 0.06	0.12	7.5 ± 0.8	2.50	21.5
0.45	0.43 ± 0.06	0.10	9.5 ± 1.0	2.11	21.9
0.60	0.75 ± 0.07	0.13	12.1 ± 1.7	2.02	16.2
0.75	1.17 ± 0.17	0.16	19.7 ± 1.7	2.63	17.7
1.00	1.24 ± 0.27	0.12	31.6 ± 10.3	3.16	25.5
1.85	2.38 ± 0.56	0.13	55.3 ± 12.2	2.99	23.3
3.00	3.67 ± 0.85	0.12	77.9 ± 8.4	2.60	21.2
4.24	4.90 ± 1.60	0.12	139.3 ± 8.5	3.29	28.4
5.66	10.16 ± 2.18	0.18	156.2 ± 27.0	2.76	15.4
6.60	14.77 ± 0.66	0.22	258.1 ± 61.8	3.91	17.5
7.50	17.67 ± 4.07	0.24	318.5 ± 23.2	4.25	18.0

4. Discussion and Conclusions.

From the results presented in table 1 we can conclude the followings:

A. High doses can be reassessed with the PTTL, as well as with the residual dose.

B. For the dose range of 0.15-5.0 Gy, the value of the residual dose is a constant fraction of the first reading - 0.13±0.03%. There seems to be an increase of the residual dose for higher doses (above 5.0 Gy), probably due to the supralinearity effects (3).

C. The results of the PTTL in the dose range of 0.15-5.0 Gy are a constant fraction of the first reading, too (2.73±0.44 %), and the value of the PTTL seems also to increase for higher doses.

D. The PTTL is higher than the residual dose by more than an order of magnitude and the accuracy of the PTTL is slightly better than that of the residual dose .

The reassessment of intermediate and high doses by the PTTL is favorable, having a higher TL signal and being more accurate; but measuring the residual dose (second reading) can also be employed and is very simple to perform.

References.

1. Portal,G., "Review of the principal materials available for TLD", Rad. Prot. Dosim. 13, 351-357 (1986).
2. Cameron,J.R. et al., "Radiation dosemeter utillizing the thermoluminescence of LiF", Science 134, 333 (1961).
3. Horowitz,Y.S., "Thermoluminescence and thermoluminescent dosimetry", CRC Press, Boca Raton, Fla. (1984).
4. Mason,E.W., McKinley,A.F. and Saunders,D., "The re-estimation of absorbed doses of less than 1 rad measured with LiF thermoluminescent dosimeters", Phys. Med. Biol. 22, 29 (1977).
5. Sunta,C.M. and Watanabe,S., "Thermoluminescence of LiF TLD-100 by phototransfer", J. Phys. D:Appl. Phys. 9, 1271 (1976).

THE ENERGY DEPENDENCE OF LiF:Ti,Mg IN BADGES FOR LOW ENERGY PHOTONS

B. Ben-Shachar , U. German , E. Naim
Department of Radiation Protection and Safety
NRC - Negev, P.O.B. 9001, Beer-Sheva, 84190, Israel.

1. Introduction.

The LiF, Li2B4O7 and BeO TL phosphors are virtually tissue equivalent, because their effective Z is almost equal to the effective Z of the tissue (1). For low energy photons (30-100 keV), the LiF shows an over-response of up to 40-50% (2).

The purpose of the present work was to check the energy response of the LiF:Ti,Mg crystals contained in the badges used in the NRC-Negev for routine personnel and environmental dosimetry. Each TLD badge contains a G-1 or G-7 card, shielded by a 54 mg/cm2 layer of polyethylene and paper sheet.

2. Materials and methods.

The measurements were performed with the standard Harshaw manufactured G-1 or G-7 TLD cards, each of them containing two TLD-100 or TLD-700 chips, respectively. The cards were evaluated in a Harshaw automatic 2271 reader, which includes a built in Sr-90/Y-90 calibration source. Every TLD card was irradiated 5 times with the Sr-90/Y-90 source and the sensitivity of each chip was calculated. The standard deviation of each chip was 1-2%. The TLD cards, contained in the badges, were irradiated by a Siemens model "Stabilipan" X ray machine to five different energies of 25-105 keV photons. The irradiations were performed at the SSDL Laboratory in the Research Institute for Environmental Health, Tel-Aviv.

In table 1 the characteristics of the X rays emitted by the machine are presented.

Table 1 : The characteristics of the X ray machine.

Kilovolt peak	Filter (mm)	HVL (mm)	Mean energy (keV)
40	0.2 Cu	2.2 Al	25
60	0.2 Cu	3.3 Al	35
80	0.5 Cu	0.3 Cu	50
110	2.0 Al + 2.0 Cu	1.0 Cu	80
150	1.0Al+0.25Cu+0.8Sn	1.85 Cu	105

3. Results.

The dose response of each TLD phosphor was calculated by subtracting the second reading (the residual dose) from the first one. An individual sensitivity normalization was performed for each chip. The deviations of the average dose of 8 chips from the calculated one (2 mGy) for TLD-100 and TLD-700 dosimeters are given in table 2. The over-response of bare TLD-100 chips (from ref. 3) is given, too.

Table 2 : The energy dependence of TLD-100 and TLD-700 phosphors contained in badges and the energy dependence of the bare TLD-100 (ref. 3).

Photon energy (keV)	Deviation (%) TLD-100	TLD-700	Deviation (%) bare TLD-100 (ref.3)
25	-(7.0±4.3)	-(4.7±1.2)	32.0
35	-(10.0±3.7)	-(9.0±1.5)	43.0
50	15.5±4.9	21.6±1.0	35.0
80	14.0±2.3	17.4±0.5	22.0
105	9.1±2.3	13.9±1.3	8.0

4. Discussion .

From the results presented in table 2 we can conclude the followings:

A. Both the LiF:Ti,Mg phosphors (TLD-100 and TLD-700) have similar energy response to low energy photons (25-105 keV), as expected.

B. For the lower energy photons (25-35 keV), an under-response of up to 10% was received. The maximum over-response is at 50 keV (20%) and it decreases to about 10% at 105 keV.

C. The energy dependence of LiF:Mg,Ti in the badges used in the NRC-Negev is lower than that of the bare chips, especially for the low energy photons (25-50 keV). The reason is an emphasized absorption of the low energy photons by the shield (polyethylene and paper sheet).

The energy response of the bare LiF:Ti,Mg phosphors has been reported in many papers. This presentation characterizes the energy dependence of the LiF phosphors in badges, which are the actual dosimeters. For a known spectrum of low energy photons, the dose can be corrected according to the energy dependence.

5. References.

1. Cameron,J.R., Suntharalingam,N. and Kenney,G.N. : "Thermoluminescent Dosimetry", University of Wisconsin Press, Madison, 1968.

2. Oberhofer,M. and Scharmann,A. (eds.) : "Applied Thermoluminescent Dosimetry", Bristol: Adam Hilger for CEC, 1979.

3. Horowitz, Y.S., "Thermoluminescence and Thermoluminescent Dosimetry", vol. 2, CRC Press, Boca Raton, Fla., 1984.

Radiation Survey of a Medical Accelerator

Y. Shamai, O. Even, and A. Aharoni, Radiation Safety Department,
Soreq Nuclear Research Center
and J. Chai, The ministry of Health

This document describes the procedures used to establish radiation fields in several locations in a recently built medical linear accelerator and the actual fields, including information about the dose delivered to the patient.

The accelerator peak voltage is 18 MeV. The electron beam is used to produce energetic photons by bremsstrahlung. Neutrons are generated in the accelerator structure, in the production target and in the filters by (gamma,n) reactions, but only from photons with energies higher than about 8 MeV. Therefore we measured neutron as well as electromagnetic radiation dose in the beam and at several locations around the shielded irradiation facility.

Environmental radiation hazards around the facility were measured by conventional dose-rate-meters (Victoreen 450P ionization chamber and a "Snoopy" rem counter). Electromagnetic ionizing radiation dose delivered to the patient was checked by Thermo Luminesent LiF chips, and neutron dose by nuclear-treck-detectors of three different types as follows:

The commercial Soreq neutron dosimeter consists of CR-39, a plastic foil in which neutrons produce damage mainly by (n,p) reactions, which are then electro-chemically etched and optically counted. This detection method is sensitive to neutrons above about 200 keV, and is reasonably flat above this energy threshold[1].

"Poly-carbonate" foils get damaged from neutrons mainly via recoil of heavy elements in the plastic foil. Similar damage etching procedures reveal damage sites produced by neutrons of energies above about 1.1 MeV. Calibration of the above two detection methods was performed at the ^{252}Cf scatter free irradiation facility at Soreq.

To check the very low energy component of the neutron radiation we used detectors, in which neutrons are detected by damage produced by α particles produced in the reaction $^{10}B(n,\alpha)^{7}Li$, which are revealed in a similar manner[2]. This detectors are sensitive to neutrons from about 1 eV to 70 keV.

The radiation fields were measured at two typical accelerator energy settings, 6 and 18 MeV. A water phantom was placed in the beam are

about 1 meter from the production target. The beam was set to a spot of 40x40 cm^2 and 20x20 cm^2. The above mentioned neutron detectors were placed on the phantom in the center of the field, and at locations around the irradiated area, 10 and 20 cm from the perimeter. TL detectors were placed in the center of the field just as a rough chech, since these dosimeters are not calibrated for these high photon energies.

The accelerator was operated for 1000 "units", which are approximately 1000 rad delivered electomagnetic dose.

The measured dose rates are summarized in table 1.

Table 1: Measured dose rate levels around the accelerator facility.

Ee (MeV)	beam area (cm^2) and direction	location	dose rate (µSv/h) x	n
6	20x20 down	main door	0.2-0.3	0
	40x40 down	- " -	1 -2	0
		maximum reading above door	24	0
		control room	0.4-0.5	0
		power supply room	0.2-0.3	0
		simulator facility	0.2	0
		open main door	100	0
18	40x40 down	main door	25	18
		above the door	70	
		control room	10	10
		simulator facility door	2.5	
		power supply room	2	3
		open main door	180	400
	20x20 horizontal	control room	10	8
	facing control-	main door	35	15
	room	near door at floor level		40
		simulator facility	2	
		power supply room	30	7
		around the building	0.1-0.5	0
	20x20 horizontal	general on pathway	8 -9	0
	facing a	maximal on pathway	45	
	pedestrian path	trench near door	40	25
		control room	4	3
		utility tunnel near door	30	15
		main door	25	5
	20x20 up	on the roof	0.2	<5
		on roof in the beam	1500	<5

Table 2 summarizes the measurements of neutron dose delivered to the phantom.

Table 2. The neutron dose in the beam area, deliverd to the phantom during 1000 rad of X radiation, 1 meter ffd.

location	neutron dose (mSv)			ratio of
	>0.2 MeV (CR39)	>1.1 MeV (pc)	low energy	total n/x
beam center	45	45	3	0.5%
10 cm out	24	12	2.5	0.3%
20 cm out	19	5	2	0.2%

Neutron dose was not detected at 6 MeV as expected.

As far as environmental radiation is concerned, non-negligile X ray exposures were found in several locations, which have to be dealt with either by fencing or by limitations on the work load. For example it is essential to limit excess to the large utility door. The measured environmental dose rates require a detailed calculation of work load and ocupancy of a few locations before regular operation starts.

The x rays dose delivered to the patient was found to be in agreement with the machine specifications. The delivered neutron dose was found to be below 0.5% of the x ray dose in agreement with published information on medical linear accelerators of this kind[3]. The spectrum of the neutrons was found to be less energetic as we move out of the beam, which is reasonable for scattered radiation. As a general remark for future surveys, the regular Soreq neutron badge (CR-39) is a resonable solution for the evaluation of the neutron contaminating dose to patients in a linac when used as a high energy X-ray machine.

References

1. The Soreq Fast Neutron Personnel Dosimeter, Y. Shamai, O. Even, Y. Eisen, T. Schlesinger, Proceedings of the Israeli Health Physics Society Meeting, 49, September 1988.
2. A Wide Energy Range Personnel Neutron Dosemeter and Its Dose Evaluation System, Y. Eisen, A. Eliau, . Faerman, Z. Karpinovitz, O. Even, M. Rosman, T. Schlesinger, Y. Shamai and A. Tal, Rad. Prot. Dosimetry 3, 55, 1982.
3. D. Gur et al. Med. Phys. 5(3), 221, 1978.
and G. M. Hassib and B. Spyropoulus, Rad. Prot. Dosimetry 3, 67, 1982.

CHARACTERISTICS OF AMBIENT PARTICLES IN ISRAEL FOLLOWING SAHARAN DUST STORMS DETERMINATION OF ELEMENTAL CONCENTRATION BY INSTRUMENTAL NEUTRON ACTIVATION ANALYSIS AND INDUCTIVELY COUPLED PLASMA OPTICAL EMISSION SPECTROMETRY

E. GANOR, S. BRENNER AND E. NEEMAN
Research Institute for Environmental Health, Ministry of Health,
Tel-Aviv University, Tel-Aviv, Israel

AND

N. Lavi
Soreq Nuclear Research Center, Yavne, Israel

Abstract

The neutron activation analysis (NAA) has in recent years become one of the most promising and attractive analytical methods for simultaneous multielemental analysis of biological as well as geological materials.

Usually, the amount of the produced radionuclide has been measured by gamma-ray spectrometry either without any chemical treatment, i.e., instrumentally, or after radiochemical separation.

Non- destructive reactor neutron activation of biological or geological materials is generally not feasible because of the considerable activity produced by the major components (sodium, potassium, chlorine, bromine and phosphorus) of these matrices. Only very short irradiations may be carried out, and only short-lived isotopes can be determined by this method.

The aim of this work was to study the possibility of determining simultaneously the concentrations of Al, Ba, Br, Ca, Ce, Co, Cl, Cr, Eu, Fe, Hf, K, La, Mg, Mn, Na, Rb, Sb,Sc, Si,Ta, Th, Ti, U, V and Yb in dustfall samples (settling particles), by instrumental neutron activation analysis (INAA), using a comparator of multielement standard solution (MES) as well as by the monostandard method ("Single Comparator")[1], respectively.

Since both Al as well as Si were determined through the formation $^{27}Al(n,\gamma)^{28}Al$ (2.24 min) and $^{28}Si(n,p)^{28}Al$, respectively, a thermal and epithermal neutron activation was applied in order to determine the contribution of each radionuclide to ^{28}Al activity.

ICP was also used to compare the validity of the results obtained by INAA.

A LASER SCANNING SYSTEM FOR NTD DOSE MEASUREMENTS*

M. Margaliot, T. Schesinger and O. Even

Soreq Nuclear Research Center, Yavne 70600, Israel

and

A. Kazir

Tel-Aviv University, Ramat Aviv, Israel

Nuclear Track Detectors (NTDs) are widely used[1,2] for the quantitative detection of radon and fast neutrons. Growing public awareness of the hazardous potential of exposure to the environmental radon has increased recently the use of this type of radiation detector.

The NTD method is based on exposing a transparent plastic foil (~0.5 mm thick) to heavy particulate radiation, such as neutrons or α particles. The collisions of the particles with the plastic polymer produce structural damage, which is later rendered visible, by various etching methods.

Radiation dose assessment, in the NTD, is carried out by counting the radiation-induced damage sites ("pits").

The common method of counting these pits, even today, is manual counting with a microscope[3]. An alternative method is the use of an image analyzer, coupled to a computer. However, units of this kind, which must include microscopic magnification and computerized scan, are rather expensive[4]

* U.S. and Foreign Patents Pending.

The laser scanning system described below, is intended to replace this manual labor with an automatic PC-based counting system, at a moderate price.

Physical principle of operation

A focused laser beam (focal spot size ~ 10 μ) falls on the NTD foil, perpendicular to its plane. Undamaged areas in the NTD have good optical quality, and the light is transmitted, with almost no scattering. When the focal spot falls on a radiation-induced pit, most of the light is scattered.

Most (~ 70%) of the scattered light is captured within the NTD foil by total internal reflection, travels within it, and finally exits the foil via its edges. This phenomenon is described schematically in Figures 1a and 1b.

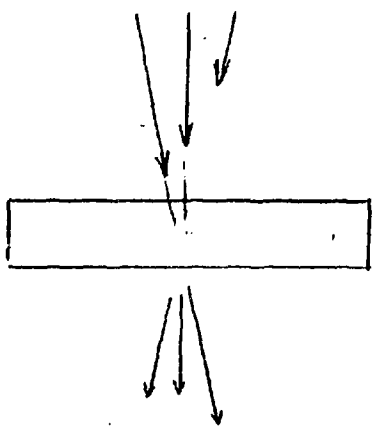

Fig. 1.a: light transmission in an undamaged NTD

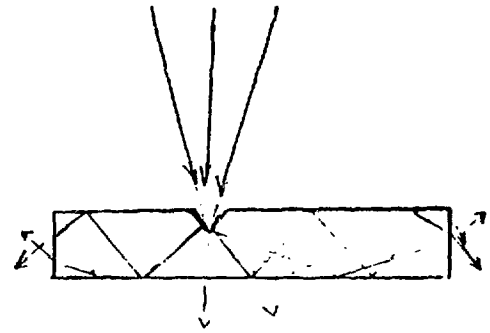

Fig. 1b: light scattering by a "pit"

Photodiodes placed around the NTD foil detect the escaping light. The signal from one of the photodiodes, as a 100 μm pit is scanned, is shown in Fig. 2..

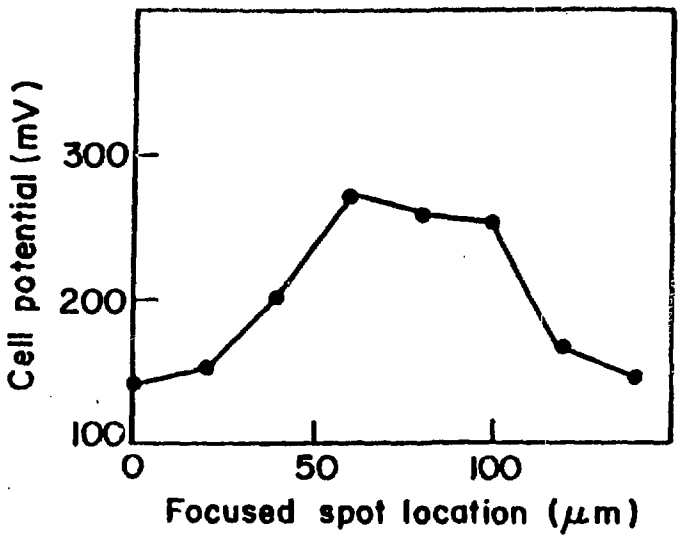

Fig. 2: The photodiode potential of in scan of a 100 μm pit.

When the focal spot hits the center of a pit, all the photodiodes around the foil are illuminated nearly equally (1/r dependence). This is due to the circular symmetry of the radiation-induced pit.

However, if an artifact, like a scratch, is encountered, the scattering loses its symmetry and only a part of the diode assembly is illuminated.

This effect is used for discrimination between real radiation pits, and various artifacts, by connecting the diodes via a coincidence circuit.

Counting of the pits is done while the light spot scans the NTD foil.

The scanning is controlled (speed and density of scan) by a computer, and the information (presence of a pit) is fed directly into the computer.

A schematic description of this sytem, is given in figure 3.

This system has been applied to NTD foils made of poly-allyldiglycol-carbonate (known commercially as CR-39), and its response was compared to the results of manual counting.

Pit densities from 0 up to 20,000 pit/cm^2 were thus examined, and agreement (within statistical fluctuations) was obtained up to densities of

8000 pits/cm^2 (corresponding to neutron doses of up to 2.5 Rem and to radon exposure of up to 50,000 Bq·day/m^3).

The results of this series of measurements is presented in fig. 3.

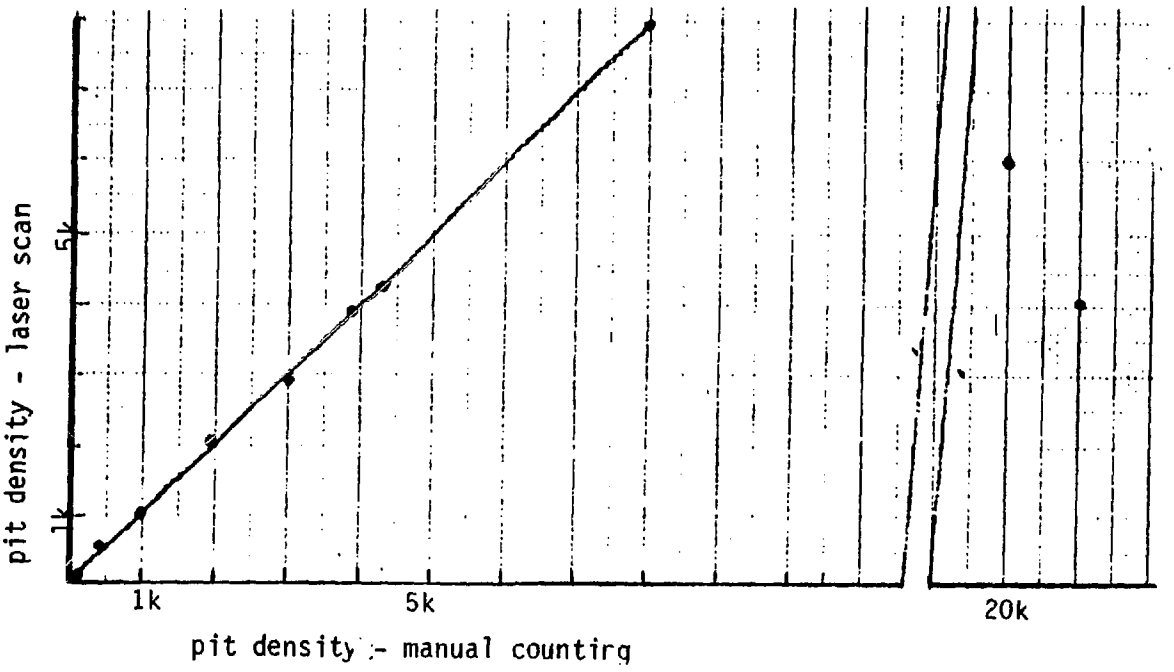

Fig. 3: pit density: manual counting versus laser scan.

The system is presently being run in by the dosimetry service of the Radiation Safety Department SNRC.

References

1. Faerman S. Ph.D. thesis, Ben-Gurion University, Be'er Sheva, Israel, 1983.

2. 14th International Conference on SSNTD, Rome, 1985.

3. Alter H.V. et al. Hlth Phys. 53: 198, 1987.

4. E. Leitz Publ. VIII/80/bx/w, 1983.

A Compton Suppression Gamma Spectrometry System for Environmental Samples

U.German, S.Levinson, E.Naim, G.Weiser
S.Piestum, H.Assido

Nuclear Research Center Negev
P.O.Box 9001, Beer-Sheva 84190

Ge(Li) gamma ray spectrometers are extensively used because of their good resolution, but their efficiency is low and the Compton continuum which covers most of the pulse height spectrum up to the full energy peak reduces the sensitivity for analysis of other full energy peaks in this region. The application of anti-coincidence shields for reducing the Compton contributions from Ge(Li) detectors is a known technique and has been described in the literature[1,2]. In most of the systems NaI(Tl) or plastic scintillator shields are used. We have built and are now operating a Compton suppression system for spectrometry of environmental samples. It is based on a Ge(Li) spectrometer surrounded by a liquid scintillator anti-coincidence shield and is able to accommodate samples of up to 1 liter volume. The detectors assembly is located in a lead chamber with 10 cm thick lead walls coated by Cd, Cu and Perspex.

The Ge(Li) detector is a 115 cm^3 coaxial detector. For the Anti-Compton shield we decided to use NE-224 [3] liquid scintillator instead of the usual NaI(Tl) despite the greater dimensions required to stop the scattered Compton gammas. The liquid scintillator is relatively cheap, insensitive to mechanical shocks and can be given any desirable form. A 60 dia. x 60 cm cylindrical container for the scintillator was designed with a cavity of 12 dia. x 37.5 cm for placing the samples. It is equipped with an expansion chamber and the scintillator is viewed by seven 5" dia. photomultipliers attached to optical glass windows glued to the container wall. The scintillator container is lifted by an electrical motor to enable the sample placement.

The block diagram of the electronic system is given in Fig. 1. The system consists of modular, commercial NIM units and the simplest possible configuration was chosen. The pulses from the photomultipliers are summed and fed to an amplifier and single-channel-analyzer which produces the gate for the Ge(Li) signals. Only the Ge(Li) pulses which are in anti-coincidence with the scintillator pulses are passed by a gated amplifier and received for analysis by a PCA/IBM-AT[4] pulse height analyzer system. Thus, Compton effects and Cosmic rays producing pulses in both detectors are rejected.

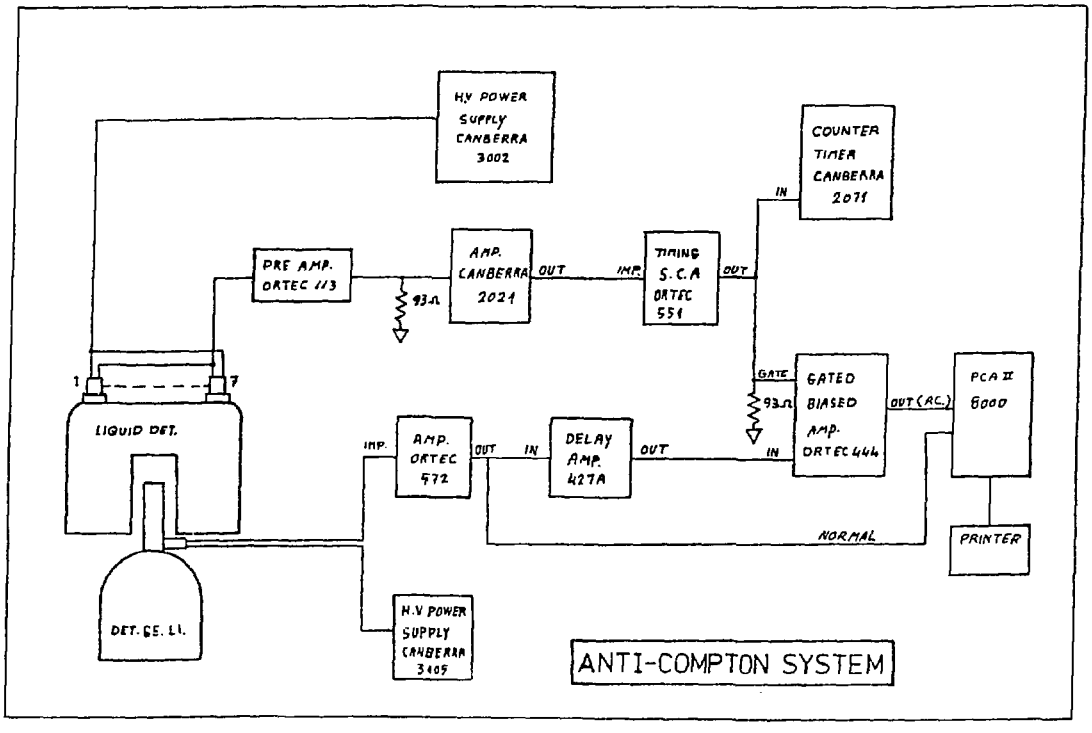

Fig. 1: The block diagram of the electronic system

First we optimized the efficiency of the scintillator detector by properly matching, balancing and summing the contributions of the seven photomultipliers. Then the adjustment of the different electronic settings was performed for optimal Compton rejection. The system was calibrated with standard gamma ray sources.

Fig. 2 shows the background reduction achieved by employing the anti-coincidence system. The greatest improvement can be seen in the lower part of the pulse height spectrum, where scattered radiation contributes most significantly.

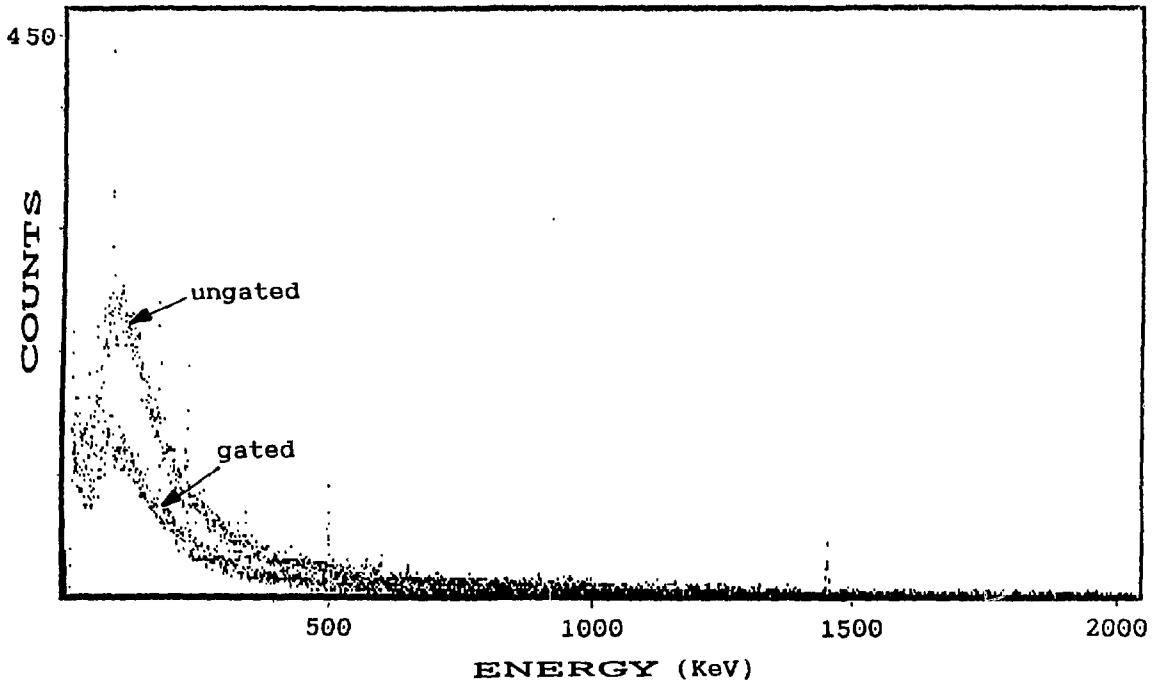

Fig. 2: Pulse height spectrum of the background (54000 sec.)

Fig. 3 shows a ^{60}Co pulse height spectrum measured with and without the anti-coincidence function. The reduction of the Compton continuum is clearly seen. In the presence of ^{60}Co the limits of the detection of lower energy isotopes are improved significantly. For ^{137}Cs, for example, the improvement of the MDA is by a factor of about 2.5 .

It should be noted that there is a photopeak efficiency decrease for isotopes emitting coincident gamma rays when employing the Anti-Compton system. For these isotopes (as ^{60}Co, ^{134}Cs, ^{207}Bi) specific calibrations should be made. In order to obtain most information from the system, both the normal and the Anti-Compton spectra are accumulated simultaneously.

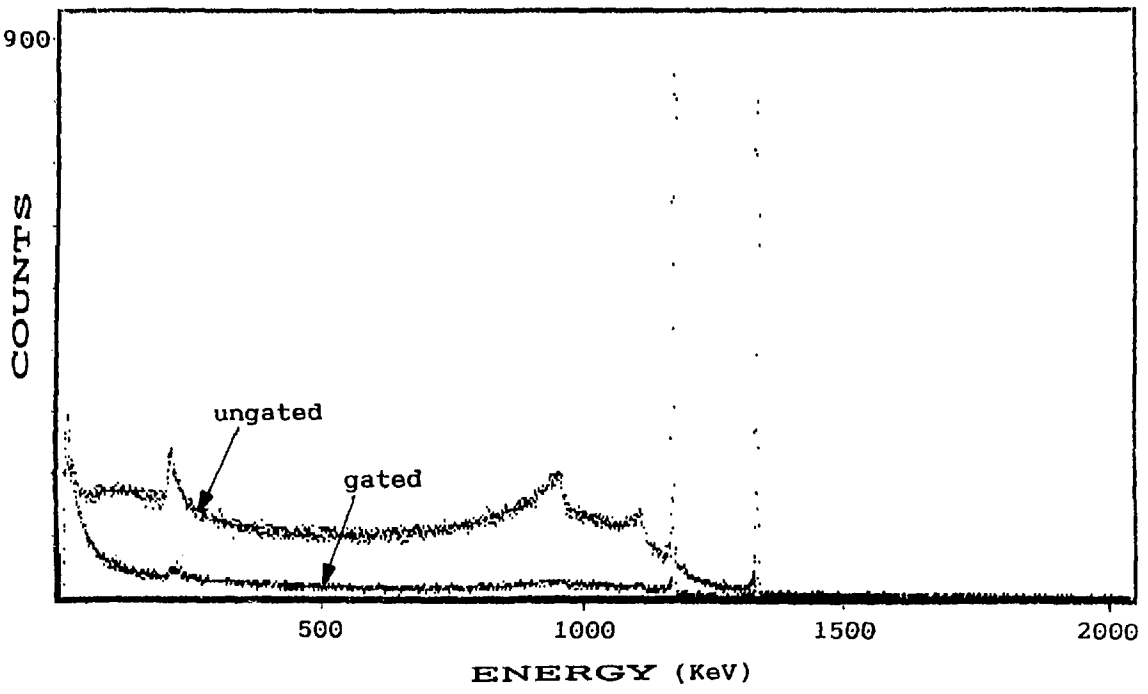

Fig. 3: Pulse height spectrum of a ^{60}Co source.

REFERENCES

[1] J.A.Cooper and R.W.Perkins
"A Versatile Ge(Li)-NaI(Tl) Coincidence-Anticoicidence Gamma-Ray Spectrometer for Environmental and Biological Problems".
Nuclear Instruments and Methods 99 (1972) 125-146.

[2] G.J.Hunt, M.C.O'Riordan and P.D.J.Whetmath
"An Anticoicidence-Shielded Ge(Li) Gamma-Ray Spectrometer with High Sensitivity for Measurement of Environmental Radionuclides".
Nuclear Instruments and Methods 156 (1978) 573-589.

[3] Nuclear Enterprises Ltd., Sighthill, Edinburgh EH11 4EY, Scotland.

[4] PCA - Personal Computer Analyzer
Tennelec/Nucleus Inc. P.O.Box 2561, 761 Emory Valllley Road, Oak Ridge, TN 3783111-2561, U.S.A

Dual 5" Scintillation System for Alpha and Beta Counting

H.Assido, S.Piestum, N.Ankry, Y.Gilad, R.Kol, S.Levinson

Nuclear Research Center Negev
P.O.Box 9001, Beer-Sheva 84190

A portable radiation survey meter [1-3] - RAM-D(1) was modified in order to replace the old electronics of an alpha and beta counting system. Suitable electronic changes and improvements were made on the RAM-D unit and on the appropriate PMT circuits.

An alpha and beta counting system, based on two 5" scintillation detectors, was connected to two RAM-D Survey Meters. A new HV-Divider was built for the old Phillips 9530-KA 5" PMT's, mounted on a sample changer. Appropriate changes were made in the HV power supply, pre-amplifier, amplifier and discrimination unit of the RAM's PM-10(2) electronics. Since the RAM electronics is battery operated, an external low voltage 5V DC power supply was added. (See Fig. 1)

Measurement of radioactive samples is made in count mode, therefore suitable changes were made in the firmware in the counting mode, and display tasks. CPM results are displayed according to different periods of counting time.

A special base was built for the RAM units to enable convenient operation and fastening of the electronic units to the detectors' sample changer (see Fig. 2).

---

(1) RAM-D: A portable Radiation Monitor with Digital Display
The RAM microprocessor system consists of one monitor and several interchangeable probes, for different types of radiation. Each probe contains a detector and its own HV power supply, together with a built-in signal processing analog circuit, (made by Rotem Ind.)

(2) PM-10: The RAM PMT scintillation detector for X-ray and soft gamma, (made by Rotem Ind.)

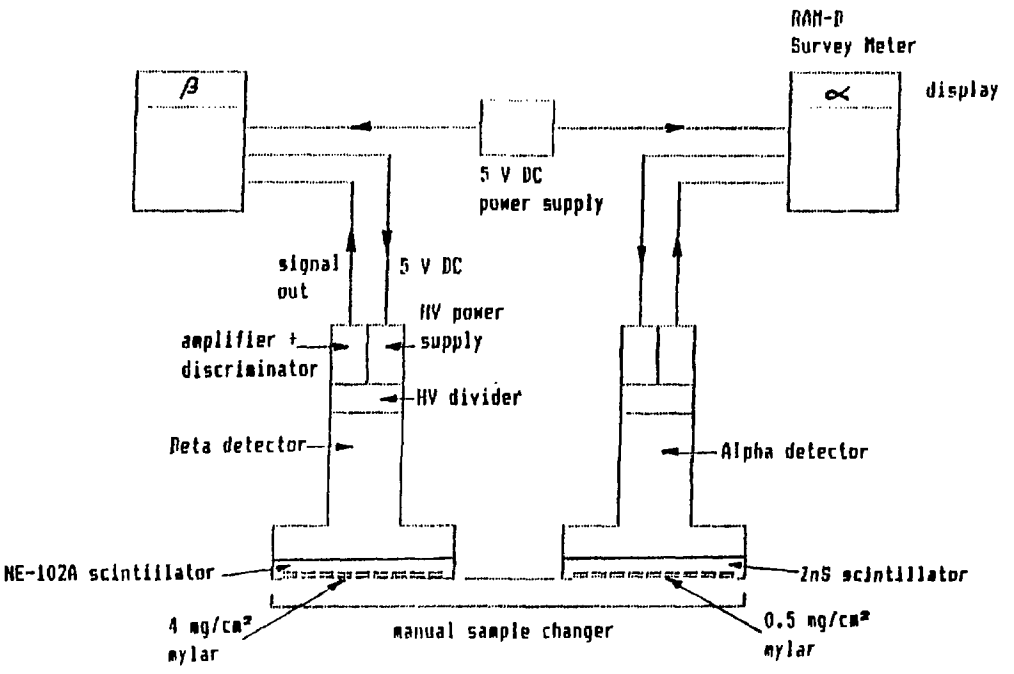

Figure 1: The 5" Scintillation Counting System Scheme

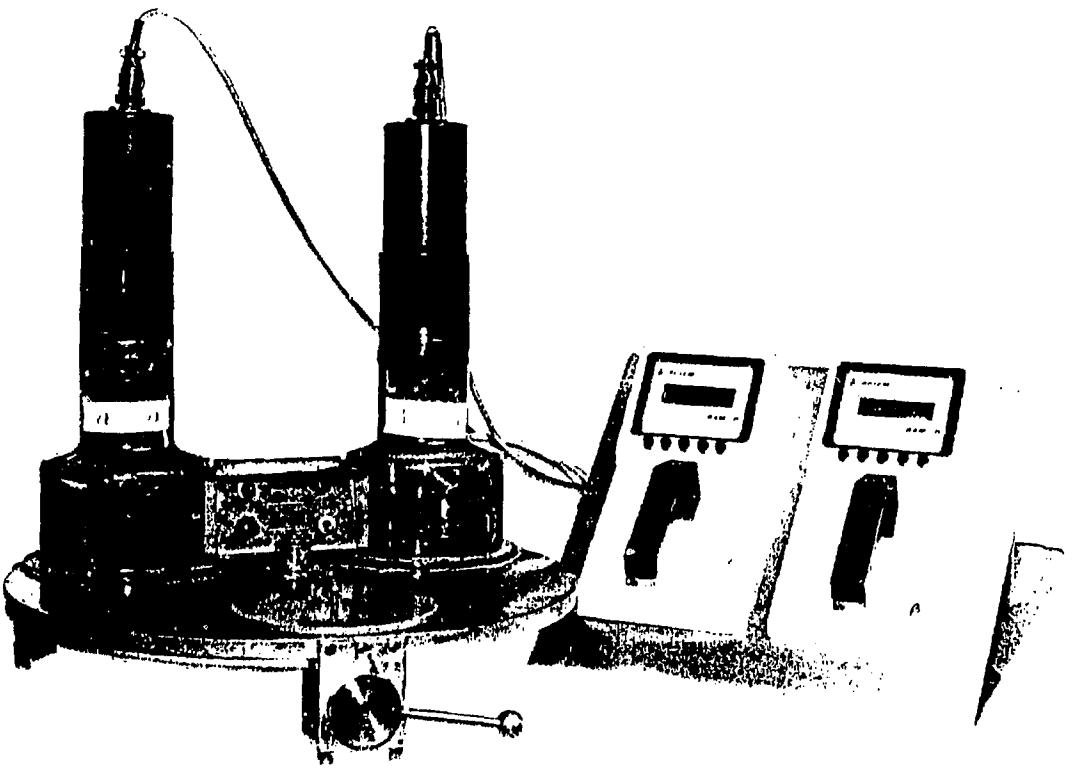

Figure 2: The 5" Scintillation Counting System

The alpha scintillator used is a ZnS emulsion, sprayed on 0.5mm thick light-conveyor-coupler. The beta scintillator is a 1mm thick Polyvinyltoluene plastic based, Nuclear Enterprises NE-102A. Both scintillators were originally covered with a 0.5 mg/cm^2 aluminum mylar. The NE-102A scintillation is mainly sensitive to beta but also to alpha radiation (~30%). In order to enable exclusive beta emitters counting the mylar is replaced by a ~4 mg/cm^2 mylar type. Figure 3 depicts the 'loss' of counting efficiency for various beta energies, by the two types of mylar thickness.

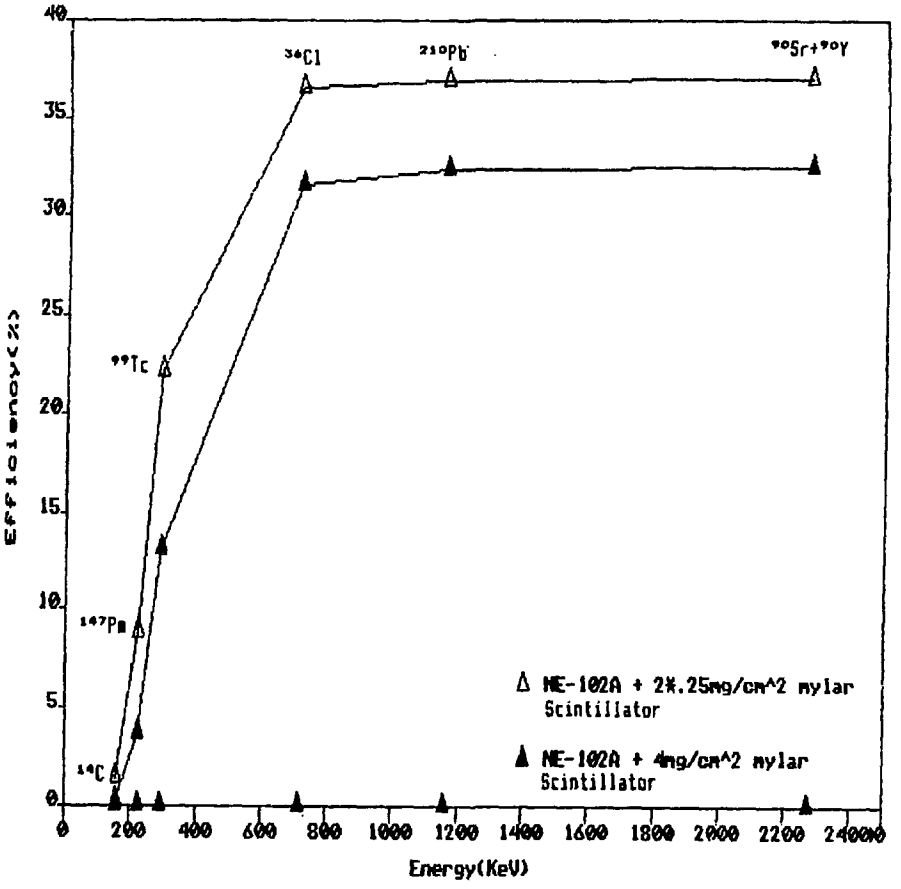

Figure 3: Beta counting efficiencies at various energies, for the two different mylar types.

The versatile, portable, multi function radiation monitor - RAM-D was successfully fitted to other type of photomultipliers, and in a non-portable large diameter scintillation system.

REFERENCES

[1] "RAM - A Sophisticated Multi Function Survey Meter"
Internal Report BN 87.030 .
Y.Paran, Y.Laichter, D.Tirosh, and N.Tal.
Rotem Industries Ltd Israel, P.O.B 9046, Beer-Sheva 84190 .

[2] "A New Approach to Portable Radiation Monitoring"
J.Paran, D.Tirosh, N.Tal, U.Wengrowicz and Y.Gabay.
Israel Research Laboratories Annual Report 1986,
IA-1427, pp. 210-212 .

[3] "Dosimeter Corporation's RAM Survey Instrument System"
Radiation Protection Management, Nov/Dec 1987, pp. 41-49 .

A Sandwich 2π Proportional Gas-Flow Counter for Simultaneous Alpha and Beta Counting

S.Levinson, H.Assido, U.German, Y.Shemesh
S.Piastun, Y.Ronen, E.Naim

Nuclear Research Center Negev
P.O.Box 9001 Beer-Sheva 84190

A prototype of a Sandwich 4.5" dia. 2π proportional gas-flow counter for simultaneous α and β counting was built. Its design is a further development of the gas-flow counter described in ref. 1 and its principle of operation is similar to that of the Sandwich large area gas-flow detectors employed by Herfurth GmbH [2]. The counter is designed for easy maintenance and changes, and its mylar windows can be conveniently replaced. In addition to the original α and then β counting option with a single proportional counter, the Sandwich counter enables simultaneous α-β counting and improves the Minimum-Detectable-Activity (MDA) for a given measurement time.

The Sandwich counter is built of two almost identical chambers, with the same counting area, mounted one above the other. The lower chamber, under which the measured sample is placed, has five 0.002" thick anode wires and is operated in the α plateau. The upper chamber has thinner wires (0.001") and is operated in the β plateau. The difference in wire diameters enables the creation of the appropriate electrical fields for the two chambers, using the same HV. The general scheme of the Sandwich counter is given in fig 1.

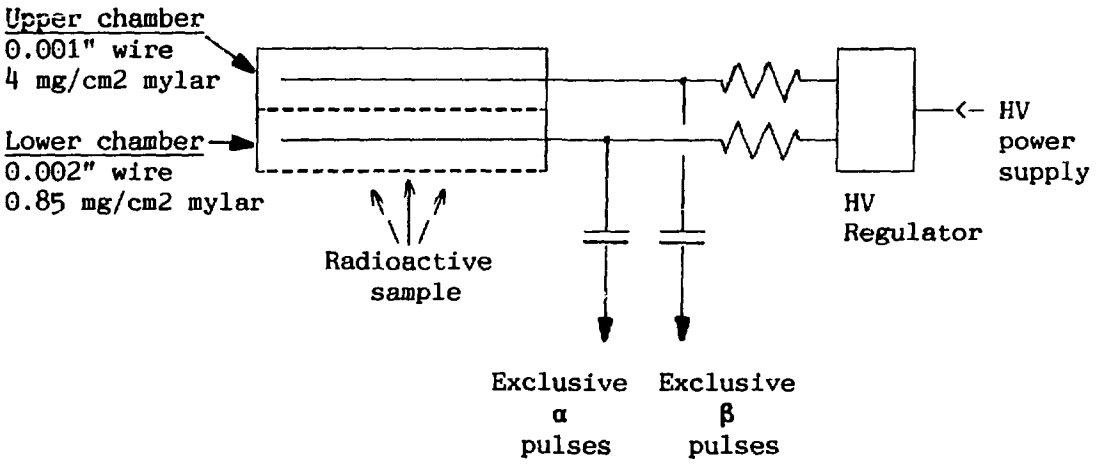

Fig. 1: General scheme of the Sandwich counter.

Most α and β particles pass the lower mylar and enter the lower chamber. The electrical field enables the counting of only α particles in this counter. The thick mylar window between the two chambers absorbs all the alphas and only the betas which enter the upper chamber are detected.

The α efficiency of the system is the same as for the original counter. The β efficiency of the system is shown in fig. 2. It is lower than that of the original single counter because of the additional absorption in the thick mylar and the greater distance of the β counting chamber from the radioactive sample. The influence of these two factors can be seen in fig. 2.

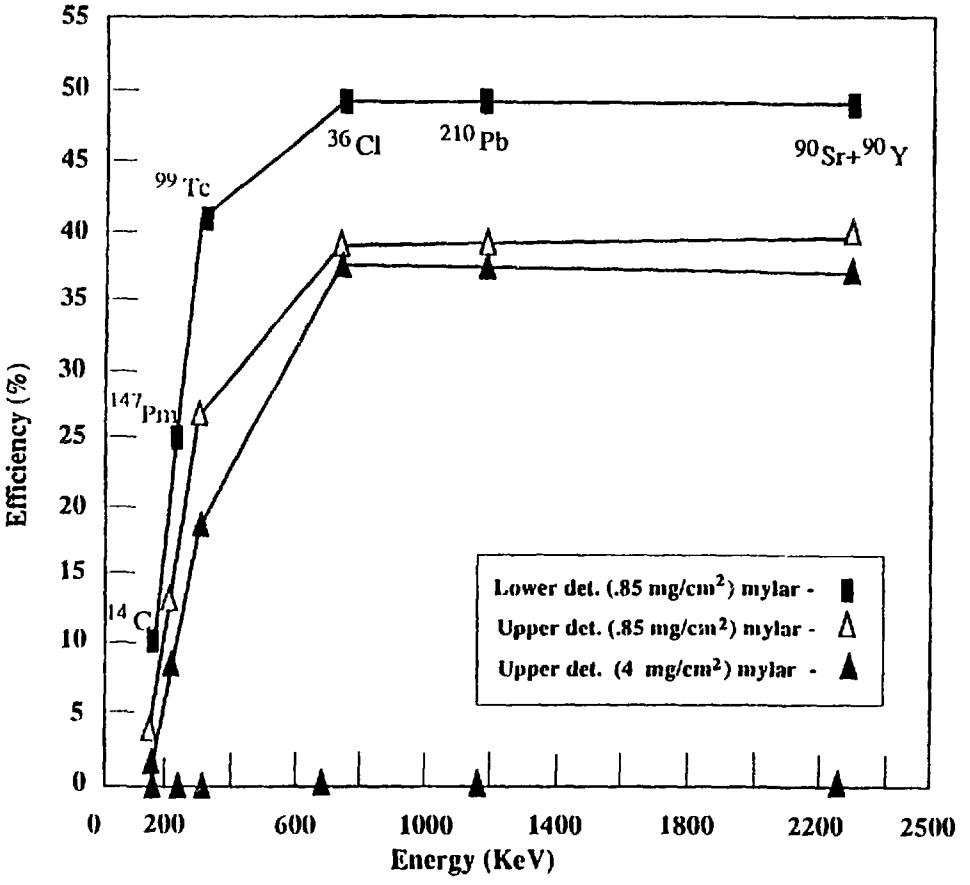

Fig. 2: Betta efficiencies of the system for various β end energies

When using the Sandwich detector configuration, both chambers are operated simultaneously, and the effective counting times are doubled relative to the α and then α+β counting mode. This obviously improves the MDA for α particles. For β particles, the MDA change is

given by:

$$\frac{MDA}{MDA_0} = \frac{1}{\sqrt{2}} * \frac{Eff_0}{Eff}$$

where:

MDA, Eff - are the MDA and β efficiency for the Sandwich configuration.

MDA_0, Eff_0 - are the MDA and β efficiency for the original configuration (single lower detector).

For a 4 mg/cm^2 mylar thickness between the two chambers and for β end energies over 700 KeV the β efficiency decreases by about 25% but because of the double counting time in the simultaneous mode, the MDA is improved by about 7% . (The same MDA can be achieved by 12% shorter total measurement time). Besides, the elimination of α particles from the β chamber improves the β counting statistics, especially for high rates of α particles. An additional improvement can be achieved by optimizing the thickness of the thick mylar. We evaluate that a thickness of about 2 mg/cm^2 will stop all α particles of up to 5 MeV energy.

The main disadvantage of the Sandwich counter is the decrease of the β efficiency for β end energies less than about 700 KeV due to the absorption in the thick mylar. However, in this cases the system can be operated in the original mode by employing only the lower detector and changing the high voltages to the appropriate values.

REFERENCES

[1] S.Levinson, H.Assido, E.Reich and U.German
"Development of a 2π Proportional Gas-Flow Counter That Can Be Taken Apart for Decontamination and Repair"
- Israel Atomic Energy Research Laboratories 1986, annual report IA-1427, pp. 201-202.
- IAEA, Health Physics Research Abstract no. 14 (1989), p. 66.

[2] Herfurth GmbH, Beerenweg 6-8, D-2000 Hamburg 50, Germany

CHANGES IN BODY COMPOSITION OF PATIENTS WITH NEUROSECRETORY GROWTH HORMONE DYSFUNCTION, DURING THE FIRST YEAR OF TREATMENT WITH GROWTH HORMONE.

Nachum Vaisman*, Yair Shamai**, Roland Dukhan**, Zvi Zadik,***

* From the Nutrition Clinic,Department of Paediatrics, Kaplan Hospital, Rehovot, and the Medical School, Hebrew University, Jerusalem, Israel.

** The Soreq Nuclear Research Center,Israel.

*** Paediatric Endocrine Unit, Kaplan Hospital, Rehovot.

Growth hormone (GH) is a potent regulator of somatic growth and was found to promote positive nitrogen balance, increase carbohydrate usage,and induce fat mobilization and oxidation (1,2). These metabolic effects should ultimately affect body composition. The present study was designed to follow the different changes in body composition in children with neurosecretory growth hormone dysfunction (3), during the first year of growth hormone therapy.

Patients and Methods

The study population consisted of 10 prepubertal subjects with neurosecretory growth hormone dysfunction (5 males, 5 females), age range 6.5-12.4 years.

All our patients were preadolescent and none of them developed any signs of puberty during the study period.

All participants were treated with daily subcutaneous GH injections (NORDITROPIN, authentic recombinant GH, Nordisk, Denmark), at a dose of 0.05 U/kg, at bedtime. Patients underwent a series of tests to evaluate body composition prior to initiation of GH treatment, and at 6 (period 1) and 12 months

(period 2) after initiation of treatment. These included: weight, height, four-site subcutaneous skinfolds, total body potassium content, corrected bromide space, and bone mineral density.
Standing heights were measured using a HARPENDEN stadiometer while children were barefoot. Weight was measured while children were wearing light under-wear. Triceps, biceps, subscapular and suprailiac skinfold thicknesses were measured by means of a Holtain skinfold caliper and used to calculate fat body mass (FBM) (4). Mid-arm muscle circumference (MAMC) was calculated from the triceps skinfold thickness and the mid-arm circumference (5).

Total body potassium was measured by whole body gamma-counting at Soreq Nuclear Center. The system consists of a large shadow shielded NaI(Tl) crystal. The subject is placed on a moving bed under the detector for about 20 minutes in order to get a homegenous response for the whole body, obtaining a statistical accuracy of better than 5% (standard deviation).

Extra cellular water was measured by administration of 3% NaBr, 1 ml/kg body weight, and measurement of Br concentration in blood at equilibrium (3 hours)(5). Br concentration was measured by neutron activation of the blood using the high resolution gamma spectroscopy system in the radiation safety department at Soreq N.R.C., using the long lived 82Br isotope. Vertebrae's size and bone mineral content were measured by dual photon absorptiometry (7).

In order to account for the age differences and the abnormal body composition of our subjects, we chose to express the different parameters as a percentage of the 50th percentile of their age at each point of the study. Fat body mass and mid-arm muscle circumference were expressed as a percent of normal predicted values based on Cheeks's tables (8). TBK was expressed as a percent of the predicted value based on Reba and Cheek's formulas (8):

for boys : TBK (meq) = 53.674 x weight - 60.168
for girls: TBK (meq) = 37.074 x weight + 308.087

Repeated measures analysis of variance was used to compare the three time periods. When the overall F value was significant, pairs of time periods were compared by paired t-tests, with a Bonferroni correction for simultaneity.

RESULTS

The changes in body composition during GH treatment are illusrated in the following table:

Compartment		Pretreatment	6 months	12 months	p
Height	cm	118.2-8.9	122.3-8.9	125.8-8.8	0.0001
Weight	kg	21.25-3.93	22.84-4.35	25.43-5.53	0.0001
FBM*	kg	3.90-1.54	3.72-1.63	4.19-2.04	0.06
FBM/WT	%	18.2-4.9	16.3-4.5	16.3-4.9	0.005
ECW/WT**	%	24.0-3.3	23.3-2.1	23.8-3.0	n.s
TBK***	g	42.5-4.5	45.4-8.1	50.6-9.2	0.09
MAMC****	mm	154.5-15.6	157.6-14.9	164.8-15.7	0.04

* FBM - fat body mass
** ECW - extracellular water
*** TBK - total body potassium
**** MAMC- mid arm muscle circumference

In conclusion, our results indicate that growth hormone has a short term lypolitic effect on body composition during the first months of therapy. The changes in lean body mass and bone mineral density are not different than the predicted values.In contrast to other sudies in adults no significant changes were found in the extracellular water compartment. Further studies with respect to the relation between changes in body composition and the diet, especially protein content, should be carried out in order to find ways to maximize these beneficial effects.

REFERENCES.

1. Snyder DK, Clemmons DR, Underwood LE. Treatment of obese, diet-restricted subjects with growth hormone for 11 weeks: Effects on anabolism, lipolysis and body composition. J Clin Endocrinol Metab. 1988;67:54-61.

2. Crist DM, Peake GT, Egan PA, Waters DL. Body composition response to exogenous GH during training in highly conditioned adults. J Appl Physiol. 1988;65(2):579-584.

3. Zadik Z, Chalew SA, Raiti S, Kowarski A. Do short children secrete insufficient growth hormone? Pediatrics. 1985;75:355.

4. Durnin JV, Rahaman MM. The assessment of the amount of fat in the human body from measurements of skinfold thickness. Br J Nutr. 1967;21:681-9.

5.Frisancho AR. New norms of upper limb fat and muscle areas for assessment of nutritional status. Am J Clin Nutr. 1981; 34:2540-5.

6. Vaisman N, Pencharz PB, Koren G, Johnson JK. Comparison of oral and intravenous administration of sodium bromide for extracellular water measurements. Am J Clin Nutr. 1987;46:1-4.

7. Nuti R, Righi G, Martini G,et al. Methods and clinical applications of total body absorptiometry. J Nucl Med. 1987; 31:213-221.

8. Reba RC, Cheek DB, Leitnaker FC. Body potassium and lean body mass. In: Cheek DB: Human growth. Philadelphia: Lea & Febiger. 1968.

HIGH TEMPERATURE GAS REACTORS

APPLICATION OF THE VOSP CODE SYSTEM TO HTGR PEBBLE BED REACTORS

B.Tavron and L. Reznik
Nuclear Engineering Department, Israel Electric Corporation

W. Rothenstein
Nuclear Engineering, Technion

Abstract

VSOP [1] is a package of well proven reactor physics and fuel cycle simulation codes, including special treatments for HTGR pebble bed reactors. In the first part of this paper the code system is presented, with emphasis on its application to the pebble bed HTGR. In the second part, an improvement to VSOP, the implementation of the CITATION code for 2D diffusion calculations, is described. A comparison of results obtained by CITATION, and simpler 1D synthesis treatments in the code FEVER, are presented.

Description of VSOP

The VSOP flow diagram is shown in Fig.1. The first step consists of basic data preparation for the fuel elements of Pebble Bed and other HTGR Reactors (up to 60 materials) by sub-program DATA2, on a file which supplies these data in a suitable format to all other parts of the system. Core design is also handled at this stage or within VSOP itself.

In the second step, resonance calculations are performed by the ZUT code, using data from DATA2 and from resonance data files. The double heterogeneity in the HTGR pebble bed fuel is dealt with by the Teuchert method [2].

The second step may be repeated for each type of fuel and temperature. The results are stored as tables of effective resonance integrals for different temperatures in order to allow spectrum calculations (by the epithermal GAM code) to be performed by simple linear interpolation in these tables.

In the VSOP code itself, the neutron spectrum, diffusion, burnup, fuel management and cost calculations are performed at will in almost any order and frequency. The core is divided into a maximum of 200 geometric regions and 22 spectrum zones. The neutron spectrum is calculated by a combination of the codes GAM and THERMOS, and can be applied to the various spectrum zones differing in temperature, burnup and fuel type. The thermal spectrum calculation code THERMOS has been extended to treat the grain structure of pebble bed HTGR fuel elements. Epithermal spectrum calculations are done by the GAM code using resonance absorber cross sections prepared by ZUT. These spectrum calculations yield up to 4 broad energy group macroscopic cross sections for each spectrum zone.

The diffusion calculations can be made in 1D-R, 1D-Z and 2D-RZ synthesis by the FEVER code, or else by using the full 2D-RZ calculations of the CITATION code, as described subsequenly.

The flux computed by the diffusion section is used by the burnup section of FEVER, which updates the core composition and accounts for fission product chains containing up to 40 fission product nuclides.

The fuel management section of VSOP shuffles the fuel elements in the different core regions, and inserts new fuel into specified regions in the core, thus allowing simulation of the special fuel management schemes of HTGR pebble bed reactors such as OTTO or MEDUL. Cost calculations are performed by the KPD code. Additional thermohydraulics calculations can be made by the TIK code.

Implementation of CITATION in VSOP

In order to improve the diffusion calculation model by using full 2D-RZ computation, the CITATION code was incorporated into VSOP as an alternative option in the code system. This code provides also the option of using finer mesh.

The implementation of CITATION was facilitated by using data and subroutines supplied by KFA in Juelich. The subroutines were adapted to the VSOP version running at the IEC and the Technion. The principal ones are:

1. REMOD, a routine to match the VSOP and the CITATION grids.
2. MACROC, to provide macroscopic cross sections for CITATION.
3. Control subroutine.
4. A subroutine for normalizing and organizing the CITATION output in a manner suitable to VSOP.

The input file for CITATION needs to be fully prepared for the first call only. For the remainder of the calls, a simplified Restart File is sufficient.

The link between CITATION and VSOP is fairly simple; only minor changes had to be introduced in CITATION.

Comparison of VSOP results using CITATION vs. FEVER

In order to test the changes which were necessary to use CITATION in conjunction with VSOP a comparison was made between results caculated by CITATION and FEVER for a specific reactor. It is specified in table (1) [3].

The problem consists of data preparation, and then calculations of resonance, spectrum, diffusion and burn-up. Results are summarized in table (2) and figs. (2,3).

The results in table (2) and figs. (2,3) show good general agreement between the two options. As anticipated, there is more disparity in the flux distributions than in lumped parameters such as k_{eff}, leakage or absorption, since the diffusion model is more sophisticated, when CITATION is used.

Table 1: Design parameters

Reactor Core				
Thermal Power	(MW)	3000		
Power Density	(MW/m^3)	5		
Efficiency		0.4		
Height	(cm)	550		
Radius	(cm)	589		
Reflectors		upper	bottom	radial
Thickness	(cm)	200	150	100
Graphite Density	(gr/cm^3)	0.32	1.6	1.6
Homogenized Control-poison	(Σ_a)	$\pi*10^{-4}$	-	-
Fuel-elements				
Radius	(cm)	3		
Outer Shell Thickness	(cm)	0.5		
Graphite Density	(gr/cm^3)	1.7		
Coated Particles				
Kernel Diameter	(μm)	400		
Density	(gr/cm^3)	$9.5((U+Th)O_2)$		
Material of Coating		C	C	C
Thickness	(μm)	85	30	80
Density	(gr/cm^3)	1.0	1.6	1.85

Table 2 : Results

	FEVER	CITATION	Diff.
K_{eff}	0.986316	0.980557	0.58%
Leakage per source neutron	0.092040	0.093265	-1.30%
Absorbtion per source neutron	0.907959	0.906735	0.13%

REFERENCES

[1] E.Teuchert, U.Hansen, K.A.Hass, "VSOP-Computer Code System for Reactor Physics and Fuel Cycle Simulation", KFA, Juelich, Jul-1649,March 1980

[2] W.Rothenstein, "Final Report for the period 1/10/87 - 30/9/89", IEC & Technion,1989

[3] E.Teuchert, "Brennstoffzyklen Des Kugelhaufen-Hochtemperaturreaktors In Der Computersimulation", KFA, Juelich, Februar, 1984

THE VSOP FLOW DIAGRAM

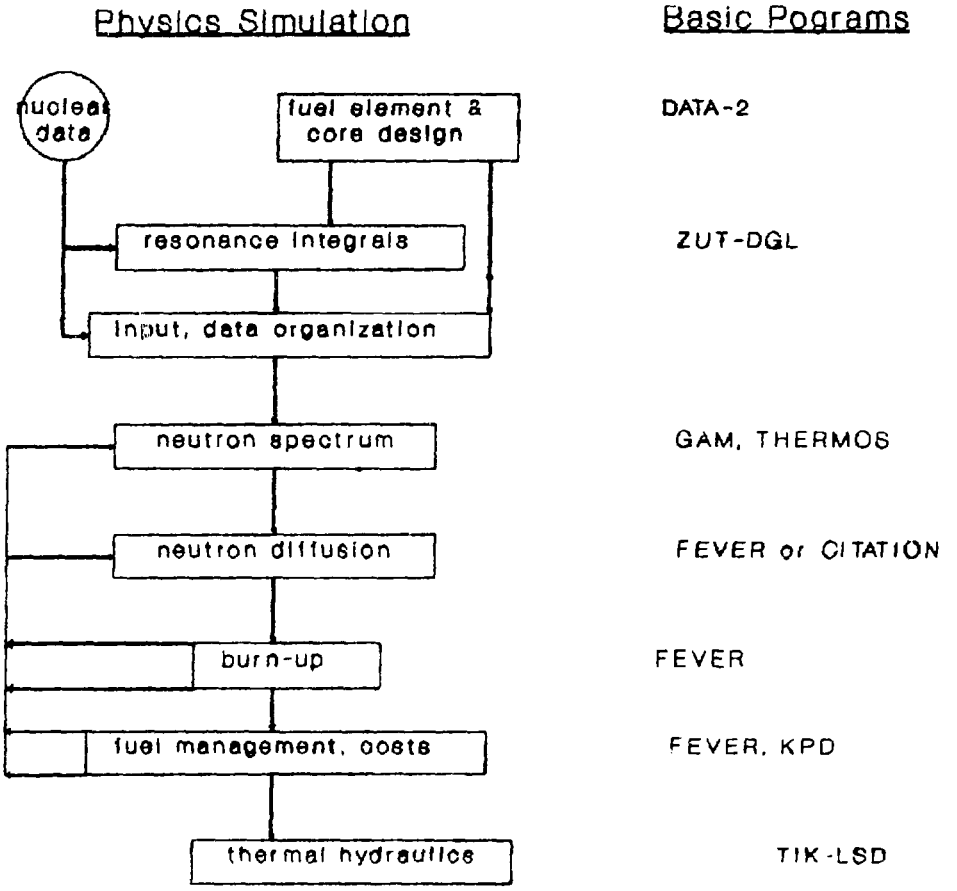

Fig 1

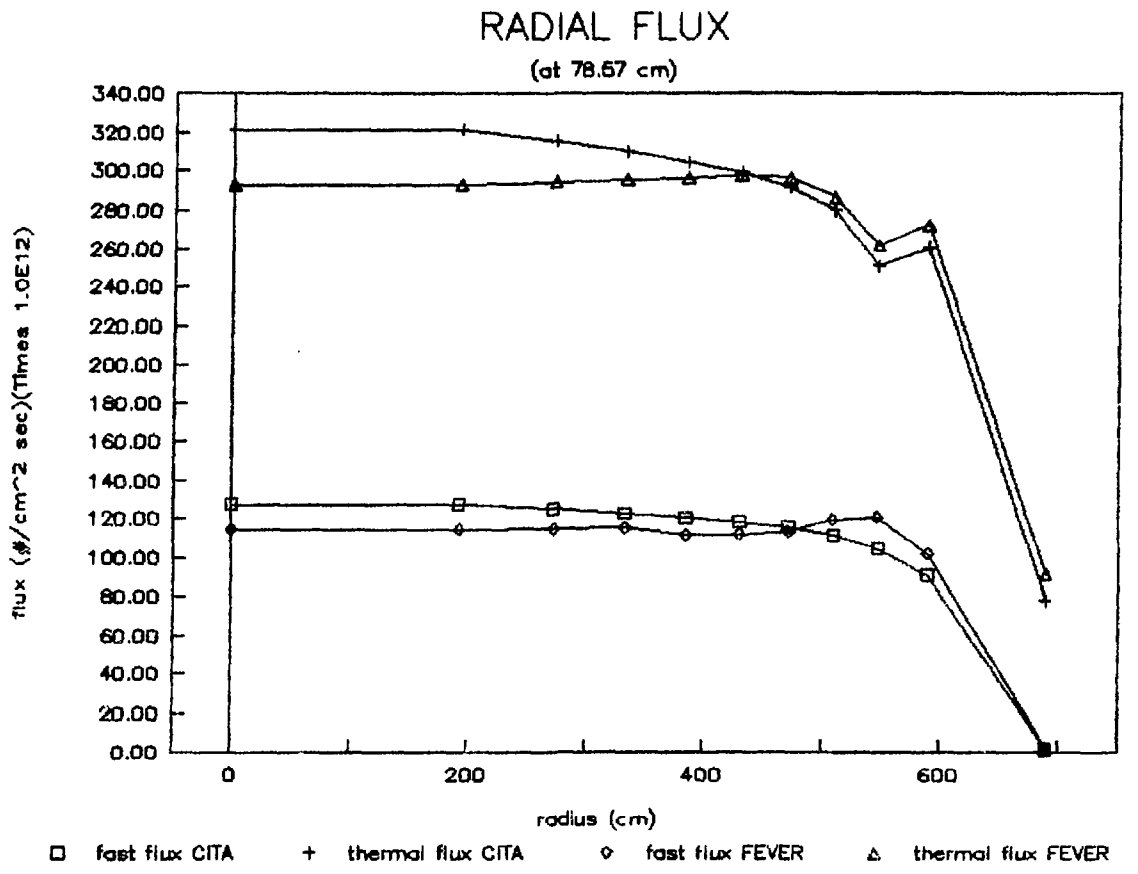
RADIAL FLUX
(at 78.67 cm)
flux (#/cm^2 sec)(Times 1.0E12)
340.00
320.00
300.00
280.00
260.00
240.00
220.00
200.00
180.00
160.00
140.00
120.00
100.00
80.00
60.00
40.00
20.00
0.00
0
200
400
600
radius (cm)
fast flux CITA
thermal flux CITA
fast flux FEVER
thermal flux FEVER

Fig 2

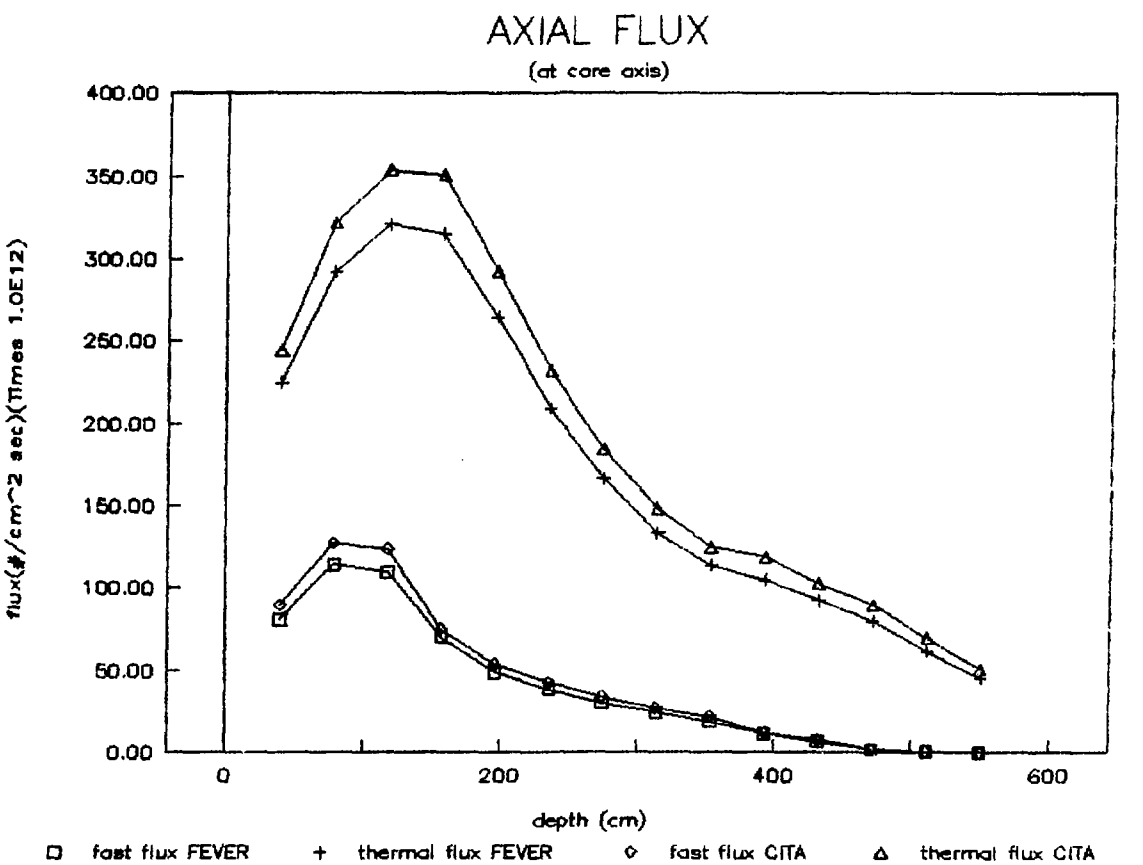
AXIAL FLUX
(at core axis)
flux(#/cm^2 sec)(Times 1.0E12)
400.00
350.00
300.00
250.00
200.00
150.00
100.00
50.00
0.00
0
200
400
600
depth (cm)
fast flux FEVER
thermal flux FEVER
fast flux CITA
thermal flux CITA

Fig 3

VSOP SIMULATION OF "KAHTER" TEST FACILITY

B.Tavron and L. Reznik
Nuclear Engineering Department, Israel Electric Corporation

Introduction

The critical HTGR test facility KAHTER (Kritische Anlage Hochtemperaturreaktor) in KFA Jülich's Institut fur Reaktorentwicklung was set up and made critical in 1973, with the aim of testing, comparing, and if necessary correcting the HTGR pebble bed theoretical models, codes and data bases. The experiments involved different core configurations with different moderation ratios, fuel element types (AVR, THTR), absorber element ratios (Boron, Hafnium), upper reflector (or void) and control rod positions. Details and results of these experiments can be found in [1-3].

VSOP is a computer package for reactor physics and fuel cycle simulation with special treatments for HTGR reactors. A description of VSOP and its implementation on the IEC and Technion computers - including incorporation of CITATION - is described elsewhere in these Transactions [4]. In order to test the performance of the version of VSOP used here, calculations were made for the KAHTER reference homogeneous core. The results were compared with theoretical and experimental values obtained at the KFA.

Description of the Facility and the Experiment

The core of KAHTER has a diameter of 216 cm and a maximum height of 276 cm. The bottom reflector is 24-50 cm thick graphite, the radial reflector 40 cm thick graphite. A top reflector of graphite with a height of 10 to 50 cm is optional. The core can be filled with up to 50,000 pebbles. By mixing fuel and graphite pebbles it is possible to vary the ratio of graphite to heavy metal between 340 and 1350.

From among the many different experiments performed with KAHTER, the "reference core" experiment was chosen for our calculations. The composition of the fuel elements (THTR) for this experiment is listed in table (1), the core loading in table (2).

Table 1: Fuel elements composition

nuclide	concentration (g)
^{235}U	0.96187
^{238}U	0.06190
^{232}Th	10.2
Carbon	192.2

Table 2: Core loading

FE	11500 elements
GE	8050 elements
Height	151.88±0.5 cm
Critical Mass ^{235}U	11.0607 Kg

Comparison between VSOP and KFA results

The results were obtained using VSOP with the FEVER 2D-RZ synthesis diffusion calculation option (Calculations with the CITATION option are now in progress). At KFA the code systems GAMTEREX and RSYST for KAHTER simulation were used, as described in [1-3]. Table (3) summarizes k_{eff} results for the reference core from the various methods, as well as from the experiments.

Table 3: Results for k_{eff} (reference core)

Method	k_{eff}	Difference from experiment (%)
Experiment	0.99681 0.99899	- -
RSYST	0.99882	0.201 -0.017
GAMTEREX	1.00247	0.566 0.348
VSOP/FEVER	0.99809	0.128 -0.090

The results of VSOP/FEVER are in good agreement with the experimental values. However, since the modelling and the calculational methods in VSOP/FEVER do not take some of the effects included in the KFA analysis into account, this degree of precision may be partly fortuitous. Further studies and calculations of the KAHTER experiments are currently in progress.

Some of the more important differences between the KFA and VSOP investigations are the following:

1. Design data for the fuel element: There are missing data in the KAHTER reports; they were taken from published THTR data [5].

2. VSOP unit cell calculations use cross-section data for two homogenised regions. Four such regions were used at KFA.

3. VSOP diffusion calculations use cross-section data for four broad-energy groups, whereas seven such groups were used at KFA.

4. In the KFA calculations special neutron streaming corrections for HTGR pebble cores were applied [6].

REFERENCES

[1] Scherer, Gerwin and Neef, "Theoretische Analyse des Kritischen HTR-Experimentes KAHTER", JUL-1136-RG, 1974.

[2] Druke et al, "Heterogeneous Poisoning of the Critical HTGR Facility KAHTER: A Study for the Initial Loading of Pebble Bed Reactors", Nuclear Technology, 55(1981), 549.

[3] Druke and Filges, "The Critical HTGR Facility KAHTER - An Experimental Program for Verification of Theoretical Models, Codes and Nuclear Data Bases", Nuclear Science and Engineering, 97 (1987), 30.

[4] Tavron, Reznik and Rothenstein, "Application of the VSOP Code System to HTGR Pebble Bed Reactors", Transactions of the 16th Annual Meeting of the INS (elsewhere in this issue).

[5] Wolf, Ballensiefen and Frohling, "Fuel Elements of the High Temperature Pebble Bed Reactor", Nuclear Engineering and Design, 34 (1975), 93.

[6] Lieberoth and Stojadinovic, "Neutron Streaming in Pebble Beds", Nuclear Science and Engineering, 76 (1980), 336.

CONSEQUENCE ANALYSIS OF POSTULATED ACCIDENTS FOR A 500 MWe HTGR HYPOTHETICALLY LOCATED IN THE NORTHWESTERN NEGEV, ISRAEL

J. Koch and D. Ilberg

Soreq Nuclear Research Center, 70600 Yavne, Israel

An assessment of the radiological consequences following postulated accidents was performed for a 500 MWe High Temperature Gas-cooled Reactor (HTGR), hypothetically located at Shivta in the Northwestern Negev, Israel, as part of a Probabilistic Safety Assessment (PSA).

Computations were carried out by means of the REMAND probabilistic consequence model (Stern et al. 1987), using site-specific input data, i.e. the meteorological conditions prevailing at the site and the population distribution around it. According to a study conducted at KFA-ISF for the HTR-500 (Kröger, Wolters et al. 1983, Nabbi et al. 1984), six different release categories were defined and their release parameters are presented in Table 1. It was assumed that no short-term protective measure is taken and that consumption of contaminated food is banned.

Calculations show that the incidence of non-stochastic health effects, including early fatalities, prodromal symptoms, pneumonitis, eye cataract and permanent male sterility, is not expected. The radiation doses at inhabited locations are lower than the threshold for each particular effect, even without considering protective measures.

The incidence of stochastic effects is estimated to be very low: about one late fatality is expected following the most severe assumed accident (a core heat-up with failure of the liner cooling system), up to about 20 fatalities for the worst meteorological conditions.

Table 1: The assumed release categories for HTR-500 (from KFA-ISF studies)

Category	Frequency 1/yr	Time (h)	Cumulative Fraction of Core Inventory Released to Atmosphere				
			Kr-Xe (1.3×10^6)	Iodine (1.7×10^4)	Cesium (9×10^6)	Sr-Ba (1.8×10^6)	Te-Sb (4.6×10^5)
K1 core heatup	10^{-7} (LoPS – 100%)	0 to 35	1.4×10^{-2}	2.4×10^{-3}	3.3×10^{-3}	3.9×10^{-3}	2.4×10^{-3}
PC open		0 to 200	2.2×10^{-2}	2.4×10^{-3}	3.3×10^{-3}	4×10^{-3}	2.4×10^{-3}
Failure of LCS		>200	2.2×10^{-2}	2.4×10^{-3}	$\sim 10^{-2}$	$\sim 8 \times 10^{-3}$	2.4×10^{-3}
RPB stack							
K2 core heatup	3×10^{-8} (LoPS – 100%)	0 to 35	1.4×10^{-2}	2.4×10^{-3}	3.3×10^{-3}	3.9×10^{-3}	2.4×10^{-3}
PC open		>35	2.2×10^{-2}	2.4×10^{-3}	3.3×10^{-3}	4×10^{-3}	2.4×10^{-3}
RPB stack							
K3 core heatup	10^{-5} (LoPS 90%)	0 to 12	3×10^{-4}	10^{-4}	10^{-5}	1.1×10^{-3}	10^{-4}
PC open		0 to 35	1.4×10^{-2}	10^{-4}	1.5×10^{-3}	3.9×10^{-3}	10^{-4}
RPB filter stack		>35	2.2×10^{-2}	10^{-4}	1.5×10^{-3}	3.9×10^{-3}	10^{-4}
K4 core heatup	10^{-4} (LMCS 85%)	0 to 12	4×10^{-4}	2×10^{-6}	---	---	2×10^{-6}
PC short term open							
RPB filter stack							
K5 depressurisation core cooling RPB stack	10^{-5}	0–5	$3.3 \cdot 10^{-6}$	$3 \cdot 10^{-9}$	---	---	---
K6 water ingress core cooling leak-stack	$5 \cdot 10^{-6}$	0–35	$3.3 \cdot 10^{-7}$	$5.9 \cdot 10^{-9}$	$6.1 \cdot 10^{-6}$	$1.1 \cdot 10^{-8}$	---

Note: PC = primary circuit, RPB = reactor protection building (confinement), ( ) = contribution to frequency, LoPS = loss of preferred power supply, and LMCS = loss of main loop cooling system, LCS: liner cooling system.

*Initial inventories of grouped nuclides are in parenthesis.

Assumed release: 100m (energy release negligible).

The societal risk for late fatalities from a 500 MWe HTGR located at Shivta is estimated by taking into account the yearly probability of occurrence of the different release categories and summing over all the categories. The societal risk of the different categories and the overall risk is found to be very low and is presented in Table 2. The overall societal risk is contributed exclusively by the core heat-up accidents.

Due to the very low population density around the Shivta site, the consequences are much lower (by more than two orders of magnitude) than corresponding results obtained in the KFA-ISF study, which assumed representative German siting conditions. The consequences for the HTGR at Shivta are also much lower than those expected for severe

Table 2: The calculated societal risk for late fatalities

Release category	Expected number of late fatalities	Probability of occurrence (yr^{-1})	Societal risk (late fatalities/yr)
K1	0.8	10^{-7}	0.8×10^{-7}
K2	0.6	3×10^{-8}	0.2×10^{-7}
K3	0.2×10^{-1}	10^{-5}	0.2×10^{-6}
K4	0.2×10^{-3}	10^{-4}	0.2×10^{-7}
K5	0.4×10^{-5}	10^{-5}	0.4×10^{-10}
K6	0.1×10^{-3}	5×10^{-6}	0.5×10^{-9}
sum (overall societal risk):			3.2×10^{-7}

accidents occurring in a PWR of equivalent power on the same site, confirming the inherent safety of the HTR-500 concept.

References

Kröger W., Wolters J. et al., 1983, Zum Störfallverhalten des HTR 500 - Eine Trendanalyse, Jül-Spez-220, KFA-ISF.

Nabbi R. et al., 1984, Sicherheitstechnische Untersuchung zum Störfallverhalten des HTR-500, Jül-Spez-240, KFA-ISF.

• Stern E., Covaliu Z., Kaufman J. and M. Stark, 1987, REMAND - A Computer Code for Assessing the Consequences of Accidents in Nuclear Power Plants (User's Guide), IA-LD-99, Israel Atomic Energy Commission.

Malfunctions and Transients Analysis in a HTGR Using Artificial Neural Networks Techniques

M. Tramer, E. Wacholder and E. Elias
Department of Mechanical Engineering
Technion - Israel Institute of Technology
Haifa 32000, Israel

Introduction

The management of malfunctions in complex systems has gained increased interest as a tool for improving their operational safety and reliability. This is particularly true in nuclear power plants, where the combination of characteristic high safety standards and strict economic requirements makes it a vital need.

Among the wide spectrum of tasks involved in malfunction management, the *detection and isolation* of incipient failures, which is concerned with identifying the malfunctioning sub-unit or sensor is exceptionally important. This is usually executed by an alarm which announces that a failure in the plant has been detected, and followed by an estimation of the location of the failure and its extent. Several approaches to malfunction detection and isolation exist, ranging from simple upper and lower bounds techniques [1], frequency domain techniques [2-4] through expert-system methods [5-7] to algorithms based on a state-space formulation [8-10]. Recent interest is directed also to Artificial Neural Networks (ANN) applications in order to study their capability to cope with this problem.

Multilayered ANNs [11,12] are potential alternatives to existing pattern recognition and signal processing techniques [13,14]. The application of neural networks to signal classification problems requires far less restrictive assumptions about the structure of the input signal and preprocessing. In addition, the inherent parallelism of these networks allows very rapid parallel search and best-match computations, alleviating much of the computational overhead incurred when applying traditional non-parametric techniques to signal interpretation problems. However, these relatively new techniques are not yet fully characterized and it would be valuable to compare their performance with that of existing techniques and human performance on a well-defined problem (benchmark problem).

ANN models, or simply "neural nets", are also known as "connectionist models", "parallel distributed processing models" or "neuromorphic systems". Generally, in these models one attempts to achieve good performance via dense interconnection of simple computational elements. All the models on this area receive their inspiration from our

present understanding of biological nervous systems. The intensive interest and study of these models by the engineering community nowdays is motivated, among other reasons, by the fact that realization of human-like performance in pattern recognition areas demand enormous amounts of processing. ANN models on the other hand provide a promising efficient tool for parallel distributed computation which can reduce computing time significantly.

In this work the feasibility of an ANN based methodology is investigated for the detection and isolation of malfunctions in the primary circuit of an existing High Temperature Gas Cooled Reactor (HTGR, THTR-300). The performance of this algorithm is critically evaluated. A benchmark which consist of several possible malfunctions and Anticipated Transients Without Scram (ATWS) as well as several possible normal operational transients was prepared for the present work. The necessary input and output patterns were generated numerically using an originally developed simulation code (HTGRSS) [15, 16]. The designed ANN network was then tested for its ability to detect and isolate failures while receiving online noisy vectors (states) as input. It was found that the present ANN algorithm was able to detect failures and locate their origin in more than 90% of the scenarios studied.

The High Temperature Gas Cooled Reactor Simulation System (HTGRSS)

The computer simulation program HTGRSS [15, 16] has been formulated to predict transient behavior of an HTGR during normal operation and hypothetical accident conditions. The program is written as a package system code describing the coupled thermal, fluid-flow and neutronic (including decay heat) behavior of the nuclear fuel and coolant in the reactor core primary circuit components and the steam generator (Fig. 1). The program has been tested and validated against many experimental results in the open literature and against available experimental data obtained at the Arbeitsgemeinshaft Versuchsreaktor (AVR) in Germany. In the study case considered here, 5 measurements have been chosen to monitor the transient behavior of the reactor system, i.e, have been selected to indicate the state of the reactor systems as follows: 1. core power, 2. core coolant inlet pressure, 3. core coolant outlet pressure, 4. core coolant inlet temperature and 5. core coolant outlet temperature. By introducing these signals to the ANN, the state of the reactor is deduced. Before we describe the architecture of the neural network designed for this study, let us first briefly describe the main characteristics of the ANN model.

Artificial Neural Networks (ANN)

Neural net models are specified by their net topology (or architecture), their processing element characteristics (summation of input signals and activation function), connection strengths (or weights) and by their training or learning rules.

In essence, a multilayered net "maps" input patterns to produce desired output patterns. It thus provides a mean for recognizing input patterns, and for producing assigned output patterns in response. The learning procedure of these nets, in which their parameters are determined, may be a long and exhausting task, even on a very powerful computer. However, once these parameters are determined, the computing speed for extracting an output pattern from a given input is extremely fast. The computation can be made even faster if a special–purpose hardware circuit (VLSI) or a general–purpose concurrent machine is adapted.

One of the most popular and best examined and verified neural network is the Back Propagation (BP) network. It is basically a feed–forward network, in which each one of its processing elements sends its output signal to layers higher than its own and receives its input only from lower layers. The BP net has two modes of operation: 1. a "learning" mode in which its parameters are determined and 2. a "performance" mode in which the network pursues its required task.

In the "learning" mode the network connection weights and neurons biases are determined. This is done through an iterative procedure (known as the "generalized delta rule" learning algorithm) in which a set of pairs of input and desired output patterns are repeatedly introduced to the network until its error is decreased to a predetermined value. This learning algorithm can be shown to actually minimize a given global error function. An adequate error function in this respect can be, e.g., the sum, over all output units and input patterns, of the squares of the differences between the actual and the desired output values. This corresponds to performing steepest descent on a surface of the error measure in the connection weights space.

A principal feature of this network is its interposition of a "hidden–layer" of nodes between the net's inputs and outputs. This enhance the net's pattern-classification powers in ways that are not immediately obvious. A two– hidden–layer network, for instance, can form arbitrarily complex decision regions that can separate between highly meshed classes of input patterns.

Results and Discussion

The BP network used in the present study possessed 50 entries in the input layer, one hidden layer of 40 neurons (processing units) and two neurons in the output layer. All the outputs of the neurons were continuous–valued signals. The activation level (potential), U_i, of each neuron i is obtained by

$$U_i = \sum \omega_{ij} V_j + \theta_i \tag{1}$$

where ω_{ij} is the connection weight from the jth to the ith unit, V_j is the output of unit j and θ_i is the bias of the ith unit. A sigmoidal transformation, $f(U_i)$, was then applied to the activation level to obtain the ith unit's state or output, V_i,

$$V_i = f(U_i) = \frac{1}{1 + \exp^{-\beta U_i}} \tag{2}$$

where β is a constant that determined the slope of the sigmoid at $U_i = 0$. In this study $\beta = 1.0$ was employed.

The 50 entries in the input layer, that we want to classify, were made up from 5 groups of 10 entries each. Each group corresponds to the output of one of the five sensors recorded in the plant (fig. 1). The signals from each sensor were recorded every time interval of $\tau = 20$ sec. The analog signals were then ideally converted to 10 discrete digital signals with 2 sec. time intervals between each two adjacent signals, and introduced to the network. No attempt to model the ADC or perform signal preprocessing was made at this stage.

The state of the first output neuron describe the plant state ; (0) represents normal operation and (1) represents the occurrence of failure. The state of the second neuron represents the coded address of the failure source in continuous numbers between 0.1 to 1.0 .

Classification

The network was trained to classify 10 base scenarios whose data were generated numerically by the HTGRSS

1. Nominal steady state operation with statistical noise at sensors output.
2. +1% positive reactivity change.
3. -1% negative reactivity change.

4. +5% positive reactivity change.
5. -5% negative reactivity change.
6. primary coolant blower 20% power drop.
7. primary coolant blower 60% power drop.
8. 5% increase in SG inlet water temperature.
9. 5% decrease in SG inlet water temperature.
10. 10% decrease in SG inlet water pressure.

The training set of signals was constructed from samples of 200 sec. transients of each sensor from the initiation of a perturbation in the system response. Thus the sum of 50 patterns for the 5 sensors is obtained which resulted in a total of 500 patterns for the 10 scenarios in each training set. The weights of the network were initialized to small values uniformly distributed between -0.3 and 0.3. The network thus designed was able to study the training set with a success of 99% (correct classification).

Two series of numerical testings were then conducted to determine the network ability to generalize and deduce its performance.

(1) The trained network was presented with sets of test signals which were excluded from the training set and corrupted with different levels of statistical noises.

(2) the trained network was presented with new test sets of input signals of additional scenarios (close to the base scenarios) such as, for instance, 2.5% positive reactivity change. The performance of the network was specified as percent correct classification.

In all the test experiments carried out, the network was found to detect failure states in 96% of success and isolate the source of failure or transient behavior in 93% of the cases. Better performance and extension of the networks classification capabilities and ranges of input patterns can be expected with more elaborated networks. the required number of hidden layers and hidden units in each layer in the network can affect the networks performance significantly. This should be studied more carefully in order to design optimized network for any given task.

References

1. R. Iserman "Process fault detection based on modeling and estimation methods – a survey", automatica, 20 (4), pp. 387–404 (1984)

2. L. G. Kemeny, Nuclear Power Plant Operetional Diagnostics and Control, 2nd Specialist's Meeting on Reactor Noise (SMORN), pp. 735–745, (1974).

3. R. Sunders and D. Wach, Monitoring and Diagnosis Systems for Incipient Failure Detection, GRS Technical Meeting on Trends in Nuclear Power Plant Control Technology, Munchen, F. R. Germany, (1985).

4. H. Jokinen and J. Heklund, Experiences in Using Multivariate AR Modeling and FFT in Analysis and Monitoring of a NPP, Proc. 6th Power Plant Dynamics, Control & Testing Symp., Knoxville, Tennessee, (1986).

5. W. R. Nelson and J. P. Jenkins, Expert System for Operator Problem Solving in Process Control, CEP, pp. 25–29, (1985).

6. S. M. Shahidehpour and G. D. Kraft, Applications of Artificial Intelligence (AI) to Distributed Processing in a Power System Environment, Proc. 6th Power Plant Dynamics, Control & Testing Symp., Knoxville, Tennessee, (1986).

7. S. B. Guarro, J. Szabo and D. Okrent, Multi–Level Approach For the Structural Definition of a Plant–Wide DAS – Disturbance Analysis System, REP. UCLA–ENG–8424, (1984).

8. Y. Ben–Haim, Malfunction Isolation In Linear Stochastic Systems : Application to Nuclear Power Plants, nuclear Science and Engineering 85, pp. 156–166, (1983).

9. E. Y. Chow and A. S. Willsky, Bayesian Design of Decision Rules for Failure Detection, IEEE Trans. on Aerosp. Electronic Systems, AES–20(6), pp. 761–774, (1984).

10. Z. Covaliu, Isolation of Small Malfunctions in a PWR Nuclear Power Plant, M.Sc. Research Thesis (october 1987), Technion I.I.T., Haifa 32000, (1987).

11. James L. McMlelland and David E. Rumelhart, Parallel Distributed Processing, vol. 1, chapter 8, MIT Press (1988).

12. Richard P. Lippmann, "An Introduction to Computing with Neural Nets", ASSP IEEE, 4-22 (1987).

13. R. L., Watrous and L., Shastri, Learning Acoustic Features From Speech Data Using Connectionist Networks, Proceedings of the Ninth Annual Conference of The Cognitive Science Society, 9, pp. 518–530, (1987).

14. R. Paul Gorman and Terrence J. Sejnowski, Analysis of Hidden Units in a Layerd Network Trained to Classify Sonar Targets, Neural Networks, vol. 1, pp. 75–89, (1988).

15. E. Elias, S. Kaizerman, B. Cohen, D. Hasan and E. Wacholder, "High Temperature Gas Cooled Reactors (HTGRs); Preliminary Simulation of THTR-300", Technion Report TNED/R-723(1989).

16. E. Elias, S. Kaizerman, B. Cohen, D. Hasan and E. Wacholder, "HTGRSS- A Computer Code for the Simulation of Transient Processes in High Temperature Gas Cooled Reactors; Control System Simulation and Code Validation", Technion Report TNED/R-729(1990).

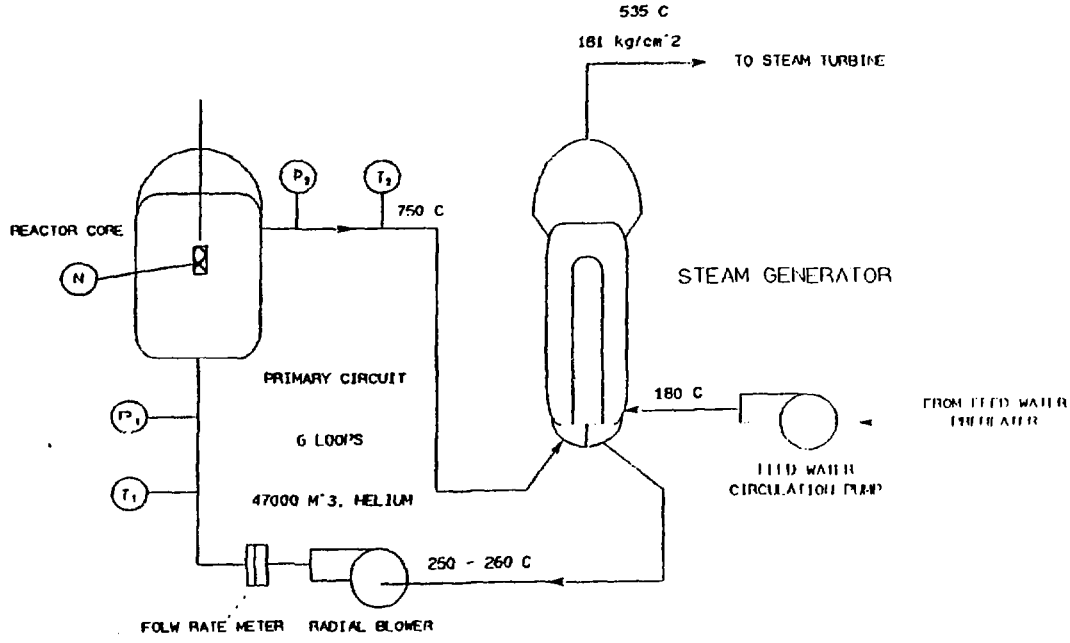

Figure 1: Schematic Diagram of the High Temperature Gas Cooled Reactors (THTR-300).

INTERNAL THERMOSYPHON IN HOT GAS DUCT

Isaac Shai and Yeshayahu Weiss
Mechanical Engineering Department
Ben Gurion University, Beer Sheva

Introduction

The HTR-500 is a 550 MWe nuclear power plant in which a pressurized helium is the cooling fluid [1].

Under normal operating conditions the helium is forced to flow, by gas circulators, downward in the pebble bed reactor core made of ceramic fuel spheres. The helium is heated up in the core from 260^{0}C to about 720^{0}C and then flows upward in the steam generators where it transfer the heat to the water, generating steam at high temperature.

The cavity formed within the concrete pressure vessel, serves as a duct for helium flowing from the circulators to the upper part of the reactor and to the reactor core, to complete the loop. The helium flows in the pebble bed is against gravity, namely , against the buoyant forces.

In the case of loss of power to the circulators, the helium has a tendency to flow in the reverse direction, namely , flowing upward in the reactor core, as for example in THTR-300 [2] , unless special arrangements are used.

In HTR-500 such special arrangement is the Hot Gas Duct (HGD) , which is a vertical cylinder filled with hot helium, just ready to start the natural circulation loop. The direction of helium flow in the reactor core, during natural circulation, is the same as at normal operating conditions.

Theoretical calculations regarding the thermal conditions in the HGD are the subject of another work [3].

In this work, an analysis is presented for the thermal conditions in the HGD when internal tube is inserted into the HGD, forming an internal thermosyphon.

1. The Physical Model

The Hot Gas Duct is a vertical cylinder connected to the reactor core in parrallel to the steam generators by a large plenum. During normal operating conditions, the hot helium leaving the reactor core, flows to the steam generators through the large plenum but also penetrates the HGD from that plenum. Due to heat loss from the outer surfaces of the HGD, a boundary layer is formed near the inner wall of the HGD, causing a downward flow of a colder fluid. The movement of hot and cold helium, within the HGD in opposite directions, creates a very complicated flow field.

The insertion of a vertical tube of smaller diameter in the HGD, forms an induced flow in the inner tube as well as in the outer annulus, due to buoyant forces. The colder fluid, flowing in the annular duct, mixes in the plenum with the hot helium coming from the reactor, and a steady state internal thermosyphon is formed.

2. The Mathematical Model

In oreder to analyze the internal thermosyphon in the HGD, the effect of energy exchange between cold and hot helium streams during mixing, is replaced by heat interaction. The mathematical and the geometrical model is shown in Figure 1. The driving force for the internal thermosyphon is the difference in densities of the cold helium in the annular duct and that of the hot helium in the inner tube. This potential pressure is balanced by the friction forces in the two ducts.

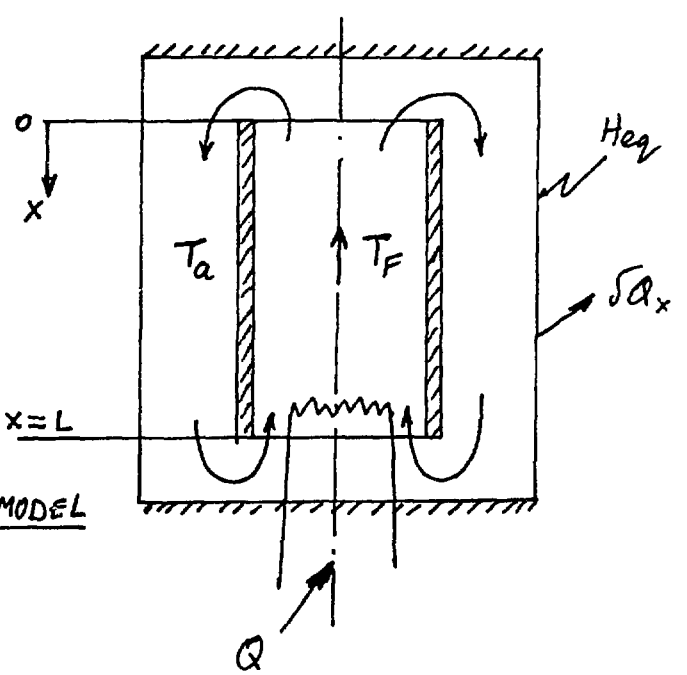

FIGURE 1: SCHEMATIC MODEL OF HGD

3. Developing the Governing Equations

The momentum equation can be written as follows:

$$g\int_0^L(\rho_a-\rho_F)dx=\frac{\dot{m}^2}{2}\left[\frac{f_F}{A_1^2 d}\int_0^L\frac{dx}{\rho_F}+\frac{f_a}{D_h A_2^2}\int_0^L\frac{dx}{\rho_a}\right] \qquad (1)$$

Where the subscript F stands for the inner tube and the subscript a is for the annulus. The friction factors f_F and f_a are:

$$f_F=\frac{0.316}{\mathrm{Re}_F^{0.25}}=\frac{0.316}{\left(\frac{4*\dot{m}}{\pi*d*\mu_F}\right)^{0.25}}; \qquad f_a=\frac{0.316}{\mathrm{Re}_a^{0.25}}=\frac{0.316}{\left(\frac{\dot{m}D_h}{\mu_a A_2}\right)^{0.25}} \qquad (2)$$

Since the flow in the two ducts is fully developed, the heat transfer coefficients are constants and are calculated by using Colburn equation:

$$h_F=0.023\frac{k_F}{d}\mathrm{Re}_F^{0.8}\mathrm{Pr}^{0.3} \qquad h_a=0.023\frac{k_a}{D_h}\mathrm{Re}_a^{0.8}\mathrm{Pr}^{0.4} \qquad (3)$$

The energy balances at the two ducts provide the following two relations:

$$\dot{m}c_p\frac{dT_F}{dx}=(\pi d)U_1(T_F-T_a) \qquad (4)$$

$$\dot{m}c_p\left(\frac{dT_F}{dx}-\frac{dT_a}{dx}\right)=(\pi D)U_2(T_a-T_\infty)=\left(\frac{\delta Q}{\delta x}\right) \qquad (5)$$

where U_1 is the film coefficient between the fluid in the inner tube and the fluid in the annular duct, and U_2 is the same value between the fluid in the annular duct and the surrounding.

Using the above set of equations the thermal conditions can be calculated for a given set of geometrical and thermal properties, as functions of the working pressure and temperature as well as the quality of the external insulation.

The results of the calculations are given in Figure 2, which provide relations between the imposed external conditions to the internal flow rate ,heat transfer and the potential pressure drop for maintaining natural circulation.

4. Conclusions

The insertion of a tube to the HGD, which is a simple physical change, insures a steady state flow in the HGD maintaining high temperature gas during normal operation.

Further work has to be done to show the complete natural circulation loop when incorporating the results of this work with other parameters of the loop.

References

(1) E.Arndt, J.Schoening and W.Wachholz, Design Status of the HTR-500 Power Plant, Nucl. Eng. and Design 121 No.2 (1990) 227-286

(2) J.Tzoref and D.Saphier, Decay Heat Removed in HTGR by Natural circulation, Trans. Israel Nucl. Soc. (1990)

(3) I.Shai and Y.Weiss, Thermal conditions in Hot Gas Duct, to be published.

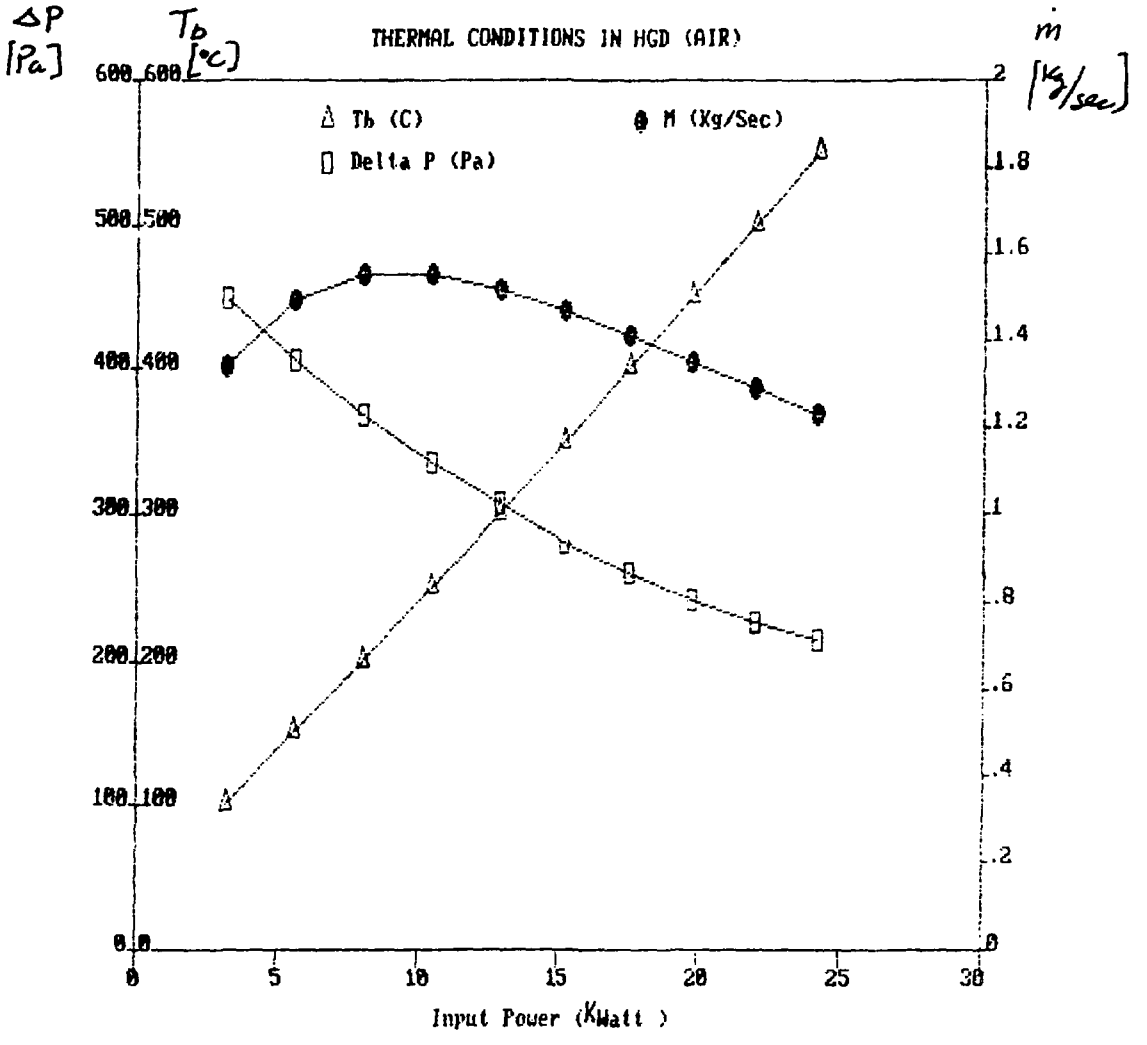

Figure 2: Thermal Conditions in HGD

AIR at 10 atm.

$L = 5.0$ m $\quad D_o = 0.75$ m $\quad d = 0.5$ m.

$H_{eq} = 5\ ^{W}/_{m^2 °C}$

DECAY HEAT REMOVAL SYSTEM in a MEDIUM SIZE HTGR

A. Ronen and D. Saphier

Soreq Nuclear Research Center
Yavne 70600

1 Introduction

The present study investigates the operation of the DHR [1] system during a LOF (Loss of Flow) accident in which the primary flow is reduced to zero at full power operation of a medium size HTGR (High Temperature Gas Reactor).

While the neutronic power is shut off immediately, the decay heat in the core has to be removed by a special DHR (Decay Heat Removal) system.

The DHR system consists of two blowers, two heat exchangers and the associated ducts.

The operation of the DHR system driving the Helium through the core during the decay heat removal is simulated in this work.

2 The Loop Model

The simulation was performed with the DSNP [2] language. The DHR loop flow diagram is shown in Fig. 1. The various components of the loop are modelled by special DSNP modules [3,4,5,6].

An improved heat exchanger module (IHXMS3) was created to represent the DHR heat exchanger. This module can simulate the reversal of the primary flow in the heat exchanger as it actually happens at the beginning of the DHR operation.

The simulation starts with a five-second steady state calculation, followed by the transient which is initiated by an exponential reduction of the primary mass flow.

The DHR operation is initiated (blowers, valves and water flow) simultaneously with the LOF event.

The reactor is scramed when the core exit temperature increases 50°C above the steady state level.

3 Results

The simulation shows that a new steady state is reached in which the DHR blowers produce a 42 kg/s mass flow in the main loop (Fig. 2). The full power mass flow was 617 kg/s. In the case where only one DHR loop is active, the new steady state mass flow is 21 kg/s as expected.

The maximum temperature in the core for the two cases (1 DHR and 2 DHR) is shown in Fig. 3. The steady state value is 945°C . At the beginning the temperature increases to a value of 968°C in the 2 DHR case and 991°C in the 1 DHR case, but decreases immediately to lower values.

The temperatures in the primary inlet and outlet cavities of the DHR heat exchanger are shown in Fig. 4. The graph shown is for the two DHR loops case. The inlet temperature (ZTGCHI) follows the trend of the core temperature as expected.

The pressures along the loop were also calculated. The general behavior is a small increase during the first seconds and then a steady decrease as a result of the temperature's reduction.

4 Conclusions

The DHR system of the proposed HTR simulated in this work can remove the reactor Decay Heat with a maximum rise of 23°C in the core temperature.

In case of a failure in one of the DHR loops, the remaining active loop will also remove successfully the decay heat with a 46°C increase. In this case, the core cooling will take a longer time but the immediate cooling to acceptable temperatures is achieved in a similar time as in the 2 DHR loops case.

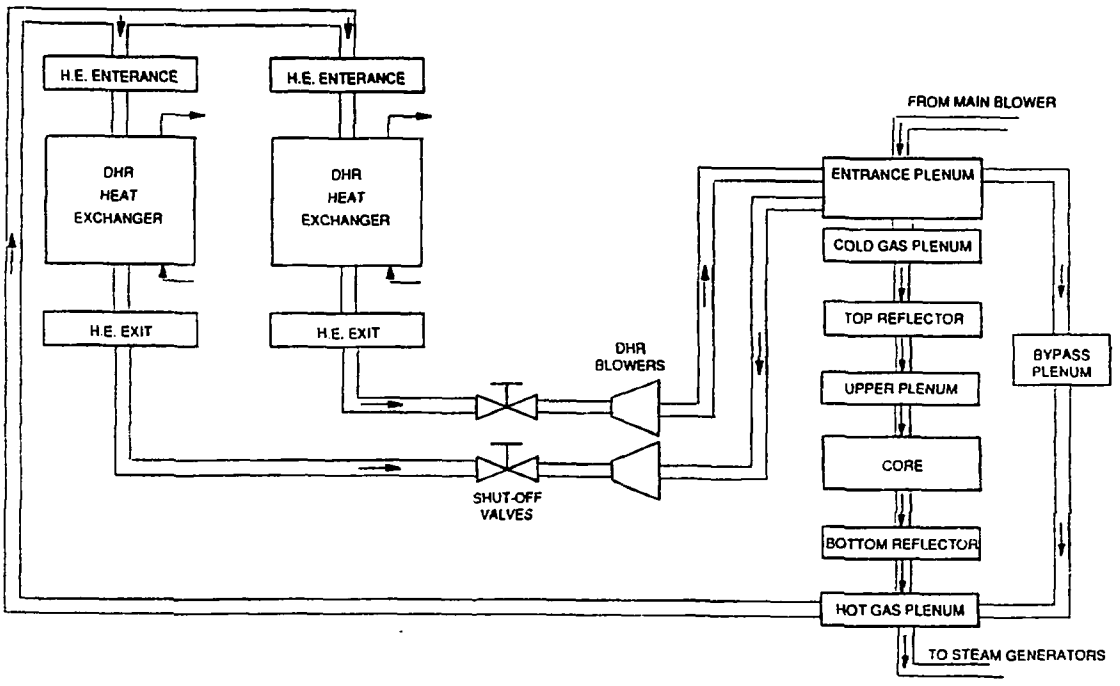

Figure 1: The DHR Loop Flow Diagram

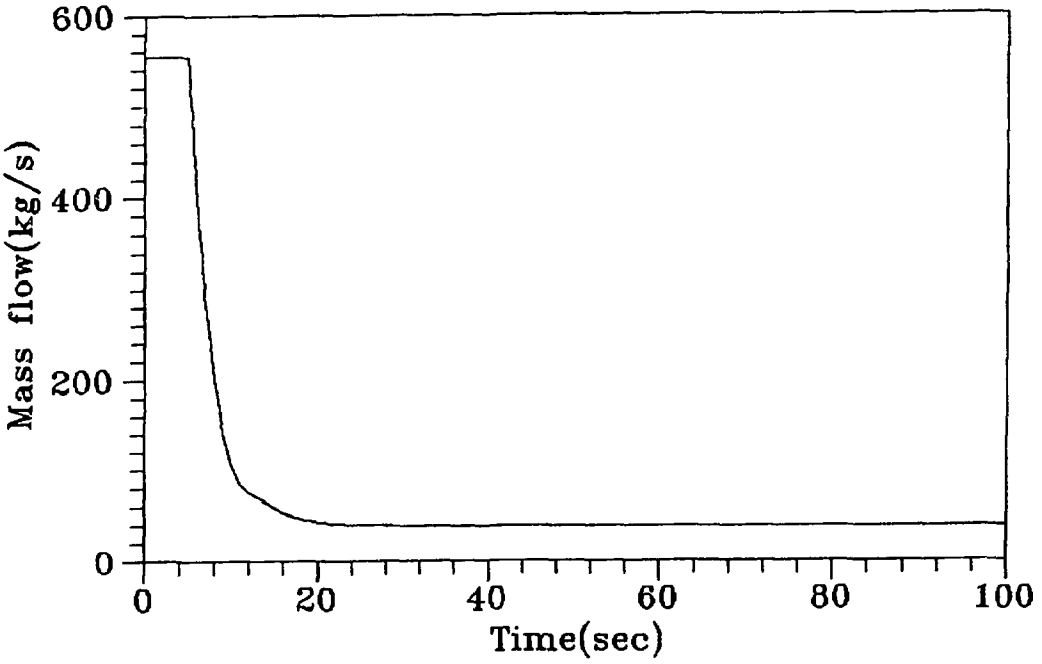

Figure 2: Core Mass Flow during the First 100 s

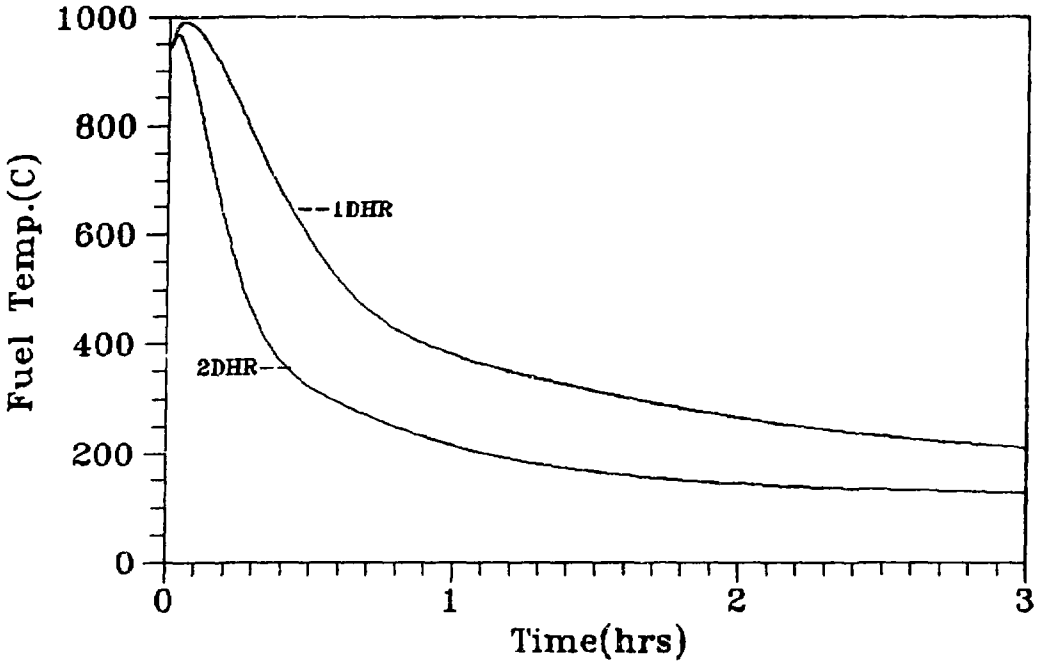

Figure 3: Maximum Core Temperature in the Two Cases

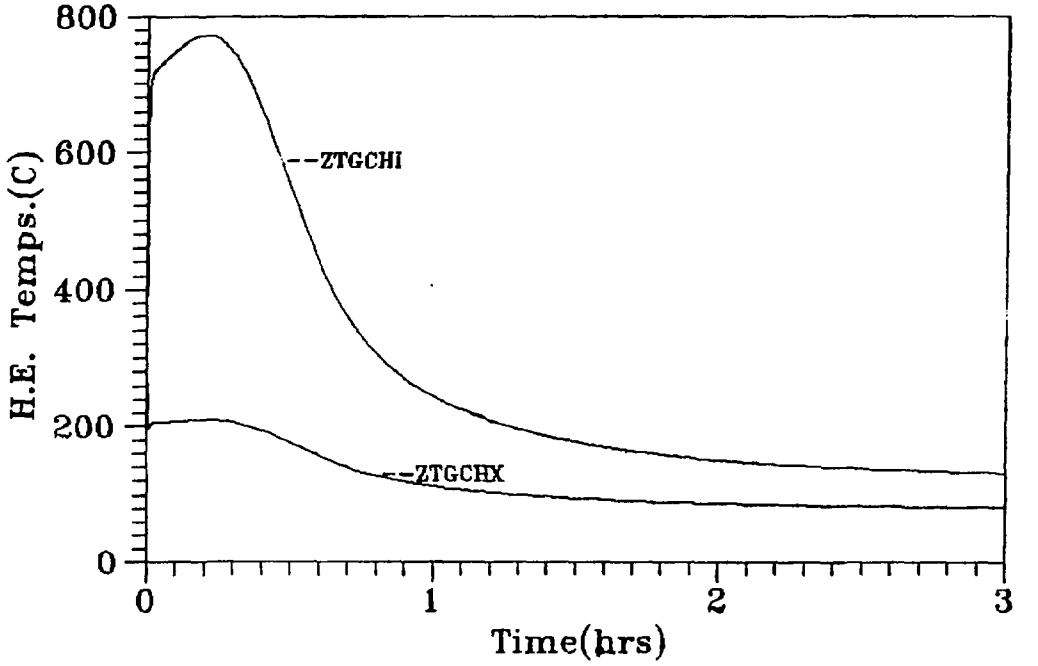

Figure 4: Inlet and Outlet H.E. Temperature-Primary Side

References

1. "Sicherheitstechnische Untersuchungen Zum Störfallverhalten des HTR-500". Jül -Spez - 240,January 1984. Edited by R. Nabbi.

2. "The DSNP User's Manual", Volume II, Rev. 4.3, 1990, RASG-112-90, Soreq NRC (1990).

3. "The DSNP Level One Components Library", Volume III, Revision 4.3, 1990, RASG-115-90, Soreq NRC (1990).

4. "The DSNP Level Two Components Library", Volume IV, Revision 4.3, 1990, RASG-115-90, Soreq NRC (1990).

5. "The DSNP Level Three Components Library", Volume V, Revision 4.3, 1990, RASG-116-90, Soreq NRC (1990).

6. D. Saphier, "The DSNP Materials Properties Library", Volume VI, Rev. 4.2, RASG-117-85, Georgia Institute of Technology (1985).

Decay Heat Removal in HTGR by Natural Circulation

J. Tzoref and D. Saphier

Soreq Nuclear Research Center
Yavne 70600

Abstract

The coolability of 1000MWt HTGR under complete loss of forced flow conditions was investigated. A Dynamic Simulator for Nuclear Power Plants (DSNP) program was developed to study the evolution of natural circulation during Loss Of Forced Flow (LOF). It was concluded that a passive cooling device, having 0.3% heat removal capacity of the nominal decay heat rate, is sufficient for emergency cooling of the proposed plant under total LOF.

Introduction

The coolability of a conceptual medium size 1000 MWt HTGR under complete loss of forced circulation is investigated. The reactor design parameters used in this study do not represent any specific reactor, rather they reflect data published in the last decade on several design concepts. The important question to be answered is whether for a given geometrical configuration and power density natural circulation can be developed within a sufficiently short period so that passive cooling devices can be used to remove the given quantity of decay heat.

The study was performed by using the DSNP [1]. A dynamic model was developed for the natural circulation flow in the primary loop of a medium size HTGR during LOF. The conceptual HTR plant was nodalized so that all the important phenomena taking place in the primary loop were described in sufficient detail. For the investigated reactor a closed-loop liner cooler was considered as the passive cooling device. The nominal passive cooling capacity of the liner cooler is defined as the percent of decay heat removed by it during the reactor normal operation. The decay heat level during the reactor normal operation is 56 MW. Hence a liner cooler designated here as having 1% passive cooling capacity is capable of removing 0.56 MW under normal operating conditions. The model was realized with the various DSNP modules capable of simulating gas dynamics phenomena. The primary loop was divided into 36 control volumes connected by flow channels. The Loss Of Flow simulation was performed for different operating conditions to find their effect on the evolution of natural circulation flow and the minimum passive cooling capacity required to prevent core heat-up above the

permitted temperature of 1600°C.

The HTGR

A schematic chart of the proposed conceptual HTGR is presented in Fig. 1. This concept is based on several published HTR designs [2], [3]. Under normal

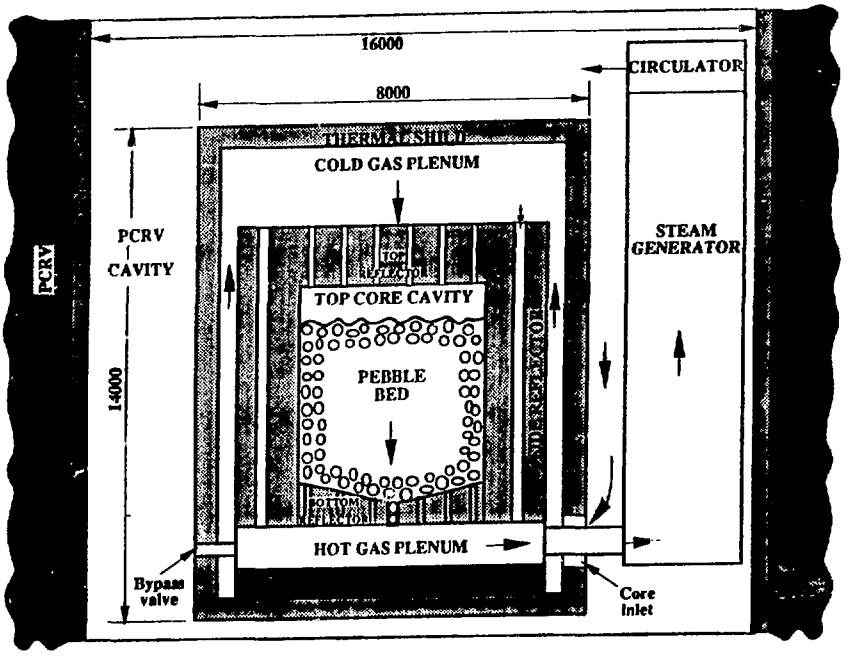

Figure 1: Schematic Chart of the HTGR

operation, a 450 kg/sec helium flow is forced by the circulator into the PCRV main cavity. From the cavity the helium flows through the core inlet and the radial gap between the thermal shield and the side reflector into the cold gas plenum. It then reverses and flows down through the top graphite reflector and top core cavity into the pebble-bed where it is warmed up by the heat generated in the fuel elements. The hot helium exits from the pebble-bed through the bottom reflector into the hot gas plenum. A bypass valve, assumed to exist between the hot gas plenum and the PCRV cavity, is closed during normal operation. Thus the helium flows back into the steam generator where it is cooled and forced by the circulator into the PCRV cavity. The PCRV is protected by a liner cooler and a thermal insulation layer which prevents the increase of the PCRV temperature above the permitted level. In the present case the PCRV average temperature during normal operation was assumed to be 35°C. The liner-cooler is a closed-loop water cooling system. Natural circulation of water in the liner is established due to fulfilment of the required conditions, i.e.: a closed fluid loop, heat source - the energy transferred from the cavity helium (by convection) and the thermal shield (by radiation) to

the water , and the heat sink - the heat transferred from the water in the external pipe array by free convection to the ambient air.

The loss of flow accident is assumed to occur when a total loss of power is experienced and emergency power does not restart the main blowers, and no other emergency cooling system (which is usually built into an HTGR plant) is activated. The power will be shut down either by the control system or by a moderate temperature increase (in case of ATWS) inside the core and the strong negative Doppler feedback effect. With the neutronic power reduced to zero, the residual decay heat, about 6% of the nominal power, has to be removed. During a Loss of Flow accident the passage through the steam generator is prevented by the automatic closure of the shut-off valve. The bypass valves are then opened manually to enable the natural circulation of helium.

The simulation

The primary loop was subdivided into 36 sections. The nodalization diagram is shown in Fig. 2. Each cavity is assumed to interact thermally with the cavity fluid

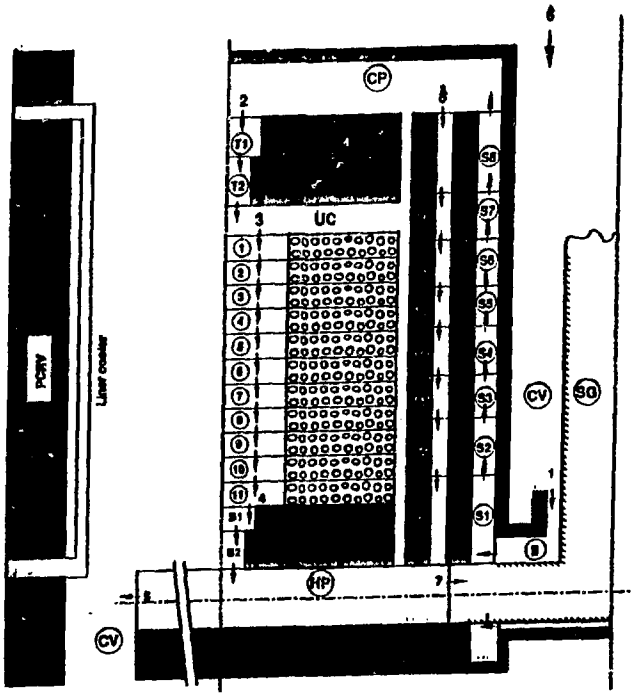

Figure 2: Nodalization diagram of the plant for the DSNP simulation program

and sometimes also with interfacing walls and fluids of the adjacent cavities. The cavity fluid interacts with neighboring cavity fluids through the flow channels.

For the thermal simulation of each cavity the DSNP [1] module GCAVT1 [4] was used. For the simulation of the flow channels between the cavities module FLOW01 [4] was used.

Various runs were carried out for different liner nominal passive cooling capacities. The range of nominal passive cooling capacities selected for the various runs was: 0.3% to 1%.

The simulation of the accident was assumed to start from forced flow steady-state conditions (450 kg/sec) of normal reactor operation. The beginning of the accident was simulated by an exponential decrease of the forced flow. The bypass valve was assumed to be open within 1 minute from the beginning of the accident. The various elements of the plant included in the simulation are presented in Fig. 2.

Results

When forced flow is reduced to zero within 30 seconds, the flow remains zero for another two minutes. Then a spontaneous natural circulation develops in the opposite (upward) direction (Fig. 3) through the bypass valve instead of the steam-generator. For all tested cases the flow reaches maximum at about 200 seconds

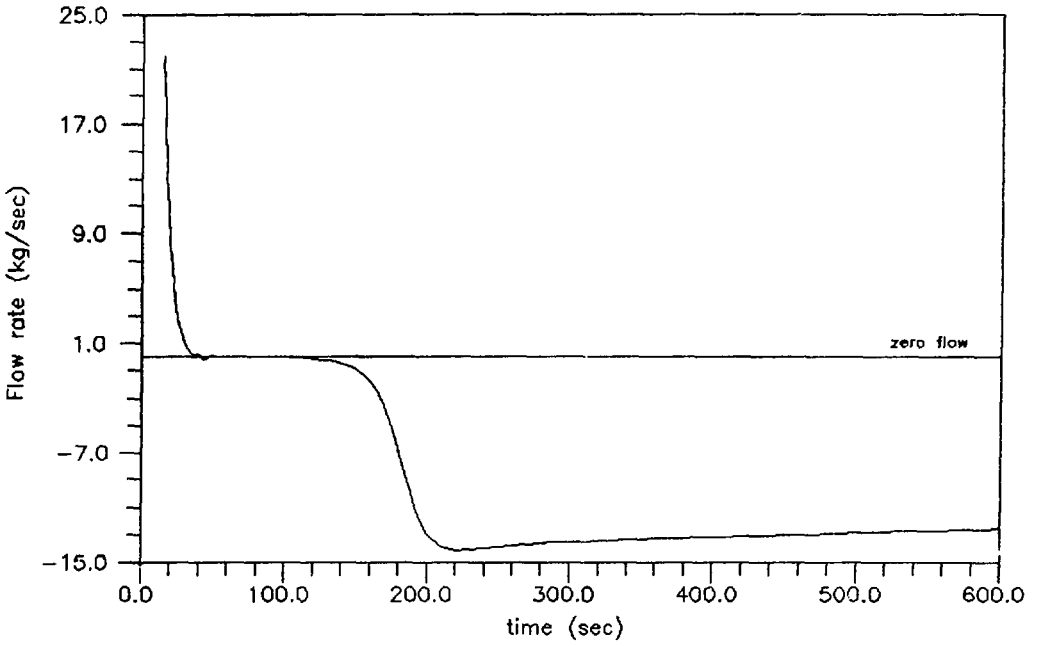

Figure 3: Core flow (15-600 sec), 1% nominal passive cooling capacity

after the beginning of the accident with the value of 15 kg/sec. Subsequently, the natural circulation decreases within 50 hours to a nearly fixed value for days and weeks later in the range of 1 to 2 kg/sec. For the 0.3% nominal passive cooling capacity the fuel reaches a maximum temperature of 1560°C after 22 days (Fig. 4).

The maximum fuel temperature versus the nominal passive cooling capacity is

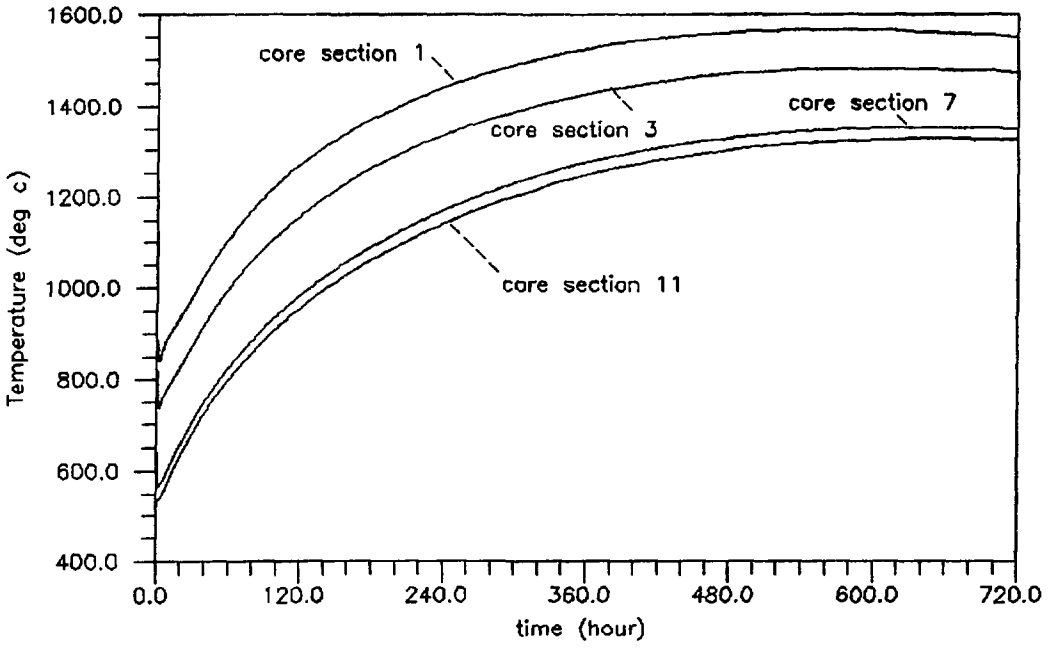

Figure 4: Fuel temperatures (30 days), 0.3% nominal passive cooling capacity

presented in Fig. 5.

Conclusions

The simulation of the given conceptual 1000 MWt HTGR primary loop under complete loss of forced circulation, has shown that a passive cooling device may be sufficient for the prevention of core heat-up above the permitted temperature of 1600°C. This will not, however, prevent the heatup of components in the core upper plenum to temperatures that will damage the components in this region.

For all tested cases of passive cooling capacities a stable natural circulation helium flow was shown to develop spontaneously in the pressurized primary loop. The maximum value of the flow is 15 kg/sec about 200 seconds after the beginning of the transient. Within 10 hours into the accident the natural circulation decreases to about 3 kg/sec, and decreases further, very slowly. For the limiting nominal passive cooling capacity of 0.3%, in which the maximum fuel temperature was found to reach the maximum allowed temperature, the flow rate is 1.4 kg/sec a month later.

For the minimum allowed nominal passive cooling capacity 0.3%, the maximum actual heat removal capacity required during the accident is 1 MW. It can be obtained by natural circulation of 4 kg/sec in the liner-cooler. This requirement can be easily met by a proper design.

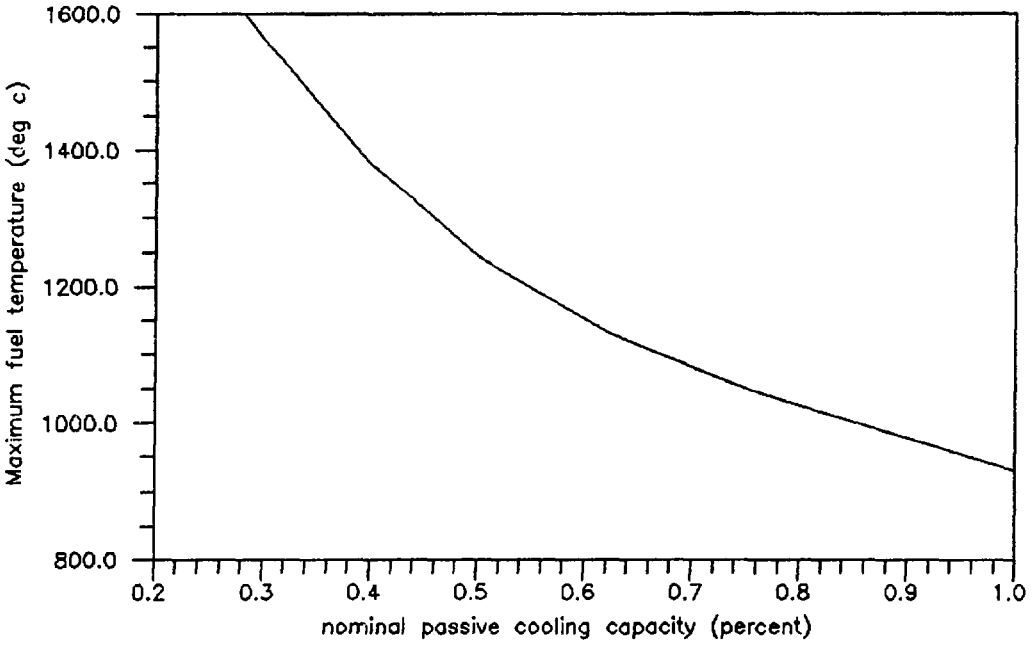

Figure 5: Maximum fuel temperature vs. nominal passive cooling capacity

References

[1] *The DSNP User's Manual* Dynamic Simulator for Nuclear Power Plants, Volume II, Revision 4.3, 1990, RASG-112-90, Soreq NRC, (1990).

[2] Projektinformation 10, *300-MW-THTR Kernkraftwerk Uentrop*, Hochtemperatur Kernkraftwerk GmbH, Uentrop, 1976.

[3] G.Melese, R.Katz, *Thermal and Flow Design of Helium-Cooled Reactors*, ANS, 1984.

[4] *The DSNP Level-One Components Library* Dynamic Simulator for Nuclear Power Plants, Volume III, Revision 4.3, 1990, RASG-114-90, Soreq NRC, (1990).

Design Base Depressurization Accident in HTR-500

J. Tzoref
Soreq Nuclear Research Center, Yavne 70600, Israel

S. Ron
Atomic Energy Commission, P.O.Box 7061, Tel-Aviv 61070, Israel

A depressurization design base accident in a medium sized HTGR (HTR-500) was investigated employing the DSNP modular code[1]. The accident is initiated by a 33cm² rupture in the fuel discharge pipe at the core bottom. Once the pressure drop is detected the six steam-generators blowers are automatically switched off. It was assumed that only one of the two Decay Heat Removal (DHR) emergency circuits starts to operate. About 160 sec after the beginning of the accident the in-core flow is increased to a value of 14.7 kg/sec. Due to the continous pressure loss of helium in the primary circuit the flow decreases. Once the internal helium flow reaches the value of 4.2 kg/sec the DHR blower automatically increases its rate so that the flow reaches a value of 16.3 kg/sec. This proceedure is repeated once again, after which a flow of 4.22 kg/sec is sustained.
The entire simulation space was divided into 8 main regions: pebble-bed core, reflector, helium gap, thermal shield, helium cavity, liner isolation, liner and PCRV. The numerical mesh is displayed in Fig. 1. The core and the reflector were divided into 11 axial core regions, and each axial layer was subdivided into 10 radial annuli.

The results are displayed in Figures 2 and 3, where the average and maximal temperatures are shown for the 11 axial core regions. The maximal temperature is obtained very early in the accident at the bottom of the core (i.e. the 11th axial region). The maximum average temperature is about 750°C. Both temperatures reflect normal operational conditions. Thus the temperatures during the accident remain far below the threshold value of 1600°C. Therefore no significant fission products are expected to be released from the fuel.
Air starts entering into the primary circuit through the rupture after about 2 hours when the pressure in the primary circuit decreases to the atmospheric pressure. The air ingress flow into the primary circuit is displayed in Fig. 4. Most of the oxygen content in the air reacts with the graphite to produce CO because of the high graphite to oxygen ratio. About 400 kg of air enters the core within 100 hours and this amount will oxidate about 60 kg of graphite. This amount is very low as compared with the total graphite content in the reactor of about 470 tons.

The DHR blower circulates the penetrating air through the relatively cold peripherial area of the side reflector and then through the relatively cold upper reflector into the relatively hot pebble-bed core, where the main graphite oxydation will occur causing no severe damage.

References:

(1) The DSNP User's Mannual Dynamic Simulation for Nuclear Power Plants, Vol. II Rev. 4.3, RASG-112-90, Soreq NRC (1990).

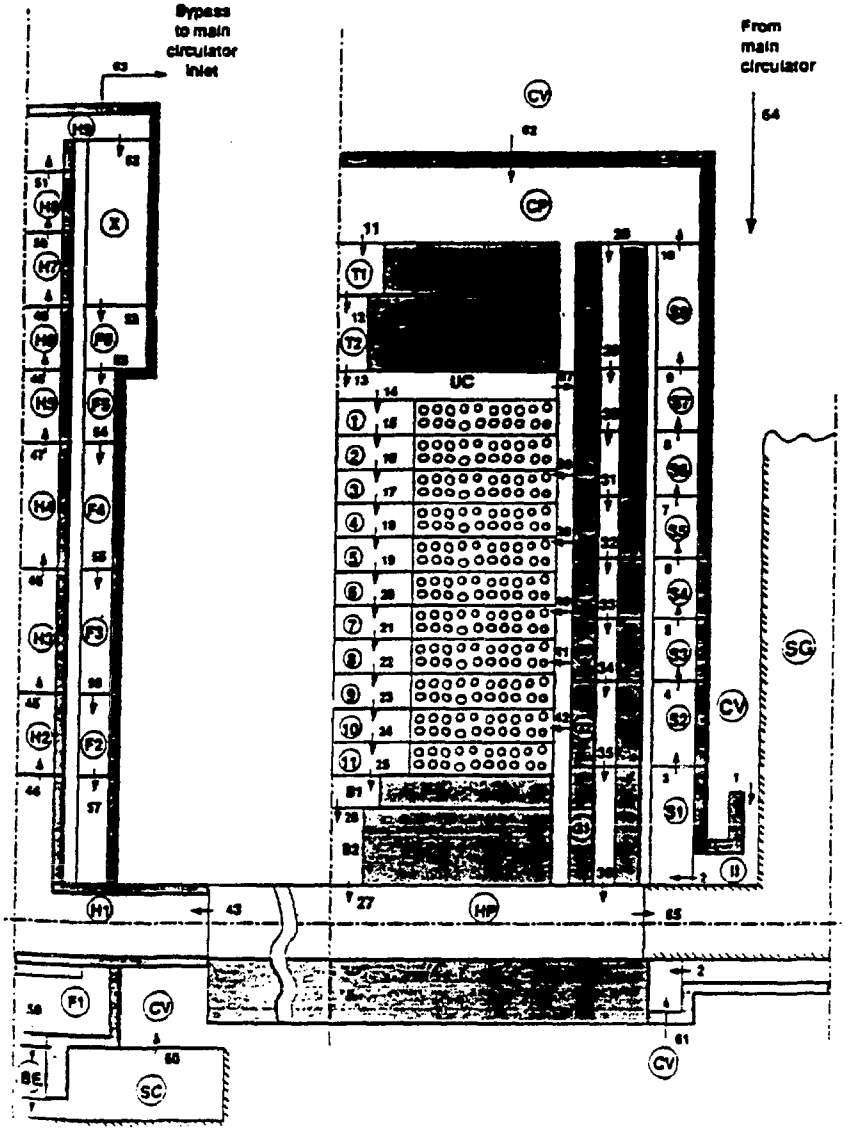

Fig. 1: Numerical mesh of the simulation

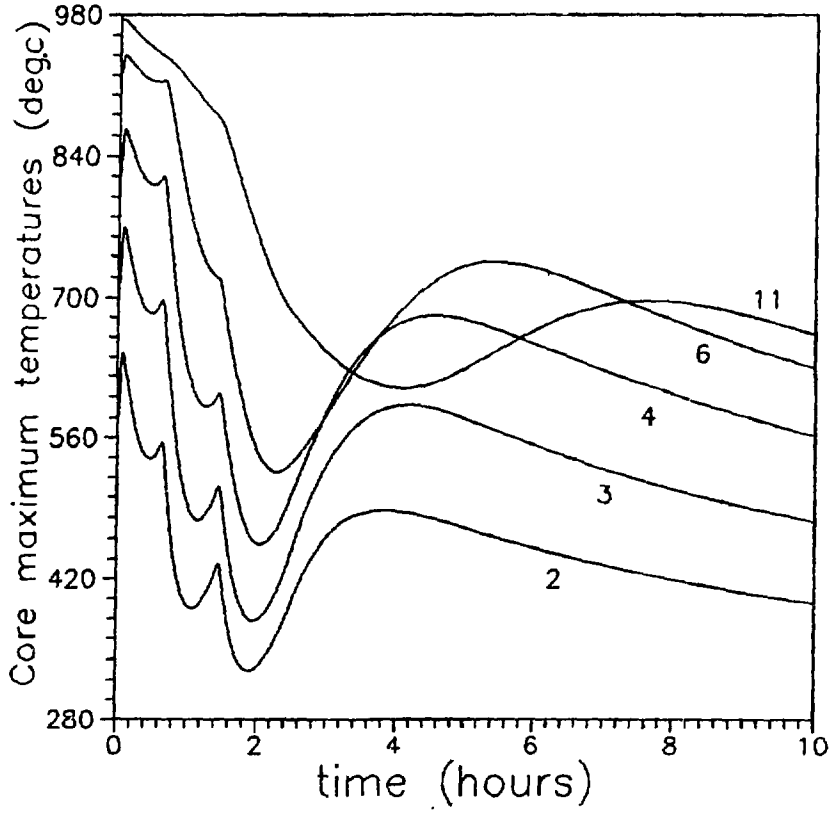

Fig. 2: Core maximum temperatures at different axial regions

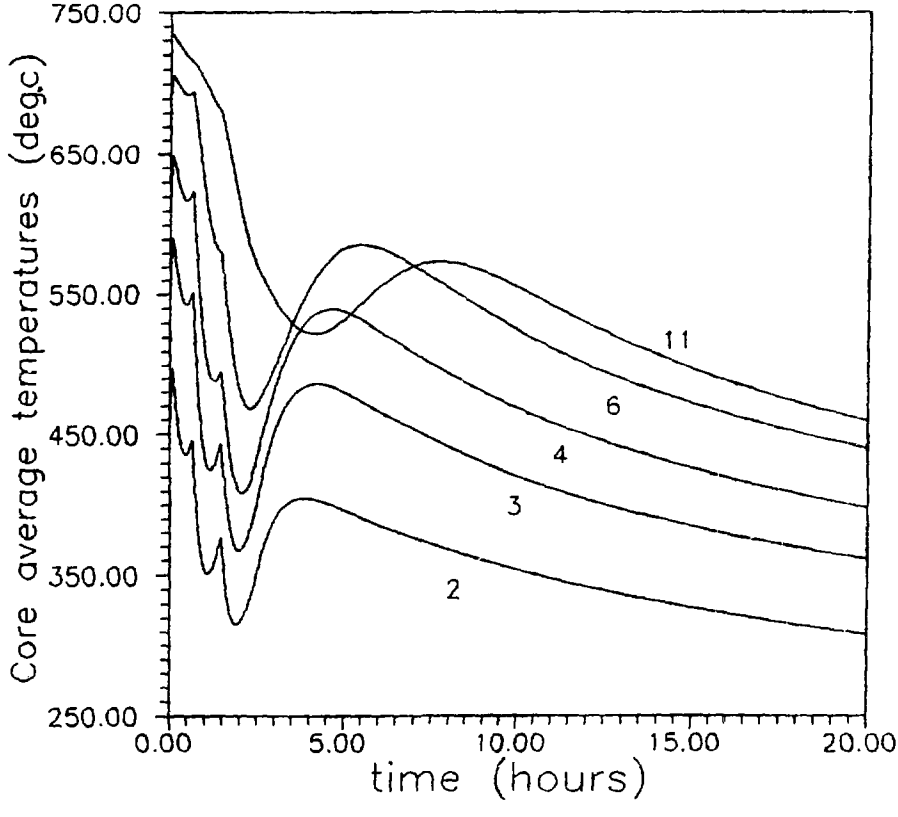

Fig. 3: Core average temperatures at different axial regions

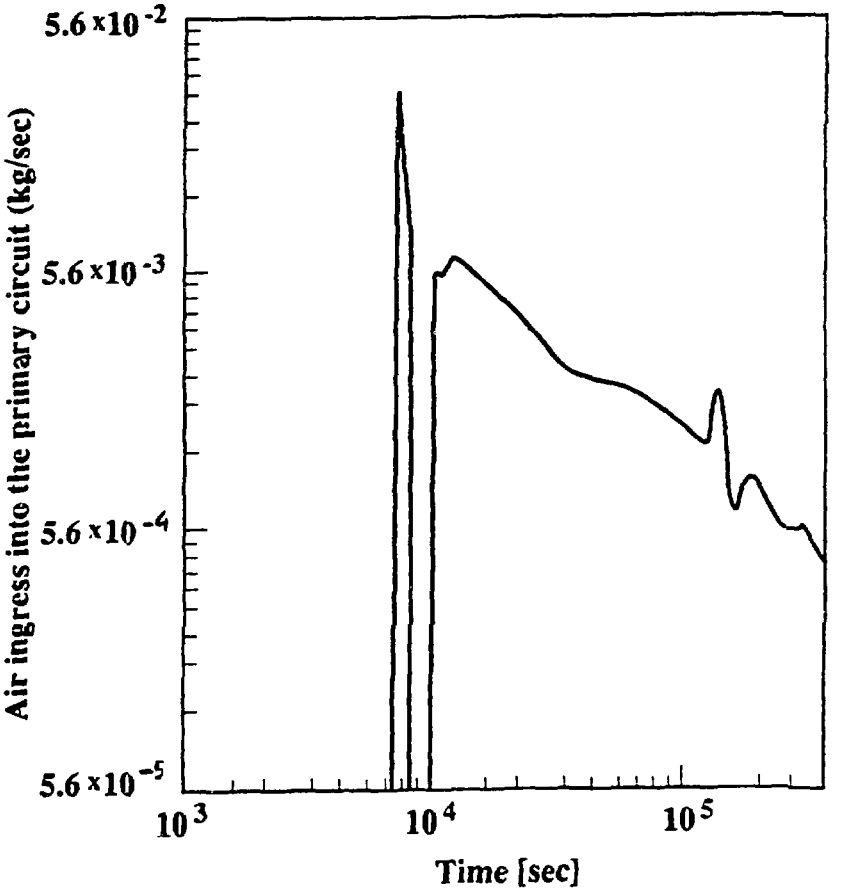

Fig. 4: Air ingress into the primary circuit.

Fission Products Sorption due to Natural Circulation Following Core Heat-up Accident in HTR-500

J. Tzoref
Soreq Nuclear Research Center, Yavnne 70600, Israel

S. Ron
Atomic Energy Commission, P.O.Box 7061, Tel-Aviv 61070, Israel

The maximum fuel temperature during a depressurization accident, coincident with the forced circulation failure of the Decay Heat Removal (DHR) system in HTR-500, may reach 3050°C[1]. Such scenario is considered as a beyond design base accident was simulated employing the DSNP modular code[2]. Figures 1 a-c show the natural circulation flow through the primary circuit. About 50 sec from the beginning of the accident the inflow direction is reversed from down-core forced flow to an upward flow due to the thermal convection force. After about 2 hours the primary circuit reaches atmospheric pressure. During this time period the natural circulation flow decreases with the primary circuit pressure. At 1 bar and high temperatures the core heat transfer by natural circulation is negligible, whereas the dominant mechanism is the radial radiation of the cylindrical core.

At the time significant fission products amounts start to be released from the fuel [i.e. about 10 hours from the beginning of the accident[1]] the natural circulation flow is higher by about one order of magnitude than the primary circuit out-flow causing the depressurization. The last is displayed in Fig. 2 where different driving forces are taken into account[1].
It was assumed that the cesium is totally sorbed (adsorbed + absorped) once it enters the DHR system, whereas the krypton is unaffected by these mechanisms. It was found[1] that 3.4% of the Cs^{137} and 2.5% of the Kr^{85} that escaped from the fuel during 100 hours, are released from the primary circuit, out of which 7% of Cs^{137} and 35% of Kr^{85} are released to the containment atmosphere due to their different sorption affinities. Therefore a three fold reduction can be attributed to the dilution in the primary circuit. An additional reduction by a factor of 5 is due to the sorption in the primary circuit. Although the present study deals with specific isotopes, general conclusion can be obtained. The cesium and krypton represent the upper and lower sorption values of the highly volatile compounds released into the primary circuit. In addition, Kr^{85} represents the fractional release of all the noble gases isotopes, after taking into account their different half-life time values.

References:

(1) Beyond Design Depressurization Accident in HTR-500, J. Tzoref, S. Ron and J. Szabo. These Transactions.

(2) The DSNP User's Mannual Dynamic Simulation for Nuclear Power Plants, Vol. II Rev. 4.3, RASG-112-90, Soreq NRC (1990).

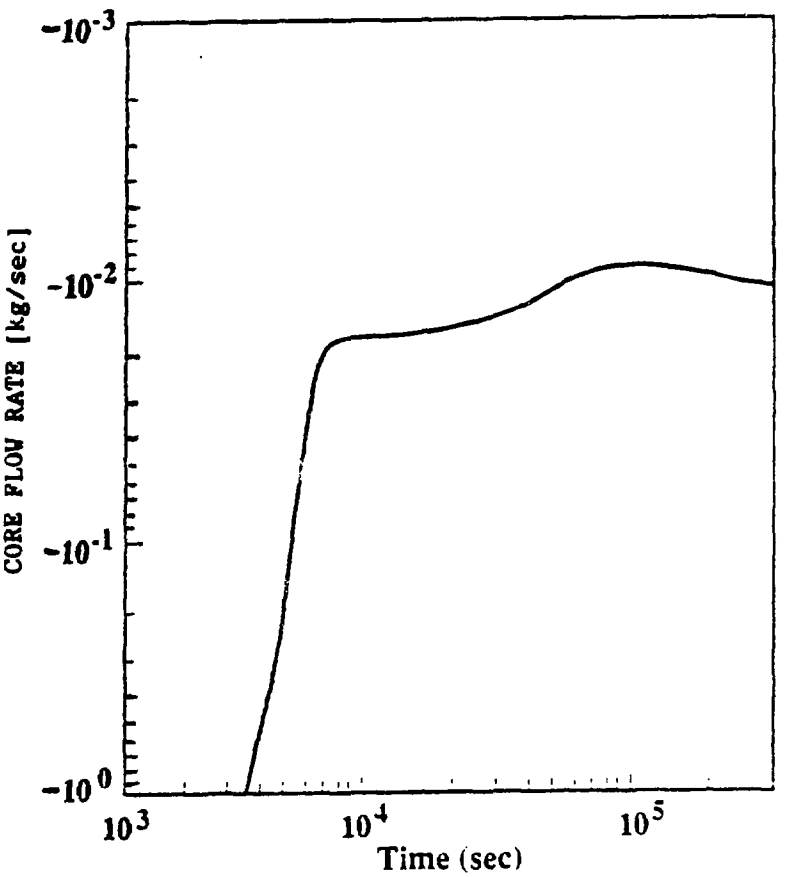

Fig. 1c

Fig. 1 a-c: Core flow rates at different time scales.

* The negative flow values refer to an upward core flow and vice versa.

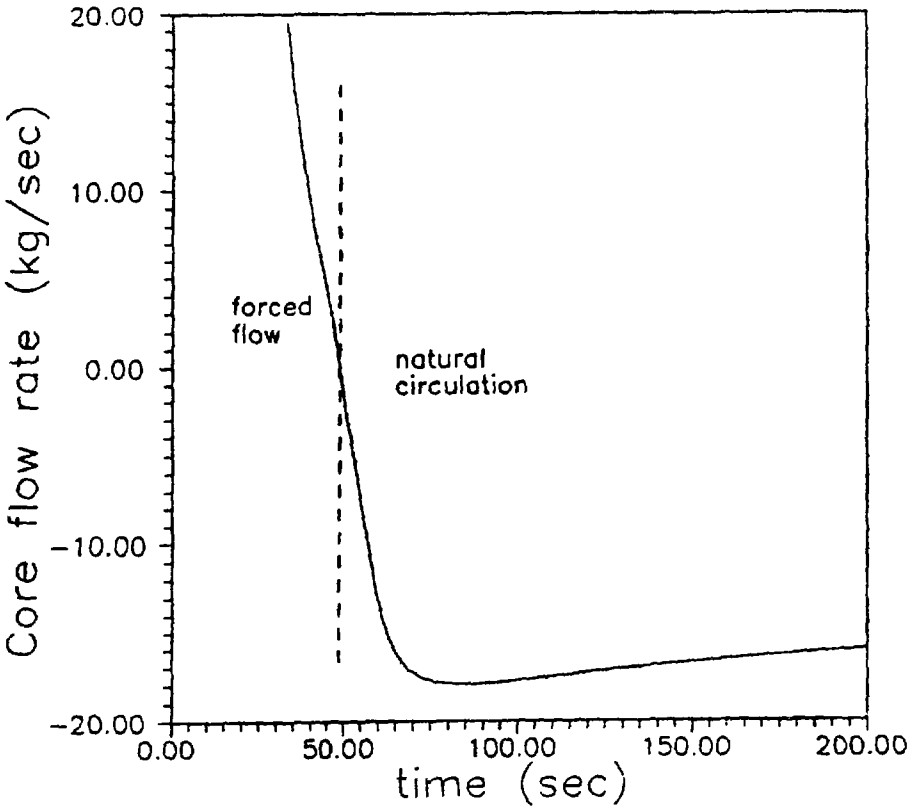
20.00
10.00
0.00
-10.00
-20.00
Core flow rate (kg/sec)
forced
flow
natural
circulation
0.00
50.00
100.00
150.00
200.00
time (sec)

Fig. 1a

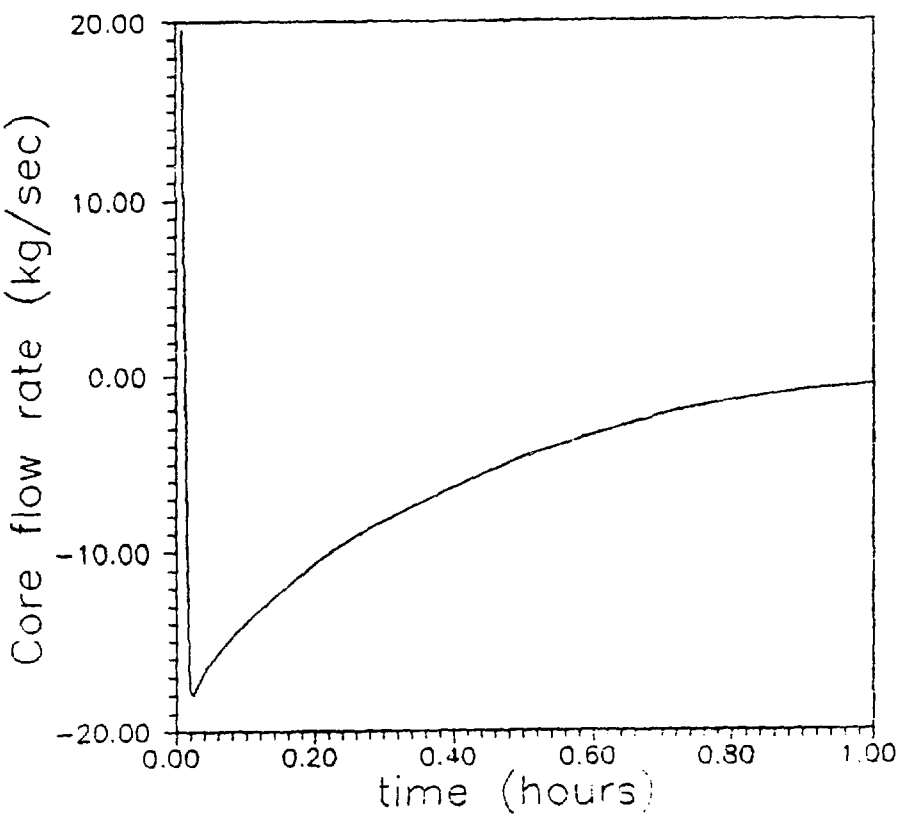
20.00
10.00
0.00
-10.00
-20.00
Core flow rate (kg/sec)
0.00
0.20
0.40
0.60
0.80
1.00
time (hours)

Fig. 1b

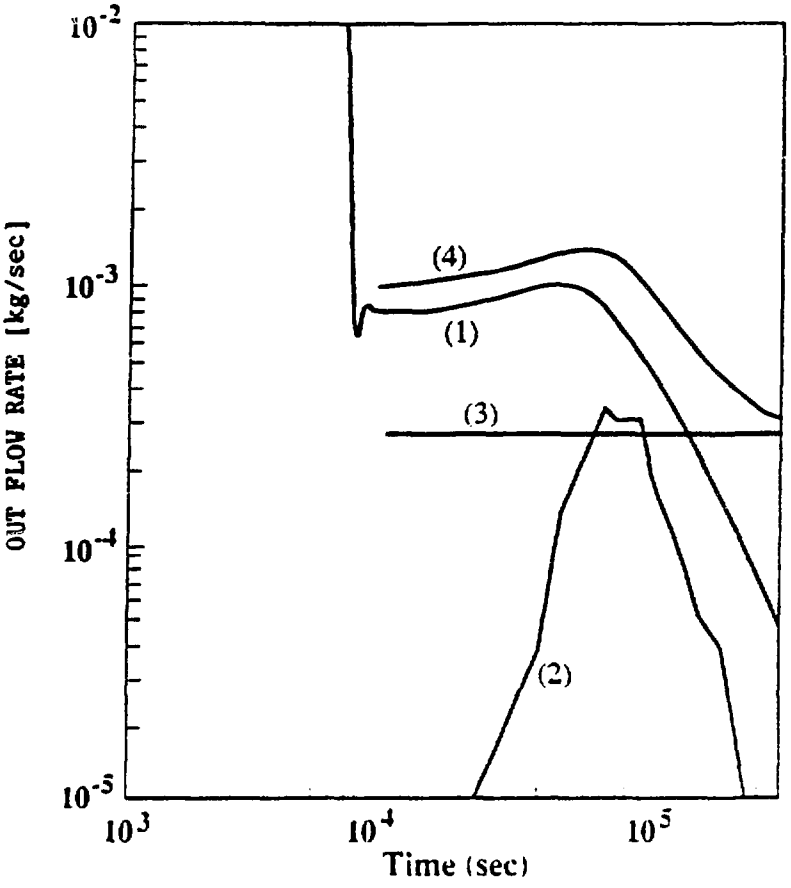

Fig. 2: Equivalent helium out-flow rate from the primary circuit as caused by various mechanisms.

(1) Thermal expansion.

(2) CO release from the graphite.

(3) Helium release from the graphite (assuming a constant rate).

(4) Total = Thermal expansion + CO + Helium releases.

BEYOND DESIGN DEPRESSURIZATION ACCIDENT IN A MEDIUM SIZED HTGR

Jehuda Tzoref
Soreq Nuclear Research Center, Yavne 70600, Israel

Shlomo Ron, Jacob Szabo
Atomic Energy Commission, P.O.B. 7061
Tel-Aviv 61070, Israel

Abstract

The potential for the release of fission products during a beyond design accident in a medium sized HTGR (HTR-500) was investigated. The DSNP modular simulation code[1], was employed in the simulation of a depressurization accident coupled with the failure of forced circulation if the decay heat removal systems. For such an extreme accident the maximal localized fuel temperature reaches 3050°C, and within 100 hours from the beginning of the accident, 3.4% of the C_s^{137} inventory will be released from the fuel elements to the primary circuit, and 4.6×10^{-2}% are estimated to be released to the environment. Fission products being swept from the primary circuit by the CO and helium released from the graphite matrix, prove to be an important factor. Although a severe accident scenario was assumed, the comparative consequence analysis points at a lower risk than in the analogous LWR severe accident.

1. Basic Assumptions

A depressurization accident was simulated following the integrity failure of the fuel discharge pipe located at the bottom of the core. The cross section area of the pipe is 33 cm^2 and this event is considered as a design base accident. Once a pressure loss is detected the six steam-generator blowers are automatically switched off. The present study further assumed failure of one of the two Decay Heat Removal (DHR) auxiliary circulators responsible for the forced cooling in a depressurization accident. The DHR bypass valve is assumed to be opened by the operator to enable the natural circulation, and the control rods were successfully inserted.

Axial heat transfer between the fuel elements in the annular layers surrounding the pebble bed (reflector, thermal shield etc.) as well as radial heat transfer were assumed.

Core severe accident conditions enable the release of a high fraction of cesium, an element which poses high potential radiological risks. Therefore the present research evaluates the cesium release fraction. The cesium and krypton temperature dependent release fractions are based on a comprehensive experimental study[2]. Data for low burnup fuel was used, since

the maximal temperatures occur in the low burnup regions. Above 2500°C the experimental results are absent. Therefore an arbitrary extrapolation increase was assumed by one order of magnitude.

Part of the primary circuit flow escapes through the break and the rest flows through the DHR. It is assumed that all cesium atoms entering the DHR pipes in both directions, will be sorbed (adsorbed + absorbed) on the cool surfaces of the DHR circuit. On the other hand due to the depressurization and the subsequent high temperature conditions in the core volume it is assumed that the graphite will not contribute to the capture or retention of fission products.

As previously[3] pointed out, the gaseous releases of CO and helium from the graphite matrix contribute to the driving force sweeping fission products from the primary circuit. The CO is released at high temperature (starting at about 2300°C) due to the chemical reaction of graphite with the UO_2 or other oxides of the fuel kernel. The release is being assumed to be proportional to the fractional amount of noble gases release in each core section. This assumption can be considered realistic, as both the CO and the noble gases are released following mechanical failure of fuel element integrity. The helium is released from the closed pores within the ceramic graphites following depressurization and the subsequent heat-up conditions. Due to the lack of quantitative information, the helium was assumed to be released at a constant rate of 6.5×10^{-2} moles/sec.

It was already shown[4] that helium penetrates into the closed pores in the ceramic matrix of the various graphites in the core and the reflector during the normal operational conditions of the reactor. The accumulated helium is released following the depressurization and heat-up from each of the volumetric regions as a function of the various graphites characteristics, temperature and time. For high temperatures, high helium release rates from the graphite are expected.

The fractional fission products release rate as a function of temperature is displayed in Fig. 1.

The outflow from the primary circuit in the present study takes into account the depressurization process, the thermal expansion of the primary circuit gas due to the core heat-up and the gaseous releases from the graphites. The thermal convection cause the natural circulation through the DHR system and incore circulation. Together with the thermophoresis and the diffusiophoresis they contributes only to homogenous mix-up of the whole primary circuit volume of about 4100 m^3.

A previous study[5] found that 19% of the Cs released into the containment escape to the atmosphere, and this value was adopted in the present study.

2. Results

Core temperatures as a function of time are shown in Fig. 2
Fission product release fractions from the fuel elements and from the primary containment are shown in Fig. 3.

3. Conclusions

Unlike the small sized modular HTGR concept which is designed as an inherently safe reactor the medium sized HTGR has the potential to pose risk to the environment. However, considering the hypothetical severe accidents, the HTGR design has three major safety advantages over the LWR design:

1) The fractional fission products release to the environment is smaller by at least two orders of magnitude.

2) The long term nature of fission product release to the atmosphere, leads to dispersal over wider areas and causes a significant decrease of the individual risk.

3) A longer time period between the beginning of the accident and the initial massive release of fission products from the fuel. Due to this time period the radioactive decay would diminish the short lived radionuclides. In addition taking advantage of this time by preparing countermeasures to be actuated once an accident occurs, could significantly decrease the risk.

REFERENCES

1. "The DSNP User's Mannual Dynamic Simulation for Nuclear Power Plants", Vol. II, Rev. 4.3, RASG-112-90, Soreq NRC (1990).

2. H. Nabielek, W. Schenk, W. Heit, A.W. Mehner and D. Goodin, "The Performance of HTR Fuel Particles at Extreme Temperature", Nuclear Technology, Vol. 84 (1989).

3. R. Moormann, N. Iniotakis, H. Barthels and S. Ron, "Gaseous Releases Acting as Driving Force to Sweep Fission Products from the Primary Circuit Following Core Heat-Up Accident in Medium Sized HTGRs", Trans., Israel Nuclear Societies , Vol. 15 (1989).

4. E. Hoinkis, "The Volume of Small Micropores in Unmodified Oxidized or Irradiated Graphite Matrix", Characterization of Porous Solids (1988).

5. W. Rehm, J. Altes, G. Breitbach, R. Nabbi and K. Verfondern, "Safety Analysis of Small and Medium HTRs under Core-Cooling Accident Conditions", IAEA-TECDOC-358, Oak- Ridge (1985).

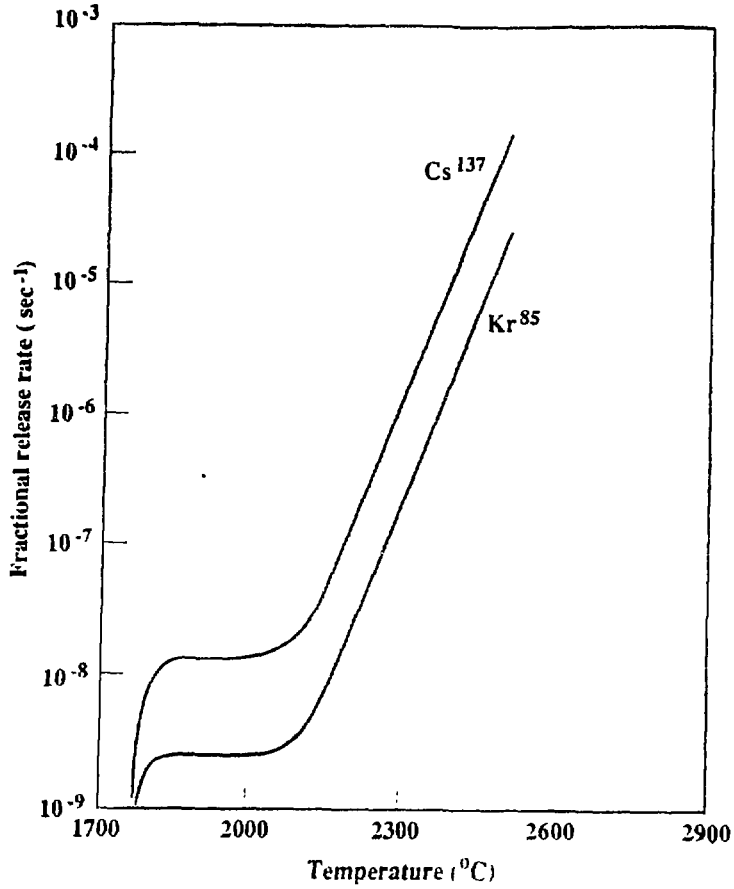

Fig. 1: Fractional temperature dependent release rate

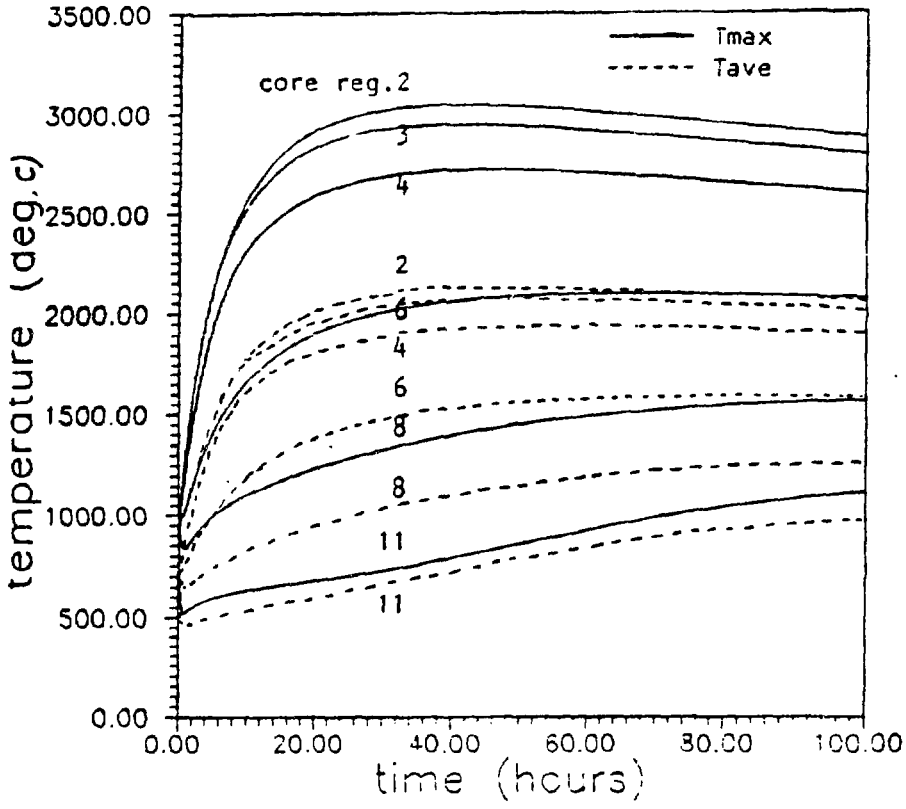

Fig. 2: Core temperatures at different axial regions

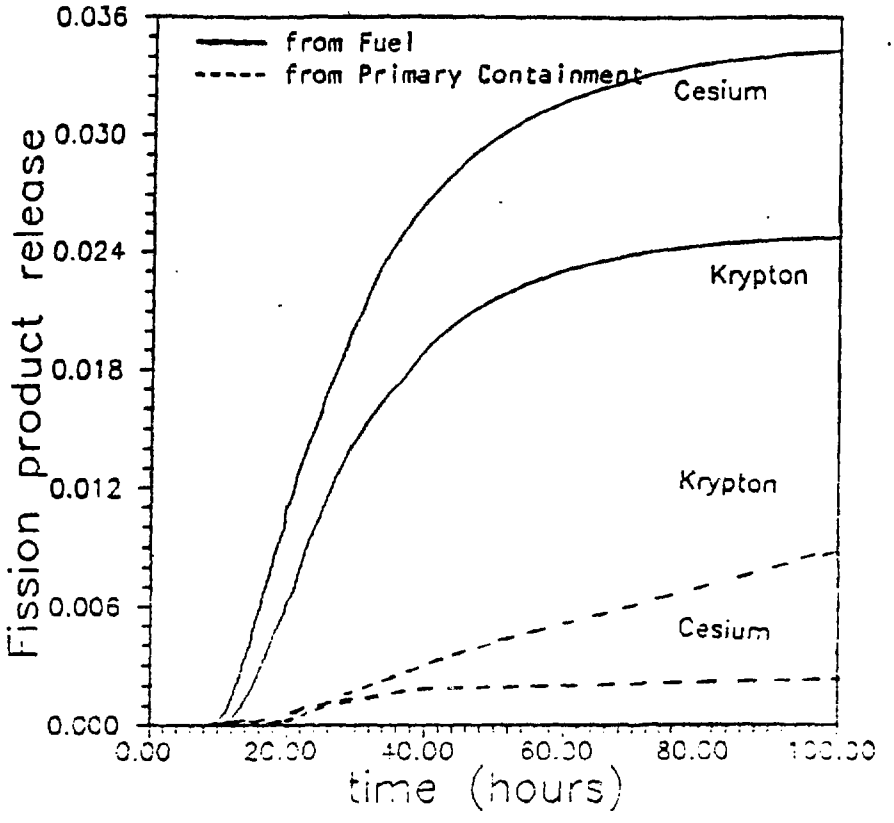

Fig. 3: Fission product release fraction

REACTOR TECHNOLOGY AND SAFETY

Development of the Argentine Nuclear Program

Sara Volman Tanis
Quality Assurance Unit

Israel Electric Corporation Ltd, P.O.B. 10, Haifa 31000, Israel

Argentine has carried out big efforts towards her nuclear development to strengthen her national autonomy. Under these perspective the nuclear plan, employing the country's own technical resources, acquired and evolved during the last forty years those technologies which should insure the national independence.

The Argentine Atomic Energy Commission (CNEA) is the only organization that conducts nuclear activities in the country and has utilized them as the fundamental tool to achieve capacity in the most vital fields to allow the development in three directions:

1. Through a nuclear power plant construction program that should avoid a shortage in the electric power supply that could hinder the country's growth.

2. By encouraging the independence in the technical and scientific field as a real support for an autonomous nuclear industry.

3. The development of components, special techniques and supplies, starting from research, through the erection of pilot plants, and up to industrial plants with appropriate technology transfer agreements; to gain autonomy in the provision of nuclear components, erection of parts of the nuclear island, main pipes, preparation of the basic and detail engineering of systems etc.

The 40 years can be divided in four periods. From 1950 till 1958 the basic infrastructure had been prepared in the country with the creation of various national organisms for research and development and to give technical assistance to the local industry. The first experimental reactor was erected with a capacity of 100KW Argonaut type, and other experimental facilities were constructed in this period.

The second period between the years 1958-1967 a reactor for experimental and irradiation purposes was designed and built with a capacity of 5MW, MTR type. CNEA developed also facilities to manipulate with radio isotopes, to fabricate the fuel elements and the local industry was able to provide vessels, tanks, etc.
A pre feasibility study for a NPP was prepared.

The third period covers the years 1967 to 78. The first power plant started operating in 1973 with a capacity of 340 MW. It was a turn-key project but conditioned to maximize the local participation in civil works, supplies and erection works. The total participation arised to 36% of the total price of the plant.

A second project was initiated for a CANDU power reactor with a capacity to generate 600MW (Embalse Nuclear Station). The project was conditioned to a major Argentine participation with a scheme of a turn-key contract.

A few important agreements were signed for the transfer of technologies like engineering of power plants; erection engineering for main piping, components of the nuclear island, etc. The total participation arised to 51% of the total cost of the plant.

The fourth period covers the finalization of the Embalse project, and start commercial operation in 1983. In 1979 a new program was announced for the construction of 4 NPP during a period of 15 years, and also industrial plants for the production of heavy water fuel elements, zircaloy parts, heavy components etc. The first project of this program was named Atucha II with a capacity of gene ration of 700MW approximately. The national participation was planned to arise to 70%.

In the last year this plan was changed and was decided not to construct the other three power plants.

Atucha II was delayed many times by economical problems. To be able to analyze and compare the technical proposals for the NPP projects or other projects CNEA developed systems of evaluation of the bids.

The subjects of main interest in the evaluation covered the possibilities which exist for national participation in:

a) engineering works in the different stages: basic, detail, procurement fabrication and erection;
b) supply of electro mechanical components;
c) erection works;
d) technological accessibility for fabrication of equipment, parts.
e) possibilities of technology transfer from the bidder and related companies;
f) special conditions and limitations to the contract.

A survey of the technical capabilities existing in the country has been done in 1979-80 between 600 industrial and engineering Argentine companies to make a pre-selection and evaluation of the possible suppliers, taking in account the manufacturing capability and quality organization.

Details of bid evaluations conclusions of the survey and the different mechanisms utilized in the technology transfer contracts made by CNEA and her suppliers will be described at the meeting.

AP600 Passive Safety System Modelling Using RELAP5/MOD1

D. Hasan, E. Elias and E. Wacholder
Department of Mechanical Engineering
Technion - Israel Institute of Technology
Haifa, Israel 32 000

A part of the passive safety system (PSS) of the Westinghouse advanced pressurized water reactor AP600 has been modelled using the RELAP5/MOD1 computer program. It consists of an accumulator vessel which injects, via a certain pipework, water straight into the AP600 Reactor Vessel.

RELAP5 is a computer code developed at the INEL (Idaho National Engineering Laboratory) [1]. It is designed to produce "best estimate" predictions of the behaviour of hydrodynamic systems during various transients. It is an advanced, one-dimensional, fast-running system analysis code based on a non-homogeneous, non-equilibrium hydrodynamic model.

The AP600 is a conceptual reactor for which data have been published, e.g., in ref. [2]. In the present work the accumulator pressure was taken as 4.2 MPa(abs) (about 600 psig). The problem analyzed was the opening of a valve feeding the water to the lines leading to the reactor pressure vessel (RPV). The valve opens when the pressure in the lines reaches 3.3 MPa(abs). The results of interest are the pressure transients upstream and downstream of the open valve.

The RELAP5/MOD1 model consists of the following types of components : ACCUMulator, PIPEs, VALVEs, BRANCHEs, SNGLJUNs (single junctions), SNGLVOLs (single volumes), TMDPVOLs (time dependent volumes). There are altogether 27 components and 65 volumes in the model.

Pressure histories for the first 20 milliseconds of transient at various points upstream and downstream of the valve opened are presented in Fig. 1. One of the points shown in Fig. 1 upstream of the valve is the accumulator itself, which for the short period of 20 milliseconds remains at a virtually constant pressure. In trial runs for extremely long periods (not presented here) the accumulator pressure decreases until it approaches the RPV pressure. Another point shown in Fig. 1 is located just upstream of the valve. This point experiences a rapid pressure decrease from 4.2 MPa to 3.65 MPa within 2 milli- seconds, and then rises (with an overshoot of about 0.1 MPa) until it approaches a pressure close to that of the accumulator. The points downstream of the valve experience initially a sharp increase in pressure, from 3.2 MPa to about 3.5 - 3.6 MPa, depending their distance from the valve. This increase coincides with the pressure decrease of the upstream point. Afterwards this increase becomes more gradual, until the whole pipeline is at nearly the same pressure, with the pressure differences determined by the pressure drop along the pipe due to friction losses.

ACKNOWLEDGEMENT This work was partially supported by the Israel Electric Corp.

References

[1] V.H. Ransom et al., RELAP5/MOD1 Code Manual, NUREG/CR-1826, EGG-2070, March 1982, EG&G Idaho Inc., Idaho Falls.

[2] S.N. Tower, T.L. Schulz and R.P. Vijuk, Passive and Simplified System Features for the Advanced Westinghouse 600 MWe PWR, Nucl.Engn.Des. 109 (1988), 147 - 154.

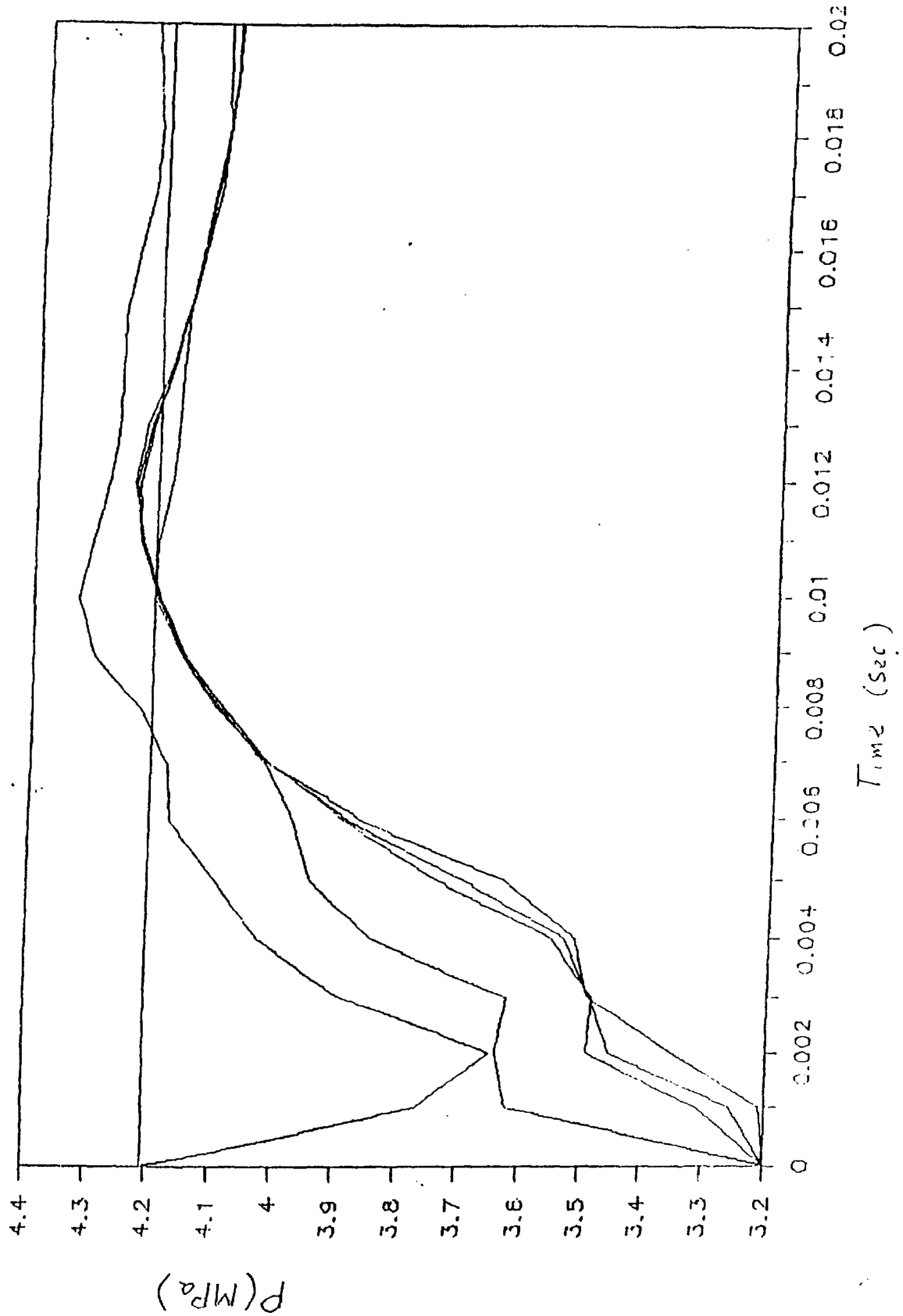

Figure 1 : Pressure Histories of an AP600 PSS Line

RELAP4/MOD6 Model for the AP600 Reactor Coolant System

D. Hasan, E. Elias and E. Wacholder
Department of Mechanical Engineering
Technion - Israel Institute of Technology
Haifa, 32000 Israel

A model of the reactor coolant system (RCS) of the Westinghouse advanced pressurized water reactor AP600 has been prepared. The model has successfully been used for the analysis of the early stages of a loss of feedwater anticipated transient without scram (LOFW ATWS) with the RELAP4/MOD6 computer program [1].

The subject of advanced light water reactors (ALWRs) has previously been addressed in the Israeli context [2]. The present work adds some quantitative results by computer modelling performed for this reactor concept.

RELAP4/MOD6 has previously been used by the authors for the analysis of some of the presently available commercial light water reactors (LWRs) [3, 4]. The long range objective of this work is to obtain quantitative safety evaluation of ALWRs, which can readily be compared to similar results obtained for LWRs.

The geometrical model was based on the schematic description of the AP600 shown in Figure 1. Information related to the dimensions and deployment of the various systems was obtained from various sources in the open literature, such as [5]. The model was graphically implemented in a "volumes" and "junctions" model for RELAP4, both for the RCS and for the passive safety system (PSS), as shown in Figure 2. At this phase of the work, the model which was used as input for RELAP includes only the AP600 RCS elements. The PSS response will be modeled in future phases of the project.

ACKNOWLEDGEMENT This work was partially supported by the Israel Electric Corp.

References

[1] S. R. Fischer et al., "RELAP4/MOD6: A Computer Program for Transient Thermal-Hydraulic Analysis of Nuclear Reactors and Related Systems", CDAP-TR-003, EG\&G Inc., 1978.

[2] A. A. Kidron, I. Kiss and D. Marouani, " The Small US ALWR Review and Considerations from an Israeli Viewpoint", Trans. Israel Nucl. Soc. 15 (1989).

[3] S. Kaizerman, S. Pryluk, E. Elias, E. Wacholder and D. Hasan, "Investigation of Thermal-Hydraulic Transients in a 3 Loop PWR Using RELAP4/MOD6", Trans. Israel Nucl. Soc. 1 (1979).

[4] D. Hasan, S. Kaizerman, E. Elias and E. Wacholder, "PWR Loss of Feedwater ATWS Analysis Using the RELAP4/MOD6 Code", Trans. Israel Nucl. Soc. 14 (1987).

[5] S. N. Tower, T. L. Schulz and R. P. Vijuk, "Passive and Simplified System Features for the Advanced Westinghouse 600 MWe PWR", Nucl. Eng. Des. 109, 147-154 (1988).

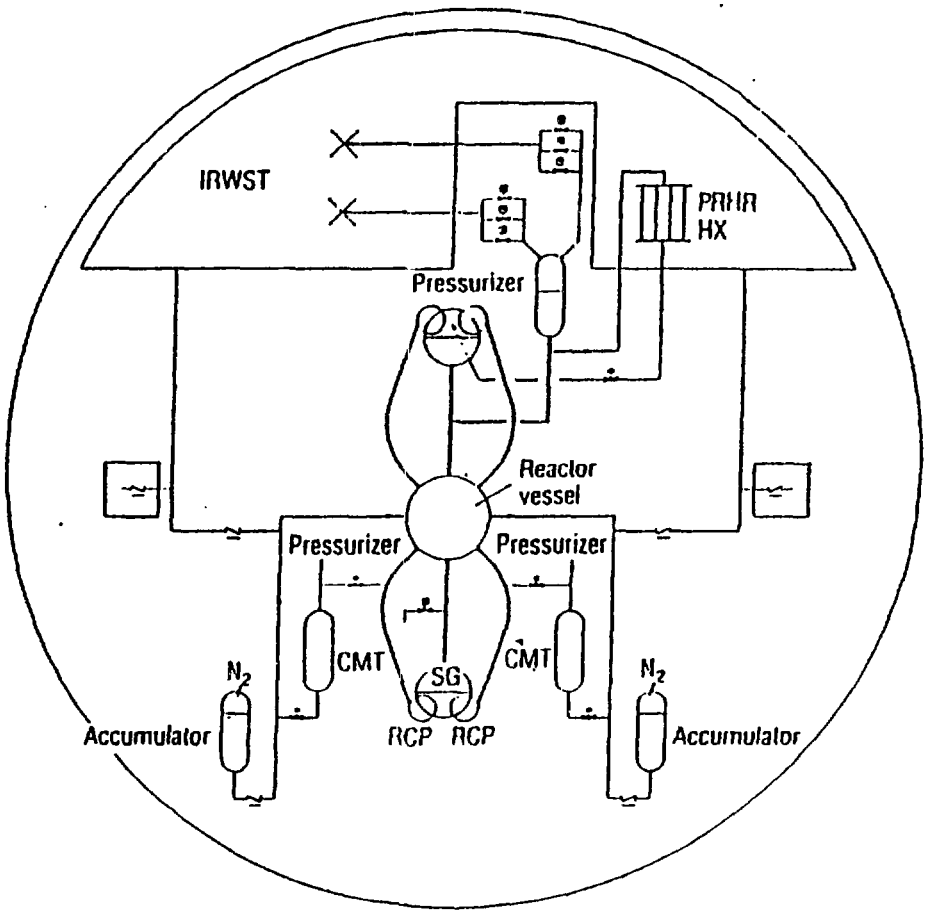

Figure 1 AP600 Reactor Schematic

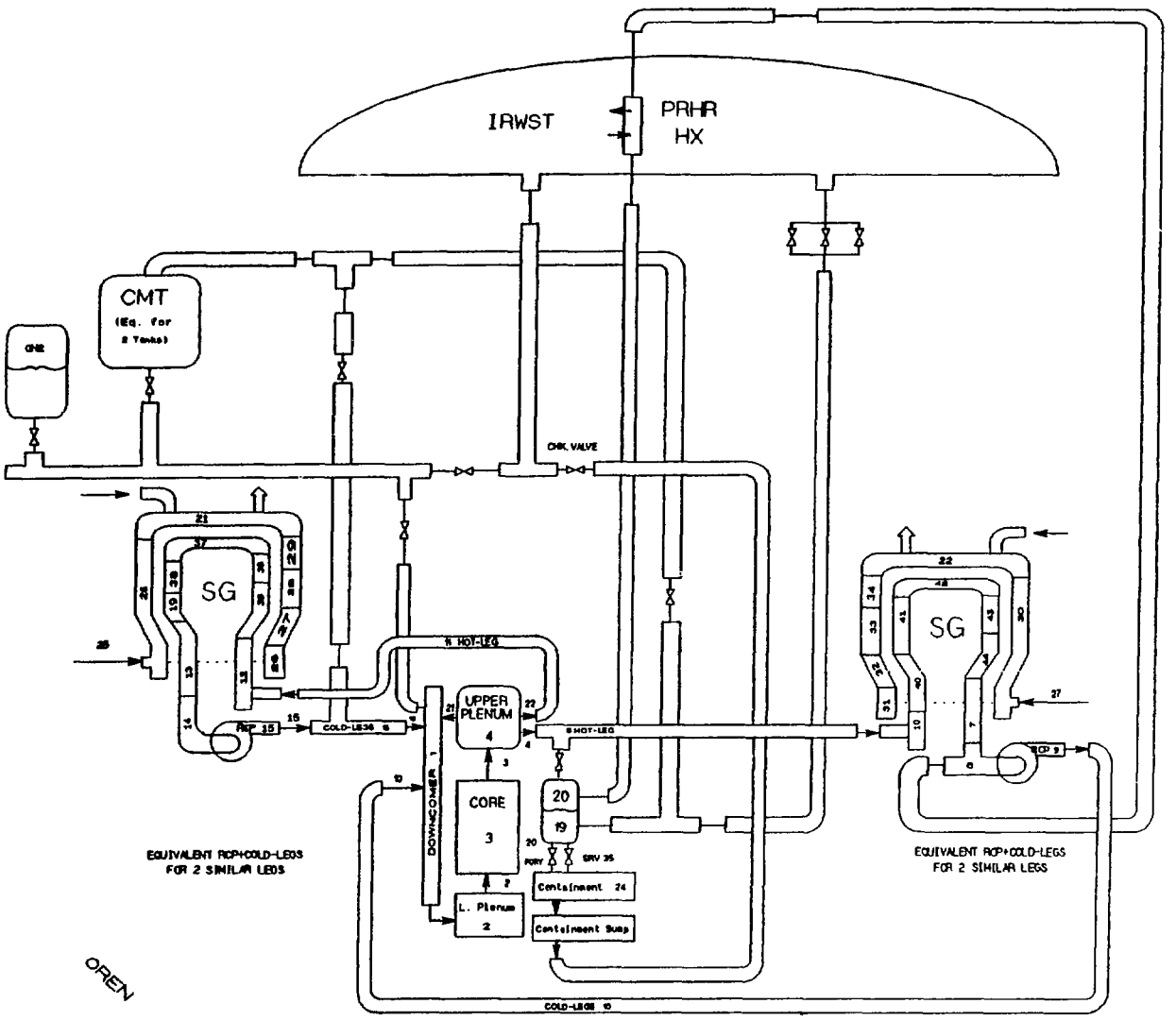

Figure 2 AP600 System Nodalization for a LOFW ATWS Analysis with RELAP4/MOD6.

A PARAMETRIC SURVEY OF SEVERE ACCIDENT CONSEQUENCES FOR A MEDIUM-SIZED ADVANCED-TYPE REACTOR

M. Rambam, L. Reznik and L. Tepper
Nuclear Engineering Department
Israel Electric Corporation

The first nuclear power plant in Israel will probably belong to a new generation of reactors. Different design concepts are currently being studied, such as the ALWR and the HTGR. It is widely accepted that a new type of reactor will possess some passive safety features, such as low power density (compared to current commercial reactors) and smaller total power. In the highly improbable case of a severe accident, these safety features should assure lower off-site release fractions for most of the radionuclides, as well as lower release rates.

Since IEC has selected the Shivta site in the Negev as a site for a future NPP, it is thought necessary to perform parametric studies of severe accident consequences for a medium-sized reactor of the above mentioned advanced type, located at Shivta. Examination of some of the important characteristics of the existing conceptual design of advanced medium and small size reactors, allows making a number of assumptions regarding power level, isotopic core inventory and accident release parameters such as heat rate and leakage fractions. The values chosen are therefore more a result of engineering judgement than that of exact calculations. However, they are consistent with parameters reported in the literature.

The aim of the study was to identify and analyze the various modelling parameters for site release and its consequences. CRAC2 [1] was chosen for this purpose, as there is considerable experience with this code at IEC [2,3].

The computer model CRAC (Calculations of Reactor Accident Consequences) was developed for the purpose of assessing population risks in the event of a major reactor accident resulting in significant atmospheric releases of radioactivity. The consequences from such a release can range from slight to catastrophic, depending upon the following key elements:

1. Amount of radioactive material released to the atmosphere and release sequence.
2. Meteorological conditions following the release.
3. Number of people exposed to the contamination and path of exposure.

Most CRAC2 studies (or other versions such as CRACIT) were performed for plants located in densely populated areas, such as Zion [4] or Indian Point. In contrast, the relatively large distances from Shivta to population centers in Israel, leads to changes in the relative importance ranking of the various CRAC2 models depicting processes of radioactive release, atmospheric transport and health effects.

For example, the impact of initial plume buoyancy rise height on the estimation of consequences for plant staff and near-by population is totally different from that which obtains for inhabitants of cities located 20 or 30 km away.

Initial plume rise height: the calculation in CRAC2 is done according to the Briggs method:

a) for stable atmospheric conditions

$$h_{init.stable} = 2.6*[3.7*10^{-5}*Q*\bar{u}*s]^{1/3} + h \qquad (1a)$$

b) for unstable and neutral conditions

$$h_{in.unstable} = 1.6*[3.7*10^{-5}*Q*X^2]^{1/3}*\bar{u}^{-1} + h \qquad (1b)$$

where $X = 2.08*[3.7*10^{-5}*Q]^{2/5}*h^{3/5}$

Q = sensible heat rate of release

$\bar{u}$ = wind speed
s = stability index
h = building release height

Lateral plume dispersion: calculated according to the Gaussian model in terms of the relative concentration C

$$C(y) = [2\pi*\sigma_y(x)]^{-1/2}*\exp\left[-\frac{y^2}{2\sigma^2_y(x)}\right] \qquad (2)$$

where x and y are the geographical coordinates related to the center of release. The dispersion coefficient $\sigma_y(x)$, dependent on the atmospheric stability conditions, is determined using Pasquill-Gifford curves [5].

Duration of release T: This is taken account of in CRAC2 by introducing a correction in σ_y for a prolonged release (compared to a "puff" release of 3 minutes):

$$\sigma_y(T) = \sigma_y(3\ min)*\left[\frac{T}{3\ min}\right]^a \qquad (3)$$

where $a = 0.2$ for $3\ min < T < 60\ min$

$a = 0.25$ for $60\ min < T < 600\ min$

Examination of equations (1) to (3) suggests the need for a sensitivity analysis of CRAC2 results regarding parameters such as plume heat rate Q and duration of release T.

In addition it is interesting to assess sensitivity to other parameters, such as effective inversion height and effective radiation shielding factors. The effective inversion height (Holzworth afternoon mixing height) is related to the meteorological conditions prevailing at the time of release and subsequent atmospheric transport. The effective radiation shielding factors in CRAC2 represent any measures taken in order to mitigate the consequences for population centers located at remote distances from the site.

The output parameters chosen for this survey include early and latent health effects and equivalent whole body dose levels. Although not in the scope of this work, CRAC2 may also be used for analyzing other accident consequences, such as the need for evacuation, loss of property due to contamination or need for decontamination measures.

Results of the study will be reported at the meeting. It will be seen from these results that the following are among the most important parameters:

1. Duration of release: There is a clear indication that a reactor with a hypothetical accident sequence in which the release is of long duration carries a significant advantage [in terms of accident consequences] over a reactor in which the anticipated release is of the short "puff"-type.

2. Effective inversion height: Meteorological parameter which should be carefully monitored.

3. Radiation cloud and ground-shine shielding factors: The results indicate that hypothetical accident consequences can be significantly mitigated with relatively simple emergency management procedures.

References

[1] Ritchie, Johnson and Blond, "Calculations of Reactor Accident Consequences Version 2, CRAC-2", SAND 81-1994 (NUREG/CR-2326), 1983.

[2] Aminpour, Gutman, Reznik and Tepper, "A Comparative Population Risk Study of the Consequences of a Severe Accident in a NPP at Various Sites in Israel", report IEC NED-T-150, 1983.

[3] Rambam, Reznik and Tepper, "Sensitivity Analysis of CRAC-2 Results", Transactions of the 14th Annual Meeting of the Israel Nuclear Societies, 1987.

[4] Pickard, Lowe and Garrick, Inc., "Zion Probabilistic Safety Study", 1981.

[5] Turner, "Workbook of Atmospheric Dispersion Estimates", Publ. 999-AP-26, US EPA Office of Air Programs, 1970.

Thermal Recovery of Lattice Constant and Strain in Naturally–Damaged $(Th, U)O_2$

Ram Evron*, Giora Kimmel+ and Yehuda Eyal‡
* Department of Nuclear Engineering
+ Department of Materials Engineering
‡ Department of Chemistry
Technion – Israel Institute of Technology
Haifa 32000, Israel

One of the prominent options considered for long-term disposal of spent nuclear reactor UO_2 and future ThO_2 fuels is direct burial of unreprocessed burnt fuel elements in deep underground repositories[1]. A potential hazard associated with burial of radioactive wastes in geologic strata is leaching of the contained radionuclides by groundwater and their subsequent transport and dispersion by the water flow. Moreover, there is concern that accumulation of radiation damage, caused by the intense radioactive decay within the waste, will significantly increase the leachability of the wasteforms[2,3]. Of particular importance is the atomic displacement damage created by nuclear stopping of energetic particles.

Radiation damage in reactor-irradiated UO_2 and ThO_2 fuels is relatively minor[4–8]. Even at high burnup, the only structural effect observed is a slight lattice expansion ($\sim$0.1% for both UO_2 and ThO_2 (Refs. 4-8)) and a slight lattice strain ($\sim$0.16% for UO_2 (Ref. 4)). On removal from the reactor, however, the material may accumulate higher levels of surviving atomic–displacement damage. First, the temperature of the fuel rod decreases gradually. As a result there is a decreasing tendency for recovery of the damaged lattice by diffusion. Second, there is an important change in the source of the damage. Whereas the main source of damage during reactor irradiation is due to fission events, the major source of damage in spent fuel is expected to be due to alpha decay of actinides, which produces $\sim$100 keV heavy alpha-recoil atoms.

The present investigation is concerned with long-term radiation effects from alpha decay in ancient specimens of the mineral thorianite, $(Th, U)O_2$. The mineral has been subjected, since its formation, to radiations from the decay of ^{232}Th, ^{238}U, ^{235}U and their many intermediate decay products, and may be considered, therefore, as natural analog of UO_2 and ThO_2 wastes. Two thorianite specimens were studied, both from Sri Lanka (specimen T3, obtained from Professor A. Pabst (specimen described in Ref. 9), and thorianite T4, obtained from the Smithsonian Institution (NMNH no. 96863)). The specimens were assemblies of nearly-perfect cubes (typical volume 3x3x3 mm^3), shown by X-ray diffraction to be single crystals with faces parallel to the {1 0 0} planes of the fluorite structure. From these assemblies, a single cube of mineral T3 and a single cube and an assembly of five cubes of mineral T4 (samples T4(1) and T4 (2), respectively) were

ground separately by mortar and pestle to fine powders (mean particle diameter $\sim 1\mu m$) that were subjected to separate examinations. This approach presents an advantage over a recent study[10] that involved a thorianite powder prepared from a batch of a large number of impure and perhaps slightly dissimilar mineral particles. For the present three samples, the abundances of Th and U were determined by radiochemistry and alpha spectrometry[3] and the concentration of Pb by a polarographic method. The analyses revealed essentially pure $(Th, U)O_2$ except for radiogenic lead. The abundances are ~ 64 wt% (weight percent) ThO_2, ~ 32 wt% UO_2 and ~ 4 wt% PbO. From this composition the age of the specimens is 550 Myr, which suggests a cumulative radiation damage of ~ 170 displacements per atom. The minerals must display, therefore, equilibrated levels of defect concentration.

Samples T3 and T4(1) were repeatedly X-rayed and isochronally annealed in air at 50°C intervals (sample T4(1)) or 200°C intervals (sample T3) from room temperature to 1000°C. Sample T4(2) was divided into two portions which were X-rayed each after each of two successive high-temperature anneals. One portion was isochronally annealed in air at 1000°C and 1200°C. The second portion was similarly isochronally annealed in pure argon atmosphere. Annealing was performed in an electric furnace. The samples were brought up to temperature in ≤ 50 minutes, held at temperature for 60 minutes, then allowed to cool freely to room temperature.

The X-ray diffraction measurements were performed with the aid of a Philips diffractometer, employing Cu K_α radiation. Tungsten metal, used as sample holder, served as an internal standard for angle calibration. At least seven diffraction maxima were examined for each annealing treatment for their lattice spacings and peak profiles.

All X-ray diffractograms indicated the presence of highly-crystalline ThO_2/UO_2 solid solutions. There was no evidence in the diffraction patterns (minimum detectable concentrations of roughly 1 wt%) for the presence of crystalline phases other then thorianite in the powder before and after annealing. The presence of certain amounts of bulk U^{6+} cannot be ruled out by the diffraction data; solid UO_{2+x} with $x \leq 0.25$ possesses the fluorite structure. The lattice constant for pure undamaged ThO_2, UO_2 and $UO_{2.25}$ are 0.5600, 0.5468 and 0.5441 nm, respectively. Considering the unknown role of Pb in the thorianite structure[11], the measured lattice constant (see below) was reasonably given by Vegard's law.

The isochronal recovery of the lattice constant for thorianite T4(1) is shown in Fig. 1. Similar results were obtained for specimen T3. As shown in Fig. 1, the lattice constant after annealing in air at 1000°C is 0.5530 ± 0.0001 nm. For sample T4(2), the values of the lattice constant after annealing in air at 1000°C and 1200°C were 0.5531 and 0.5530 nm, respectively, and after annealing in argon at 1000°C and 1200°C were 0.5531 and 0.5532 nm, respectively (uncertainties are ± 0.0001 nm). All five values coincide within the experimental error. These results have two important implications. First, the similarities between the air-anneal and argon-anneal data indicate that no oxidation of bulk U^{4+} to U^{6+} has occurred during heating of the mineral in air. Therefore, the entire contraction

of the lattice constant during heat treatments may be attributed solely to annealing of radiation damage. Second, the similarity between the results of the 1000°C anneals and the 1200°C anneals suggests that all recovery processes that significantly contribute to annealing of radiation damage at 1000°C are essentially complete after heating to 1000°C for only 60 minutes.

The recovery of the lattice constant exhibited three stages, during each of which roughly one third of the overall recovery occurred (Fig. 1). The stages were terminated at ~200, ~600 and ~ 1000°C. Very similar three isochronal recovery stages were observed in alpha-irradiatedUO_2 single crystals[12] and in fission-damaged UO_2 single crystals[6]. The recovery stages are occurring probably as a result of the migration and annealing of individual lattice defect species (interstitial atoms and vacancies in both the cation and anion sublattices) by recombination, clustering and annihilation at sinks, as well as a result of inert-gas release (helium gas from alpha-particle bombardment or internal alpha decay and krypton and xenon from fission). Discussions of possible mechanisms associated with given concrete recovery stages are presented in Refs. 12 and 13.

Although it appears that the recovery of the lattice expansion occurs by similar mechanisms independent of the nature of the source of the atomic-displacement damage, the magnitude of the lattice expansion in fission-damaged UO_2 and ThO_2 (Refs. 4-8), in $(Th,U)O_2$ damaged from alpha decay (present study) and in alpha-irradiated UO_2 (Ref. 14) is considerably different. The present experiment shows (Fig. 1) that the overall expansion of the lattice due to irradiation from alpha decay is ~0.5%, which is a factor of ~5 greater than the maximum lattice dilatation observed for reactor-irradiated UO_2 and ThO_2 (refs. 4-8). The expansion of the lattice constant in alpha-irradiated UO_2 is ~0.8% (Ref. 14). The above trend has been predicted by Weber[14], and accounts for an expected decreasing rate of defect annealing with decreasing density of Frenkel defects created by a single primary damage-producing particle[14,15].

Isochronally-annealed lattice strain and crystallite size for specimen T4(1), obtained from analyses of line broadening, are displayed in Figs. 2 and 3, respectively. The analyses were based on the Williamson and Hall model[16]. For these determinations, the measured line profiles were corrected for instrumental broadening by using as reference a measured diffractogram of highly-crystalline Al_2O_3 powder.

As shown in Fig. 2, the strain in untreated T4(1) was 0.31 ± 0.04 percent, which is about twice than the strain measured in reactor-irradiated UO_2 (Ref. 4). The strain was reduced gradually with increasing annealing temperature, and reached a value of 0.14% after annealing at 1000°C (Fig. 2). The recovery of strain by heating is fully consistent with annealing of radiation damage. However, the reason for incomplete recovery of strain after annealing at 1000°C is not clear. Longer annealing periods and perhaps higher temperatures may be required for complete recovery. It should be noted that residual line broadening may also result from possible small fluctuations in the relative ThO_2/UO_2 concentration distribution in the mineral.

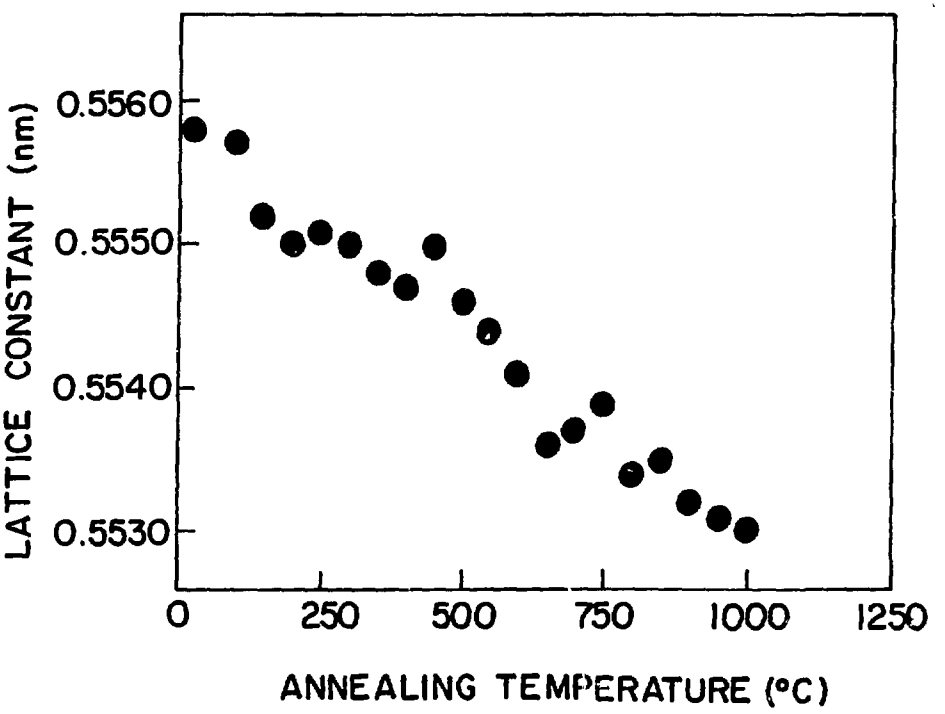

Figure 1. Lattice constant for thorianite T4(1) isochronally annealed in air. The experimental uncertainty is ±0.0001 nm and displayed by the size of the symbol.

The mean crystallite size in sample T4(1) was about 60 nm throughout the experiment (Fig. 3). In contrast to the behavior of unit cell parameter and strain, there was no evidence for any crystallite size change as a result of heat treatment.

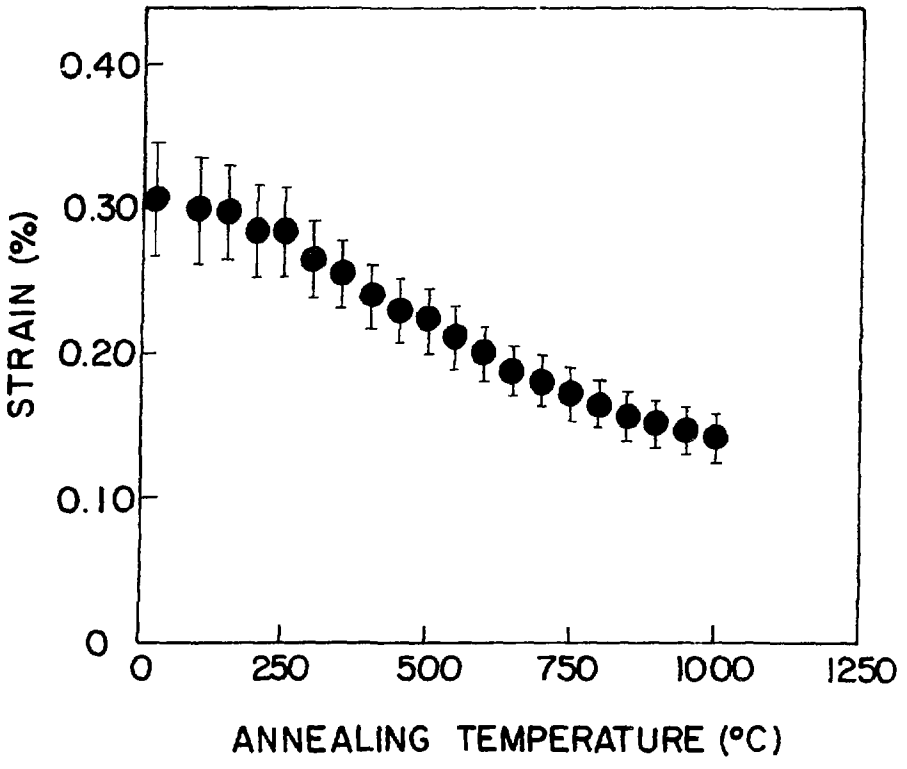

Figure 2. Lattice strain for thorianite T4(1) isochronally annealed in air.

In summary, alpha-decay events within a natural $(Th, U)O_2$ phase are observed to induce significantly higher lattice defect concentration and strain than previously observed for fission damage in UO_2 and ThO_2. These observations have practical implications in selecting the appropriate radiation damage source to simulate long-term self-irradiation effects in Np-, Pu-, Am-, and Cm-containing UO_2 or ThO_2 wastes.

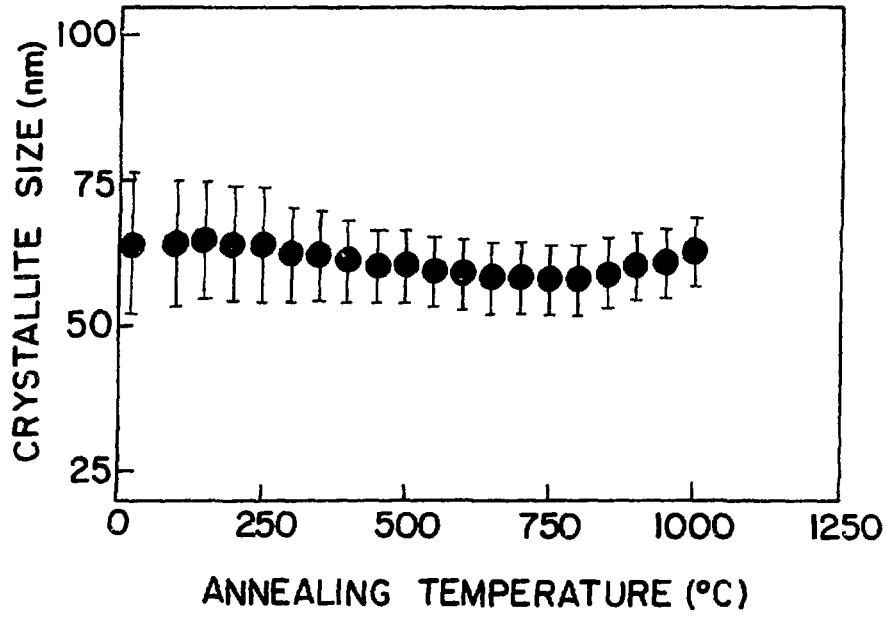

Figure 3. Crystallite size for thorianite T4(1) isochronally annealed in air.

We are grateful to Professor A. Pabst and to the Smithsonian Institution, Washington DC, USA, for providing thorianite specimens, and to Professor Ch. Yarnitzky for performing the lead analyses.

Quantitative Measurements in Precursory Cooling Regime During Bottom Reflooding

Y. Barnea and E. Elias
Department of Mechanical Engineering
Technion - Israel Institute of Technology, Haifa 32000, Israel
I. Shai
Department of Mechanical Engineering
Ben-Gurion University, Beer Sheva, Israel

Introduction

The Emergency Core Cooling System (ECCS) in water cooled reactors is activated during accident when the water level reaches the bottom of the core. In a Loss of Coolant Accident (LOCA) the activation of the ECCS marks the beginning of the reflooding phase of the accident. The fuel rods in this phase are initially at high temperature which prevents direct contact with the liquid. Later, a wetting patch is established and progresses along the rod forming a moving rewetting front. The progression of the front removes the heat from the hot surface by several heat transfer mechanisms such as axial conduction in the cladding and convection and radiation to the coolant (Fig. 1).

A large number of experimental programs have been conducted worldwide to investigate the thermal-hydraulic aspects of the reflooding phenomenon [1]. In this study, single tube experiments were conducted, at the heat transfer laboratory of the Negev Nuclear Research Center, to obtain information on the different modes of heat transfer and hydrodynamic processes which occur during the reflooding of a hot surface. The experimental setup was described previously [2]. This paper presents the test procedure and typical results.

Test Procedure

In a typical experiment the test tube was electrically heated to a predetermined temperature while keeping the system in an inert (Ar gas) or steam environment. The test was initiated by turning the power off and simultaneously injecting water at the bottom using a constant head pump. The following data was recorded as a function of time during each experiment:

1. Temperature at 12 different axial and radial positions along the test section.
2. Temperature at 5 axial positions in the annular coolant passage.
3. Time variation of the void fraction measured at a fixed level by a specially designed γ-ray densitometer.
4. Pressure differences along the coolant flow channel.
5. Flowrates of the inlet water, the exit steam and the liquid carryover.
6. Inlet and exit water temperatures and exit steam temperature.

Data collection was performed by a fast data acquisition system. A total of 26 data channels were scanned and A/D converted every 18 msec using a microcomputer with an electronic board card (LABMASTER TM-40). The raw data was converted off-line into engineering units for further processing.

The experimental program covered the range of parameters of interest in research reactor analysis including five inlet water velocities in the range of 7 to 14 cm/s, six different initial tube temperatures in the range of 350 to 600°C and two different inlet water temperatures, 30 and 60°C . All the runs were performed at atmospheric pressure. A few tests were repeated for consistency checks. Some of the runs were video taped. A total of 46 runs with complete data set are available. Some results are presented and discussed in the next section.

Results and Discussion

The quench front velocity depends on many operational parameters, such as the initial surface temperature, the inlet water flowrate etc. Figure 2 shows the effect on the transient behavior of the wall temperature of varying the inlet water temperature. The two curves in figure 2 represent the surface temperature at a given location along the tube for the same initial temperature and two different inlet water temperatures (30 and 60°C). The sharp drops in the curves correspond to the quenching of the tube at the thermocouple position. It is shown that the tube quenches earlier when colder water is injected, i.e., the quench front velocity is inversely proportional to the inlet water temperature. It is also noted that although the general form of the surface temperature vs. time curves in figure 2 is similar, the quench front temperature (the temperature at the beginning of the sharp drop in the curve) for T_{in}=60°C is somewhat lower than that obtained for T_{in}=30°C .

Figure 3 shows the transient wall temperature at a fixed position along the tube for 4 different inlet water velocities and T_{in}=30°C . The velocities indicated in the figure are nominal initial values which were varied during the tests according to the instantaneous

total pressure in the flow channel. The quench front temperature and the quench front velocity decrease with decreasing the inlet velocity.

Void fraction data combined with temperature transients are shown in figure 4 for 3 different inlet velocities. The void fraction at the quench front can be read from the figure as the void fraction value at the time the temperature curve passes through its sharpest decent. Decreasing the inlet velocity is shown to increase the void fraction at the quench front. This is not surprising since the flow regime at the quench front changes from inverted annular film boiling into an annular regime as the inlet flowrate decreases.

In summary, new experimental results have been presented which combine data related to flow and boiling processes taking place during the reflooding of hot surfaces. The simultaneous measurements of temperature and vapor film thickness presented in this work provide better physical insight into the reflooding problem.

References

1. Y. Barnea "Precursory Cooling during Bottom Reflooding of Hot Surfaces with Subcooled Liquid", D.Sc. Proposal, Technion IIT, July 1986.

2. Y. Barnea, E. Elias and I. Shai "Experimental Apparatus for Quantitative Measurements in the Precursory Cooling Regime during Bottom Reflooding", Trans. Israel Nucl. Sos. Vol 14, III–19 (1987).

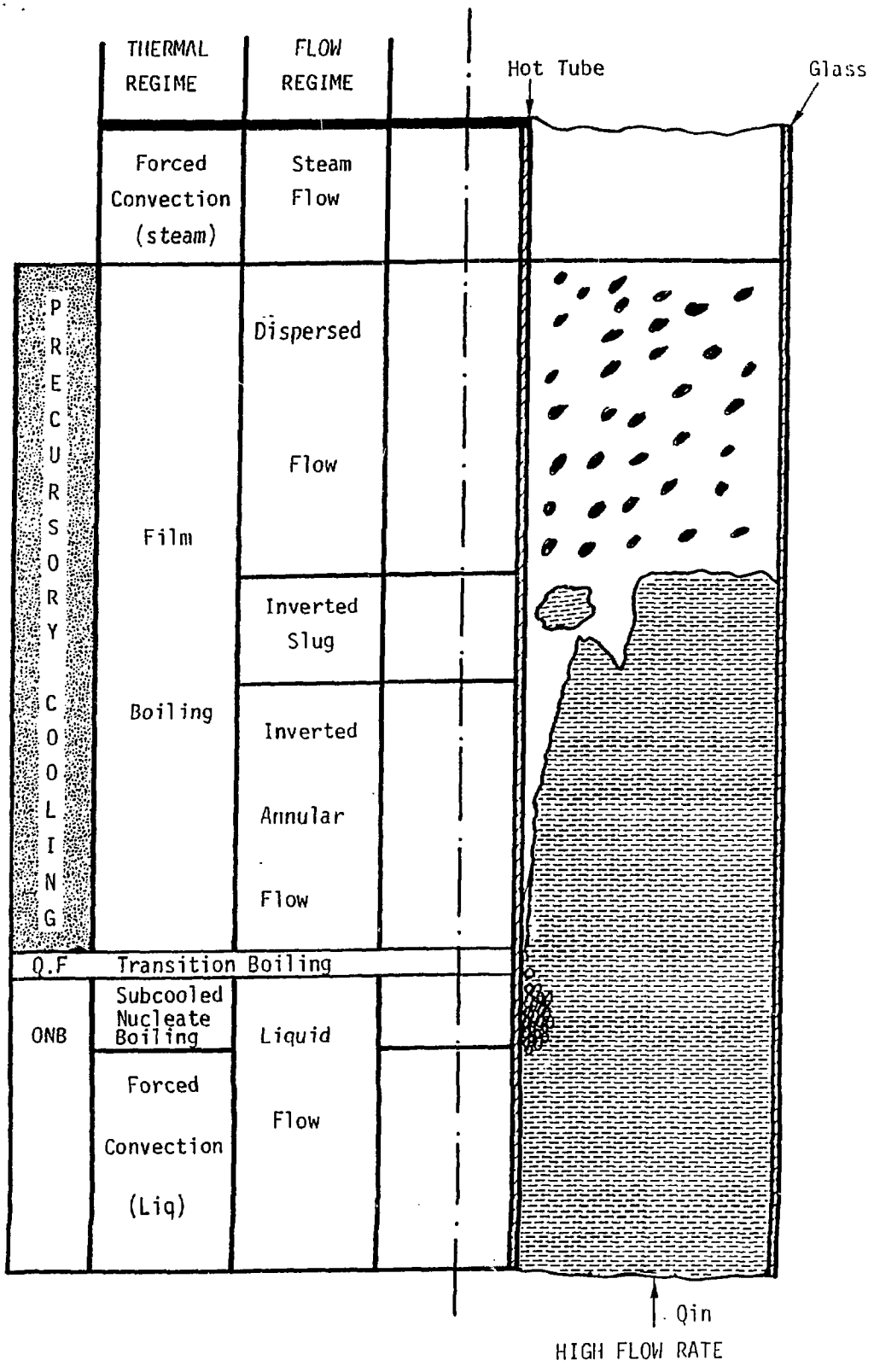

Figure 1 Flow and Boiling Regimes during Bottom Reflooding.

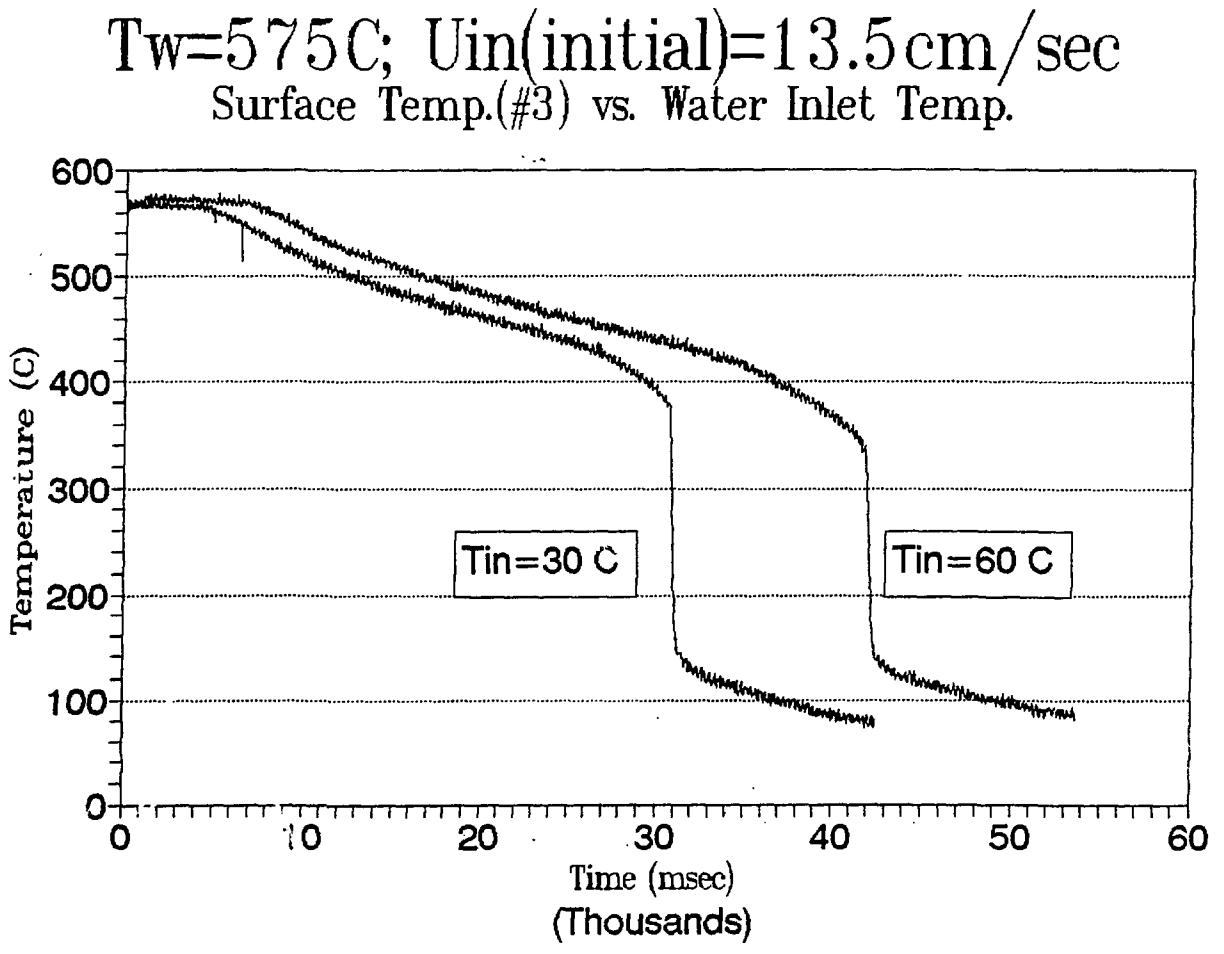

Figure 2 Effect of Water Inlet Temperature on the Surface Transient Temperature.

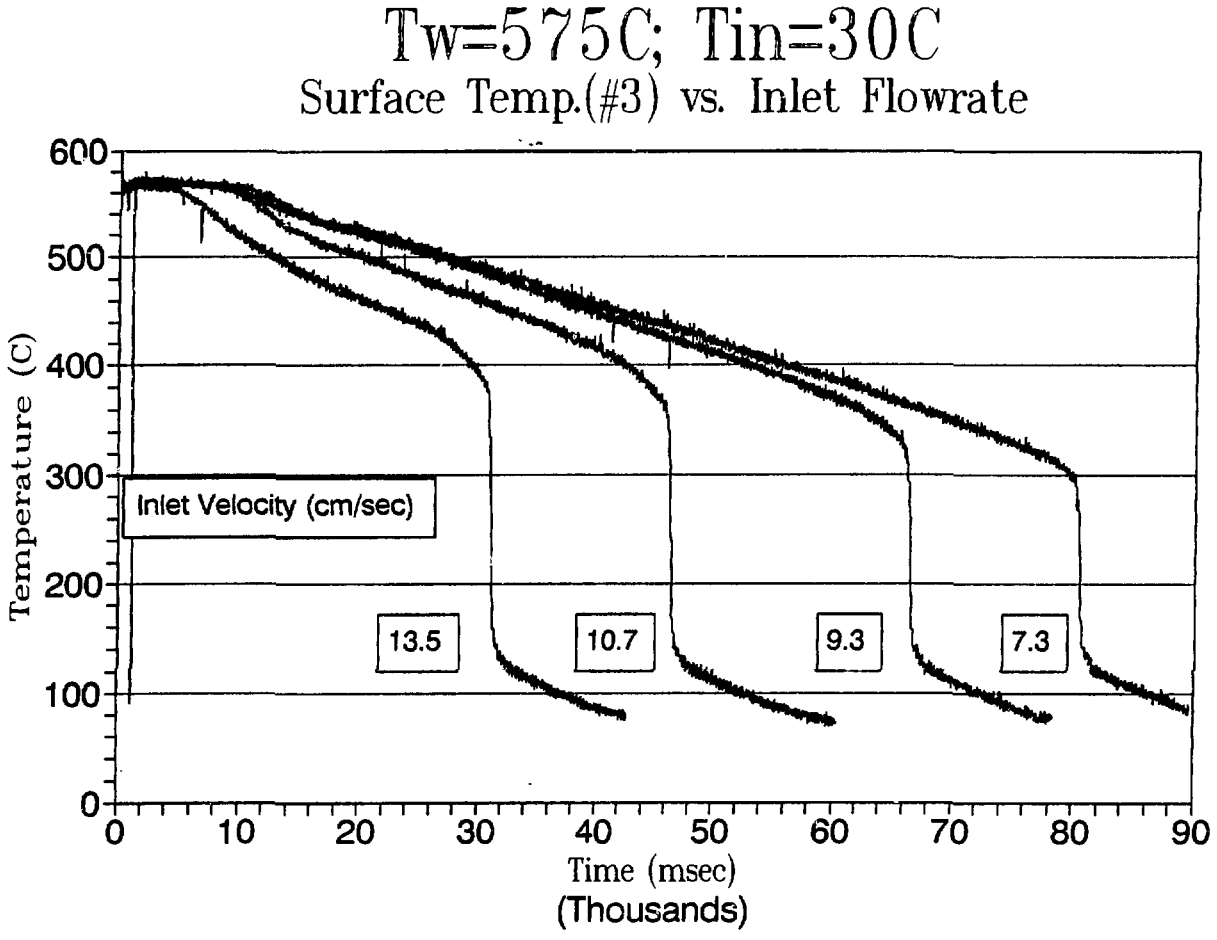

Figure 3 Effect of Water Inlet Velocity on the Surface Transient Temperature.

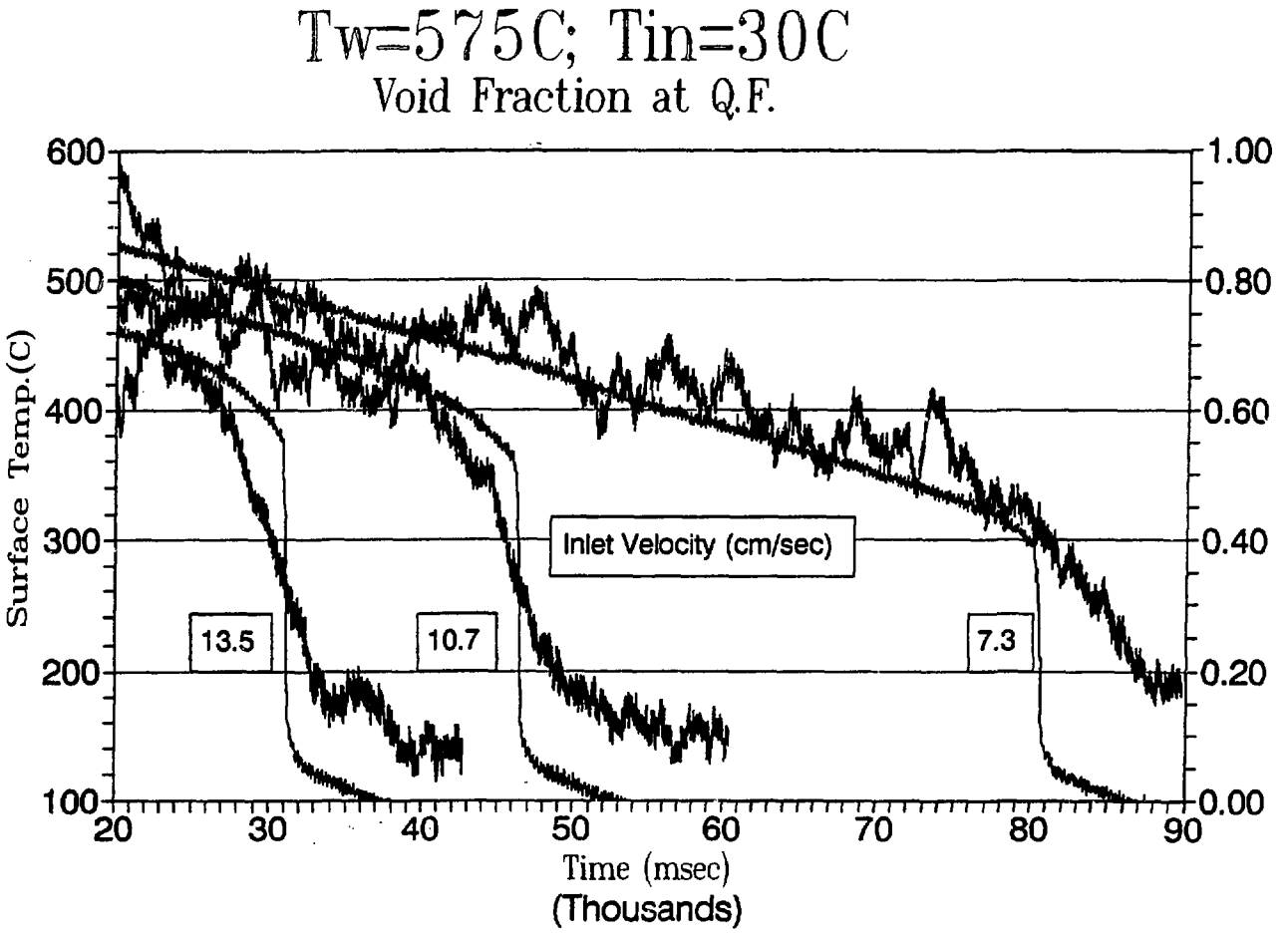

Figure 4 Effect of Water Inlet Velocity on Void Fraction and the Surface Transient Temperature.

DRY AND DRY-WET COOLING FOR POWER PLANTS IN ISRAEL

S. Weiman, A. Kidron and I. Kis
Nuclear Project Department
The Israel Electric Corporation Ltd.

1. INTRODUCTION

The Israel Electric Corporation has been involved, since the mid-seventies, in a continuing effort to introduce alternative cooling method for future Power Plants (Fossil and Nuclear) located inland and in arid areas.

Different technologies were investigated and economic studies were performed in order to establish the applicability of these technologies in Israel.

As a part of this effort, the Israel Electric Corporation Ltd.(IEC) decided in 1984 to install dry and dry-wet cooling test units with the purpose of learning about possible adverse effects of the environment on the heat exchangers in the dry and dry-wet cooling towers.

The purpose of the tests was:

- to identify the possible adverse effects of the specific environmental conditions on the equipment (external corrosion, blockage of the air passages with loes, sand etc.)

- to estimate the effect of deluging/air humidification on the heat exchangers

In addition, it was decided to install thermocouples in the test units in order to estimate the change, with time, in the performance of the heat exchangers.

2. DESCRIPTION OF THE TESTS

The tests were designed to simulate dissipation into the atmosphere of the waste heat, rejected from the Power Plant through the Circulating Water System (Condenser Cooling System), by the means of Dry Cooling (by air) and Dry - Wet Cooling (by air, assisted by water during periods of extremely hot weather).

In 1985, the IEC received three test units from EGI (Hungary) and heat exchangers and accompanying equipment from GEA (Germany).

The test units supplied by EGI feature heat exchangers with aluminum finned coated tubes.

The heat exchangers supplied by GEA were used in the test units designed and fabricated by the Israel Electric Corporation. The heat exchangers incorporate galvanized iron finned tubes.

Assembly and start-up of the test units were performed by the IEC and the first pair of the test units (one EGI and one GEA) was erected at the Ben-Gurion Solar Electricity Technologies Test Center near Sde-Boker in the Negev desert in December 1987. Routine maintenance of the test units was performed by the Test Center operators from the Petroleum Services Ltd. These test units were dismantled in December 1989 upon the completion of the tests.

The second pair of the test units was installed near Ein Haemek in Northern Israel in December 1989. These units are presently in operation.

3. MEASUREMENTS

The following parameters were continuously measured at the test units:

- water temperature at the entrance and at the exit from the heat exchangers
- air temperature in the air humidification tunnel of the German test unit
- ambient air temperature
- ambient air relative humidity
- wind direction and velocity

The measurements were continuously recorded and stored at the Datalogger and were transferred to the IEC for data processing.

This data was used to calculate the Heat Exchanger Effectiveness, used as an indicator of the thermal performance of the heat exchangers.

4. RESULTS

In January 1990, the heat exchangers from Sde-Boker were transferred to the Materials Laboratory of the IEC.

The results of the analysis indicate that the heat exchangers supplied by both manufacturers showed good resistance to environmental corrosion and erosion. The heat exchangers supplied by EGI compared favorably with those supplied by GEA.

The fins of all heat exchangers were covered with dust and sand deposits. The fins with most deposits were the fins from the

internal rows of the heat exchangers supplied by GEA.

The analysis performed at the Mechanical Department of the Technion has shown that there was no significant change, with time, in the thermal performance of the heat exchangers supplied by both manufacturers.

The analysis has also shown that there is no effect of the air humidification (German test unit) on the thermal performance of the heat exchangers.

The effect of the deluging (Hungarian unit) on the thermal performance of the heat exchangers was significant.

Experimental Techniques in Bottom Reflooding of Hot Channels

Y. Barnea, E. Elias
Department of Mechanical Engineering
Technion – Israel Institute of Technology, Haifa 32000, Israel
I. Shai
Department of Mechanical Engineering
Ben-Gurion University, Beer Sheva

A hypothetical loss of coolant accident (LOCA) in water cooled reactors may result in rapid heating of the fuel channels. To prevent the fuel from reaching a metallurgical prohibited temperature, safety systems are available to reflood the core by cold water. The reflooding phase of the LOCA essentially terminates the accident and provides a long term cooling.

Two flow regimes are characteristic during bottom reflooding of a hot channel: the inverted annular flow regime (IAF) and the dispersed flow film boiling (DFFB). These flow regimes, which typically exist downstream of the quench front, provide precursory cooling and enhance the overall heat transfer from the fuel rod. Numerous theoretical and experimental studies were carried out worldwide to investigate the heat and mass transfer mechanisms in the IAF and the DFFB regimes. Many of these studies were reviewed by Elias and Yadigaroglu [1] and more recently by Olek [2]. The main objective of the present work is to obtain quantitative experimental data on some of the less understood transient aspects of the reflooding process, such as the thickness of the vapor layer in IAF and the temperature and velocity of the liquid in IAF.

The present paper describes a few novel experimental techniques and facilities developed for transient two-phase flow measurements during bottom reflooding of hot channels. It concentrates mainly on the detection of void fraction by gamma-ray attenuation, the instantaneous mass balance measurement of the two phases using a phase separator and on a metering device for measuring low vapor flowrate.

The test facility (cf., ref. [3]) consists, basically, of an annular channel with an electrically heated stainless steel tube in the center surrounded by a quartz glass pipe. In a typical experiment, the central tube was heated up to a predetermined temperature at which time water was introduced at the bottom of the annular channel. As the water progressed along the heated tube, complicated flow boiling phenomena took place in the channel resulting in the formation of a two-phase mixture at the channel exit plane (at the top of the flow channel). In order to measure the transient exit flow quality, it was necessary to separate the steam-water mixture without changing its overall composition. An efficient separator was designed and built (see fig. 1) consisting of two concentric cylindrical vessels. The separator was fitted onto the the top of the flow channel such that the exit flow was directed

order to prevent vapor condensation in the separator, the outer vessel was insulated on its outer surface while the inner surface was kept at a temperature slightly above saturation by blowing hot air into the annulus between the two vessels and by auxiliary electrical heating. The two-phase mixture was separated into steam and liquid streams which were measured simultaneously by continuous weighing.

Void fraction and vapor film thickness were measured by the gamma attenuation method. The basic principle of this technique is the experimentally observed fact that the intensity of a collimated gamma beam decreases exponentially as it goes through matter. In a liquid-vapor two-phase flow situation this basic fact can be applied to derive a mathematical relationship between the gamma intensity and the void fraction, α as:

$$\alpha = \frac{\ln (N_o/N)}{\ln (N_o/N_\ell)} \tag{1}$$

where N_o and N_ℓ are the intensities measured in an empty and in a liquid filled channel respectively and N is the measured gamma intensity. If the ln terms in eq. (1) are close to unity, which is true in most cases of interest, the average void fraction relation can be reduced to:

$$\alpha = \frac{N - N_o}{N_\ell - N_o} \tag{2}$$

Figure 2 shows a dual beam densitometer designed for detecting the time dependent void fraction in the test channel. A 300 mCi Am-241 source emitting 60 keV gamma radiation was utilized in the measurement. The source was collimated to produce two narrow beams which pass through the channel close to the heated wall. The intensities of the attenuated beams were measured by two high efficiency 2×2" NaI(Tℓ) detectors. The average count rate obtained was about 4000 counts/sec, which allowed for a rapid and accurate detection of the void fraction in the channel. The directions of the radiation beams and the source and detectors collimators were optimized in order to yield the highest sensitivity to variations in the vapor film thickness at the heated wall. Figure 3 shows the detector response to variations in the air film thickness (used to simulate the vapor film) for four different beam directions. It is shown that the highest sensitivity (largest slope) is obtained when the beam was directed tangential to the heated wall at a relative angle of 15 degrees.

In summary, accurate measurements of basic heat and mass transfer phenomena during the bottom reflooding of hot channels calls for the development of specific experimental techniques. This paper has described some of the methods used for the transient measurement of void fraction, vapor film thickness and exit flow quality during the reflooding of a hot annular channel.

References

1. E. Elias and G. Yadigaroglu, Nucl. Safety 19(2), 160 (1978).

2. S. Olek "Analytical Models for the Rewetting of Hot Surfaces", PSI-Bericht Nr. 17 October 1988.

3. Y. Barnea, E. Elias and I. Shai, Trans. Israel Nucl. Soc. 14, III-19 (1987).

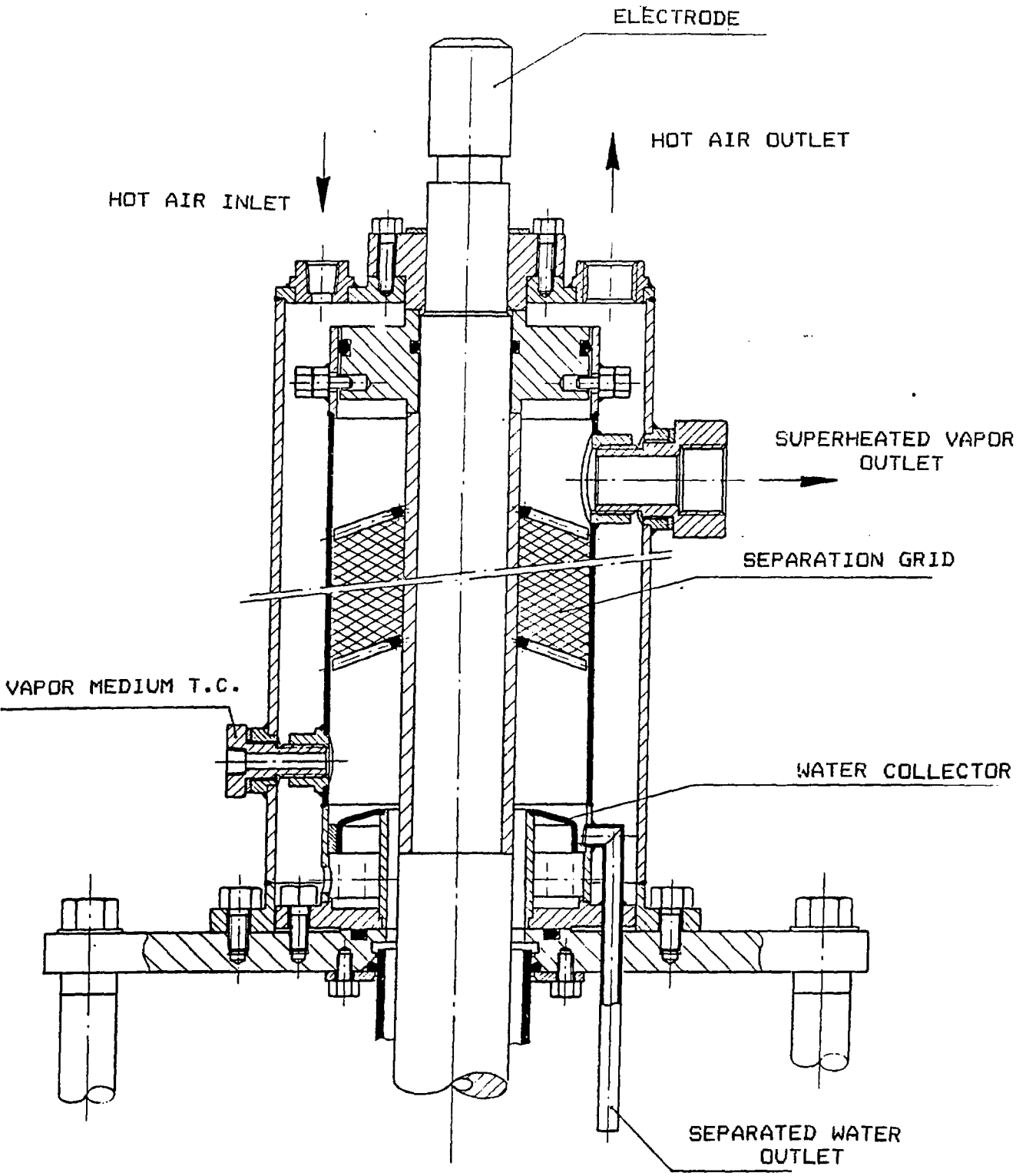

Fig.1 Two-Phase flow separator.

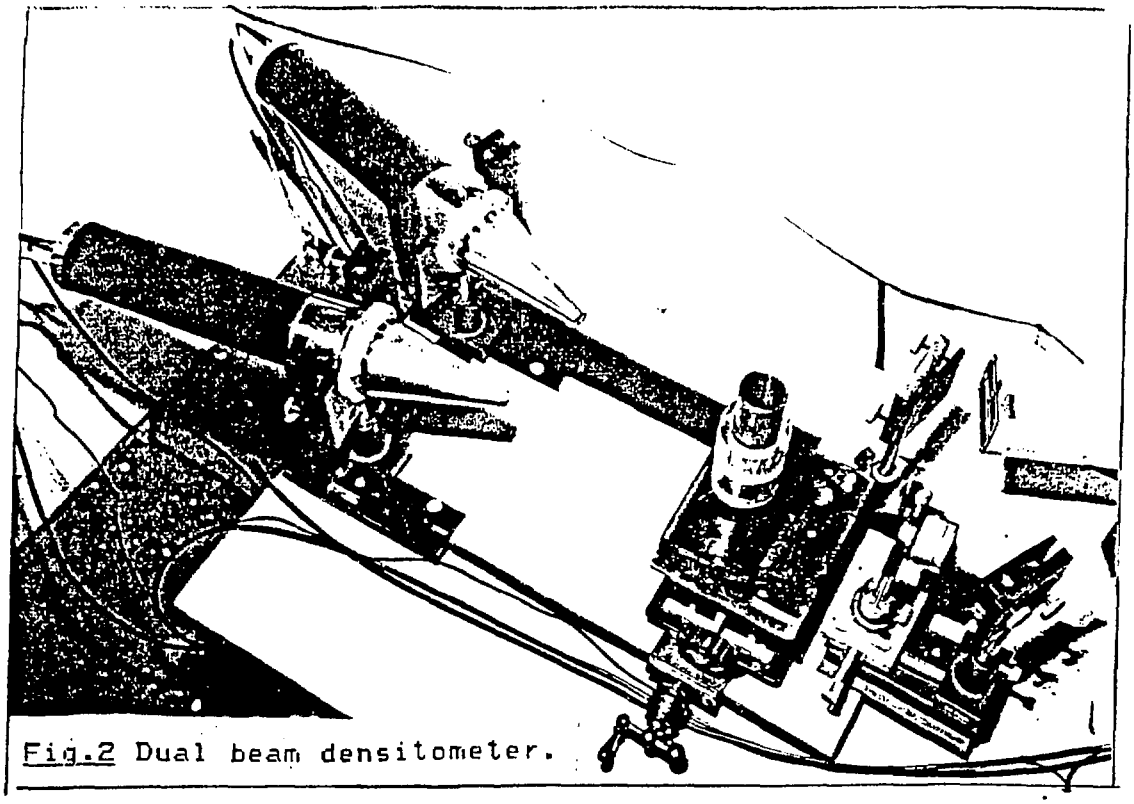

Fig.2 Dual beam densitometer.

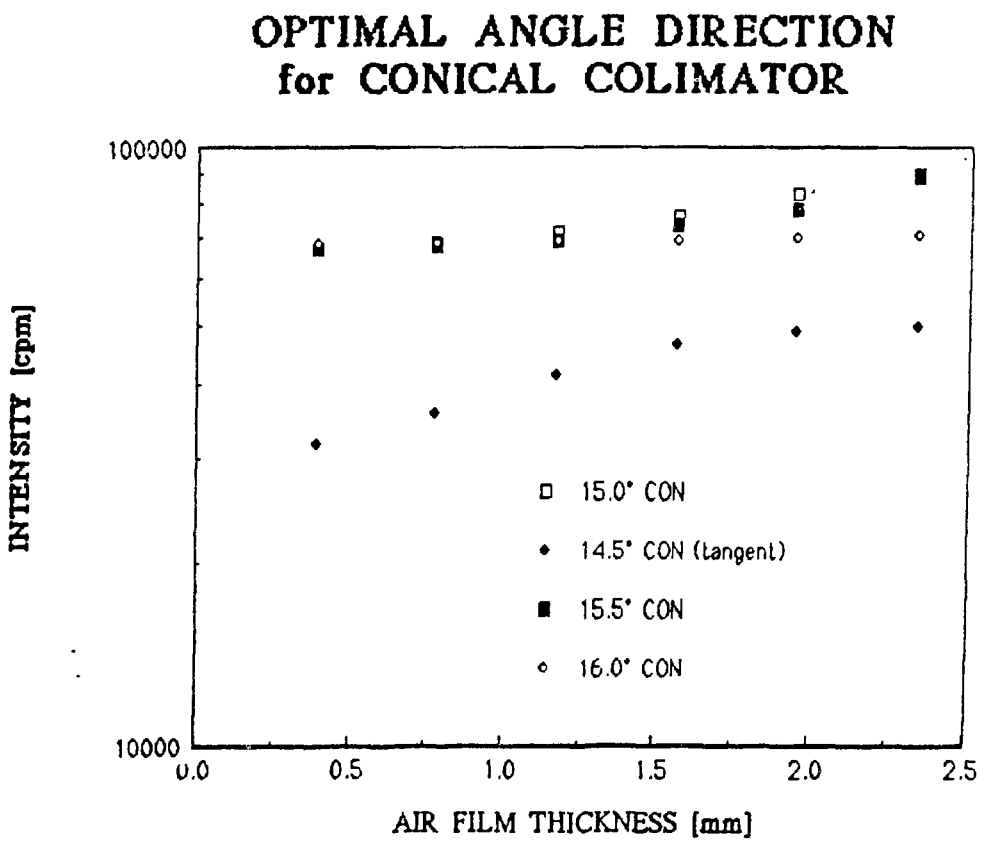

Fig.3 Optimization of source beam direction.

Nuclear Desalination

A.Z. Barak

Atomic Energy Commission, Nuclear Engineering Division
P.O.Box 7061, Tel-Aviv 61070

Various saline water desalination processes consume large amounts of various kinds of energy:

(1) Mechanical work or AC electricity,
(2) Heat at various temperatures, between 130°C and 30°C, or
(3) DC electricity.

Nuclear power reactors have specific features that may be more atractive, for desalination, than fossil fuel power plants[1],[2].
On the other hand they have potential drawbacks. It is important to make the most out of the advantages and minimize or avoid the drawbacks by identifying the most suitable combinations of desalination processes and power reactors.

The main potential advantages are:

(1) Heat and/or electricity to the desalination process are supplied directly from the power station. When these energies are cheaper than those from alternative primary energy sources, (which is usually the justification for nuclear power), then the economics of desalination improves even more than the economics of the electrical grid.

(2) Nuclear units, having relatively lower operating costs and higher investments, are therefore operated at higher load factors. This increases the annual desalted water production and reduces the costs.

(3) For combination with evaporation desalination processes the steam in the turbine expands to higher exhaust pressures so that the troublesome moisture content in the last stage is lower, improving the efficiency, the maintenance and the economics of both electricity and water.

The potential drawbacks are:

(1) For desalination by evaporation processes using heat from the nuclear system, leakages from the steam cycle to the desalination systems and/or vice versa are more dangerous.

(2) For desalination processes using only electricity (or mechanical work), the flexibility of energy utilization is reduced and advantage No. 1 becomes diminished.

These drawbacks have corrective solutions, which in turn are associated with complications and expenses. Accordingly, the various types of nuclear power reactors can be ranked from the point of view of their adaptability to desalination processes.

References:

[1] "Use of Nuclear Reactors for Seawater Desalination", IAEA-TECDOC-574, Sept. 1990.

[2] A. Barak. L.A. Kochenkov, M.J. Crijns and M. Khalid, "Nuclear Desalination: Experience, Needs and Prospects", IAEA Bulletin, Vol 32, No. 3, 1990.

Assessment of Potential Advantages of Super-conductivity Development for a Nuclear Power Program

S. Velner
Israel Electric Corporation Ltd., P.O.Box 10, Haifa

S. Ron
Israel Atomic Energy Commission, P.O.Box 7061, Tel-Aviv

Towards the end of the last decade nuclear power seemed to sense the promise of revival. Two factors may change the stagnant situation of the nuclear industry. The first is the green-house effect which might cause a global warming. The second is the significant break-through in the superconductivity field which will enable the building of nuclear power plants far from the customers with no heavy penalty of energy losses in transmission lines.

These developments pose distinct advantage for nuclear plants, as population risks decrease with distance from the plant. This approach may also enhance ideas such as off-shore nuclear reactors to be built on islands and connected to the shore through submarine cables.

Superconductivity is a phenomenon in which a large system behaves according to the laws of quantum mechanics, as if it were a single molecule, where the electron current flows without any power dissipation. A great effort was made to find materials which display this behaviour at higher temperatures[1].

An intermediate stage in the High Temperature Super-Conductivity (Htsc) development was the ceramic material based on the Y-Ba-Cu-O composition. In March 1987 it was reported that this material attained a critical temperature of 98K, a temperature higher than liquid Nitrogen (77K). A study[2], based on this intermediate superconductor, compared the investment in electricity transmission and energy losses costs of a 1 GVA, 380KV underground three phase water cooled oil and Htsc cables. The erection costs of an underground line are similar. However due to the somewhat lower Htsc cooling system costs and to the large reduction (by factor of about 5) in the operational costs (dielectric, conduction and heat leakages), the overall cost is lower by about 20% when using Htsc cable as compared with the underground oil cable for electricity transmission, table 1.

Recently new ceramic materials were developed reaching a critical temperature of about 125K, and there are indications of possible phases with transition at 230K. Therefore it can be expected that those new Htsc cables would bear a further decrease in the electrical transmission costs.

Table 1: Cost comparison of 1 GVA, 380 kV three phase cables

	Oil cable	Htsc-cable
Investment costs without underground structure (MDM/km)	4.5	4.5
Conductor losses (kW/km)	125	10
Dielectric losses (kW/km)	34	10
Additional losses, heat leaks (kW/km)	14	15
Overall losses	173	35
Cost of losses (MDM/km)	0.9-2.6	0.18-0.53
Cooling system costs (MDM/km)	0.34	0.25
Total costs (MDM/km)	5.7-7.4	4.9-5.3

References:

(1) S. Velner "Superconductivity - A survey", Israel Electric Corporation Ltd., RM-666 (1989).

(2) F. Schauer, K.P. Jungst, P. Komarek and W. Mancer, "Assessment of Potential Advantages of High Temperature Superconductors for Technical Application of Superconductivity", KFA, Germany, KFK-4308 (1987).

HEALTH PHYSICS AND RADIATION PROTECTION

X-Ray Exposure Rates in the Vicinity of VDT's (PC Screens) Measured with LiF TLD-100.

T. Biran, M. Barshad, S. Malchi, Y. Shamai, T. Schlesinger

Soreq Nuclear Research Center, Yavne

The exposure to ionizing radiation to users of personal computers and other video display terminals (VDT) is known to be small. This is a report on actual measurements performed in Israel in order to make sure that the commonly used units in our country, which are in part rather new and are likely not have been checked in reported works, comply with the required safety standards.

The radiation exposure rates at the screens of 8 personal computers were measured with thermoluminscence pellets (LiF, TLD-100). Three pairs of pellets, each size: 3.2 x 3.2 x 0.89 mm^3 were attached to the right hand corner, the left hand corner and to the center point of each white-black screen. The dosemeters were attached to the screens for a period of one month while the actual working hours of each computer were recorded and varied between 190 hours to 520 hours. The pellets were read with the Harshaw 4000 TLD Manual Reader. Three pellets placed in the same building in a room without PC's for the same period of time were used as background. Table 1 summarises the cummulative exposures in mR. The net radiation exposures were calculated by substracting the background radiation from the mean exposure measured at a specific station. The calculated exposure rates are also shown in Table 1.

Table 1 - Radiation Exposure and Exposure Rates of PC Screens

Station No	Work. Hours	Radiation Exposure / mR Pel 1	Pel 2	Pel 3	Pel 4	Pel 5	Pel 6	Mean	Net	Exposure Rates mR/h
Backg.		12.8	11.4	12.2				12.1 ± 0.7		
Colormn No 1	480	33.4	32.4	29.0	31.3	31.6		31.5 ±1.6	19.4 ±1.7	0.040
VTR062	520	23.4	21.9	28.0	18.9	25.9		23.6 ±3.5	11.5 ±3.6	0.022
VTR025	450	32.6	40.5	53.4	55.0	27.5		41.8 ±12.2	29.7 ±12.2	0.066
Colormn No 2	480	24.3	28.0	26.6	35.1	30.9	24.6	28.3 ±4.1	16.2 ±4.2	0.034
VTR060	520	24.8	22.9	26.1	23.8	24.4		24.4 ±1.1	12.3 ±1.3	0.024
VTR031	450	32.4	24.4	27.5	25.1	24.1	26.1	26.6 ±3.1	14.5 ±3.2	0.032
VPC023	190	24.6	21.3	23.3	22.8	23.3	13.9	21.5 ±4.3	9.4 ±4.3	0.050
VPC614M	190	28.4	24.1	23.8	25.0	23.4	24.6	24.8 ±1.8	12.7 ±1.9	0.067

It has to be mentioned that LiF dosemeters show a slight over response (~10-30%) when measuring X-rays in the range of

10-25keV, emited by most VDT's [1]. As the exact energy distribution emited by each VDT is not known, the measured radiation exposures were not corrected for the over response.

As can be seen from Table 1 the exposure rates measured are in the range of 0.02 - 0.07 mR/h with mean exposure rate of ~0.042 mR/h. These values are in agreement with reported values for VDT's in the literature [1,3,4], and well below the safety standard for VDT of 0.5mR/h [1].

The angular distribution of X-rays leaving the front face of a VDT is strongly forward-peaked. The relative X-ray intensity as a function of distance from the screen is given in Fig. 1[3]. As can be seen from the graph, the X-ray exposure rate decreases rather slowly as a function of distance from the screen, up to distances comparable to the dimensions of the screen.

At a distance of 1 dimension of the screen, ~30cm for a PC screen with 30 cm diagonal, the exposure-to -dose factor for 25 keV photons to the skin and to the eyes are:
0.91(rem/R) [5] x 0.4 (the relative exposure at a distance of 1 dimension from the screen as compared to the exposure 5 cm from the screen, from Fig.1) x 1.24 (backscatter factor) x 1/100 Sv/rem = 0.0045 Sv/R [3].
A VDT operator who spends 1500 hr per year in front of a screen would therefore recieve an annual skin (eye) dose of 0.042 mR/h x 0.0045 mSv/mR x 1500 h = ~0.28 mSv (~28 mrem) to that portion of the skin near the tube axis and/or to the eyes. As the annual dose limits to the to skin and eyes of the general population are 500 mSv (50000 mrem) and 150 mSv (15000 mrem) respectively, dose contributions of 0.28mSv to the skin and/or to the eyes are insignificant.

The dose contributions from the PC's screens to the two tissues which are more radiosensitive for carcinogenesis, the female breast and the thyroid gland were calculated using a similar procedure [3]. The predicted additional doses to the two organs are :~0.07 mSv (~7 mrem) and ~0.16 mSv (~16 mrem) respectively. As the annual limiting doses to those organs for the general population are 300 mSv (3000 mrem) and 500 mSv (5000 mrem) respectively, the additional doses caused by the emitted X-rays of VDT's to those organs are also insignificant.

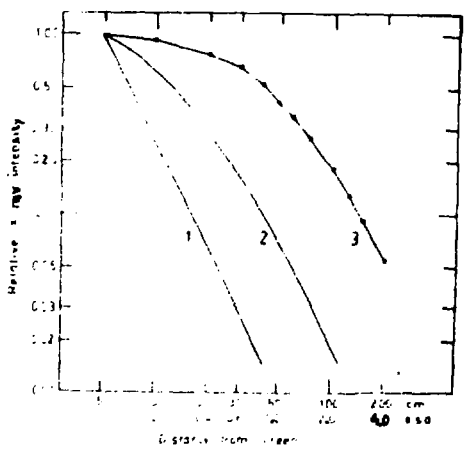

FIG. 1. X-Ray intensity as a function of distance along the central axis of a CRT. Distances are given both in cm and in multiples of effective screen diameters, defined as 50 cm for the 25-in. TV screen used. Curve 1 gives the inverse-square relationship which would result from a point source; curve 2 is calculated for a distributed, isotropic, circular source of 50 cm dia.; and curve 3 is the measured function.

References

1. An Evaluation of Radiation Emission from Video Display Terminals. U. S. Department of Health and Human Services, HHS 81-8153 Feb. 1981.
2. Personal communucation, M. Rosenstein, Director, Office of Health Physics, Center for Devices and Radiological Health, 14 May 1988.
3. Cathode-ray Tube X-ray emission Standard for Video Display Terminals. C. R. Hirning and J. H. Aitken, Health Phys. 43 727 1982.
4. Video Display Terminals. B. G. Phillips, The 2nd Annual General Meeting of the Canadian Radiation Protection Association May 5-6 1981, Ottawa Canada.
5. Radiation Dosimetry: X-Rays Generated at Potentials of 5 to 150 kV ICRU Rep. 17, International Commission on Radiation Units and Measurements 1970.

Occupational Exposure to Ionizing Radiation in Israel in 1989

S. Malchi, Y. Shamai, T. Biran

Soreq Nuclear Research Center, Yavne, 70600

A statistical analysis of the occupational radiation exposure of 7883 radiation workers in Isarel in 1989 was carried out using the central data-base of the National Personnel Dosimetry Service. The analysis refers to whole-body exposure to external penetrating ionizing radiations: X-ray, gamma, thermal neutrons, fast neutron. Radiation doses were measured by TLD badges(chest, hand, leg, head), TLD rings or CR-39 nuclear track etch detector.

One thouhand, one hundred and fourty seven radiation workers (14.5% out of 7883) monitored were exposed to radiation doses above the detection limits at least once in the year: ~0.15mSv for gamma and X radiation, ~0.1mSv for thermal neutrons and ~0.3mSv for fast neutrons for one dosimetry period (of 1 or 2 months). Most of those workers were exposed to radiation level lower then the annual dose level excepted to the general population. Table 1 groups all radiation workers acocrding to their annual dose-equivalent.

Table 1- Distribution of the level of exposure among all the radiation workers in 1989

Exposure	<det.lim*	up 5 mSv	5-15 mSv	15-50 mSv	>50 mSv
No of workers	6736	1069	58	12	8
Percent of workers	85.5%	13.5%	0.7%	0.2%	0.1%

* detection limit of 0.1-0.3 mSv per reading, as defined in the text.

An investigation is initiated whenever 0.3 of the dose limit is exceeded in a single dosimetry period: 1.25 mSv/month for whole-body, 3.75 mSv/month for head, 12.5 mSv/month for hands, legs. In 1989, 112 such cases were detected, of which 8 exceeded the annual dose limit of 50 mSv.

Workers and working places were classified into 9 groups according to the type of source and radiation exposure trends. Nuclear medicine staff and industrial workers using nuclear guages have the highest percentage of exposed workers. Also 15-20% of the monitored oncology, radiotherapy and diagnostic radiology personnel and monitored raiographers show exposure above the detection limits. Table 2 summarized the dosimetric data and the collective effective dose equivalent calculated for the differnt types of work. The collective dose equivalent of each group is calculated by multipling the number of radiation workers by the mean radiation dose of that group.

Table 2-Distribution of the annual effective dose equivalent according to working place

Type	No of Workers	No of Exposed Workers *	% of Exposed Workers	Collective /eff. dose-equ. Man.mSv
Nuclear Medicine	328	122	37.2	230
Industry, Nuc.gauges	89	30	33.7	31
Radiother. (Oncology)	278	56	20.0	77
Diagnostic Rad. X-ray	2260	371	16.4	565
Industry, Radiography	1360	210	15.5	806
Cardiology	966	136	14.0	365
Dental Clinic	662	61	9.4	512
Industry	552	44	8.0	52
Research Institutes	1288	99	7.7	106
Others	93	11	11.8	12
Total	7883		14.5	2756

* Workers exposed beyond the detection limit at least once during the year.

As can be seen from table 2 the collective annual effective dose equivalent for the ensemble of the monitored workers in Israel was about 2.7 man-Sv.

ENVIRONMENTAL HEALTH IMPLICATIONS OF ^{238}U-SERIES DISEQUILIBRIA ENCOUNTERED IN ISRAELI OIL SHALES

E. Ne'eman[1], T. Minster[2], J. Kronfeld[3], S. Brenner[1]

[1]Research Institute for Environmental Health, 69978 Tel-Aviv

[2]Geological Survey of Israel, 95501 Jerusalem

[3]Dept. of Geophysics & Planetary Sciences, Tel-Aviv University, 69978 Tel-Aviv

Oil shales are a potentially economic supplementary energy source for Israel. Indeed, a working pilot plant is currently in operation in Mishor Rotem, Northern Negev. Yet, laboratory analyses of the oil shales have discovered that they are characterized by a significant disequilibrium in the ^{238}U-series decay chain, in which the ^{214}Bi daugther yields significantly lower equivalent U than warranted by direct measurement of U by DNA. Analysis of the oil shale γ-ray spectrum, using a high precision Ge crystal detector, revealed a ^{226}Ra deficiency in addition to ^{222}Rn loss.

The amount of U in the oil shales is actually considerably greater (15-40 ppm) than preliminary field or laboratory analyses using a standard NaI (Tl) detector would indicate. The uranium is not fixed within a crystal structure, but it and its subsequent decay products are associated with exchange positions on clays or with organic complexes. Therefore, the incineration of the oil

shale results in concentrating U-series elements that may be only weakly bound to the ash surface, while the Rn gas may be efficiently released to the local atmosphere. Therefore it is suggested that:

(a) Rn should be monitored in the flume, being a potential hazard to the plant workers and/or local residents;

(b) Storage of uncovered or uncontained waste ash possess the potential of leaching and migration into the local groundwater environment;

(c) Dumping of the waste ash into the ocean may result in the effective leaching of soluble radium chloride and transfer of Ra to the food chain;

(d) Use of the waste ash as an industrial resource such as a cement industry, or as a primary material for building bricks may introduce higher amounts of radiation to the environment than the preliminary radiometric analyses would suggest.

(e) If at one stage underground mining will be considered a very well aeration system would be essential.

Radon exposure measurements of non-smoking lung-cancer patients

R. Biberman, Y. Tal, E. Neeman, A. Lusky, B. Modan
Department of Clinical Epidemiology, Chaim Sheba Medical Center
Tel Aviv University Medical School, Tel Hashomer

This is a preliminary report of exposure to radon of non-smoking lung cancer patients and/or with small cell carcinoma. Radon levels were measured in the homes of 57 cases and 51 controls. Exposure was measured with the aid canisters placed in the bedrooms of all study subjects for 5 days, and integrated detectors left for 6 months. Information was also obtained on life time residental, smoking and occupational history. Preliminary results of the data, based on the analysis or the short term measuring device, indicate a higher exposure to radon among lung cancer patients. The significance of these findings and the ensuing policy will be discussed in the light of the lung cancer problem in Israel.

ESTIMATION OF THE CONTRIBUTION OF ^{222}Rn IN DWELLINGS TO LUNG CANCER MORTALITY IN ISRAEL-BASED ON THE BEIR IV (1988) REPORT.

T. Schlesinger, M. Margaliot and Y. Shamai

Radiation Safety Department Soreq Nuclear Research Center,

Yavne 70600, Israel

I. Introduction

The possibility of lung cancer induction by radon in dwellings is now widely accepted. Radon is the largest single source of exposure to ionizing radiation of the population. According to the recent UNSCEAR report[1] Radon is contributing about 50% of the environmental ionizing radiation exposure. Recently (in 1988) the committee on the Biological Effects of Ionizing Radiation (BEIR) of the National Research Council of the U.S.A., published the BEIR IV report[2] related mainly to the health risks of radon and radon daughters. Among other findings this report presents an estimation of the lung cancer mortality due to exposure to radon and radon. progeny based on "epidemiological approach" and the "relative risk" model.

Using the same approach and model we try in this work to estimate the contribution of ^{222}Rn in dwellings to lung cancer mortality in Israel for a set of presumed mean radon concentrations in Israeli dwellings.

II. The BEIR IV Estimates of Lung Cancer Mortality Risks Due to Radon

The BEIR IV report reviewed the epidemiological evidence of excess lung cancer mortality in different underground miner groups as related to their

exposure to radon and radon progeny. Based on this, the BEIR IV report extrapolated lung cancer risks to the general population in indoor environment, using a modified relative risk model. In this modified model the excess relative risk varies with time after exposure, rather than remaining constant and depending only on age at risk. This is a departure from previous risk models which have assumed that the excess relative risk is constant over time.

The probability r(a) of dying of lung cancer at age a according to the new model is given by

$$r(a) = r_o(a)\,[1 + 0.025\,\gamma(a)\,(w_1 + 0.5\,w_2)]$$

where r(a) is the lung cancer mortality rate at age a, $r_o(a)$ is the baseline lung cancer mortality rate $\gamma(a)$ is 1.2 for ages less than 55 yr, 1.0 for ages 55-64 y and 0.4 for ages 65 y or greater, w_1, is the cummulative radiation exposure in WLM units from 5 to 15 y before age a; and w_2 is the cummulative exposure in WLM, 15 y or more before age a.

Based on all the above considerations the BEIR IV report estimated that the lifetime risk of lung cancer mortality due to lifetime exposure to Radon progeny of the USA population is 350 deaths per 10^6 person-WLM. This estimation is about half of the value given by the BEIR III 1980 report[3] (based on the absolute risk model) but twice the estimation of the NCRP in NCRP rep. 78 1984[4].

III. Lung Cancer Risks and Lung Cancer Mortality Due to Radon in the USA

The BEIR IV Model is based on lung cancer incidence and mortality rates in the USA. The EPA estimates[6] that the excess lifetime risk associated

with an average lifetime of 74 y (typical for the USA) and a mean residental exposure of 1 pCi/(37 Bq/m^3) is $5 \cdot 10^{-3}$ or 0.5%. The average annual lung cancer mortality rate is then about 70 per 10^6 per year or about 17500/y for the USA population of 250 million.

IV. Lung Cancer Mortality in Israel Due to Radon

An estimation of the lung cancer risks and lung cancer mortality and mortality rates due to radon in Israel can be derived from the BEIR IV model and the EPA estimations taking into account the differences in the baseline lung cancer mortality rates between the USA and Israel, and assuming that the age distributions and life expectancies of the Israeli and USA populations are similar.

According to the Israeli cancer registry lung cancer mortality in Israel is estimated to be about 160 per 10^6/y[5] as compared to about 500 in the USA[2], namely 3 times lower than in the U.S.A. Therefore we can estimate that excess annual lung cancer mortality rate due to radon in Israel may reach about 23 per 10^6 per year or about 115 deaths per year for the entire population of 5 million, if the average radon concentration in dwellings is 37 Bq/m^3 (1 PCi/l). Based on preliminar radon concentration measurements in about 200 homes in Israel we estimate that the average radon concentration in detached houses and first floors is of the order of 30 Bq/m^3 and in higher floors is only about 20 Bq/m^3. Assuming that about 40 to 70 percent of the population live in high story buildings above ground level we estimate that the actual annual excess lung cancer mortality rate due to radon in Israel is in the range 70-80 cases per year.

References

1. Sources, Effects and Risks of Ionizing Radiation - UNSCEAR Report 1988, U.N. 1988.

2. Health Risks of Radon and ohter Internally Deposited Alpha Emitters-BEIR IV (1988) Report, National Academy Press 1988.

3. The Effects on Populations of Exposure to Low Levels of Ionizing Radiation - BEIR III (1980) Report. National Academy Press 1980.

4. NCRP Rep. No. 78 - Evaluation of Occupational and Environmental Exposures to Radon and Radon Daughters in the U.S.A., NCRP 1984.

5. Israel Cancer Registry - 1988.

6. Estimation of Risks from Indoor Radon Exposure. EPA Feb. 1990.

THE IMPACT OF IMPROVED SEALING OF DWELLINGS ON INDOOR RADON LEVELS IN ARAD - ISRAEL*

M. Margaliot, T. Schlesinger, O. Even, M. Israeli, Y. Shamay
and D. Zakoski
Soreq Nuclear Reseasrch Center, Yavne 70600, Israel
and
O. Elikam, E. N'eeman and S. Brenner
Environmental Health Institute

Introduction

Indoor radon levels are normally higher than the corresponding outdoors levels[1,2,3] due to reduced ventilation rates indoors.

The present work was conducted to examine the enhancement in indoor Rn levels, that might result from improvement of dwelling sealing, (intended to save energy) in typical Israeli housing.

Experimental

The measurements were conducted in Arad in Southern Israel, which is known to reside in a relatively radium-rich region.

The dwellings in the present work were available for a few days only, and hence short-term radon measurements, by activated charcoal canisters were used.

* Sponsored by the Israel Ministry of Energy
Cont. 88-8-06

This Rn measurement method consists of exposing activated charcoal grains (contained in a canister) to the ambient atmosphere. The charcoal adsorbes the radon and after a few days (2-7) of exposure to air, the canister containing the charcoal is sealed, and the radioactivity of the Rn progeny in it is measured spectroscopically.

Calibration

The radon adsorption efficiency of the canisters in the present work was determined by exposing them in a radon chamber; with a calibrated radon concentration of 32 KBq/m^3.

(An U.S. NBS calibrated Ra-226 source, emanating 7.9 kBq/sec Rn, in a 246 l chamber).

Humidity has a reducing effect on the radon adsorption efficiency of charcoal[4]. To examine this effect, the calibration procedure was conducted under various humidity conditions (16% to 95% RH). It was shown, in this series of measurements, that humidity adsorption by the charcoal, raises measurably the charcoal's weight. The humidity dependent adsorption efficiency thus obtained from this series of measurements for the canister in the present work (containing 26 $\pm$ 1 grams of charcoal), is given by eq. 1.

$$e = 86 - 5 \cdot d \qquad (1)$$

where e is the Rn adsorption coefficient (liters of air per canister) and d is the weight change of the canister in grams. Eq. 1 is a linear least square fit to the experimental results mentioned above (correlation coefficient = 0.925) eq. 1 holds only for 72-h exposures. (Slightly different numerically coefficients are obtained for different exposure periods, but the linear form is retained).

The activity measurement consists of detecting the Bi-214 (one of the Rn-222 progeny) γ-rays by a well type NaI detector (30 cm high, 24.5 cm external diameter and 10 cm internal diameter).

Field measurements

Five houses were made available for the present work.

Various sealing conditions were imposed on the said houses, and the corresponding ventilation rates were measured.

These measurements were conducted by injecting a tracer gas (SF_6) into the house, and by subsequently measuring the time gradient of the SF_6 concentration.

Following the ventilation rate measurements, the Rn levels were measured, under the same sealing conditions (thus leading to approximately the same ventilation rates) by exposing the said open charcoal canisters, for 72 hours, to the air in the said dwellings. Subsequently, the Bi-214 activity was measured and the Rn concentration was computed using eq. 1.

The results of these measurements, namely, the Rn levels versus the ventilation rates, are presented in fig. 1, and in eq. 2.

$$R = 230\ A_c^{-0.57} \qquad (2)$$

R in eq. 2 is the Rn level (Bq/m^3), and Ac - the ventilation rate (air changes per hour).

Eq. 2 presents a least square fit of a linear equation to the data in fig. 1 (absolute correlation coefficient = 0.95).

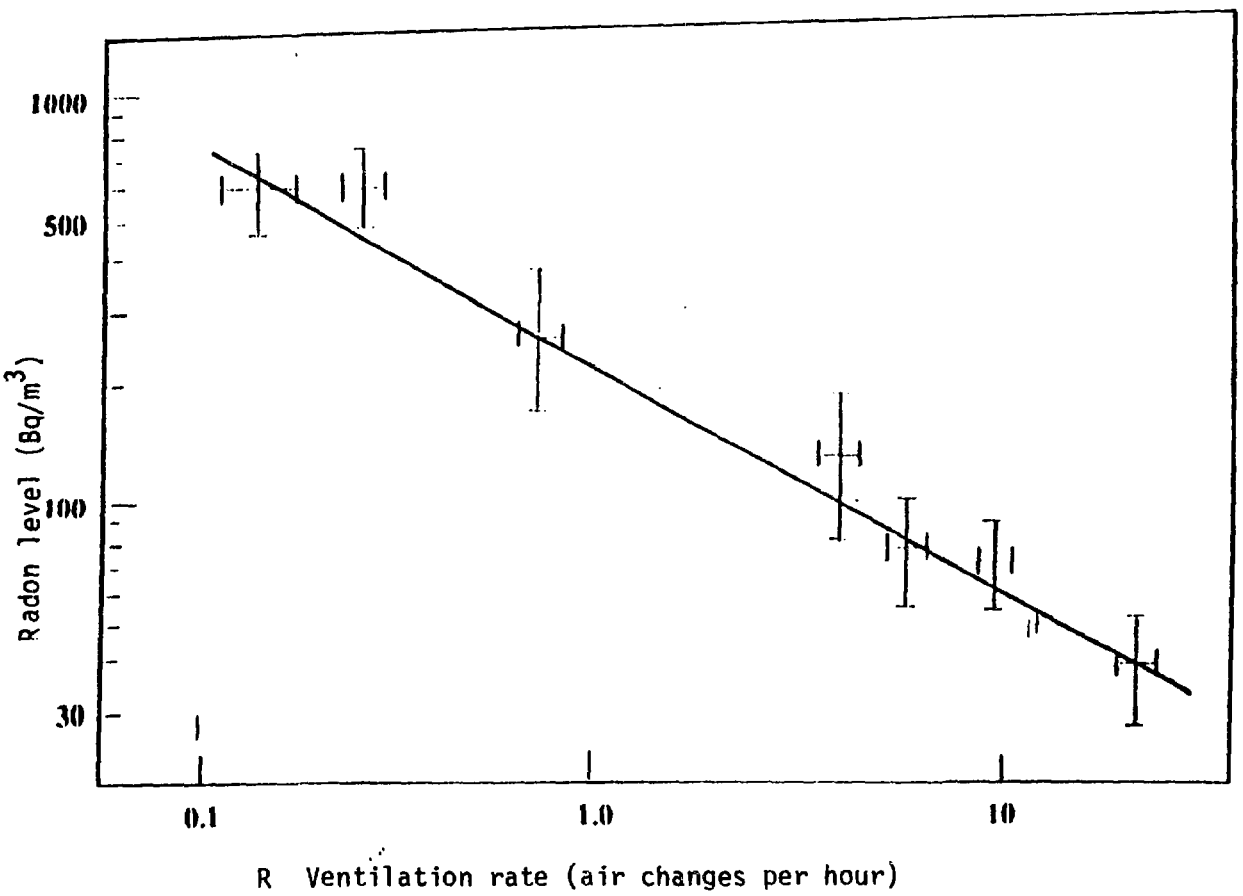

Fig. 1: Rn level versus ventilation rate, in Arad dwellings.

The error bars present the various uncertainties involved, in the ventilation rate (effects of external wind and atmospheric pressure on the ventilation rate) and in the Rn level (statistical uncertainties in radiation measurements and in accuracy of the adsorption coefficient).

Discussion

Due to economical considerations, the present work was conducted under unfavorable conditions. The measurements were not performed all in the same house. The ventilation rates were measured only once in each location, and that was not during the Rn measurements but before.

In spite of these methodological shortcomings, it is apparent that the Arad indoor Rn level is related to the ventilation rate by the approximation

given in eq. 2. This relation should be applied only to the actual range of ventilation rates in the present work (0.14 - 15 air changes per hour). It is noteable that eq. 2 differs from the theoretical relation $R=B\ A_c^{-1}$ (5), where B is a constant and R and A_c are as in eq. 2. This difference can be attributed to the fact that while the above theoretical relation assumes the external Rn level to be zero, the actual outdoors Rn level in Arad is significantly higher.

References

1. Cohen B.L. (1979) Prog. Nucl. Energy 4:1.
2. Jacobi W. and Eisfeld K. (1979), GSF Rep. S-626.
3. IAEA: Facts about low-level radiation, IAEA/PI/A14E, 1989.
4. Cohen B.L. and Cohen E.S. (1983), Health Phys. 45:501.
5. Nazarof et al. Atmos. Environ. 15: 263, 1981.

A SMALL RADON CALIBRATION CHAMBER- PROPERTIES AND MODE OF OPERATION

M. Margaliot, T. Schlesinger, O. Even, R. Duchan and Y. Shamai

Soreq Nuclear Research center, Yavneh 70600, Israel

Introduction:

The growing number of radon-222 measurements conducted recently in Israel, and the variety of the measurement methods, necessitated the operation of a calibration facility for this kind of measuring instruments. Due to economical limitations, an existing glove box was adapted for this purpose. This calibration chamber is described shortly in the following.

Chamber: a conventional glove box with a volume of 246 liters (an additional 32 liter passage chamber is attached, thus increasing the volume to 278 liters). A manometer is connected to the chamber for leak checks, and a 230 vac power supply is located in the chamber. The chamber walls material is nonconducting conventinal 5 mm thick plexiglass.

Radon source: two sources are available:

1) An 5 μCi Ra-226 solution in which Rn-222 is normally in equilibrium with the Ra-226. This solution can be bubbled by a hand pump (located inside the chamber), and about 99% of the Rn is thus released into the chamber, producing in it an Rn-222 concentration of 5 μCi/246 l = 20.3 nCi/l = 752,000 Bq/m^3 ($\pm$5%).

The Ra-226 activity in the said solution is stated by the manufacturer (Amershan) to be 5 μCi and this was verified by the radiation counting lab in SNRC.

2) A dry Ra-226 source (Pylon-Canda) with a constant Rn-222 emanation rate of 213 nCi/sec (7900 Bq/sec). This emanation rate was measured and certified by the U.S. NBS, with an accuracy of ± 4%. Having this source open in the chamber, produces in it a 866 PCi/l (32100 Bq/m^3) Rn-222 concentration. The 5 μCi source produces, following bubbling, a peak radon concentration which decays with the 3.8 day half life of Rn-222, while the 213 nCi source, due to its autonomic constant emanation rate, produces constant Rn-222 level.

Both sources need an appropriate buildup period (~ 5 Rn-222 halflives = 19 days).

The Rn-222 levels in the chamber are very high in comparison to environmental levels (1 PCi/l or 40 Bq/m^3). This necessitates relatively short (a few hours) calibration exposures of some of the integrative Rn measurement devices, such as SSNTD or electret ionization cells, and great care must be taken to ensure correct timing in the calibration procedure. Another problem which stems from the relatively small volume of the chamber is apparent when calibrating charcoal canisters: charcoal is known to adsorb radon (one gram of charcoal adsorbs the radon content of 2-6 liters of air[1]). The presence of a canister containing some 30 - 70 grams of charcoal, increases the effective volume (for radon) of the chamber by 60-400 liters, thus reducing the Rn level in the chamber. To overcome the last shortcoming, we derive the adsorption efficiency of a given charcoal canister (which is actually its calibration coefficient) in the following manner:

Let V be the chamber volume and v be the radon adsorption efficiency of the charcoal canister (in equivalent liters of air). v is thus the effective increase the chambers volume. Let a be the Rn activity detected

in the canister, and let **A** be the total activity of Rn in the chamber (as obtained from the Rn source in the chamber) we have then:

$$v = aV/(A-a) \qquad (1)$$

the v thus obtained serves as the calibration factor of the given charcoal canister, in liters of air per canister.

SSNTD Intercomparison: SSNTD's (of identical production batches) were exposed in both the described chamber, and in the EPA Las-Vegas Rn calibration facility. The SSNTD calibration coefficients obtained, agreed within $\pm$ 3%.

Relative humidity:

Humidity is known to affect the accuracy of some radon measuring techniques (mainly charcoal canisters). The present chamber has an internal hygrometer for measuring the humidity in it and the relative humidity can be controlled by placing silica-gel (in appropriate amounts) inside the chamber.

Working Level (WL) measurement calibration

WL measurements consist of measuring the levels of the Rn progeny. The present chamber, being small, has a large surface/volume ratio, as compared to normal rooms ($\sim$ 30 m^3) and hence, a larger part of the radon progeny gets attached electrostatically to the chamber's walls. This chamber is thus not suitable for WL calibration.

Reference

1. Cohen B.L. and Cohen E.S., (1983), Health Phys. 45: 501.

A Whole-Body Counting System Employing Two 5" Phoswich Detectors

U.German, S.Levinson, R.Kol, E.Naim
S.Piestum, H.Assido, Y.Ronen

Nuclear Research Center Negev
P.O.Box 9001 Beer-Sheva 84190

A whole-body counting system is essential for the assessment of Radionuclides in human lungs. A Phoswich detector is needed for the assessment of Actinides. NRCN operated for several years a system based on a 8" dia. NaI(Tl)-CsI(Tl) Phoswich detector[1,2,3]. The detector had to be replaced and it was decided to operate a new system with two 5" detectors, this for two main reasons:

- When employing one detector placed over the chest, the Sternum absorbs a part of the radiation originating in the lungs. When using two detectors placed over the lungs an improvement of the overall efficiency is expected.
- In case of malfunction of one of the detectors the system can still be operated with only one detector, but with reduced efficiency.

The two detectors system required changes in the mechanics and electronics. A special holder for two 5" dia. Phoswich detectors was designed and built[4], for mounting them into the existing compartment (Nuclear Enterprises (GB) Ltd. Edinburgh). The new holder (see Fig. 1) enables adjustment of the detectors' angle to fit their position to different chest geometries. The holder and its parts are built of oxygen-free-high-conductivity copper (OFHC) for minimal background .

The system is placed in a 2x2x2 meters rectangular compartment, situated in a basement with walls made of 50 cm thick concrete. The compartment is shielded with 15 cm thick 'pre-nuclear age' iron and 0.5 cm of lead.

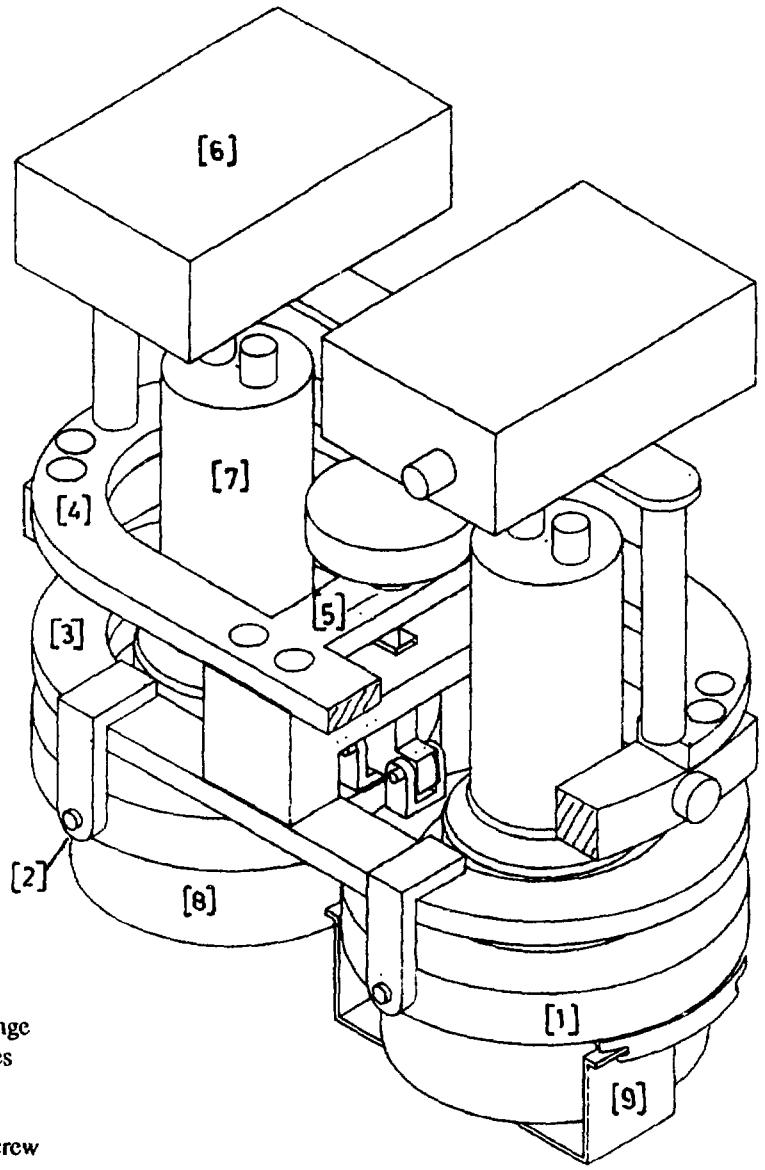

1. Detector flange
2. Detector axes
3. Lower ring
4. Upper ring
5. Adjusting screw
6. Pre-amplifier
7. PMT
8. Scintillators
9. Drawer

Fig 1.: Isometric drawing of the new adjustable holder for 5" dia. Phoswich detectors.

The principle of operation of a Phoswich system is described in ref. 1 to 3. The electronic components were replaced by new, commercial, modular and standard NIM units. A block diagram of the present system is given in Fig 2. Each of the two 5" NaI(Tl)-CsI(Tl) Phoswich detectors is connected through a preamplifier to a summing-amplifier. Since the same high voltage is supplied to the two PMTs, a balance unit was built in order to compensate for small gain

differences between the two detectors. The pulse shape analysis is performed by a delay-line amplifier and a pulse-shape analyzer. The time information gates two amplifiers which receive the linear pulses of the low and high energy ranges, through two amplifiers and delay-line amplifiers. The gated pulses are fed to a router multiplexer, and the low and high energy spectra are accumulated simultaneously, by a pulse height analyzer card mounted in an IBM/XT computer. A precision pulse generator is used for continuous monitoring of the electronics stability. Different settings of the electronic system were chosen for optimal performance with respect to time resolution, efficiency and background.

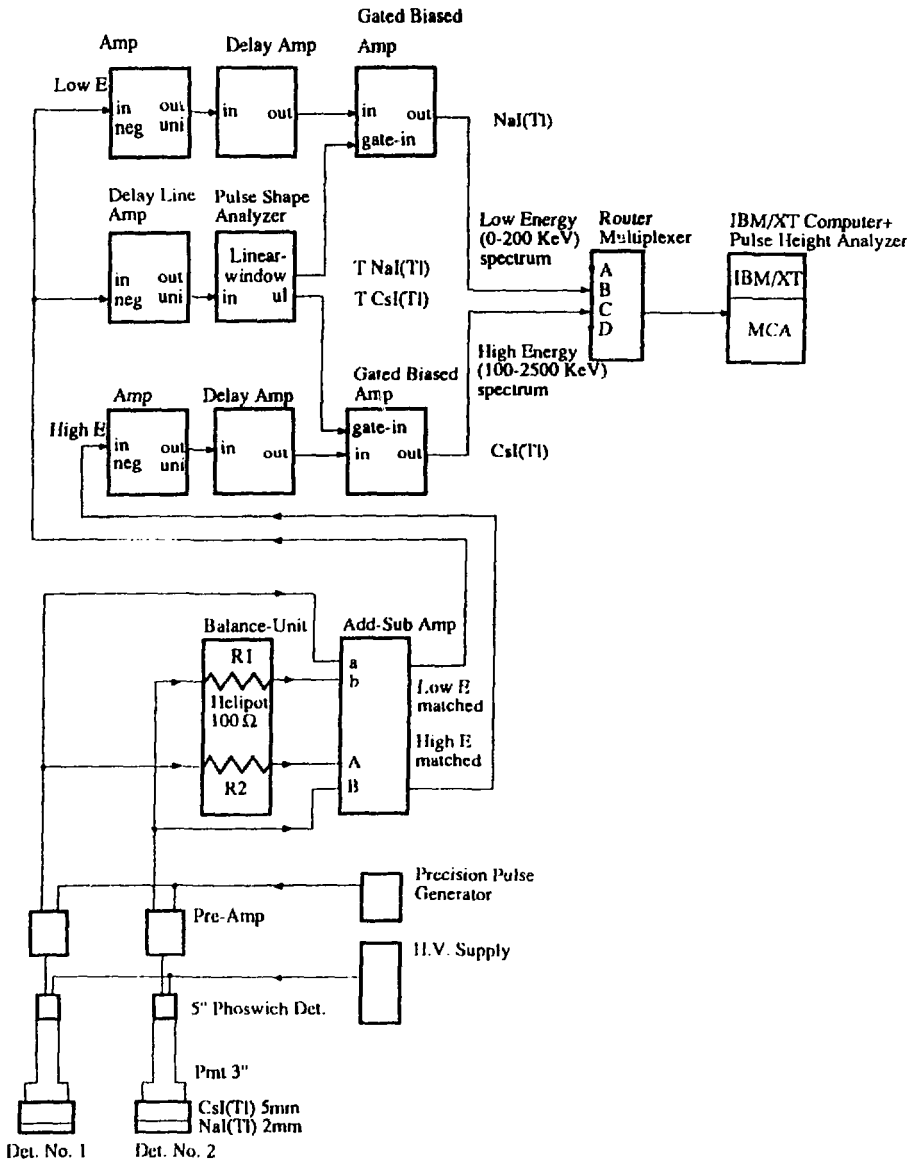

Fig. 2: Block diagram of the electronic system

The pulse shape time spectrum of a ^{241}Am + ^{137}Cs source is given in Fig. 3. The two peaks originating in the NaI(Tl) and CsI(Tl) scintillators determine the time windows used for gating.

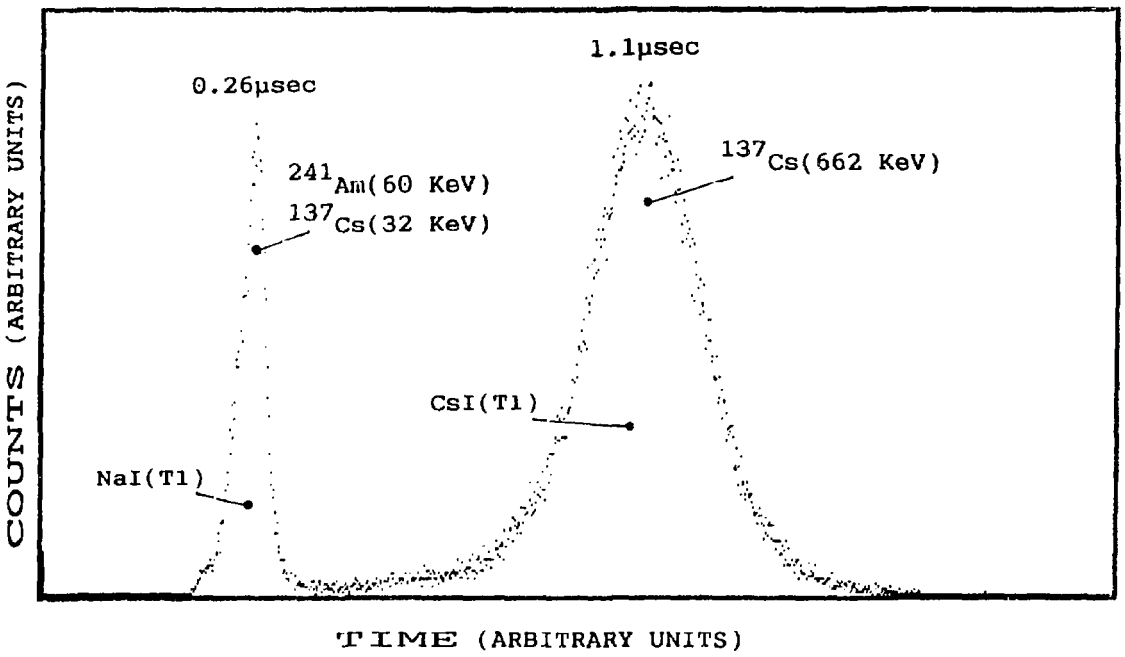

Fig. 3: The pulse shape time spectrum of ^{241}Am + ^{137}Cs source.

Fig. 4 shows the low energy pulse height spectra of a typical "clean-man" measured by the NaI(Tl): (a) with the electronic system in normal (gated) operation, (b) the direct spectrum from the detectors. The improvement achieved by the suppression system is clearly seen. The low energy spectrum and the high energy spectrum from the CsI(Tl) detector are accumulated simultaneously and analyzed in the IBM/XT computer.

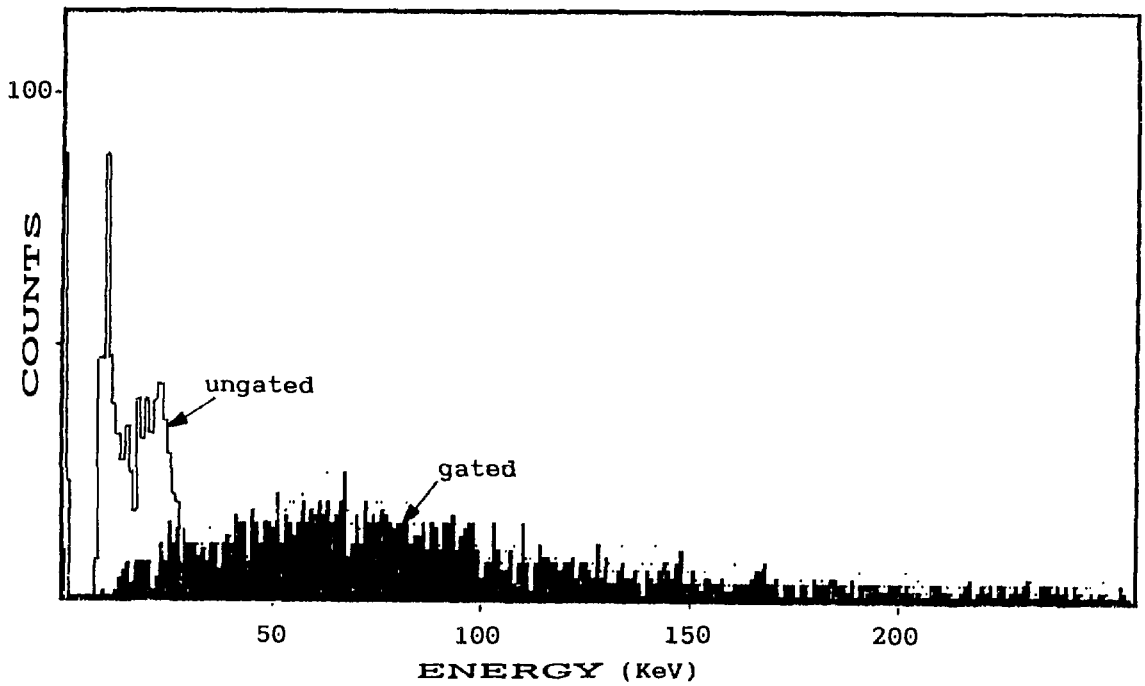

Fig. 4: The low energy pulse height spectra of a "clean-man" (600 sec)

REFERENCES

[1] S.Levinson, Y.Laichter
"Whole-Body counting of photons in the energy range 10-2500 keV by a Phoswich detector".
1987 Israeli Health Physics Society, annual meeting, pp. 20-25.

[2] S.Levinson, H.Assido, S.Piaston, Y.Ronen
"Improving a measurement system of radionuclides in human body".
Israeli Atomic Energy Research Laboratories Annual Report 1987
IA-1440, pp. 277-279

[3] Y.Laichter, U.German, E.Romm, G.Weiser
"External Measurement of ^{239}Pu Contamination in Human Lungs with A NaI-CsI Phoswich Detector"
1984, NRCN(TN)-075.

[4] S.Levinson, E.Reich, U.German, R.Kol, H.Assido, S.Piestun, E.Naim
"Adjustable Holder for whole-Body Counting with Two 5" Detectors"
Israeli Atomic Energy Research Laboratories Annual Report 1989
IA-1448, p. 176-178

ARTIFICIAL INTELEGENCE, SIMULATION AND RELIABILITY

EXPERT SYSTEMS AND NEURAL NETWORK APPLICATIONS IN THE NUCLEAR INDUSTRY

Shimon Yiftah

TECHNION - Israel Institute of Technology
Department of Nuclear Engineering

Two areas in advanced digital technology have started to make important contributions to the safe and efficient use of nuclear energy: Artificial Intelligence Expert Systems and Neural Networks[1].

Nuclear Expert System Applications

Because of development and advances in microprocessor technology and the resulting increasing power and wide availability of personal computers*, there is a clear trend of concentrating on personal computers and workstations as the platforms of choice for AI- and expert-system-based development and deployment. Surveys performed by "Future Technology Surveys, Inc." (Madison, GA) who interviewed leading experts on the subject, are summarized in the following four figures. Figure 1 shows a reduction in the use of supercomputers, mainframes and Lisp machines for expert system development and a corresponding increase of personal computers and workstations as platforms of choice for this development. In fact, if the projections to 1995 come true, over 75% of all expert system development will be done on personal computers and workstations. Figure 2 shows that the applications of expert systems will also be done on the same platform. Figure 3 shows that by 1995 the percentage of application packages will be more than double that of Tools and Shells, compared with a quarter and less than half, two years ago and today. Figure 4 shows the cost distribution of High-end Tools ($40,000-$50,000), less than $10,000 Tools, and Low-end less than $1000 Tools, by 1995. For instance, the well-known High-end Shell Kee, of IntelliCorp., in the $50,000 range has now been ported to personal computers and its price reduced to $10,000.

In summary, we quote,

> "Fifteen years ago, there was no such thing as an expert system. One could not be bought at any price. Ten years ago, it cost $500,000 or more to produce an expert system. Five years ago, an expert system shell might be available for $50,000. Today, some excellent (development) tools are available for less than $500".[2]

Finally it may be appropriate to quote Tom Peter, co-author of "In Search of Excellence", in his foreword to the book "The Rise of the Expert Company" by Feigenbaum, McCorduck and Nii[3]:

---

* In one year, 1987, nine million personal computers were sold in the U.S.

> "I came to this book and to the task of writing this foreword, interested, even fascinated, by this topic, about which I am largely naive. I leave the process of digesting the manuscript and writing the foreword mesmerized. The emerging world, brilliantly and pragmatically described in "The Rise of the Expert Company", is not the world we now know. The consequences are exciting and a bit frightening - and clearly monumental.

I conclude that any senior manager in any business of almost any size who isn't at least learning about artificial intelligence (AI), and sticking a tent. 're toe or two into AI's waters, is simply out of step, dangerously so".

Figure 1

Estimated Computer Use for Expert System Development

	1988	1990	1995
Super Computers	28.0%	3.6%	5.2%
Mainframes	8.8%	10.4%	11.2%
Symbolic/lisp machine	31.7%	19.6%	8.6%
Workstations	26.5%	35.7%	34.0%
PCs	30.2%	30.7%	41.0%

* Future Technology Surveys Inc. (Madison, GA)

Figure 2

Estimated Systems Delivery/
Hardware Platform Distribution

	1988	1990	1995
Super Computers	1.3%	3.1%	4.0%
Mainframes	9.4%	12.6%	11.8%
Symbolic/lisp machine	24.8%	13.7%	5.5%
Workstations	28.9%	30.6%	25.0%
PCs	35.6%	40.0%	53.7%

* Future Technology Surveys Inc. (Madison, GA)

Figure 3

	1988	1990	1995
KBS Tools	74.5%	54.1%	30.5%
KBS Applications and Packages	25.5%	45.9%	69.5%

Figure 4

	1988	1990	1995
High-end Tools ($40,000-$50,000)	40.5%	26.7%	13.2%
Medium-priced Tools (less than $10,000)	28.5%	35.3%	39.7%
Low-end Tools for PCs (less than $1,000)	31.0%	38.0%	46.6%

* Future Technology Surveys Inc. (Madison, GA)

A recent compilation of nuclear expert systems, developed using modern computerize methods for literature research, lists 298 expert systems corresponding to more than 6 distinct fields of application within the nuclear industry[4].

Most of these sytems are under development, with some having attained the prototyp stage and a few actually being in routine commercial use. Several, particularly thos designed for turbine-generator diagnostics, have proven to be of exceptional economic value.

This compilation, performed by John A. Bernard and Takashi Washio of MIT[4], covers mainly nuclear expert systems in the United States, Japan and Canada. Because of languag difficulties, European systems and activities are not covered fully. All over the world, th total number of nuclear expert systems may therefore be in the range of 350-400 or more If we consider not only nuclear expert systems, there are already, according to Feigenbaum et al., 2000 expert systems being used worldwide, with about 10,000 other expert system being developed and/or field-tested. Also, roughly half of the Fortune 500 firms ar investing in expert systems and expert system tools/shells[5].

To quote from the preface of Bernard and Washio: "We are both strong proponents of th use of nuclear energy for the commercial generation of electricity and as a power source fo the exploration of space. It is truly the only environmentally benign source of energy that i widely available in large quantity. We also believe firmly in the contribution that advance digital technology can make to the safe and efficient use of nuclear energy".

Approximately 25% of all expert systems either in use or under development within th nuclear industry are for the purpose of providing advice to reactor operators during bot abnormal and emergency conditions.

Expert systems used in the commercial electric power industry:

United States	145
Japan	71
France	29
Elsewhere	42
Total	287

These can be further grouped in major application areas as follows:

Decision Support	20.6%
Real-Time Diagnostics	15.0%
Maintenance	12.2%
Plant Management	10.1%
Control	8.7%
Engineering Tools	7.3%
Plant Design	7.3%
Other (Capturing Human Expertise, Emergency Response and Cognitive Model Development)	19.2%
Total	100.0%

The nuclear industry is attempting to use expert systems in a manner very different from that envisioned by the originators of the technology. Whereas the technology was developed for interactive use, it is being applied in real time. Whereas expert systems were intended to assist skilled humans by reducing their time committments, they are being modified to provide immediate diagnoses of plant malfunctions.

Several turbine-generator expert systems have met with outstanding economic success. These systems are intended for both fossil and nuclear applications.

Expert Systems available commercially for this purpose are: GenAID by Westinghouse, GEMS by Ontario Hydro (Canada), EPRI and SRI International, DIVA by EDF. Several examples of Expert Systems for the Nuclear Industry developed by Architect Engineers are listed in reference (1); others, as examples, are also listed.

Neural Network Applications

Several neural network applications to Reactor Safety were presented recently at the ANS Annual Meeting, June 10-14, 1990, Nashville, Tennessee(6). These are:

1) Use of Neural Networks in an Expert System to Enhance Nuclear Power Plant Safety
2) A Neural Network Application to Control a Nuclear Reactor
3) Using Artificial Neural Networks to Identify Nuclear Power Plant States.
4) Identification of Nonlinear Dynamics in Power Plant Components Using Neural Networks.
5) Neural Control of Temperature and Pressure During PWR Start-Up.

The use of neural networks to interpret multiple alarms is discussed in reference (7). See also reference (1). Other neural network applications are included in the three Application Sessions at the International Joint Conference on Neural Networks (IJCNN), June 17-21, 1990, San Diego, California.

REFERENCES

1. S. Yiftah, Artificial Intelligence Expert Systems and Neural Network Applications in the Nuclear Industry, TNED-R/731, Technion (August 1990).
2. T. Walker and R. Miller, Expert Systems 1990: An Assessment of Technology and Applications, *SEAI Technical Publications.*
3. E. Feigenbaum, P. McCorduck and H.P. Nii, *The Rise of the Expert Company,* Times Books, A Division of Random House, Inc. New York, foreword by Tom Peters (1988).
4. J.A. Bernard and T. Washio, Expert Systems Applications Within the Nuclear Industry, American Nuclear Society, La Grange Park, Illinois, U.S.A., Appendix, pp. 139-199 (1989).
5. *Expert Systems with Applications, An International Journal,* Vol. 1, Number 1, p. 1, Pergamon Press (1990).
6. TANSAO 61, pp. 215-220 (June 1990).
7. H.P. Chan, Using Neural Network to Interpret Multiple Alarms, *IEEE Computer Applications in Power,* pp. 33-37 (April 1990).

Applications of Neural Network Techniques for Fault Detection

Zvi Boger, Nuclear Research Center - Negev

Abstract

On-line fault detection by AI techniques, such as Expert Systems, is regarded as one way to increase safety and plant reliability. However, the successful implementation of such systems is slowed by the need to analyze the detailed behaviour of the plant, and the derivation of the Expert Rules can be difficult in a complex systems. Neural Network (NN) techniques can be used to help in some tasks: Automatic learning of process and equipment behaviour models; Extraction of Expert Rules from these models; Sensor fault validation by pattern recognition; Enhancement of sensor sensitivity in noisy environments. Research in these areas was hindered by the slow learning rates of NN, especially in real time complex systems. However, the newly developed Guterman - Boger fast teaching and network reduction algorithms allow quick experimentation with NN for such purposes. (1,2).

Results of recent and on - going research will be presented, showing the potential of the application of NN techniques to fault detection and other areas of interest in nuclear engineering.

References:

1. H. Guterman: Application of principal component analysis to the design of neural networks. Submitted to Neural Networks, 1990.
2. Z. Boger, H. Guterman and M.A. Kramer: Neural network reduction: Application of a statistical relevence approach. Submitted to IEEE Transactions on Neural Networks, 1990.

Optimizing The Multi-Hypothesis Diagnosis of Control Actuator Malfunction in a Multi-Input Multi-Output Thermal System

Osnat Katzanek, Interdisciplinary Committee for Nuclear Engineering, Technion, Haifa
Yakov Ben-Haim, Faculty of Mechanical Engineering, Technion, Haifa

Introduction

Diagnosis and identification of a malfunction in a system is a necessary prerequisite for its correction. The earlier the identification is, the control system will become more efficient. When considering a nuclear reactor, safety plays a primary role.

Probabilistic methods for identifying malfunctions need extensive prior information about the system operation in steady state and in malfunction. Usually, reliable information is unavailable, especially when considering a complex system with a high degree of uncertainty. A nuclear reactor is an example of a complicated nonlinear system with a high degree of uncertainty. A linear approximation enables a relatively quick estimation of the state of the system at a specific time, given the history of the inputs.

Benchmark Method for Malfunction Identification

The benchmark method (Ben-Haim, 1986, 1990), enables one to calculate the best malfunction distinguishability of a given control system. We shall assume our failure sets to be convex. This demand is fulfilled in many physical systems, and thermal systemsin particular, since the inputs vary continuously within uniform bounds. Considering control actuator malfunction, it is convenient to define a malfunction set by a certain range of values within the range of the actuator. The complete response set is the set of all the measurements resulting from a certain failure set. The response set is convex too (in additive malfunctions). Identification of a malfunction is based on distinguishing between response sets, caused by different malfunction sets. If we can always distinguish between two response sets, we can, theoretically, always distinguish between the malfunction sets which caused them. This means that the two types of failures are "benchmark distinguishable". When there is an intersection between the response sets, it means that no

algorithm can always distinguish between every possible occurrence of these failure types. The failure sets are thus "benchmark indistinguishable". The method compares any proposed diagnostic algorithm against the benchmark performance. The closer the proposed algorithm to the benchmark, the better.

Experimental System

The experimental system consists of a water bath with 5 heaters as inputs, and 8 thermometers (PRT) as outputs. They are all connected to an IBM PS/2 model 30 computer. The experimental system, like most thermal systems, is not linear. There are many heat-induced vortexes that complicate the dynamics. The system is represented by a linear state space model in a narrow range of temperatures. When the system is in steady state, and in the beginning of a malfunction, this linearity is fulfilled. The design of a malfunction diagnosis algorithm is greatly simplified if it can be based on a linear model of the normal behavior of the system. The research concentrates on validating the predictions of the benchmark distinguishable and indistinguishable failure sets, based on the linear model.

Experiments and Results

The ability of a linear model to regulate the nonlinear system's response was evaluated. The thermal system was stabilized on a steady state by active temperature feedback. As a check of stability, cold water was introduced into the bath, causing a temperature drop of 2°C. The control system restored the temperature within 7 minutes.

The second stage of the experiments checked the ability of the linear-model-based control system to distinguish between different sets of malfunctions. Heater malfunctions were initiated by the computer, causing abnormal fluctuations of the heater power. Each malfunction is in one heater and in a certain power range, while the control system continues to operate as if it controls the system. The temperature of one thermometer was recorded by the computer 200 seconds after the malfunction began. The distinguishable and indistinguishable failure sets were found with these temperatures. Comparing the experimental results and the theoretical predictions of distinguishable failure sets shows a

somewhat wider distinguishable range in the theoretical than the experimental results. This is caused primarily by the measurement noise ($\pm$ 0.15°C) of the thermometers.

Future Work

In the next stage of the project, the advantage of adding one more measurement will be checked. The degree of improvement in the distinguishability will be evaluated.

References

1. Y. Ben-Haim, Convexity Analysis: A Tool for Optimization of Malfunction Isolation, 25th IEEE Conference on Decision and Control, Dec. 1986, Athens, Greece, pp. 1570 - 1575.

2. Y. Ben-Haim, Optimizing Multi-Hypothesis Diagnosis of Control - Actuator Failures in Linear Systems, AIAA J. Guidance and Control. To appear, 1990.

Solving Optimization Problems with Neural Nets

D. Ingman Y. Merlis

October, 1990

Quality Assurance and Reliability

Technion – Israel Institute of Technology

Haifa, 32000, *Israel*

The problems of optimization are an important part of applied science. In the field of nuclear engineering, they cover a wide scope of areas, like signal analysis and processing, organization and management problems, simulations of actual physical processes, etc. A method of real time solution of complex optimization problems can provide a powerful tool in nuclear engineering and related areas.

The objective of optimization problems is to minimize a given target function, which is often called "an energy function". The problem is, that usually the energy functions are not convex. Therefore, they possess a number of local minima, most of which corresponding to unacceptable solutions. Multivariable nonconvex optimization is notorious for the multitude of the local minima. There is much of a need for a tool of elimination of the local minima in favor to the global one.

One way to carry out real time multivariable optimization is by means of neural nets [1]. The idea is to create a multicomponent interconnected system, with a state of each component corresponding to value of one of the problem's variables. The state of the whole network defines a point on

the target function pattern. A properly defined neural net will attempt to minimize the energy function and, therefore, to solve the optimization problem. The paper is devoted to the analysis of such networks.

We consider N-variable binary optimization problems. The solution space is confined to the hypercube of $0 \leq v_i \leq 1$, where v_i are the variables of the problem (and also, the states of corresponding neurons). The feasible solutions are assumed to lie in the corners of the hypercube. We assume, that the problem is "well-posed", that is, the feasible solutions correspond to the local minima of the target function. Finally, we assume that there is an appropriate neural net capable of solving the problem.

The direct analysis of the behavior of the net is very complicated. However, some light can be cast on it by means of the thermodynamic fluctuations theory.

The characteristic features of an N-particle thermodynamic system are its internal energy $U(\underline{v})$ and entropy $S(\underline{v})$, with $\underline{v}$ being a state vector. According to the theory, a system fluctuating about the equilibrium state can be described by the time-evolution equation

$$\frac{dx_i}{dt} = -\lambda(x_i - \frac{f_i}{T}) \ , \ i = 1..N \tag{1}$$

where T is the temperature, λ is a parameter and

$$x_i = -\frac{\partial S(\underline{v})}{\partial v_i} \tag{2}$$

The internal forces f_i are defined by

$$f_i = -\frac{\partial U}{\partial v_i} \tag{3}$$

The variable v_i can be associated with a probability measure [2,3]. Therefore, the entropy can be defined as

$$S(\underline{v}) = -\sum_i [v_i \cdot ln(v_i) + (1 - v_i) \cdot ln(1 - v_i)] \tag{4}$$

Substituting (4) into (2) and rearranging the terms yields

$$v_i = \frac{1}{1 + e^{-x_i}} \tag{5}$$

which is the usual sigmoidal response of neuron. Moreover, for quadratic energy

$$U = \frac{1}{2}\sum_i \sum_j W_{ij} v_i v_j + \sum_i I_i v_i \tag{6}$$

with W being a connection matrix, the eqn. (1) reads

$$\frac{dx_i}{dt} = -\lambda(x_i + \frac{1}{T}(\sum_j W_{ij} v_j + I_i)) \tag{7}$$

which, for a constant T, together with (5) define the usual Hopfield net [1].

For a time-varying temperature an important property of the net can be derived. By developing eqn. (1), it can be shown that the free energy function $F = U - TS$ is a Lyapunov function of the system

$$\frac{d}{dt}F(\underline{v}) \leq 0 \tag{8}$$

provided that $\frac{dT(t)}{dt} \geq 0$. That is, the net performs a descent on the free energy function.

However, the free energy comprises two terms: the target function U and the entropy S. The temperature T assigns the relative weight to the entropy term. When T is increased, the entropy term acquires more influence, and the state of the net is "pushed" towards the maximum entropy state in the center of the hypercube. That is, if for a low temperature the system was trapped in a local minimum of the energy function, the rise of the temperature will enable it to "climb uphill" the energy pattern. Moreover, if the final state is feasible (that is, $S \approx 0$), and was reached by heating only, it will be characterized by a lower internal energy level, due to (8).

The described procedure was applied to solution of the TSP (Traveling Salesman Problem). This is a problem of finding a closed route of minimum length, which passes through all the given points (cities). We considered the 6, 9 and 12-city problems. In all the cases, the optimal solution was achieved after a small number of temperature trials.

The major disadvantage of the discussed approach is, that it requires temperature iterations. The exact temperature strategy is unknown. However, some preliminary results show, that in many cases the temperature dependence of the system can be accurately predicted. Presentation of these results is out of the scope of this paper.

References

[1] - Hopfield, J. J., Tank, D. W. (1985). Neural computation of decisions in optimization problems. *Biological Cybernetics*, 52, 141- 152.

[2] - Ingman, D., Merlis, Y. (1989). Local minimum escape using thermodynamic properties of neural networks. To be published in *Neural Networks*.

[3] - Ingman, D., Merlis, Y. (1990). Maximum entropy signal reconstruction with neural networks.

Submitted to *IEEE Transactions on Neural Networks*.

Neural Nets for the Coolant Channel Blockage Modeling

D. Ingman Y. Merlis

October, 1990

Quality Assurance and Reliability

Technion – Israel Institute of Technology

Haifa, 32000, *Israel*

One of the most serious problems of the nuclear reactors safety is blockage of the coolant channels. The problem is of a high dimensionality, considerable data unavailability, and is extremely difficult for any physical analysis.

In [4], Ingman and Reznik introduced a thermodynamic model of channels blockage propagation. We propose to insignificantly change it, in order to obtain real time simulations of the blockage. We will show, that a properly defined neural network can describe the dynamic behavior of the updated model. The network, implemented in hardware or even in software, can provide real time simulations of the failure, starting from any initial conditions and for a wide range of the model parameters.

There is an additional advantage of the neural network implementation. In the original model, there is a significant number of parameters estimated empirically, semi-empirically, or not estimated at all. The authors admit, that the direct evaluation of many parameters is practically impossible. On the other hand, neural networks are capable of learning the parameters from examples. That is, given a sufficient number of actual blocked-unblocked channels configurations, the values of the parameters can be obtained using

one of the neural nets learning procedures, like the back-propagation or the Hebb rule [5].

The characteristic function of the model is the Gibbs free energy

$$F = U - \theta S \tag{1}$$

where U is the energy accumulated in the system, θ is (nondecreasing) equivalent temperature, and S is the entropy of the system. The whole system fluctuates while creating clusters of channels, until a minimum of F is reached.

The temperature θ corresponds to the average energy accumulation. The internal energy U is defined by

$$\begin{aligned} U(t) &= \frac{1}{2N_0}\sum_{i=1}^{N_0}\sum_{j=1}^{N_0}[\gamma^1_{ij}v_iv_j + \gamma^2_{ij}((v_i(1-v_j)+(1-v_i)v_j)+ \\ &+ \gamma^3_{ij}(1-v_i)(1-v_j)] + P_0\sum_{i=1}^{N_0}(\alpha_i v_i + \beta_i(1-v_i)) \end{aligned} \tag{2}$$

where N_0 is a number of subchannels, v_i is a binary variable corresponding to the state of channel i, $\gamma^{1,2,3}$ are the interaction matrices, and α, β, P_0 are coefficients. We assume, that all the parameters vary in time slowly enough to be quasi constant.

In practice, the states of the channels are not binary. Therefore, we allow the variables v_i to be continuous in the interval $[0,1]$, and associate them with the probability that the respective channel i is either unblocked ($v_i = 1$) or blocked ($v_i = 0$) [2,3]. In this case, (2) is equivalent to the energy of continuous time Hopfield net.

Instead of the configurational entropy defined in [4], we use the entropy measure [2]

$$S(t) = -\sum_i[\frac{v_i \cdot ln(v_i)}{X_U(t)} + \frac{(1-v_i)\cdot ln(1-v_i)}{X_B(t)}] \tag{3}$$

where $X_U(t)$ and $X_B(t)$ are the clusterization parameters [4]. Again, we assume that both are quasi constant.

Neural networks characterized by the energy and entropy functions in the form of (2), (3) respectively, have been analyzed in [2]. It was shown, that for nondecreasing (as in our case) temperature, the net minimizes the free

energy function (1). Therefore, the net described by (2), (3) simulates the phenomenon of the channel blockage.

It should be noted, that although the neural net learning rule can estimate the parameters $\gamma_{ij}^{1,2,3}$, α_i, β_i (provided that the data set is sufficient), the parameters $X_U(t)$ and $X_B(t)$ are still have to be evaluated by some other approach.

We believe, that the association of neural networks with the blockage problem is a promising area of investigation.

References

[1] - Hopfield, J. J., Tank, D. W. (1985). Neural computation of decisions in optimization problems. *Biological Cybernetics*, 52, 141- 152.

[2] - Ingman, D., Merlis, Y. (1989). Local minimum escape using thermodynamic properties of neural networks. To be published in *Neural Networks*.

[3] - Ingman, D., Merlis, Y. (1990). Maximum entropy signal reconstruction with neural networks.

Submitted to *IEEE Transactions on Neural Networks*.

[4] - Ingman, D., Reznik, L. (1986). An approach of statistical thermodynamics to effects of coherent blockages of reactor core coolant channels. *Nuclear Technology*, 74, 243-259.

[5] - Lippmann, R., P. (1987). An introduction to computing with neural nets. *IEEE – ASSP Magazine*, vol. 4, no. 2.

Detection of Spatial Distribution of Gamma Emitters in a 2–D Box using Neural Networks Techniques

I. Eliash, E. Wacholder and E. Elias

Department of Mechanical Engineering

Technion - Israel Institute of Technology Haifa 32000, Israel

Introduction

Non–destructive measurement of the intensity and spatial distribution of gamma emitters non–uniformly scattered in a finite volume of matter has many practical applications in industry and medicine. Processing the detectors signals into a visible picture, typically calls for a solution of an inverse radiation transport problem. Several approximate solution schemes have been developed for medical applications in the field of emission tomography, the most popular of which is the Furrier transform method [1-3]. More recently, a probabilistic approach has been developed for industrial applications [4]. Generally, Accurate results can be obtained when the measured data is free of noise. However, in all practical measurements, the data processing requires elaborate filtering and the utilization of a large number of detectors to improve the picture resolution.

The present work investigates the feasibility of implementing neural–network techniques for evaluating the location and intensity of gamma emitters non–uniformly distributed in a two–dimensional rectengular box. For this purpose, an adequate computational neural–network architecture has been developed which is capable of processing noisy detectors signals. The neural–network method is shown to yield a fairly good resolution with a small number of detectors. In the following the neural–network method is briefly described and results are presented for a specific non–destructive measurement of 10.8 MeV gamma sources using two and four detectors.

Artificial Neural–Networks

"Artificial Neural–Networks" (ANN), are computational models which have received their inspiration from biological neural networks [6]. The increasing interest in these models

is motivated by the enormous potential of parallel data processing evident in biological networks. Biological neural–networks solve difficult signal processing problems such as vision and hearing in admirably short times. In various research efforts, ANN were used also in solving difficult combinatorial optimization problems [7-9], implementation of associative memory [10], classification and signal processing [11], pattern recognition [12] etc.

One of the principle features of neural nets is that they can incorporate a learning mechanism, i.e., being able to modify their operation based on their previous operating history. Typically, a set of given examples is used to train the network to solve a given problem.

In our work we have used a popular neural net architecture; the Back–Propagation (BP) network, originally developed by Rumelhart et al.[5]. This net generally maps input patterns to produce desired output patterns. Thus, it provides a means for recognizing input patterns, and for producing assigned output patterns in response. A principal feature of the BP scheme is its interposition of a "hidden layer" of nodes between the net's inputs and outputs. This enhances the net's pattern-classification power [6].

A back propagation net has two distinct modes of operations:

a. A "training" (or "learning") mode, and

b. A "performance" mode.

In the "training" mode, pairs of associated input and output patterns are presented to the net. Using the input patterns, the net generates a corresponding set of output patterns and defines a set of errors by comparing the calculated and the given output patterns. These errors are propagated backwards through the network and change the value of link-weights, with the intent of reducing the difference between the calculated and the desired outputs.

In the "performance" mode, learned patterns are produced in response to presented input patterns. In this mode, it is important to realize that the net is able to "generalize" from its input patterns (this feature gives the hope the net will be capable of solving the inverse problem). The net's response is based on the stored pattern which is the closest to the presented input pattern. It is not necessary for the input pattern to match a learned pattern exactly.

Results and Discussion

The BP Neural–network method was implemented for analyzing the spatial distribution of gamma sources in a $26'' \times 16''$ ($\approx 61 \times 38$ cm) 2-D box, assumed to be filled uniformly with CH_2 with density of 0.1 gr/cm^3. For analysis purposes, the box was divided into 20 equal

area cells. Detectors responses (count rates) were generated numerically for a single 2 μCi point gamma source with energy of 10.8 MeV placed at the center of each cell.

Two detection configurations were considered: The first consists of using two $4''\times4''$ NaI(Tℓ) scintillation detectors (70% efficiency) positioned at a distance of about 3" (7.62 cm) from the box along its diagonal. In the second configuration, four detectors were considered. The detectors were positioned at given locations outside the box.

Figure 1 shows the calculated nominal count rate vs. source position in the 2-detector system. For source addresses 9 to 12 (corresponding to points of symmetry with respect to the line connecting the two detectors) the detectors responses are shown to be similar. Obviously, developing a mathematical model to resolve the source location given the measured count rates in this range is an exhausting task. Figure 2 is an enlargement of the region of addresses 8 to 14 including statistical errors in the detectors signals. In this specific case, the nominal count rates were perturbed randomly within $\pm1.5\%$ (corresponding to 10 sec measurement). Here again, close and sometimes overlapping, responses are obtained for different source locations (cf., addresses 9, 11 and 10, 12). The main objective of this study was, therefore, to establish a neural-network system capable of resolving the source location in that quite demanding test case.

The calculated detectors responses, for the 20 different source positions, along with the corresponding source locations (addresses) were introduced as input data to the neural-network in the "training" mode in order to establish its architecture, i.e., connectivity, connections strength, activation functions and biases. In order to overcome the difficulties of separation between close signals, a fully connected 3-layer network with 2 hidden layers was chosen. The network consists of 2 input neurons, 5 neurons in each hidden layer and a single neuron in the output layer. Thus, a total of 57 connection strengths and 11 biases were determined through the "training" process. All neurons' activation functions implemented in this network were regular sigmoids with a gain coefficient of 1. The input signals as well as the desired output addresses were normalized to have values between 0 and 1.

For testing the network, a new data set was prepared by introducing statistical errors ($\pm1\sigma$) to the calculated nominal detectors responses. The new set was then presented to the network in the "performance" mode in order to deduce the source address from the given noisy detectors responses. The percentage of successful address identification was recorded (Table 1) for each detection configuration as a function of the relative statistical error in the input (measuring time). It is shown that for a 2-detector system and 10 sec measuring time (statistical errors of about 1.5%), the network can identify successfully the source location in 81.9% of the cases studied with expectation of 0.5. Better performance is achieved when the statistical errors are lower (longer measurement time) or when more than two detectors are utilized. For 10 sec measurement, a 4-detector system identifies the source address in all cases tested. Further investigations are underway to determine the effect on the system performance of the number of detectors and their method of deployment.

Table 1 Comparison between the performances of two detection configurations using two and four detectors.

Measurement Time (sec) (Statistical error)	% Identification	
	2 Detectors	4 Detectors
1 (5%)	50.0	88.3
10 (1.5%)	81.9	100
100 (0.5%)	100	100

References

1. Rodney A. Brooks and Di chiro, G., "Principles of Computer Assisted Tomography (CAT) in Radiographic and Radioisotopic Imaging.", Phys. Med. Biol, Vol. 21, No. 5, pp. 689-732, 1976.

2. Goodenough, D.J. and Weaver, K.E., "Image levels and accuracy in computed tomography", IEEE Transactions on Nuclear Sience, Vol. NS-28, No. 2, pp. 1712-1716, April 1981.

3. Michel M. Ter-Pogossian, Marcus E. Raichle and Burton E. Sobel, "Positron Emission Tomography", Scientific American, Vol. 243, No. 4, pp. 140-155, october 1980.

4. Y. Ben-haim, E. Elias and T. Gozani, "Probabilistic approach to NDA of container with non-uniform SNM distribution", Nuclear Materials Management, Vol. 11, No. 2, summer 1982

5. Rumelhart, D.E. ,McClelland, J.L., and the PDP Research Group, Parallel Distributed Processing, (2 volumes), MIT Press, 1986

6. Lippmann, R.P, "An introduction to computing with Neural Nets", IEEE ASSP Magazine, april 1987

7. J. Hopfield and D. W. Tank, "Neural Computation of Decision in Optimization Problems", Biological Cybernetics, Vol. 52, pp. 141-152, 1985

8. E.Wacholder, J.Han and R. C. Mann, "A Neural Network Algorithem for the Multiple Traveling Salesmen Problem", Biological Cybernetics, Vol. 61, pp. 11-19, 1988 Also: ORNL/TM-10799, CESAR-88/49, (1988)

9. E.Wacholder, "A Neural Network – Based Optimization Algorithem for Weapon-Target Assignment Problem", ORSA journal on computing, Vol. 1, No. 4, pp. 232-246, 1989 Also: ORNL/TM-11025 (1989)

10. T. Kohonen, "Self Organizing and Associative Memory", Springer-Verlage, 1984

11. R. Paul. Gorman and T. J. Sejnowski, "Analysis of Hidden Units in a Layered Network Trained to Classify Sonar Targets", Neural Networks. Vol. 1, pp. 75-89, 1988

12. Yoh-Han Pao, "Adaptive Pattern Recognition and Neural Network", Addison-Wesley Publishing Company, Inc., 1989

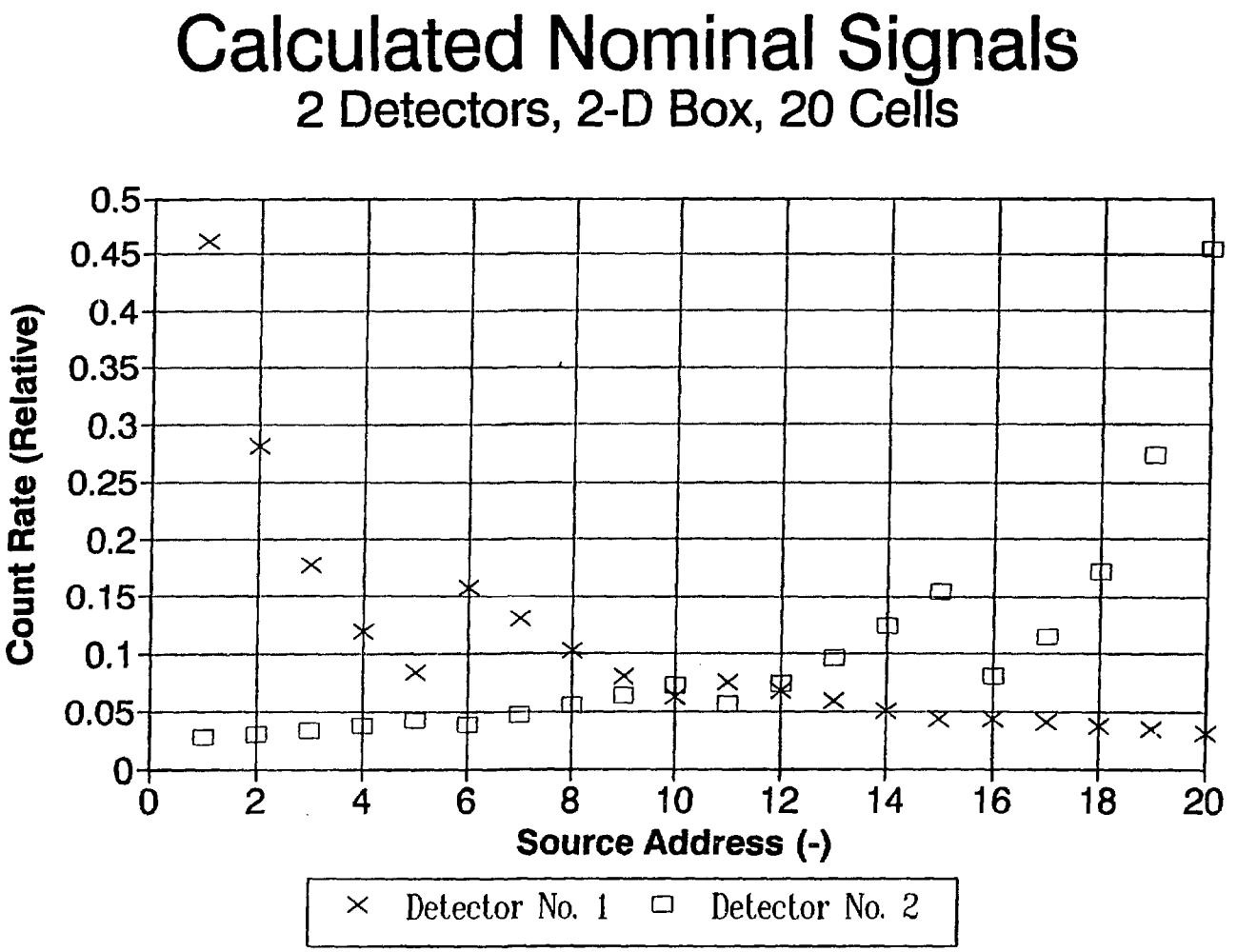

Figure 1 Calculated Nominal Signals For 2-Detector System.

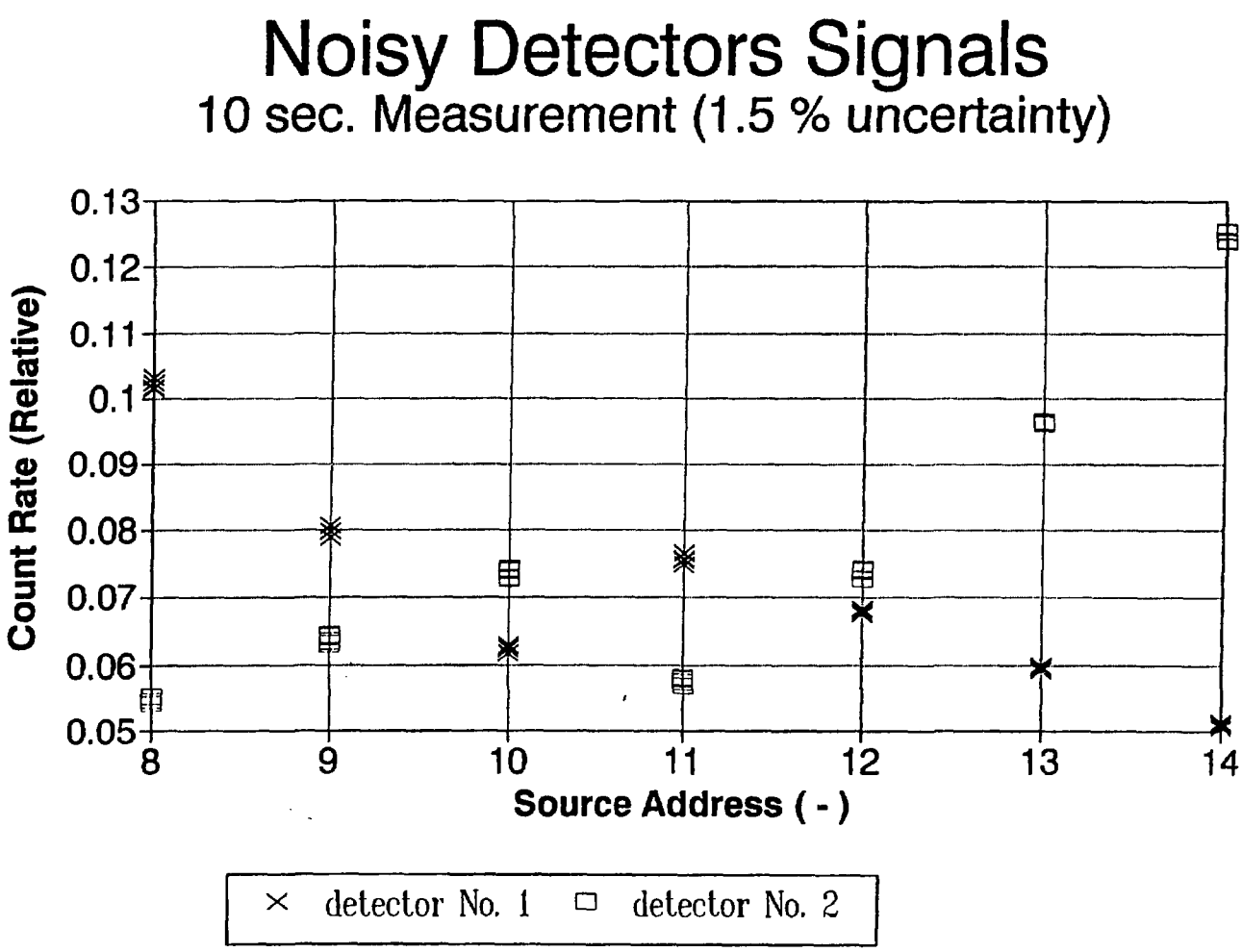

Figure 2 Noisy Detectors Signals For 10 sec. Measurement.

A REVIEW OF COMPUTER PROGRAMS APPLIED IN LEVEL 1 PROBABILISTIC SAFETY ASSESSMENT

D. Ilberg

Dept. of Applied Physics and Mathematics
Soreq Nuclear Research Center,
Yavne 70600, Israel

Introduction

Computer codes are powerful tools to perform tasks of large complexity that manual treatment can perform only with very high economic and time prices. Probabilistic Safety Assessment (PSA) entails several laborious tasks suitable for computer code assistance. During the period 1970 to 1990 a large number of computer codes intended to assist in performing the various PSA tasks were developed and employed. Reviews of the computer codes available for PSA were published in the past [NU83, NK85, CO86]. These reviews covered a partial list of the codes. A study [IA90] was initiated by IAEA in 1989 to perform a more complete review of PSA related computer codes. The study was performed as a part of a work to prepare guidelines on the selection and use of computer programs for level 1 PSA, and is published in the IAEA TECDOC - 553 [IA90] publication. This paper describes the resutls of the updated PSA code's review.

A Review of PSA Computer Codes

A review of the computer programs used in PSA studies was performed. The review covered codes used over the period from 1970 to 1990 and addressed only those relevant to level 1 PSA. About 80 codes were covered, which relate to that part of the PSA. The codes were categorized according to eleven classes, each one includes codes relevant for a particular field of application. The description of the codes and its attributes were given in some detail together with information on the hardware suited to run the codes as well as the institute that may provide them. The eleven categories of code application are:

(a) Computer codes mainly used for fault tree analysis
(b) Computer codes mainly used for uncertainty and importance analysis
(c) Computer codes mainly for dependent failure analysis
(d) Computer codes for fault tree construction
(e) Computer codes for event tree evaluation
(f) Computer codes for time dependent component unavailability
(g) Computer code packages for PSA
(h) Computer codes for PSA results processing
(i) Computer codes for overall PSA results
(j) Computer codes for state diagram analysis
(k) Other codes which are related to PSA studies

Categories (a), (b) and (g), include a large selection of computer codes. The categories (a) to (f) are well known types of PSA codes which were covered in previous reviews (e.g. [CO86], [NK85], [NU83]). Category (g) is relatively new, and includes codes which were all developed in the recent years. Most of the category (g) codes are intended for use on personal computers (PC) or minicomputer workstations.

The review include several tables that summarize, in a condensed form, the relevant information to each one of the codes covered. Two of the tables list the various codes and indicate their main field of applications (table 1 for fault tree analysis codes and table 2 for all other types of codes). These two tables are given below.

Next the review inlude eleven tables (one for each of the above listed categories) which include descriptions of the various codes found in each category. The descriptions include the following characteristics of these codes.

(a) Name of the program
(b) Application fields
(c) Brief description of the code main features and powerful options.
(d) Computer type on which the code can be run
(e) A source of the code that may be willing to distribute the code
(f) Reference to code description or additional explanations of code features.

Finally, the review covers over 130 references on PSA computer codes.

Some observations

Based on the eleven categories of the collection of PSA computer codes, Table 3 was prepared. The table 3 shows that a very large number of fault tree analysis codes exist. A large number of codes for uncertainty studies and of PSA code packages exist too. Computer codes for assistance in other PSA tasks are relatively very small in their number.

The reason for the large number of fault tree codes may be explained by two factors.

(a) Various nationalities prefer to develop their own computer code.
(b) The variety of methodologies of fault tree analysis that are implemented in differing codes. The following is an incomplete list of FTA methodologies:
(1) Fault trees
(2) Digraph (fault graph methods)
(3) GO or GO-Flow methodology

The fault tree codes can be further subdivided according to their algorithms into:

(1) Top-Down approach
(2) Bottom-Up
(3) Nelson's algorithm
(4) Qualitative (Cutsets only)
(5) Quantitative (Cutsets and probability evaluation)

The large number of PSA code-packages is a recent development (of the last five years). The 19 codes identified in the review are from 11 different countries showing that today even though a standardized tool such as the Personal Computer is available, very few cooperations in PSA code package development are found.

Computer Codes for Level-1 PSA

Area of Application	Event sequence Analysis	Plot FT	Fault Tree Analysis	State Graphs	Dependent Failure Analysis	Uncertainty Analysis	PSA Code Packages	Importance Analysis	Time Dependency	Failure Data Base	PSA Output Process	Use of Expert System	Ref.
Computer Tables Codes	4.3e	4.3d	4.3a	4.3k	4.3c	4.3b	4.3g 4.3j	4.3b	4.3f		4.3h		
CAFTA		++	++					+		++		Yes	KOS?
CAFTS		++										Yes	PO86a
EI-Intern.	+	+	++				++			++	++		QU89
EPSAP		+	++				++						EPS89
ESSM					+			++		++	++		PU87
EXPRESS		++									++	Yes	AN89,AN87
FAULT TREE								++	++	+			AR89
FAUNET			++										PL78
FTAP			++					++					RA78
FTTA			++										MA86
GO			++										GA78,EP83
GO-FLOW			++	++					++				MA88,MA89,TA89,MA85
GSI/EXPGSI				++									AN89
ISA	++												DU83
ISO-GRAM	+	++	++			+	++						ISO89
IRRAS	+	++	++			++	++	++					BA87, RU88
LESSEPS			++				++						AM89
MARKSMP			++										
MODULE		++	++			++		++					BA88
NUPRA	++	++	++			++	++	++	+	++	++		PU89
NUSSAR			++		++			++					LUXX
ORACLE			++		++		++	++			++	Yes	BA87
ORCHARD	++		++					++					OR86
PHAMISS	+	++	++		+	++		++	++				TE86
PHRASE													PHR89
PNC-CODE	++	++	++		++	++	++	++		++	++	Yes	HI89
PRISIM								++		++	++		FU87
PSAPACK(vec.2.2)	++	+	++			++	++			++			IA89
RALLY			++		++								GU84
RAPID			++		++		++		++	++	++		AP88, CH87
RELPACK							++						DR89
RELTREE		++	++					++	+				RE88
RELVEC			++		++			++					NI86, JA88
RISA		++	++			++	++	++	++	+			BE83, CA86
RISKMAN		++	++			++	++	++					AR87
SAIC							++						
SAIS							++						BA88
SALP-PC		+	++										CO87
SALP-MP			++										AS80
SARA			++		++			++			++		SA87, TU88
SETS	++		++		++		++						WO78, ST84
STARS	+		+		+		++	+			++	Yes	PO89
SUPERNET		++	++		++	++	++	++	++	+	+		RU88, BE87
SUPERPOCUS			++										FU77
THPSA	++	++	++	++	++	++	++	++					ZH89
TREE MASTER		++	++		++			+					WI88
UITAPS							++						
UPM-PIACR						++	++						LE76
WAM SUITE			++				++						ER78
WESTINGHOUSE PSA			++										ER83

++ Code intended for covering this area of application.
+ Program provides partial coverage compared to other codes in same area.

Table 2. Computer Codes for Special Application in Areas of PSA

Area of Application	Importance and Uncertainty Analysis	Dependent Failure (CMF) Analysis	Estimating Reliability Parameters	Time Dependent Maintenance & Tech. Spec. Analysis	Plotting Fault Trees	Ref.
Computer Codes	4.3b	4.3c		4.3f	4.3d	
BOUNDS	++					LE76b
COVAL	++					AS77
CONFFSI	++					NK85
DETECT	++					CO88
DPD	++					KA81
IMPORTANCE	++					LA77a
LHS	++					IM84
MOCARS	++					MA79
PROSA-2	++					VA81
SAMPLE	++					WA75
SEP*	++					WU78
SPASM	++					LE81
STADIC-II	++					OR81
STREUSL	++					SC80
TEMAC	++					IM86
BACFIRE		++				CA77
COMCAN		++				BU76
COMCAN-II		++				RA78
RIKKE		++			++ HA85,	TA81
WAMCOM		++				PU81
BAESUM			++			CO82
BAYES			++			PA89
BIDIPES			++			CO82
BROLS			++			NU83
PLG			++			KA83
FRANTIC				++		VE77
FRANTIC-III				++		GI84
SOCRATES				++		WA876
ICARUS				++		VA79
FTD					++	OL73
MAPLE-II					++	PO86b
NUPRA					++	FU89

* Principally used for importance analyses, and MCS processing

Table 3. No. of codes in each code application category

Code Category	a	b	c	d	e	f	g	h	i	j	k
No. of Codes Covered in Survey	41	18	6	9	6	4	19	3	2	5	4

References

[CO86] S. Contini and A. Poucet, "European Reliability Computer Code Index", CFC, JRC Ispra, Special Publication No. S.P.I. 05. E3. 86.90, P.E.R. 1986.

[IA90] IAEA-TECDOC-553, "Computer Codes for Level 1 Probabilistic Safety Assessment", Int. Atomic Energy Agency, Vienna, June 1990.

[NK85] NKA, "PSA Uses and Techniques - A Nordic Perspective", Nordic Liaison Committee for Atomic Energy, June 1985.

[NU83] US Nuclear Regulatory Commission, "PRA Procedure Guide", NUREG/CR-2300,1983.

CONCEPTS OF A FAILURE DATA BASE

Shimshon Arueti

Rafael A.D.A. Reliability Center

1. Introduction

A component and subsystem failure data base is one of many issues involved in system reliability and safety analysis. It is different from other related issues in several aspects:

a. The data base issue combines subjects that are technically sophisticated, such as analysis and generation of probability distributions, with subjects that are technically simple but require managerial sophistication, such as a data collection system.

b. The data base characteristics are influenced by many subjective parameters, among which are: selection of classification parameters, selection of data sources, selection of the proper specific events to be included in the data base, etc.

c. Analysis and computational methods become public domain when published in the professional literature. Data bases, on the other hand, are usually kept as proprietary or classified information. The data base often turns into a weak point due to lack of detailed and accessible data. Such data are recollected for each project, sometimes with high cost and without being able to restore lost data. This weakness can be turned into a source of strength if data are systematically collected. Such effort can give a considerable advantage over competitors.

2. Problem Description

Assume a probabilistic risk assessment (PRA) project as a typical customer for the data base, and a fault tree as the tool for system reliability analysis. PRA is usually done on systems that have low failure probabilities, which is why these probabilities cannot be directly obtained from whole system failure statistics. Component failure data are, therefore, the basis for system failure analysis. These data have to be summarized in a format that is consistent with the system model and the way they are used in it. A constant failure rate λ is an example of a parameter that can be computed from the raw data and used for the analysis. Alternatively, a distribution of λ can be used. Efficiency of the data collection and analysis process efficiency can be improved by designing a data base that contains algorithms for data analysis in addition to raw data. Such algorithms will give as output λ values or distributions for use in the fault tree.

3. Data Bases and their Application

Current application of failure data bases can be classified into the following three major groups: "use of standard generic data sources," "creation of ad-hoc specific data bases," and "combination of generic and specific data sources."

3.1 Use of Standard Data Sources

Standard data bases are such sources as American MIL-Handbooks, Rome Air Development Center (RADC) publications and other such sources that are based on standard component tests which are translated into point failure rate estimates. The main advantage of these sources is their ease of accessibility. Their disadvantages are numerous, including: specific data cannot be reported, uncertainty information is often relevant to a single test rather than to the population of similar components, updating of the data base is difficult, inconsistencies between different sources are possible, etc.

3.2 Creation of Ad-Hoc Data Bases

Assessors often recognize the need to combine generic information such as referred to in section 3.1, with system specific data based on tests and operational experience. In most cases the specific information requires mathematical and technical analysis to become useful. Some of the analysis includes: assurance of raw data relevance, identification of exposure time, classification by failure modes, adaptation to various environments, etc. Furthermore, in some cases vital information might be unavailable or inaccessible. Data analyses are done, therefore, for different projects on different levels of detail, depending on resources and availability of data.

3.3 Combination of Generic and Specific Data

The American nuclear industry will serve as a model for this approach. This industry has some unique characteristics as far as data analysis is concerned:

a. Reporting of every deviation from nominal safety conditions is mandatory. Such deviations include: component failures, human errors, loss of power, etc.

b. Many PRA specialists have translated raw failure data to generic failure rate distributions. Such distributions are then used as a basis for Bayesian updating for a specific plant using specific data.

The nuclear industry has, therefore, available data bases which include lists of components, accompanied with failure rate distributions and lists of events on which the

distributions are based. Such a data base (e.g. Ref. 1) is much more sophisticated than its predecessors, but it still has some deficiencies, such as: rigid component definitions do not allow modifications and use of data in various cross sections. There is no automatic distribution updating when new raw information is added. The data base structure is such that it is accessible to experts only.

4. Concepts for Constructing an Efficient Data Base

Section 4.1 contains a list of some objective needs for an efficient failure data base. Section 4.2 lists general characteristics for constructing such a data base.

4.1 Objective Needs for an Efficient Data Base

a. Ease of adding information to the data base.
b. Ease of adding parameters to the data base, i.e. changing interrelations between existing pieces of information.
c. The option, based on parametric data classification, to choose a subset of data for use in the analysis.
d. Immediate accessibility to the raw data sources.
e. Containment of all the relevant sources in a single data base, including expert opinion and information from tests and operational experience on various systems, under various environmental conditions, etc.
f. Ability to distinguish between acceptance tests and results from operation in nominal conditions.
g. Information on common cause failures (CCF) and other dependent events.
h. Availability of both failure and exposure data.
i. Incorporation of computational algorithms in the data base, such as:
   - Algorithm for Bayesian updating of generic distributions with specific data.
   - Algorithms for performing sensitivity studies.
   - Graphic routines for plotting distributions, time dependence charts, etc.
j. In addition to failure rates, it is useful to have information on repair times, on failure modes and on failure causes.

Aspects related to data collection must also be taken into account in addition to the technical needs listed above:

k. Creation of a mandatory and reliable reporting system, such that the data base will not rely on voluntary and partial information.
l. Data collection from a variety of sources, to assure accounting for various aspects of the information.
m. Consultation with every potential customer of the data, to avoid separate efforts for redundant data bases.

4.2 Recommended Data Base Characteristics

References 2,3 contain additional information on the recommended model. Ref. 3 is a Ph.D. dissertation in which an experimental data base with similar characteristics has been applied. I do not know of a commercial data base that is based on similar principles. The general characteristics are listed below.

a. The data base will be computerized, iterative and programmed in an object oriented language. Some examples for such languages are Smalltalk, Modula, C++ and frame based expert system shells such as KEE[4]. These languages have the capability of manipulating complex data structures, termed "objects", rather then single characters. Each object can contain text, numerical information and program routines. As an example, a component can be represented by an object that contains all the information about the component, including values of its parameters (e.g. size, energy source, failure modes and rates, etc.) and subroutines to simulate its behavior.

b. The data base will be hierarchical. Components will be grouped into "families" and "tribes" by classifying parameters. Such hierarchy enables information sharing between objects, in addition to the advantage of getting an organized and easily accessible data base. Furthermore, subroutines that simulate components' behavior can use their location in the hierarchy as a basis for decisions.

c. Some of the parameters characterizing each object (regardless of whether it represents a component or a family of components) will be a list of failure modes and prior and posterior failure distributions for each failure mode. The list will include information such as operating time before failure, failure mode and cause, severity of the failure, its repair time, and information on suspected CCFs. Generic family failure distributions will be automatically computed as a function of the specific family member distributions. It will similarly be possible to use the family generic distribution as a prior for Bayesian updating of each member using specific data.

d. Some of the behaviors that each object will be given are:
   - The capability to specify a prior failure rate by the user.
   - The capability to use the family generic distribution as a default option for a component's prior distribution.
   - The capability to create a family generic distribution as a function of the component distributions.
   - The capability for Bayesian updating of a prior failure distribution by the specific list of failures that is attached to the component.
   - The capability to classify a list of failures to "relevant" and "irrelevant" events, based on parameter values.
   - The capability to plot probability distributions and to

compute their major parameters(e.g. mean, standard deviation and median).

- The capability to compute trends, such as reliability growth.

5. References

1. A.Mosleh, S.Arueti, V.M.Bier, and S.B.Rao, "A Generic Data Base for Risk and Reliability Analysis of Light Water Reactors," PLG-500, 1988.

2. S. Arueti and G. Apostolakis, "PRA-Based Data Analysis Procedure for Use in Computerized Decision Aids, "The American Nuclear Society Topical Meeting on "Artificial Intelligence and Other Innovative Computer Applications in the Nuclear Industry," Snowbird, Utah, August 31-September 2, 1987.

3. S. Arueti, "A Prototype Knowledge Based System for Preventive Maintenance Optimization, "Ph. D. Dissertation, University of California, Los Angeles, UCLA-ENG-8942, March 1989.

4. IntelliCorp, "KEE Software Development System User's Manual," 1986.

AN EVALUATION OF THE RELIABILITY OF THE ISRAEL SEISMOGRAPH NETWORKS IN DETECTING AND RECORDING SEISMIC EVENTS AT THE SHIVTA SITE.

D. Marouani
Nuclear Project, Israel Electric Corporation Ltd
P.O.Box 10, Haifa

A. Shapira
Petroleum Infrastucture Corporation Ltd
Hamashbir 1,Holon

The purpose of this study is to evaluate the reliability of the seismograph networks in Israel, in detecting and recording seismic events which could occur at the Shivta site. The Shivta site, located in the Negev (Southern Israel), undergoes geologic and seismologic investigations for the siting of a Nuclear Power Station.

The evaluation of the probability that seismic events would not be detected or recorded, is based on a systematic quantitative analysis of the capabilities of the Shivta and Israel seismograph networks, to detect and record low magnitude events which could give indications of seismicity at the Shivta site.

In a first stage, the scenarios of total loss of detection or recording, which would lead to the impossibility to locate and assess the magnitude of these seismic events, were selected.

In the following, by means of fault-trees construction, the scenarios were developed as combinations of failures of basic instrumentation or equipment forming the Shivta and the Israel seismograph networks. Disturbances or noises which could affect transmission or reception of the seismic signals from the seismograph stations, were also included in the fault-trees.

Using the fault-trees, the scenario probabilities were calculated as a function of the empirical failure probabilities of the basic equipment, and of the likelihood of occurrence of disturbances or noises.

A very low annual probability of 3.10^{-4} was found, for loss of detection or recording of seismic events of magnitude $3 \leq M_L < 4.5$ occurring at the Shivta site. The strong radio noise occurring at the IPRG recording center due to presence of communication industries in the vicinity of the center, has been found to be the main contributor to the loss of such seismic events.

A low annual probability of about 2.10^{-3} was also found, for loss of detection of microearthquakes of magnitude $2 \leq M_L < 3$ occuring at the Shivta site. In this case, computer malfunction at the IPRG center appeared to be an important contributor ($1.5\ 10^{-4}$) to the loss of microearthquakes.

The likelihood to have a loss of detection or recording of low magnitude microearthquakes (magnitude $M_L < 2$) occurring at the Shivta site was also found to be low, 6.10^{-3} per year.
Total loss of electrical power supply at the Shivta recording center was found to be an important contributor (about 3.10^{-3} per year) to the loss of low magnitude microearthquakes occurring at Shivta.

In all the cases considered, due to the great redundancy of the seismograph stations, loss of detection has not appeared to be an important contributor to the loss of the network capabilities.

Software System Safety in N.P.P. - Problems to be Addressed

Jacob Rodnizki and Dan Ilberg
Soreq Nuclear Research Center, 70600 - Yavne, Israel

Introduction

The reactor protection system in nuclear power plants is required to be based on special safety systems which are completely independent of the plant process and control systems. These systems include: shutdown systems, emergency cooling systems, containment systems and their monitoring/actuation systems.

Until recent years computers were used for control of reactor power, but only a few designs used them in safety systems, due to the very high reliability required. However, the implementation of computers for the monitoring of safety systems in nuclear power plants, which quite accelerated in the recent years, changed this situation [Draily and Cavaco 1989, Book et al. 1988, Crowther and Cummins 1986, Ichiyen et al. 1983].

The evolution started by using software embedded systems able to analyze complex monitoring data in real time, e.g. DNBR (Departure from Nuclear Boiling Ratio) and local power density [Book et al. 1988], individual subassembly temperature [Crowther and Cummins 1986, Keats 1980], while using hardware analog devices to perform simpler functions. The TMI and Chernobyl accidents have emphasized the need for monitoring safety systems and automatic safety systems independent of human intervention.

The state of implementation of software for safety systems in nuclear power plants is most advanced in shutdown systems. The trend today is to implement fully automatic systems, using microprocessors at all levels (sensing, decision and actuation), e.g. the reactor protection system for PWRs in Belgium [Draily and Cavaco 1989] and the fully computerized shutdown system for CANDU reactors [Ichiyen et al. 1983]. The implementation of those systems includes the use of redundancy and voting, due to the conflict between availability and safety requirements.

The level of reliability requirements for safety systems is very high. For example, British requirements for reactor safety systems mandate that no single fault shall cause a reactor trip and that there be a 10^{-7} average probability, over 5000 hours, of failure to meet a demand to trip.
In software embedded systems for safety applications, where high reliability is required, a top priority should be given to the software-hardware interface.

The software-hardware interface

According to Leveson's review paper [Leveson 1986], system safety deals with the problem of insuring that a mishap does not occur during performance of a required task by a system including hardware and software subsystems. (The term mishap is used to denote an unplanned event or a series of events that results in death, injury, occupational illness, damage to or loss of equipment or property, or enviromental harm.) The use of software in critical systems introduces failures in the interface between software and hardware components, as well as between the software modules themselves. It appears to be easier to analyze the components than the interfaces between the components.
Many hardware-oriented system engineers are not software experts, because of the newness of software engineering and the significant differences between software and hardware. The same is true in reverse for software engineers [Leveson 1986].
After studying serious mishaps related to computers, safety engineers have concluded that inadequate design foresight and specification errors are the greatest cause of software safety problems. Testing can show consistency only with the requirement as specified. It cannot identify misunderstandings about the requirements. The software requirements are the specific representation of the interface between software and the processes or devices being controlled [Leveson 1986].
The two greatest difficulties encountered at the specification phase are that many of the actual requirements are not known and that system-subsystem interfaces are not accurately described or understood [Eisenbeisz 1985].

Methods to address the software hardware interface problems - recent experience

(a) Bit patterns

The use of bit patterns is recommended in order to prevent or minimize the possibility that wrong values of critical data, resulting from CMFs, could be accepted by the software [Eisenbeisz 1985]. A bit pattern consist of non-trivial combination of "zeroes" and "ones" that is unprobable as a result of a memory failure or of uncontrolled functioning of the computer. Bit patterns are used for transmitting critical logical data from a hardware end-item to a software port, for keeping safety information in flags and for generating hardware critical commands by the software.
Our review of a safety software for an embedded system has shown that the requirement to use bit patterns is achievable. Their use can be verified by the software reviewer. The review emphasized the following points:

- several port bits should be used in order to transmit critical data from a hardware end-item to the software;
- the use of flags to denote safety states should be done directly, without using temporary single-bit logical values;
- each legitimate value of a flag should be significantly different from its other legitimate values. In that respect it is recommended to include a definition for safety flags in compilers for safety software.

(b) Controlled execution of safety commands

During the generation of safety commands, undesired critical operations can be executed due to transients effects in the bits of the command port. It is therefore recommended to execute safety commands in several steps and to use more than one port to execute the command. The bits of the command port should be restored to a neutral safe state after the generation of the safety command.
Our review of a safety software (mentioned above) has shown that controlled execution of safety commands is applicable as a design requirement and can be verified by review. The review has also shown that the following points should be considered:

- In each step of the command generation, several bits should remain in a safe state;
- The bit pattern of each safety command should be significantly different from the bit pattern of the neutral state.

Summary

Design requirements regarding the use of bit patterns and controlled execution in software for embedded systems can be specified and verified. A rigorous review of their implementation contributes significantly to software safety and reliability.

References

Book, M.A. Neuschaefer, H.E. Thomsen, O.T. Wilkins, R.M. 1988. Digital protection systems upgrades. Trans. of the A.N.S., Vol. 56, 463-464.

Crowther, C. Cummins, J.D. 1986. The evolution of a computer-based reactor protection system using a fail-safe mode of operation. Science and Technology of Fast Reactor Safety. Proc. of an Int. Conf., BNES, London, Vol. 2, 265-270.

Draily, F. Cavaco, A. 1989. Evolution of the structure of the reactor protection system in Belgian nuclear power plants. nucl. Saf., Vol. 30, No. 4, (december), 511-518.

Eisenbeisz, E. 1985. Software system safety. AFISC SSH 1-1, (sept.), 1-39.

Ichiyen, N.M. Fieguth, Gelman, 1983. Digital computers in CANDU safety systems, part 1: history and concepts. IEEE Trans. on Nucl. Science, Vol. Ns-20, No.3, (June), 1908-1911.

Keats, A.B. 1980. Fail safe design criteria for computer-based reactor protection systems. Nucl. Ener., Vol. 19. No. 6. 306-317.

Leveson, N.G. 1986. Software safety: why, what, and how. Computing Surveys, Vol. 18. No. 2, (June), 125-163.

A NEW DSNP OPTION FOR HYDRAULIC NETWORKS SIMULATION

D.Gal
Soreq Nuclear Research Centre
Yavne 70600

The DSNP [1] (Dynamic Simulator for Nuclear power Plants), is a modular modeling software, developed originally for the simulation of nuclear power plants. Being based on the DSNP simulation language, the DSNP as an open-ended software, has evolved to become a general purpose modeling system for the numerical solution of mixed systems of time dependent algebraic and ordinary differential equations (ODEs). The dynamic simulation of hydraulic networks by DSNP, is based on the control volume - junction method. By this method, the energy and mass balance equations, are solved for the fluid inside a conrol volume, while the momentum balance equations, are solved for the junctions between adjacent control volumes. While the RELAP [2] and RETRAN [3] computer codes, for example, use the Porsching scheme [4] for the solution of the above balance equations, the DSNP uses for that purpose, the backward differentiation formulas (BDF) method developed by Gear [5] as implemented in the LSODE [6] code. The BDF method calls for the evaluation of the jacobian matrix either numerically or analytically. The DSNP, as a general purpose modeling system, would usually compute the jacobian numerically. Since most of the computation time is involved with the numerical evaluation of the jacobian , an effort was made to develop an algorithm which will enable the automatic evaluation of the analytical jacobian terms associated with the mass,energy and momentum balance equations.

A substantial saving of computation time (up to 70%) was achieved through the use of the new option.

1 DSNP Balance Equations

Consider a fluid flowing through the junctions ij and jl defined between three control volumes i , j , l. The DSNP employs the intensive parameter formulation of the mass energy and momentum balance equations for the description of the fluid motion.

The energy balance equation:

$$\dot{h}_j = [w_{ij}(h_i - h_j) - Q_{in} + (w_{ij} - w_{jl})/\frac{\partial \rho_j}{\partial p}]/(V_j(\rho_j + \frac{\partial \rho_j}{\partial h}/\frac{\partial \rho_j}{\partial p}) \qquad (1)$$

The mass balance equation:

$$\dot{p}_j = [(w_{ij} - w_{jl})/V_j - \frac{\partial \rho_j}{\partial h}\dot{h}_j]/\frac{\partial \rho_j}{\partial p} \tag{2}$$

The momentum balance equation:

$$\dot{w}_{ij} = (p_i - p_j - f_{ij}|w_{ij}|w_{ij} + \rho_{ij} g \Delta Z_{ij})/I_{ij} \tag{3}$$

$$I_{ij} = L_{ij}/A_{i,j} \tag{4}$$

where:

p - control volume pressure.
h - control volume specific enthalpy.
ρ - control volume mass density.
w - mass flow.
g - gravity acceleration.
Q - Power.
V - Volume.
ΔZ - elevation difference.
A - flow cross section.
I - inertance.
L - flow path length.

2 Jacobian Terms Evaluation

The new computation option, is based on performing the analytical calculation of the jacobian terms associated with equations 1-2 in each control volume module, while those associated with equation 3 are calculated in the junctions module. Assuming M control volumes and N junctions with 2M mass and energy balance equations followed by N momentum balance equations, the Jacobian terms are evaluated in the following way:

$$J_{2M+n,2M+n} = \frac{\partial \dot{w}_n}{\partial w_n} \tag{5}$$

$$J_{2M+n,2m} = \frac{\partial \dot{w}_n}{\partial p_m} \tag{6}$$

$$J_{2m-1,2M+n} = \frac{\partial \dot{h}_m}{\partial w_n} \tag{7}$$

$$J_{2m-1,2m'-1} = \frac{\partial \dot{h}_m}{\partial h_{m'}} \tag{8}$$

$$J_{2m,2M+n} = \frac{\partial \dot{p}_m}{\partial w_n} \tag{9}$$

$$J_{2m,2m'-1} = \frac{\partial \dot{p}_m}{\partial h_{m'}} \tag{10}$$

with all the other jacobian terms equal zero. The jacobian terms J_{ij} are evaluated in a new DSNP module - JACOB4.

References

[1] D. SAPHIER ,*The DSNP User's Manual*, DSNP vol. II, Rev. 4.2, RASG-112-85, Georgia Institute of Technology (1985).

[2] S. R. FISHER et al., *RELAP4/MOD6 - A Computer Program for Transient Themal-Hydraulic Analysis of Nuclear Reactors and Related Systems - User's Manual* ,CDAP-TR-003 (1978).

[3] J. H. McFADDEN et al., RETRAN-02, A Program for Transient Thrmal-Hydraulic Analysis of Complex Fluid Flow Systems, NP-1850-CCM, Electric Power Research Institute (1981).

[4] T. A. PORSCHING, J. H. MURPHY and J. A. REDFIELD, Stable Numerical Integration of Conservation Equations for Hydraulic Networks, Nucl. Sci. Eng. 43, 218-225 (1971).

[5] C. W. GEAR , *Numerical Initial Value Problems in Ordinary Differential Equations*, Prentice Hall,(1971).

[6] A. C. HINDMARSH, *LSODE and LSODI, Two New Initial Value Ordinary Differential Equation Solvers* ACM-Signum Newsletter, No. 4 pp. 10-11,(1980).

The Once Through Steam Generator Model

J. Tzoref, D. Saphier and D. Gal

Soreq Nuclear Research Center
Yavne 70600

1 The Steam Generator

A general type once through steam generator model is being developed. This model can be applied to any type of steam generator. At present its applicability to a crossflow helical tube SG used in HTGR is investigated. The steam generator consists of two concentric pipes. Between these two pipes hot primary fluid is flowing from the bottom part to the top and transfers heat to the water flowing in a bank of tubes from top to bottom. The tube bank starts from the upper part of the steam generator and winds down in helical configuration through the gap between the two pipes to the lower part of the steam generator. It then reverses and returns upwards through the inner pipe.

The steam generator can be defined as a counter-flow heat exchanger. The heat transfer process is continuous throughout both sides of this multitube and shell heat exchanger.

2 The OTSGM DSNP Module

The DSNP [1] OTSGM module, installed in the DSNP Level-Three Library [2], simulates the Once Through Steam Generator with a changeable number of nodes. The primary side, the wall and secondary side are divided into four parts, in each of which the number of nodes is provided as input data free to be selected by the user. The four parts are: subcooled, nucleate boiling, film boiling and superheated regions.

The module calculates the moving boundaries of the various regions, the temperatures and enthalpies of both primary and secondary sides and the secondary flow rate. The primary side can accommodate any fluid, such as helium, sodium or water.

3 Sample Problem

The problem selected to demonstrate the model's operation is a loss of feedwater accident. The transient is initiated by 50% decrease of the water flow within 30 seconds. The results are displayed in figures 1 to 4. The water outlet temperature (Fig. 1) responds in rapid increase until it reaches 690.5 °C within 350 seconds.

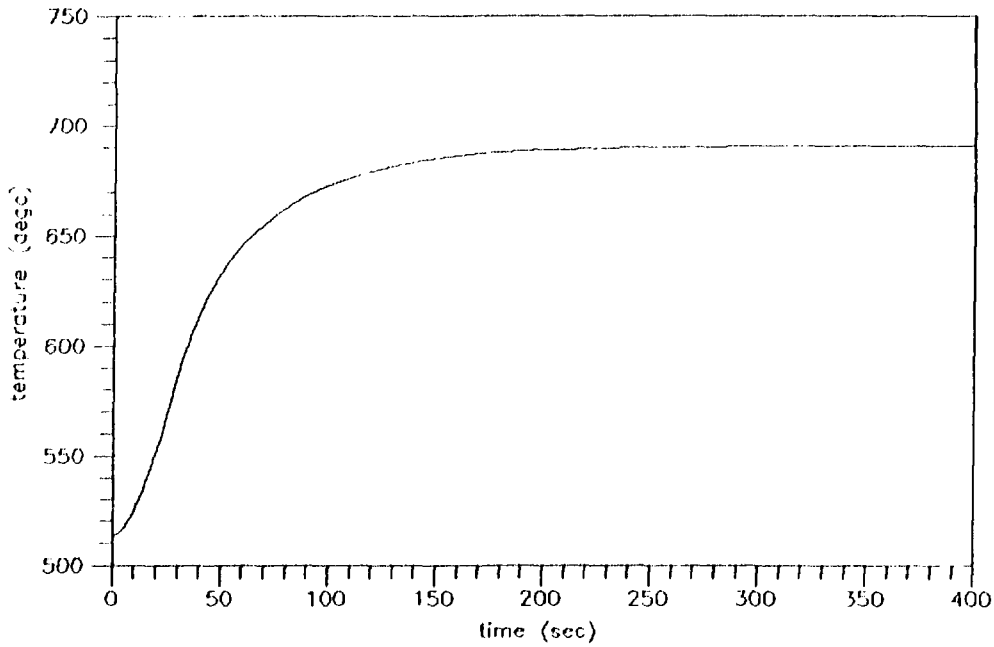

Figure 1: Secondary fluid (water) outlet temperatures

This is the limit imposed by the inlet primary fluid (helium) temperature. The helium outlet temperature increases and stabilizes on 432 °C 650 seconds (Fig. 2) after the beginning of the event, where the system reaches a new steady state. The loss of water in the steam generator constitutes a dryout, which results in the reduction of the subcooled region and expansion of the superheated region. This is demonstrated in Fig. 3, which displays the lengths of the subcooled and superheated regions during the event. The subcooled region shrinks from its initial length of 110 m to 16.5 m, whereas the superheated region expands from 28 m to 146.2 m. The boiling regions are shortened respectively. The length of the nucleate boiling region is shown in Fig. 4.

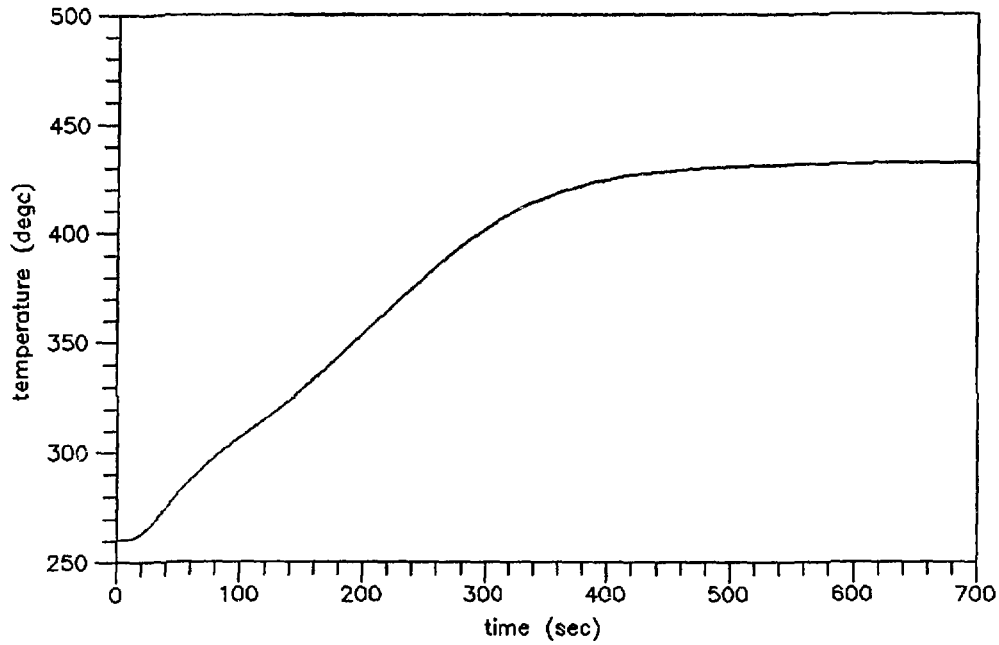

Figure 2: Primary fluid (helium) outlet temperature

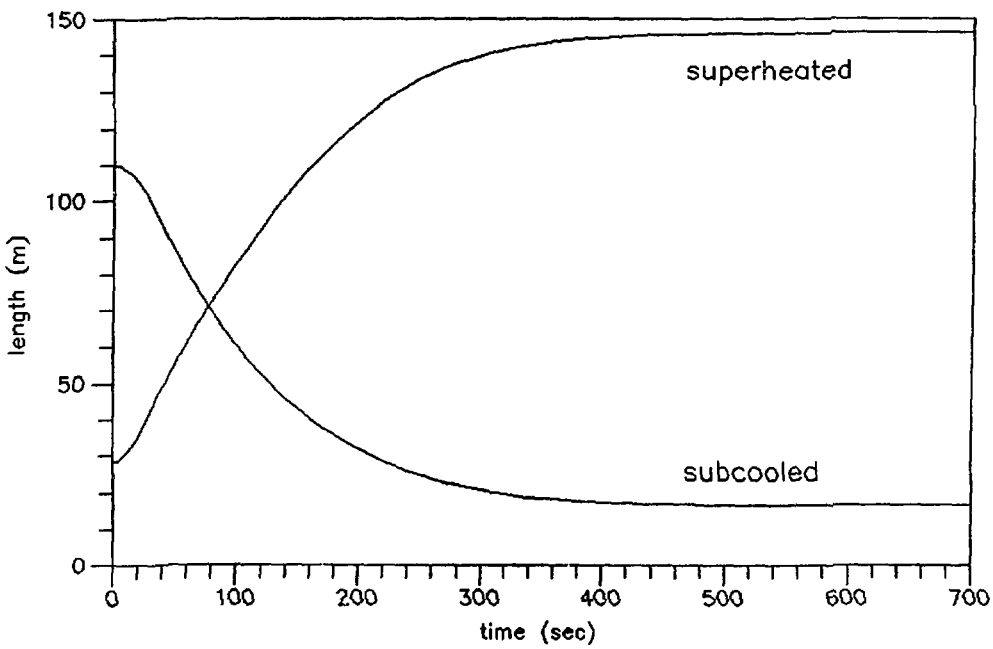

Figure 3: Lengths of the subcooled and the superheated regions

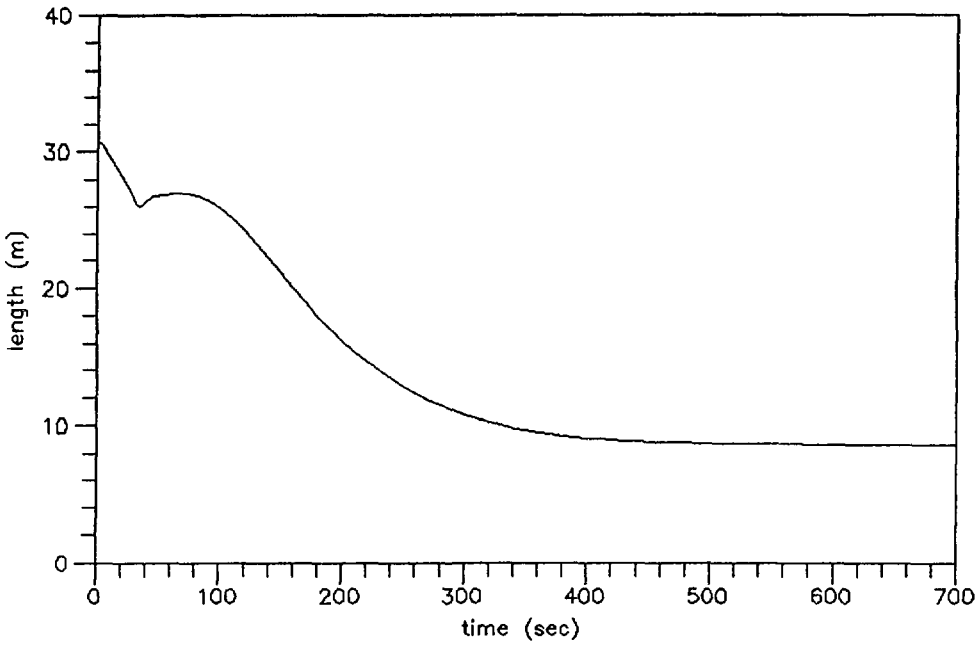

Figure 4: Length of the nucleate boiling region

References

[1] *The DSNP User's Manual* Dynamic Simulator for Nuclear Power Plants, Volume II, Revision 4.3, 1990, RASG-112-90, Soreq NRC, (1990).

[2] *The DSNP Level-Three Components Library* Dynamic Simulator for Nuclear Power Plants, Volume V, Revision 4.3, 1990, RASG-116-90, Soreq NRC, (1990).

A two-fluid model for two-phase critical flow in tubes

R. Dagan, E. Elias and E. Wacholder
Nuclear Engineering
Technion – Israel Institute of Technology, Haifa 32000, Israel

and

S. Olek
Israel Electric Corporation Ltd., P.O.B. 10, Haifa 31000, Israel

An important phase in the thermohydraulic safety design of light water nuclear reactors (especially PWR's) involves the determination of the water conditions in the various parts of the primary cooling system during depressurization, as a result of a hypothetical loss of coolant accident. The knowledge of the maximum flow coming out from the broken circuit is vital in this case as it determines the time for core uncover. This maximum two–phase flow is known as a critical or choked flow.

In single phase flow the phenomena of critical flow is well understood and can be easily computed once the initial stagnation conditions and the geometry of the flow channel are given. However, critical two–phase flow is more complicated due to the existence of different flow patterns (flow regimes) and the possibility of thermal and mechanical non–equilibrium between the phases.

Several approaches were used to solve the critical mass flow (e.g., HEM, mechanical non–equilibrium etc.), but it seems that all those methods lack some important properties of the flow. In the last decade two new attitudes were proposed, both of which are based on a two–fluid model solution. The first model, called the drift flux model deals mainly

with the momentum transfer at the interface between the phases. The second model (separated two-fluid model) emphasizes the heat and mass transfer while the momentum transfer is believed to have a minor effect on the critical flow (Richter, 1981).

Three different two-fluid models were presented by Ardron (1978), Richter (1981) and Dobran (1987), which differ in the way the interfacial heat and mass transfer processes are treated. The present work extends these models, emphasizing some new aspects, in particular with respect to the heat and mass transfer.

The model is based on five conservation equations that include mass and momentum equations for each phase and a combined energy equation. A sixth state equation is added to describe the growth of the vapor bubbles along the flow path and a seventh equation relates time to the axial position along the pipe. The model equations can be presented in a matrix form as:

$$\underline{\underline{A}}\frac{d\underline{Y}}{dz} = \underline{C} \tag{1}$$

where $\underline{\underline{A}}$ is a coefficients matrix, $\underline{C}$ is a vector containing the non-homogeneous terms of the equations and $\underline{Y}$ is vector of the seven non-dimensional state variables, $y(1) - -y(7)$, describing the liquid temperature, gas velocity, liquid velocity, flow quality, pressure, vapor bubble diameter and time, respectively. Fig. 1 shows the coefficients matrix and the right hand side vector of eq. (1). Variables in Fig. 1 have a common notation.

The matrix shown in Fig. 1, contains in the fourth row two non-zero terms. Neglecting the first one: $-y(4)/y(2)$, means that the excess latent heat due to the depressurized fluid, contributes to the vapor acceleration in addition to the mass transfer (from liquid to vapor). Solving the matrix as it is in Fig. 1 means physically that all the excess heat is assumed to increase the vapor mass only, which consequently reduces the critical flow. This kind of an assumption gave satisfactory results in a previous work (Dagan et al. 1989).

The predictions of the critical flow rate, based on the last approach, are in good agreement with a wide range of experimental resuls in laboratory and commercial pipes. The comparison between the present theoretical predictions and the experimental results of the Marviken (1982) tests in commercial pipes (Fig. 2) are representative of the success of the present model.

An important parameter in the heat transfer model, is the bubbles density number and radii along the flow channel. Ardron (1978) developed a laborious model for bubble growth and formation in the flow conduit but used an incomplete energy equation. Richter (1981) and Dobran (1987) used a constant bubble density number for all the experimental data assuming that the bubble density number is of minor importance. The present model shows that there is a substantial influence of the bubble density number on the predicted

critical mass flow rate and suggests a dependence between the bubble density number and the channel's length to diameter ratio, which is an important parameter in predicting the critical flow.

The importance of the thermal non–equilibrium effect is demonstrated in the present model. The adiabatic pressure drop at the entrance to the flow conduit is shown to control the initial degree of thermal non–equilibrium which consequently governs the critical flow rate.

In summary, a two–fluid model was presented for solving one–dimensional critical two phase flow phenomena. The model was validated against data measured in small and large scale test systems. It is shown that good agreement with experiments depends mainly on the modeling of heat and mass transfer. A recent work by Olek et al. (1990) showed that other parameters, such as bubble inertia, which were not considered here, may also be important. This subject is currently being investigated.

References

Ardron K. H., 1978, "A Two–Fluid Model for Critical Vapor Liquid Flow". Int. J. Multiphase Flow 4, 323-337.

Dagan R., Elias E., Wacholder E. and Olek S., 1989, "Two–Fluid Model for Critical Two–Phase Flow", Trans. Israel Nuc. Soc. 15, 72-75.

Dobran F., 1987, "Non–Equilibrium Modeling of Two–Phase Critical Flows in Tubes", J. heat Transfer 109, 731-738.

Olek S., Zvirin Y. and Elias E., 1990, "Bubble Growth Predictions by the Hyperbolic and Parabolic Heat Conduction Equations", Wärme und Stoffübertragung, 25, 17-26.

Richter H. J., 1981, "Separated Two–phase flow Model: Application to Critical Two–phase flow", EPRI Report NP-1800.

The Marviken project, 1982, "The Marviken full scale Critical Flow tests", EPRI Report NP-2370.

Coefficients matrix

$$\begin{Bmatrix}
\frac{(1-y(4))c_{pf}T_{fo}}{H_0} & \frac{u_g x c^*}{H_0} & \frac{u_l(1-x)c^*}{H_0} & \frac{\triangle H_v+0.5(u_g^2-u_l^2)}{H_0} & \frac{(1-x)P_0(\rho_l+T_l(\frac{\partial \rho_l}{\partial T})_P)}{H_0\rho_l^2}+\frac{y(4)P_0\frac{dH_g}{dP_{sat}}}{H_0} & 0 & 0 \\
0 & y(4)(1+\frac{\rho_l}{2\rho_g}) & -y(4)\frac{\rho_l}{2\rho_g} & \frac{y(2)-y(3)}{2} & \frac{\alpha A P_0}{Wc^*} & 0 & 0 \\
\frac{1}{\rho_l}(\frac{\partial \rho_l}{\partial T})_P T_{fo} & 0 & \frac{1}{y(3)} & \frac{1}{1-y(4)} & \frac{1}{\rho_l}(\frac{\partial \rho_l}{\partial P})_T p_0 & -\frac{3\alpha}{1-\alpha}\frac{1}{y(6)} & 0 \\
0 & \frac{y(4)}{y(2)} & 0 & -1 & \frac{y(4)P_0}{\rho_g}\left[(\frac{\partial \rho_g}{\partial P})_H+(\frac{\partial \rho_g}{\partial H})_P\frac{dH_g}{dP_{sat}}\right] & \frac{3y(4)}{y(6)} & 0 \\
0 & -y(4)\frac{\rho_l}{2\rho_g} & y(4)(\frac{\rho_l}{2\rho_g}-1)+1 & \frac{y(2)-y(3)}{2} & \frac{(1-\alpha)AP_0}{Wc^*} & 0 & 0 \\
0 & 0 & 0 & 0 & \frac{P_0}{3\rho_g}\left[(\frac{\partial \rho_g}{\partial P})_H+(\frac{\partial \rho_g}{\partial H})_P\frac{dH_g}{dP_{sat}}\right] & \frac{1}{y(6)} & 0 \\
0 & 0 & 0 & 0 & 0 & 0 & 1
\end{Bmatrix}$$

Right hand side vector

$$\left\{ 0 \quad -\frac{F_{lg}^* A}{c^* W} \quad -\frac{1}{A}\frac{dA}{dZ} \quad -\frac{y(4)}{A}\frac{dA}{dZ} \quad \frac{(F_{lg}^*-F_{wl})A}{c^* W} \quad \frac{2k_l}{D\rho_g \triangle H_v u_g}\left[\frac{\triangle T+at}{R}+\frac{\triangle T+2at}{\sqrt{\alpha_D \pi t}}+\frac{\triangle T 0.6 Re^{0.5} P_r^{0.33}}{2R}\right] \quad \frac{1}{u_g} \right\}^T$$

Fig. 1 Non-dimensional matrix for the model solution

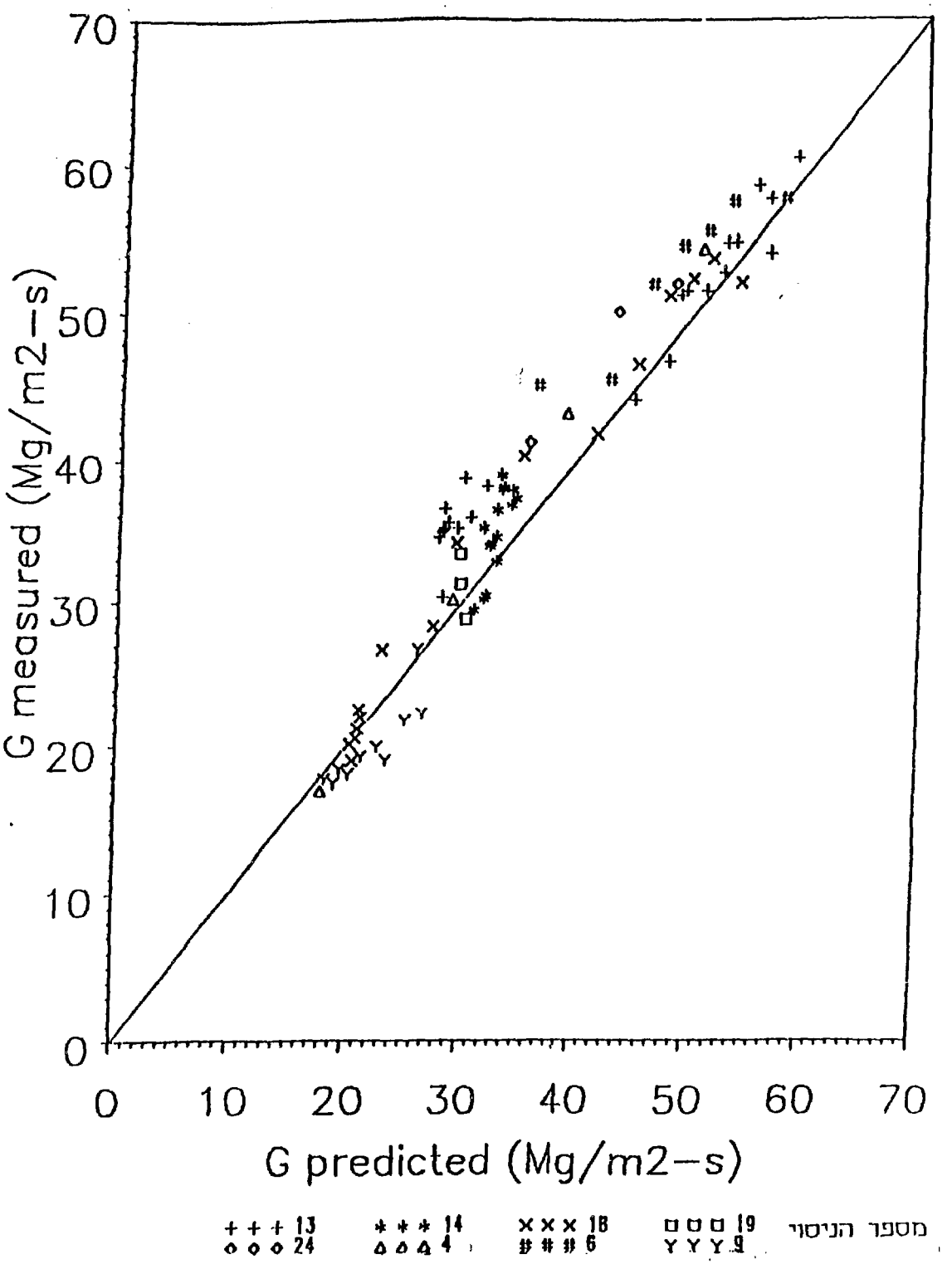

Fig. 2. Comparison of present theoretical predictions to the experimental results of Marviken 1982. The stagnation conditions are a subcooled liquid with a converging nozzle at the inlet of the pipe.

AN ANALYTICAL SOLUTION TO A BUBBLE GROWTH PROBLEM

Shmuel Olek

Research and Development division,
Israel Electric Corporation Ltd.,
P.O. Box 10, Haifa 31000, Israel

1 Introduction

Extensive work has been done on bubble growth because of its importance in the fields of boiling and two-phase flow. Generally, the studies have been devided into growth rates controlled by inertia forces, applicable in the range of a relatively low pressure and high Jakob numbers, e.g. Rayleigh (1917) and, growth rates for heat difussion controlled growth, e.g. Plesset and Zwick (1954) and Forster and Zuber (1954).

In this investigation an analytical solution is derived for a bubble growth equation originally obtained by Plesset and Zwick (1954) for a conduction-controlled growth. For a long time only approximate solutions to this equation were presented by solving for the bubble as though it was of plane shape with a correction factor to compensate for sphericity. Only recently, an exact solution was presented by Olek et al. (1990). In the present work we revisit the solution of this equation by another powerful method, the decomposition method. An advantage of the decomposition method is that it can provide analytical approximation to a rather wide class of nonlinear (and stochastic) equations without linearization, perturbation, closure approximations, or discretization methods which can result in massive numerical computation. While the solution obtained by decomposition is generally an infinite sereis, an n-term approximation, ϕ_n, usually serves as a practical solution. An accurate solution is often obtained with very small values of n. The decomposition method has some features in common with other methods, but it is distinctly different on closer examination, and it offers significant advantages (Adomian, 1988).

2 The Decomposition Method

Begin with an equation $Fu(t) = g(t)$, where F represents a general nonlinear differential operator involving both linear and nonlinear terms. The linear term is decomposed into $L + R$, where L is easily invertible and R is the remainder of the linear operator. For convenience, L may be taken as the highest order derivative that avoids difficult integrations which result when complicated Green's functions are involved. Thus, the equation may be written

$$Lu + Ru + Nu = g, \tag{1}$$

where Nu represents the nonlinear terms. Solving for Lu,

$$Lu = g - Ru - Nu. \tag{2}$$

Because L is invertible, an equivalent expression is

$$L^{-1}Lu = L^{-1}g - L^{-1}Ru - L^{-1}Nu. \tag{3}$$

If this corresponds to an initial-value problem, the integral operator L^{-1} may be regarded as definite integrals from t_0 to t. If L is a second-order operator, L^{-1} is a twofold integration operator and $L^{-1}Lu = u - u(t_0) - (t - t_0)u'(t_0)$. For boundary value problems (and, if desired, for initial-value problems as well), indefinite integrations are used and the constants are evaluated from the given conditions. Solving (3) for u yields

$$u = A + Bt + L^{-1}g - L^{-1}Ru - L^{-1}Nu. \tag{4}$$

The nonlinear term Nu will be equated to $\sum_{n=0}^{\infty} A_n$, where the A_n are special polynomials to be discussed, and u will be decomposed into $\sum_{n=0}^{\infty} u_n$, with u_0 identified as $A+Bt+L^{-1}g$

$$\sum_{n=0}^{\infty} u_n = u_0 - L^{-1}R\sum_{n=0}^{\infty} u_n - L^{-1}N\sum_{n=0}^{\infty} A_n. \tag{5}$$

Consequently, we can write

$$u_1 = -L^{-1}Ru_0 - L^{-1}A_0$$

$$u_2 = -L^{-1}Ru_1 - L^{-1}A_1$$

$$\vdots$$

$$u_{n+1} = -L^{-1}Ru_n - L^{-1}A_n \tag{6}$$

The polynomials A_n are generated for each nonlinearity so that A_0 depends only on u_0, A_1 depends only on u_0 and u_1, A_2 depends on u_0, u_1, u_2, etc. All of the u_n components are calculable, and $u = \sum_{n=0}^{\infty} u_n$. If the series converges, the n-term partial sum $\phi_n = \sum_{i=0}^{n-1} u_i$ will be the approximate solution since $\lim_{n\to\infty} \phi_n = \sum_{i=0}^{\infty} = u$ by definition. It is important to emphasize that the A_n can be calculated for complicated nonlinearities of the form $f(u, u', \ldots)$ or $f(g(u))$ (Adomian 1988).

The A_n polynomials are defined by (Adomian, 1986)

$$A_0 = f(u_0)$$

$$A_1 = u_1(d/du_0)f(u_0)$$

$$A_2 = u_2(d/du_0)f(u_0) + (u_1^2/2!)(d^2/du_0^2)f(u_0)$$

$$A_3 = u_3(d/du_0)f(u_0) + u_1u_2(d^2/du_0^2)f(u_0) + (u_1^3/3!)(d^3/du_0^3)f(u_0) \tag{7}$$

$$\vdots$$

Alternative definitions and formulas have been discussed in Adomian (1986) and elsewhere. One form for A_n is

$$A_n = (1/n!)\sum_{\nu=1}^{n} c(\nu, n)d^{\nu}f/du^{\nu} \tag{8}$$

where the second index in the coefficient is the order of the derivative and the first index progresses from 1 to n along with the order of the derivative. In the linear case $f(u) = u$, and the A_n reduce to u_n. Otherwise $A_n = A_n(u_0, u_1, \ldots, u_n)$. For $f(u) = u^2$, for example, $A_0 = u_0^2$, $A_1 = 2u_0u_1$, $A_2 = u_1^2 + 2u_0u_2$, $A_3 = 2u_1u_2 + 2u_0u_3, \ldots$ It is to be noted that in this scheme, the sum of the subscripts in each term of the A_n are equal to n. It is possible to find simple symmetry rules for writing the A_n quickly to high orders, see e.g. Adomian (1986).

3 Analysis

The equation describing a conduction-controlled bubble growth in dimensionless variables is given by, e.g. Olek et al. (1990)

$$\frac{dR}{dt} = 2Ja[R^{-1} + (2\pi t)^{-1/2}] \tag{9}$$

where R is the radius, t denotes time and Ja is the Jakob number. Upon introducing a new variable $x = (2Jat)^{-1/2}$, equation (10) becomes

$$\frac{dR}{dx} = 2xR^{-1} + 2c \tag{10}$$

where $c = (Ja/\pi)^{1/2}$. Following the steps outlined above for the decomposition method, the following solution is obtained

$$R(x) = R_0 + R_1 + R_2 + \ldots \tag{11}$$

with the first few terms given by

$$R_0 = R(0) + 2cx \tag{12}$$

$$R_1 = \{2cx - \log[R(0) - 2cx]R(0)\}/2c^2 \tag{13}$$

$$R_2 = \{2\log[R(0) - 2cx]^2 cR(0) + \log[R(0) - 2cx]^2 R(0)^2 + 8\log[R(0) - 2cx]cR(0)x$$

$$+6\log[R(0) - 2cx]R(0)^2 - 8c^2x^2 - 12cR(0)x\}/\{8c^4[R(0) + 2cx]\} \tag{14}$$

4 Results and Discussion

The exact solution obtained by Olek et al. (1990) has the following implicit form

$$t = (4Ja)^{-1}R(0)^2[(4Jat)^{-1/2}R^2 - (2\pi t)^{-1/2}R - 1]^{-1}$$

$$\times\left\{\frac{(2Ja^{-1}t^{-1/2}R - (2\pi)^{-1/2} - [(2\pi)^{-1} + Ja^{-1}]^{1/2}}{(2Ja^{-1}t^{-1/2}R - (2\pi)^{-1/2} + [(2\pi)^{-1} + Ja^{-1}]^{1/2}}\right\}^{(-1+2\pi Ja^{-1})^{-1/2}} \tag{15}$$

The prsesent solution is obviously more convenient to use since it has an explicit form. Few terms are needed to achieve an excellent accuracy, as can be realized from the example presented in Table 1. It shows a comparison between analytical and numerical solutions of the bubble growth equation. The numerical solution is obtained by using Gear's method with subroutine DIVPAG from the IMSL library, and the analytical solution consists of only two terms in the series.

Table 1. A comparison between an analytical and a numerical solution for bubble growth, for $R(0) = 10^{-6}$ and $Ja = 100$.

t	R (analytical)	R (numerical)
0.000	0.000	0.000
0.001	5.124	5.125
0.002	7.247	7.248
0.003	8.876	8.877
0.004	10.249	10.250
0.005	11.458	11.459
0.006	12.552	12.553
0.007	13.558	13.559
0.008	14.494	14.495
0.009	15.373	15.374
0.010	16.205	16.206

The use of the decomposition method for solving nonlinear equations has been demonstrated for a relatively simple bubble growth equation. It can be employed for the solution of more complicated nonlinear bubble growth equations.

Literature

Adomian, G. 1986. "Nonlinear Stochastic Operator Equation". Academic Press.

Adomian, G. 1988. "A Review of the Decomposition Method in Applied Mathematics". J. Math. Anal. Appl. **135**, 501-544.

Forster, H. K. and Zuber, N. 1954. "Growth of a Vapour Bubble in a Superheated Liquid". J. Appl. Phys. **25**, 474-478.

Plesset, M. S. and Zwick, S. A. 1954. "The Growth of Bubbles in Superheated Liquids". J. Appl. Phys. **25** , 493-500.

Rayleigh, L. 1917. "Pressure due to Collapse of Bubbles". Phil. Mag. **94**.

NUCLEAR MEDICINE

Breast Cancer from View-Point of Nuclear Medicine

L. Csernay

Department of Nuclear Medicine
Albert Szent-Gyorgyi Medical University Szeged, Hungary

Abstract

Breast cancer is the most serious malignancy of women in Hungary with increasing morbidity and mortality. Early diagnosis of the primary and its recurrences is of great importance in therapeutic success. Radionuclide studies were applied at the primary staging (1.) and follow-up (2.) of the disease.

Conclusions:

1. Preoperative axillary lymph node scan using radiolabelled microcolloids is of limited value in primary nodal staging (mainly in localized diseases) because of the high rate of false negative cases. At the same time preoperative (pretreatment) internal mammary lymph node scan is of great value in centrally and medially localized tumours, and mastitis carcinometosa.
   Whole body bone scan should be performed at primary staging in every case, even in young patients with localized tumour.

2. After primary therapy, axillary lymph node scan is suitable for prediction of axillary recurrence;
   Internal mammary lymph node scan is a useful diagnostic tool when local/regional recurrence, sternal solitary, and contralateral tumour are suspected, and in planning of therapy.
   Whole body bone scan should be performed yearly independently of the patient's complaints and the primary staging. When the occurence of bone metastases is suspected, the follow-up, enlarged images of the vertebrae by pinhole collimator, and/or bone marrow scan by radiocolloids may offer prompt differential diagnosis of the lesion(s).
   ECG-gated radionuclide ventriculography is suggested before and after chemotherapy (anthracyclines).

The speaker reviews in detail the results at his institute based on a 10-year follow-up of 950 breast cancer patients.

SCANNING OF MURINE TRANSPLANTED TUMORS IN VIVO WITH INDIUM-111 DIHEMATOPORPHYRIN ETHER

[1]Quastel, M.R., [2]Richter, A.M, and [3]Levy, J.G.

[1]Institute of Nuclear Medicine, Soroka Medical Center and Faculty of Health Sciences, Ben Gurion University of the Negev, Beer Sheva, TRIUMF, Vancouver, Canada
[2]Quadralogic Technologies, Vancouver, B.C., Canada
[3]Department of Microbiology,University of British Columbia, Vancouver, Canada

Dihematoporphyrin ether (DHE, Photofrin II), a preparation of hematoporphyrin derivative enriched for di- and oligoporphyrin ethers (or esters), is useful for photodynamic therapy due to light-induced release of a singlet oxygen leading to photosensitivity and cytotoxicity. A radiolabeled DHE which could be used for the quantiative measurement of tumor uptake would be of value in this type of therapy.

DHE was radiolabeled with In-111 by an adaption of the method of Lavallee and Fawwaz (1) in which heating of DHE was kept not greater than 65 degrees C. Its uptake and distribution in tumor bearing mice was examined, in comparison to that of In-111 chloride. The tumors were murine M1 rhabdomyosarcoma cells originally induced by methylcholanthrene. Gamma camera images were obtained at various intervals after i.v. injection. Measurements of organ biodistribution of the agents were made following sacrifice by cervical dislocation, and the results compared to those of *in vivo* imaging. The agents were extracted from the tumor and other tissues by a technique based on the solubility of In-111 DHE in ethylacetate, and estimates of the degree of dissociation of In-111 from DHE in the tissues were made after various time intervals. The effect of excess unlabeled DHE on the distribution of In-111 DHE was examined to assess the change in tissue affinity for DHE caused by In-111 metallation. The results of the study were as follows:

1. In-111 DHE showed distribution in the tissues closely corresponding to that found for H-3- and C-141-HPD by Gomer and Dougherty (2) and for C-14-DHE by Bellnier et al (3). The distribution in the tissues of In-111 given as the chloride differed markedly from that of In-111 DHE and corresponded well to that reported by Saha and Farrer (4).

2. Tumors showed marked uptake of both In-111 preparations. However, In-111 DHE was taken up and retained in the peripheral tissues much less than In-111 chloride, except for liver and kidneys which took up heavy concentrations of both agents, and the tumor:muscle ratios for In-111 DHE were2-3 times greater than for In-111 when given as the chloride.

3. Scintiscanning *in vivo* showed intense tumor concentrations of both agents. However, the fraction of In-111 DHE appearing in the tumor images (about 5% of the total injected agent) corresponded well with that found by direct counting of the dissected tumor tissue. In contrast, about 70% of the In-111 chloride observed by scanning over the tumors *in vivo* appeared to be in the swollen and edematous tissue surrounding the tumors and not in the tumor tissue itself.

3. About 80% of the In-111 DHE extracted from tumors remained undissociated one day after administration, and more than 70% of the extractable agent in tumors was found undissociated after 4 days. None of the In-111 given as chloride was extracted from tumors or from other tissues into ethylacetate.

4. When cold DHE was given in excess (molar ratio increased by a factor of 16), the In-111 DHE was partly displaced from liver and appeared in significantly higher concentrations in the tumor. This suggests that binding sites in the liver may have higher affinity for the DHE than for In-111 DHE, but that the mechanism of tumor uptake of DHE is not inhibited by the In-111 metallation.

It is concluded that In-111 DHE distributes biologically and is concentrated by tumors *in vivo* in a way similar to that of DHE, and may therefore be of potential use to photodynamic therapy for the quantitative estimate of DHE tumor uptake.

(1) Lavallee DK and Fawwaz R (1986) Nuc Med Biol **13**; 639
(2) Gomer CJ and Dougherty TJ (1979) Cancer Res **39**; 146
(3) Bellnier DA, Ho YK, Pandey RK, Missert JR and Dougherty TJ Photochem Photobiol **50**, 221
(4) Saha GB and Farrer PA (1975) *in* 'Radiopharmaceuticals' (Eds Subramaian G, Rhodes BA, Cooper JF and Sodd VJ) p 435, Soc Nuc Med, New York.

Tl-201 SPECT IN DETERMINING RESIDUAL MALIGNANT BRAIN TUMOR BURDEN

M. Lorberboym,* A. Hercbergs,+ and L. Lieberman*

* Department of Nuclear Medicine and + Department of Oncology, Sheba Medical Center, Tel Hashomer

High grade astrocytoma and glioblastoma multiforme are the most common primary malignant brain tumors in adults. The use of combined radiation and chemotherapy have been shown to improve the survival time of these patients. However, identification of tumor residual or tumor recurrence has been unreliable with computerized tomography (CT) and magnetic resonance imaging (MRI) because of brain and tumor necrosis following treatment.

Recent studies with Thallium-201 (Tl-201) suggest that brain imaging with this radionuclide may correlate better with the presence of residual tumor tissue than CT or MRI. Tl-201 was first used by Kawana et al. in 1970 for myocardial imaging. Being a potassium analog Tl-201 depends on regional blood flow and has been used to study pulmonary tumors, melanoma, skeletal muscle function, and is used extensively in nuclear cardiology.

Several mechanisms have been suggested for the improved accuracy of Tl-201 imaging for residual or recurrent brain tumor after therapy. Normal brain tissue has low uptake of Tl-201 but breakdown of the normal blood brain barrier allows an increase in Tl-201 concentration in the affected brain tissue. More importantly, malignant tissue shows an increase in the Na-K-ATPase pump and as Tl-201 is a K analog increaed Tl-201 uptake can be seen. Thus the combination of blood flow, breakdown of the normal blood brain barrier, and the increased K uptake due to the Na-K-ATPase pump provides the possibility of grading the malignancy based on Tl-201 concentration.

We have studied 16 patients with malignant brain tumors using single photon emission computerized tomography (SPECT) and IV Tl-201. Patients were referred from the Department of Oncology for identification of residual tumor tissue after chemotherapy and/or radiation therapy. Fourteen males and 2 females aged 21-65 years were studied after IV injection of 4 mCi Tl-201. SPECT, using an Elscint SP4 digital gamma camera was begun 5 minutes after injection. Sixty frames were acquired in 64X64 matrix in approximately 30 minutes. Reconstruction was done using a Butterworth filter with no attenuation correction. Images were reconstructed in saggital, coronal, and transverse planes. Results of the SPECT findings were compared with CT and/or MRI studies that were done within a week to 10 days of the SPECT.

In 13 of the 16 patients the SPECT studies were positive showing lesions that were usually smaller in size and more discrete than the lesions seen on CT or MRI. All lesions had tumor to contalateral normal tissue ratios above 2.0 agreeing with published reports suggesting that ratios over 1.5 represent grade 3-4 malignancy. Three patients had negative SPECT studies; 1 patient with tumor grade 1-2 and 2 patients with tumors grade 3-4.

SPECT scans generally showed lesions that were more discrete than those seen on CT or MRI suggesting that cerebral edema, fibrosis, and necrosis are not imaged by Tl-201 SPECT in the same manner as CT or MRI. A number of patients were noted to have additional lesions on SPECT that were not noted on CT or MRI.

Our results confirm previous reports in the literature that Tl-201 offers the most accurate technique for assessing the response to therapy in patients with brain tumors. CT and MRI cannot distinguish residual viable tumor from tumor necrosis. Tl-201 shows good target to normal tissue ratios within minutes after injection and persists for a period long enough to perform SPECT. Blood brain barrier injury caused by cerebral edema does not cause an increased concentration of Tl-201 and neither fibrosis nor necrosis causes abnormal Tl-201 uptake. It has been reported that steroid therapy does not interfere with Tl-201 SPECT.

Compared with other available imaging modalities Tl-201 provides the most accurate representation of tumor burden following chemotherapy and/or radiation therapy. It offers an excellent complimentary technique to the anatomic results obtained with CT and MRI. Although all of our patient were studied after surgery and adjuvant therapy we are extending our studies to patients suspected of having brain tumors to determine the utility of Tl-201 SPECT prior to surgery.

A NEW SCINTIGRAPHIC METHOD FOR DIAGNOSING INFLAMMATION OR INFECTION USING IN-111 LABELED NON-SPECIFIC HUMAN IgG

I. Garty, A.N. Serafini, and G. Sfakianakis

The University of Miami
Jackson Memorial Medical Center,
Miami, Florida

Radiolabeled non-specific immunoglobulin was first used by Rubin et al. to image infection. He suggested that the mechanism of localization was probably due to the Fc portion of the IgG molecule.

We studied 35 patients with an In-111 DTPA IgG kit provided by the R. W. Johnson Pharmaceutical Research Institute as part of a Phase 2 study to determine safety and efficacy of the kit preparation.

Thirty-five patients with suspected inflammation/infection were entered into the Phase 2 study. The patients ranged in age from 22-83 years. There were 20 females and 15 males. In order to enter the study all patients were required to fulfill one or more of the following requirements:

a. A focal collection seen on an imaging study such as ultrasound, CT, MRI, or conventional radiography, within one week of the In-DTPA IgG study.

b. All patients had to manifest fever greater than 100.5 F for more than 3 days duration.

c. Patients had to have abdominal and/or pelvic pain greater than 3 days duration not related to a diarrheal disease; or, presence of vascular prosthesis or aneurysm or orthopedic prosthesis; or positive culture at the suspected site of inflammation.

All patients had physical examination, and appropriate laboratory studies. Patients were injected with 1.4-2.3 mCi of In-111-DTPA. Using an LFOV with a medium energy collimator anterior and posterior images of the head and neck, chest, abdomen, pelvis and extremities were obtained at approximately 9, 24, and usually 48 hr after injection. If images were negative or equivocal SPECT images were done at 24 and 48 hr.

The primary sites of infection in the 35 patients included 2 head/neck, 9 chest, 2 abdomen, 12 pelvis, and 10 extremities. The duration of the infection/inflammation ranged from 3-180 days.

Four of the 35 patients were excluded because they were unevaluable due to technical problems or lack of follow-up data. Thirty of the 31 evaluable patients (96%) showed a positive In-111 DTPA IgG study. One patient had hydronephrosis with a urine culture positive for E. Coli in whom the scan was considered to be negative. There were no adverse reactions or significant changes in any of the baseline studies thought to be due to the radiopharmaceutical.

Our study suggests that In-111 DTPA IgG can be used with no untoward effects and has a high sensitivity for detecting a wide variety of infections in various organs and for infections/inflammations of varying durations. In addition, all but 1 patient showed a positive scan within 9 hr and only 2 patients showed better localization at 24 hr than at the earlier time period. The kit has several major advantages that include ease of preparation and high quality images with a readily available radionuclide. We believe that it will provide a major advance in the imaging of infection.

SCINTISCANNING OF SOFT TISSUE TUMORS WITH ^{99m}Tc-DTPA

[1]Goshen, E., [2]Meller, I., [1]Lantsberg, S. and [1]Quastel, M. R.

[1]Institute of Nuclear Medicine and [2]Department of Orthopedics
Soroka Medical Center and Faculty of Health Sciences,
Ben Gurion University of the Negev
Beer Sheva, Israel

Several reports have described localization of Tc-99m DTPA in the soft tissue lesions of neurofibromatosis (1-4) and have thus suggested the possible use of this agent in the diagnostic evaluation of other soft tissue tumors. We describe a prospective investigation of soft tissue tumor imaging with Tc-99m DTPA. Emphasis is placed on the correlation between results of 3 phase scintiscans (dynamic flow, 5 minute blood pool and 2 hour late imaging) and consequent histopathological findings.

Three phase DTPA scans were carried out for over 50 patients and the results categorized as being consistently positive (12 cases), progressively positive (7 cases), progressively negative (6 cases) and consistently negative (25 cases). The soft tissue tumors which localized DTPA in any or all of the 3 phases belonged to a heterogeneous group of pathologies with the common denominator appearing to be fibrous tissue. On the other hand, the consistently negative group was comprised solely of lipomatous tissue. No lipomas appeared in other groups and no histopathologies other than lipomas were reported for the consistently negative groups. With the exclusion of the lipomas, all soft tissue tumors demonstrated DTPA uptake in at least one of the phases of the study.

Fifteen randomly selected patients underwent blood flow studies with Tc-99m labeled red cells to evaluate the possibility of a correlation between DTPA localization and the vascularity of the soft tissue tumors. The consistently negative DTPA group did not show any evidence of increased vascularity. However, no correlation with vascularity was observed in most cases with positive DTPA localization.

The following conclusions may be drawn from this study:

1. Increased DTPA uptake is not specific for neurofibroma as it occurs in various other soft tissue tumors.

2. Absence of Tc-99m DTPA uptake in all 3 phases is highly suggestive of lipoma (predictive probability 94.8%).

3. DTPA localization does not appear to be related to vascularity in the tumor. Our current working hypothesis is that it is associated with the tumor content of fibrous tissue.

4. DTPA localization does not differentiate between benign and malignant lesions.

Alterations of Regional Cerebral Blood Flow Detected by Tc-99m-HMPAO SPECT in Pediatric Epileptic Disorders

Clara Ben-Horin,+ Eli Shahar,++ Natan Brand,++ and Lionel Lieberman,+ Department of Nuclear Medicine,+ and Child Neurology Unit,++ Chaim Sheba Medical Center, Tel Hashomer and Sackler School of Medicine, Tel-Aviv University, Israel

Regional cerebral blood flow (rCBF) perturbations in nine infants and children with epileptic disorders between the ages of 9 months and 13 years were studied with single photon emission computerized tomography (SPECT) using Tc-99m-HMPAO. The rCBF patterns were correlated with the patient's clinical presentation and EEG patterns and with radiologic data that included CT and MRI studies.

Seven children with focal or multi-focal disturbances on EEG had either focal seizures or focal seizures with secondary generalization. Tc-99m-HMPAO SPECT showed focal rCBF alterations in all seven children. Four children had a focal structural abnormality of the brain best demonstrated by MRI and both EEG and HMPAO SPECT showed findings that correlated with the structural abnormality. Three patients with overt seizures had focally increased rCBF that correlated with EEG aberrations suggestive of ictal phenomena. Four children had focally decreased rCBF suggestive of an inter-ictal pattern. One patient showed a rCBF abnormality that was more widespread than suggested by EEG and CT findings. In two patients with generalized epileptic disturbances there was no correlation between the SPECT findings and the EEG and radiologic studies.

Our preliminary data suggests that Tc-99m-HMPAO SPECT brain imaging is a safe and sensitive diagnostic procedure for the detection and localization of altered rCBF in children with focal epileptic disorders.

A NOTE OF CAUTION REGARDING THE USE OF THE 75-SeHCAT TEST TO DIAGNOSE BILE ACID MALABSORPTION.

David L. Chamovitz, Rafael Bruck and Simon Bar-Meir
Departments of Nuclear Medicine and Gastroenterology
The Edith Wolfson Hospital, Holon and Tel-Aviv University,
Sackler School of Medicine, Israel.

INTRODUCTION

Bile acid malabsorption (BAM), either primary idiopathic or secondary to ileal disease or resection is one of the causes for chronic diarrhea. In practice however, it may be difficult to prove the role of BAM in a patient with chronic diarrhea and complicated tests are needed. Recently, a test was introduced for the diagnosis of BAM, based on a substance labeled with selenium-75, 23-selena-homocholyltaurine (75-SeHCAT), with biological characteristics very similar to cholyltaurine (1 - 4).

A hint that the actual retention values may vary in different populations was indicatd by Merrick et al (4). They mentioned the lower retention values found in northern Sweden and postulated a higher fiber diet to be responsible.

The present study was undertaken to evaluate the accuracy of the 75-SeHCAT test.

PATIENTS AND METHODS

Patients

Nineteen subjects who were studied, were divided into 3 groups. The first group which served as a control consisted of 8 subjects, 5 men and 3 women. Their ages ranged from 25 - 64 years. None had a history of chronic diarrhea and in all a normal ileum and colon were demonstrated on barium studies. Their routine blood chemistry, d-xylose test and 24 hour stool fat were within normal limits. The second group consisted of 9 patients, 3 men and 6 women.

Their ages ranged from 17-67 years. All had chronic unexplained diarrhea (CUD) (3-6 watery movements/day) of more than 6 months duration and a normal work up for diarrhea, including barium studies of the gastrointestinal tract, flexible sigmoidoscopy with mucosal biopsy and laboratory investigations including blood count, routine blood chemistry, serum carotene, serum immunoglobulins, thyroxine, 24 hour stool fat and d-xylose test. The third group included 2 patients with Crohn's disease after partial resection of the terminal ileum.

75-SeHCAT Test

Following an 8 hour fast, a 370 KBq (10 μCi) 75-SeHCAT capsule (provided by Amersham Radiochemical Centre) was administered orally. The 75-Se activity in the abdomen was measured both by a large field of view uncollimated gamma camera (Apex Elscint) and by a collimated 2 inch sodium iodide crystal probe (Picker). The results with varied techniques differed by no more than 1% retention at least in the lower retention range. For camera counting a 270±20% window was employed with distances maximized for each patients (approximately 35 cm); for the probe, a 60-320 keV window and a distance of 40 cm. Anterior and posterior recording s were made and geometrically averaged. Measurements were made with continued fast at 3 hours after administration of 75-SeHCAT and 7 days later.

Cholestyramine Test

Cholestyramine was given to 8 of the patients with chronic diarrhea and to the 2 patients with ileal resection twice daily for a total dose of 6-8 gm/day for one week. When cholestyramine was not effective in relieving diarrhea, the drug was discontinued and test was considered negative. In those patients for whom cholestyramine was effective, it was discontinued for 7 days and restarted if diarrhea recurred. The test was considered positive when diarrhea ceased during cholestyramine treatment and recurred on its discontinuation. Stool frequency was deemed the average number of bowel movements per day. Return to a more solid state accompanied each reduction in stool frequency after cholestyramine.

Results

Retention of less than 8% was found in 4 of the 9 patients with CUD, in both patients with ileal resection and in 2 of the 8 normal controls. If a retention of less than 4% is considered pathologic, only one patient with CUD (3% retention) and 2 patients with ileal resection (0 and 1% retention) would have been considered to have BAM.

On the other hand, cholestyramine was effective in relieving diarrhea in 5 patients, 2 patients with ileal resection and 3 patients with CUD who had 6,7 and 26% retention. The latter patient pre-treatment excreted 1150 gm stool /24 hr. Two other CUD patients without ileal resection who retained 3% (500gm stool/24 hr pre-treatment) and 4%, respectively, had no response to 8 gm/day of cholestyramine.

Discussion

Previous reports indicated lower limits of normal retention of 6 to 19% with positive correlation with cholestyramine treatment. Our failure to find a lower limit of normal for 75-SeHCAT retention and the lack of correlation between test results and response to cholestyramine represent a significant variance from the literature.

Possible reasons for this variance have been considered and discounted. Measuring techniques: Multiple methods with two measuring instruments with varying distances, windows, etc. revealed 1% variations. Conflicting medications such as antispasmotics, antacids, antibiotics and cholestyramine: None. Prior cholecystectomy or vagotomy: None. Dietary fiber content: No difference from a "western" type diet nor correlation with individual intakes were noted. Dose of cholestyramine: Our dose of 6 - 8 gm/day compared favorably to the 2 - 8 gm/day reported.

Conclusion

In this limited study of 19 patients it is evident using treatment with cholestyramine as the "gold standard" for diagnosing BAM that the 75-SeCHAT test gives spurious results. Of 9 patients with CUD there were 2 false positive and 1 false negative tests.

Contrary to all published results our preliminary study casts doubt on the accuracy of 75-SeHCAT retention test in diagnosing BAM in patiens with CUD.

REFERENCES

1. Thaysen EH, Orholm M, Arnfred T, et al. Assessment of ileal function by abdominal counting of the retention of a gamma emitting bile acid analogue. Gut 1982;23:862-5.

2. Fagan EA, Chadwick VS, Baird I McL. SeHCAT absorption: a simple test of ileal dysfunction. Digestion 1983;26:159-65.

3. Merrick MV, Eastwood MA, Ford MJ. Is bile acid malabsorption underdiagnosed? An evaluation of accuracy of diagnosis by measurement of SeHCAT retention. Br Med J 1985;290:665-8.

4. Sciarretta G, Fagioli G, Furno A, et al. 75-SeHCAT test in the detection of bile acid malabsorption in functional diarrhea and its correlation with small bowel transit. Gut 1987;28:970-5.

The Hemodynamic Effects of Nisoldipine on Silent Myocardial Ischemia

A radionuclide ventriculographic study

Steinmetz A, Shemesh J, Fisman EZ, Kellerman JJ

Cardiac Rehabilitation Institute
Department of Nuclear Medicine
Sheba Medical Center

Sackler Faculty of Medicine
Tel-Aviv University

The purpose of this study was to assess the influence of Nisoldipine (NP) on patients with silent myocardial ischemia. We evaluated the hemodynamic effects of short-term oral administration of NP by means of radionuclide ventriculography(RNV).

Nineteen male patients (mean age 62 +/- 6 years) with documented coronary artery disease, but without angina pectoris or impaired left ventricular function were selected. In a randomized double blind manner 10 mg of NP was given once a day in the morning during two weeks and placebo in the next fortnight or vice versa. Resting and stress RNV-s were performed at the beginning of the study as baseline,after the first two weeks and after the second two weeks.

During the resting studies mean heart rate rose from 68 to 73 ($p<0.05$ compared to placebo and baseline).Left ventricular end diastolic volume (EDV) and end systolic volume (ESV) did not show significant differences.However ejection fraction (EF) increased from 62% to 66% ($p<0.05$). Peak ejection rate (PER) increased from 2.9 to 3.2 EDV/sec and peak filling rate (PFR) from 2.10 to 2.55 EDV/sec ($p<0.05$ for both).Cardiac output (CO) rose from 5.6 to 6.5 l/min ($p<0.01$).Estimated systemic vascular resistance (ESVR) decreased from baseline 1382 to 1082 dyn_sec_cm-5 with NP and to 1357 with placebo.

At stress ESV increased from 51 to 74 ml in the baseline study and from 47 to 61 ml with NP ($p<0.01$),but EF did not show significant differences. PER rose from 3.2 to 4.0 EDV/sec and PFR from 2.55 to 5.50 EDV/sec ($p<0.05$ compared to placebo).

Our conclusion is that Nisoldipine (compared to placebo) reduces, but does not completely abolish the stress induced myocardial ischemia as reflected by the mild increase in ESV. NP did not show undesirable hemodynamic effects, on the contrary, there was a significant improvement in some parameters (EF,PER,PFR,ESVR).

AUTHOR INDEX

האגודות הגרעיניות בישראל

האגודה הישראלית למדעי הגרעין
האגודה הישראלית להגנה מקרינה
האגודה הישראלית לרפואה גרעינית
האגודה הישראלית לפיסיקה רפואית
האגודה הישראלית לחקר הקרינה

כנס האגודות הגרעיניות תשנ"א

דברי הכנס

ה ר צ ל י ה

חנוכה תשנ"א

כרך 16

האגודות הגרעיניות בישראל

האגודה הישראלית למדעי הגרעין
האגודה הישראלית להגנה מקרינה
האגודה הישראלית לרפואה גרעינית
האגודה הישראלית לפיסיקה רפואית
האגודה הישראלית לחקר הקרינה

כנס האגודות הגרעיניות תשנ"א

דברי הכנס

ח ו צ ל י ה

חנוכה תשנ"א